Nonlinear Instability of Compressible Mixing Layers

by

Clifford Anthony Sparks

A thesis presented for the degree of
Doctor of Philosophy of the University of London
and for the
Diploma of Membership of Imperial College

Department of Mathematics
Imperial College London
180 Queen's Gate
London SW7 2BZ

© Clifford Anthony Sparks 2006

Abstract

The transition of laminar flow to turbulence is one of the unresolved fundamental problems in fluid mechanics, and also a problem of great practical significance. A particular prototype flow is a free shear layer, which can support the well-known Kelvin-Helmholtz instability. The resulting spatially amplifying waves roll up to form large-scale coherent structures, which subsequently break down into random small-scale motions. Both the large- and small-scale motions have a profound effect on mixing, which controls radiation of noise and also combustion in the case of chemically reacting fuel-oxidizer mixing layers.

Since the Reynolds numbers (R) of interest are usually very high, asymptotic techniques based on a large-R assumption have been used to develop relevant mathematical theories for the evolution of the instability waves. An important recent advance is non-equilibrium critical-layer theory, which focuses on the crucial role of the critical layer (i.e. the region surrounding the level at which the phase velocity of the wave equals the mean-flow velocity). Various competing effects such as nonlinearity, viscosity and non-equilibrium, which are negligible in the main bulk of the flow, have to be taken into account in the critical layer because they control the nonlinear dynamics in a delicate manner. Mixing primarily takes place in this layer.

Previous studies show that in the incompressible regime (i.e. Mach number $M = 0$), the critical-layer dynamics is strongly nonlinear, with nonlinearity being associated with the logarithmic singularity of the velocity fluctuation. In the fully compressible regime ($M = \mathcal{O}(1)$), nonlinearity is associated with a simple-pole singularity of the temperature fluctuation, and enters in a weakly nonlinear fashion. The former theory can describe vortex roll-up whilst the latter cannot.

In this thesis, we are first concerned with the weakly compressible mixing layer, corresponding to a distinguished small-Mach-number regime $M = \mathcal{O}(\epsilon^{1/4})$ (where $\epsilon \ll 1$ is a measure of the instability wave amplitude), in which both compressibility and strong nonlinearity are included. A nonlinear evolution system describing the development of vorticity and temperature disturbances is derived. It is further noted that for typical base-flow profiles, T_c', the mean temperature gradient at the critical level controlling the strength of the pole singularity, is small, even when $M = \mathcal{O}(1)$. By treating T_c' as an independent parameter of $\mathcal{O}(\epsilon^{1/2})$, we develop a composite strongly nonlinear theory which is valid for moderate $\mathcal{O}(1)$ Mach numbers, for which subsonic modes are the most unstable. We demonstrate further that the key result in the weakly nonlinear theory for $M = \mathcal{O}(1)$ can be derived from

the strongly nonlinear system. Thus the two theories can be unified. Numerical solutions show that the strongly nonlinear theory is able to describe the nonlinear evolution of the subsonic modes in the mixing layer from $M = 0$ to $M = \mathcal{O}(1)$, in particular the vortex roll-up process, which is the most prominent characteristic of mixing-layer transition. The theory offers an effective tool for investigating the nonlinear instability of mixing layers at high Reynolds numbers, from which one may infer the mixing properties.

The mathematical framework is employed to study the nonlinear evolution of disturbances of the sideband form, consisting of a dominant fundamental wave and two modes in its sideband. It is found that for suitable initial conditions, the sideband interaction can cause one or both sideband modes to amplify rapidly, generate a difference-frequency mode with an exceptionally large amplitude, and in the fully interactive stage, cause the amplitude of the disturbance to exhibit oscillation. These predictions are in qualitative agreement with experimental observations.

Contents

1 Introduction **4**

1.1 Incompressible flows 6

1.1.1 Linear instability theory 6

1.1.2 Nonlinear instability theory 12

1.2 Compressible flows 15

1.2.1 Linear instability theory 15

1.2.2 Nonlinear instability theory 19

1.3 Instability and transition of the compressible mixing layer: practical relevance and experimental studies 21

1.4 Scope of the present study 24

2 Formulation & Outer Flow **27**

2.1 Problem specifIcation and governing equations 27

2.2 Basic flow 30

2.3 Perturbations 33

2.4 Outer flow 33

3 Nonlinear Critical Layer **40**

3.1 Scaling arguments 40

3.2 Critical layer analysis 44

4 Extensions to the Fully Compressible Regime **48**

4.1 The case $T_c' \approx 0, M = \mathcal{O}(1)$ 48

4.2 Composite theory 50

4.3 Decomposition of solution 51

4.4 Upstream linear critical layer 53

4.5 Weakly nonlinear limit: amplitude equation 54

5 Numerical Solution **60**
5.1 Solution of eigenvalue problem and evaluation of coefficients 60
5.1.1 Viscosity laws 72
5.1.2 Upstream linear solutions 73
5.2 Nonlinear calculation 76
5.2.1 Strongly nonlinear evolution system 76
5.2.2 Weakly nonlinear amplitude equation 81
5.3 Vorticity and temperature within the critical layer 81
5.4 A note on scaling 82
5.5 Results 83
5.5.1 Case I: $\beta_T = 1$, $M = 1/2$ 84
5.5.2 Case II: $\beta_T \neq 1$, $M = 1/2$ 92
5.5.3 Case III: $\beta_T = 1$, $M = \mathcal{O}(1)$ 101
5.5.4 Case IV: $\beta_T \neq 1$, $M = \mathcal{O}(1)$ 109
5.6 Effect of β_U 118
5.7 Effect of base profile 129
5.8 Comparisons between strongly and weakly nonlinear predictions . . . 136
5.9 Unusual large-$\bar{\mathcal{X}}$ behaviour 142

6 Sideband Instability **143**
6.1 Introduction 143
6.2 Linear sideband instability 144
6.2.1 Results 149
6.3 Nonlinear evolution of sideband waves 156
6.3.1 Results 160
6.4 Conclusions 167

7 Summary & Further Work **168**
7.1 Summary 168
7.2 Further work 170

A Complementary Solutions of Equations (4.4.37) & (4.4.38) **172**

B Role of β_U in the Critical-layer System **174**

C Code Validation **177**

Acknowledgments **184**

References **185**

Chapter 1

Introduction

Transition of a laminar flow to a turbulent state is one of the many fundamental processes of interest in fluid dynamics. Laminar flow refers to a state of fluid flow exhibiting relatively simple spatial and temporal order. A precise definition of turbulence is lacking, but it is characterised by apparent spatial and temporal randomness, consisting of motions at different length and time scales. In many practical applications, turbulence is unwanted, for example when it emits noise in a jet or increases drag over an aerofoil. On other occasions, it can be beneficial, for example in chemical reactions and combustion, where turbulence can improve mixing efficiency. In any case an understanding of when and/or where turbulence occurs is extremely valuable for flow control.

Transition to turbulence is a complicated process involving a sequence of changes in flow states, which may take place in different fashions. For closed or semi-closed flows, transition from one state to another occurs when a relevant parameter goes through a critical value. Such an abrupt change of state is called bifurcation. A famous example is Taylor-Couette flow (Taylor 1923), the flow between rotating coaxial cylinders. As the angular velocity of rotation Ω (or Taylor number in non-dimensional terms) exceeds a critical value, the axially uniform flow gives way to axially periodic cellular patterns, which are referred to as Taylor vortices. As Ω is further increased, the steady cells become unsteady and lose the axisymmetry. Wavy vortices travelling in the circumferential direction appear (see, for example, Swinney & Gollub 1981). The exact sequence leading to turbulence has yet to be established. One of possible scenarios, first conjectured by Landau (1944), is that the flow may undergo a sequence of period-doubling bifurcations, leading ultimately to a complete chaotic state.

Another example demonstrating a sequence of bifurcations before turbulence is

the flow past a circular cylinder. As the flow speed is increased, the initially symmetric steady flow begins to lose its fore-and-aft symmetry. The flow separates behind the cylinder and elliptical recirculation zones form in the wake, growing to several cylinder radii. The flow is still steady, but further flow speed increase causes time-periodic behaviour in the wake. The flow continues to exhibit more complex quasi-periodic patterns before three-dimensional effects occur, shortly followed by the onset of turbulence (see, for example, Jackson 1987).

For open flows, such as the flow around an aircraft wing, transition takes place in space, i.e. for a given flow conflguration and parameters, part of the flow may be laminar whilst the other part is turbulent. For flow past a flat plate, the fluid is laminar near the leading edge but it is turbulent downstream. Sandwiched between the laminar and turbulent states is a complex and often three-dimensional transition region (Kachanov 1994). The idea of successive bifurcations is not directly applicable in this case since transition is not controlled by a global parameter.

The reason that bifurcation occurs is that the current flow becomes unstable. Stability analyses therefore represent a first step towards understanding transition. The initial stage of instability is investigated by introducing a (small) disturbance to an otherwise undisturbed mean flow. The resulting mathematical system constitutes an initial-(boundary)-value problem that describes the evolution of the disturbance. If there exists a type of disturbance that eventually becomes large, then the flow is said to be unstable, while if all disturbances are found to decay, then the flow is said to be stable.

Sufficiently small disturbances permit linearisation of the evolution system. However even this simplified system is often difficult to solve analytically for a general flow. Moreover, the problem is complicated by the need to specify all initial conditions. To simplify, one is forced to consider a relatively simple class of flows, which exhibit homogeneity in one or two directions. For these flows, it is possible to seek solutions of normal-mode form. Physically, these represent travelling waves. This so-called normal-mode approach transforms the initial-value problem into a much more tractable eigenvalue problem. By solving the eigenvalue problem, one is able to identify the critical parameter at which a change of flow state (bifurcation) occurs. Also, for a given parameter, it allows one to determine the most rapidly growing mode. It must be mentioned that normal modes are special forms of disturbance, and there arises a question as to their relevance to the evolution of an arbitrary disturbance. Mathematically, the latter may be represented as a superposition of normal modes if and only if the set of eigenfunctions is complete.

The modes grow exponentially, with the most rapidly growing mode outgrowing the other modes and eventually becoming large. A nonlinear theory must then be developed to describe the continued evolution of the disturbance. Nonlinear effects can come into play in different ways. Firstly, in the simplest (and idealised) case of a single normal mode, the disturbance interacts with itself to generate various harmonics and a mean-flow distortion. As a result, the mode no longer follows exponential growth. Secondly, co-existing normal modes can interact with each other rather than evolving independently (as in the linear theory).

A very common form of disturbance consists of a discrete or continuous band of modes with nearly the same frequencies. This is known as a *sideband* disturbance. The mutual interaction of the components within the sideband may lead to interesting energy exchanges among them. Another important form of disturbance is the so-called *resonant triad*, which consists of three normal modes such that the sums of the frequencies and wavenumbers of any two modes equal those of the other. This allows the interaction between any two of the modes to affect the other. Such a resonant interaction can cause some of the modes to experience very rapid amplification (Craik 1985).

In the next section, we introduce and review in greater detail the normal-mode approach to linear instability and the issues relating to nonlinear interactions of normal modes, with particular attention paid to mixing layers.

1.1 Incompressible flows

1.1.1 Linear instability theory

Inviscid instability

One of the simplest flows satisfying the Navier-Stokes equations is unidirectional parallel flow, which has a non-zero velocity $\boldsymbol{U} = U(y)\mathbf{i}$ in the direction $\mathbf{i}$ say, where y is a coordinate transverse to $\mathbf{i}$. An example of this type of flow is plane Poiseuille flow. Suppose that this basic flow is perturbed by a small perturbation $\tilde{\boldsymbol{u}}(\boldsymbol{x}, t) = (\tilde{u}, \tilde{v}, \tilde{w})$, where $\boldsymbol{x}$ is the position $\boldsymbol{x} = (x, y, z)$ and t the time, so that the perturbed velocity field can be written as

$$\boldsymbol{u}(\boldsymbol{x}, t) = \boldsymbol{U}(y) + \tilde{\boldsymbol{u}}(\boldsymbol{x}, t). \tag{1.1.1}$$

Similarly if the basic pressure is P then

$$p(\boldsymbol{x}, t) = P + \tilde{p}(\boldsymbol{x}, t) \tag{1.1.2}$$

is the perturbed pressure field, where $\tilde{p}(\boldsymbol{x},t)$ is the perturbation pressure. Such perturbations may be generated from wall roughness effects, residual fluctuations in the free-stream, or more often the interaction between them. The complex process by which such factors excite instability waves is called *receptivity*. However, our concern here is not with the origin of the waves, rather it is with the characteristic waves that a mean flow can support and the subsequent development after they are excited.

Now substitute $\boldsymbol{u}$ into the Navier-Stokes equations, neglecting the small nonlinear terms to obtain a set of linearised equations. In the inviscid flow limit they may be written as

$$\nabla \cdot \tilde{\boldsymbol{u}} = 0, \tag{1.1.3}$$

$$\left(\frac{\partial}{\partial t} + U\frac{\partial}{\partial x}\right)\tilde{\boldsymbol{u}} + \frac{\mathrm{d}U}{\mathrm{d}y}\tilde{v}\mathbf{i} = -\nabla\tilde{p}. \tag{1.1.4}$$

For exactly parallel flows, the coefficients in the equations are independent of x, z and t. This allows us to take the so-called normal-mode approach, whereby the perturbations are of the form

$$\tilde{\boldsymbol{q}}(\boldsymbol{x},t) = \hat{\boldsymbol{q}}(y)\mathrm{e}^{\mathrm{i}(\alpha x+\beta z-\alpha ct)} + \text{c.c.} \tag{1.1.5}$$

where α and β are the wavenumbers in the x and z directions respectively, c is the phase speed and c.c. stands for complex conjugate. Each perturbation represents a travelling wave, with frequency $\omega = \alpha c$.

We can choose to analyse spatial stability by fixing ω and β real, or temporal stability by fixing α and β real. A flow is spatially unstable if $(-\alpha_{\mathrm{i}}) > 0$ (where $\alpha = \alpha_{\mathrm{r}} + \mathrm{i}\alpha_{\mathrm{i}}$) so that perturbations grow without bound as they propagate downstream. A flow is temporally unstable if $c_{\mathrm{i}} > 0$ (where $c = c_{\mathrm{r}} + \mathrm{i}c_{\mathrm{i}}$) so that perturbations grow without bound at each fixed point of the flow for large enough time. In many experimental situations it is spatial instability rather than temporal instability that is observed.

Substitution of the normal modes into equations (1.1.3) and (1.1.4) leads to a second-order ordinary differential equation

$$\big(U-c\big)\big(\hat{p}'' - (\alpha^2+\beta^2)\hat{p}\big) - 2U'\hat{p}' = 0, \tag{1.1.6}$$

which is known as *Rayleigh's stability equation* (Rayleigh 1880).

A famous transformation by Squire (1933) (originally used for viscous instability), namely

$$\bar{\alpha} = \sqrt{(\alpha^2+\beta^2)} \tag{1.1.7}$$

and

$$\bar{u} = \frac{(\alpha\hat{u} + \beta\hat{w})}{\bar{\alpha}}, \qquad \bar{p} = \frac{\bar{\alpha}\hat{p}}{\alpha}, \tag{1.1.8}$$

reduces the instability problem from three spatial dimensions to two with an equivalent wavenumber $\bar{\alpha}$. This is advantageous because for temporal modes each unstable three-dimensional mode corresponds to a more unstable two-dimensional mode, and so we need only study the two-dimensional problem. Unfortunately this is not true in general if spatial modes and/or viscous effects are considered. Transformations of Squire-type can also be used for other cases, such as magnetohydrodynamic and compressible problems, but again it is not always the case that three-dimensional modes are less unstable than two-dimensional modes (see, for example, Betchov & Criminale 1967).

For the two-dimensional case, we may introduce a streamfunction, whereby $\tilde{u} = \partial\widetilde{\psi}/\partial y$ and $\tilde{v} = -\partial\widetilde{\psi}/\partial x$ with $\widetilde{\psi} = \phi(y)\mathrm{e}^{\mathrm{i}\bar{\alpha}(x-ct)}$. We then obtain

$$(U - c)(\phi'' - \bar{\alpha}^2\phi) - U''\phi = 0, \tag{1.1.9}$$

which is the more familiar form of Rayleigh's equation. The boundary conditions for a bounded flow would be $\phi(y) = 0$ at $y = y_1, y_2$, and for an unbounded flow $\phi(y) = 0$ at $y = -\infty, \infty$. These conditions correspond to the vanishing of normal velocity at the boundaries. The solutions of Rayleigh's equation satisfying the boundary conditions exist only when an eigenvalue relation, $\mathcal{F}(\bar{\alpha}, c) = 0$, is satisfied. Inspection of this eigenvalue problem shows that to each damped stable mode there is a corresponding amplified unstable mode, and vice versa. This may seem paradoxical, but we note that we have excluded viscosity, inclusion of which destroys such a "mirror" relation (for example see Drazin 2002, p143).

We see that if c is real, i.e. if the mode is neutrally stable, Rayleigh's stability equation may have a singularity at the point or points y_c in the domain of flow where $U(y_\mathrm{c}) = c$. If this occurs, the plane where $y = y_\mathrm{c}$ is called a *critical level*, and the thin layer centred at y_c is called a *critical layer*. As will be seen, the critical layer plays a significant role in the dynamics of instability waves.

Rayleigh (1880) showed that occurrence of an inflectional point (i.e. $U''(y) = 0$) in the basic velocity profile is a necessary condition for instability. Fjϕrtoft (1950) improved this by showing that a necessary condition for instability is that $U''(U - U_\mathrm{s}) < 0$ somewhere in the flow field, where y_s is a point at which $U''(y_\mathrm{s}) = 0$ and $U_\mathrm{s} = U(y_\mathrm{s})$. Balmforth & Morrison (1999) found a necessary and sufficient condition. Howard (1961) showed that if a mode is unstable then

$$\left(c_\mathrm{r} - \frac{1}{2}(U_\mathrm{min} + U_\mathrm{max})\right)^2 + c_\mathrm{i}^2 \leqslant \frac{1}{4}(U_\mathrm{max} - U_\mathrm{min})^2 \tag{1.1.10}$$

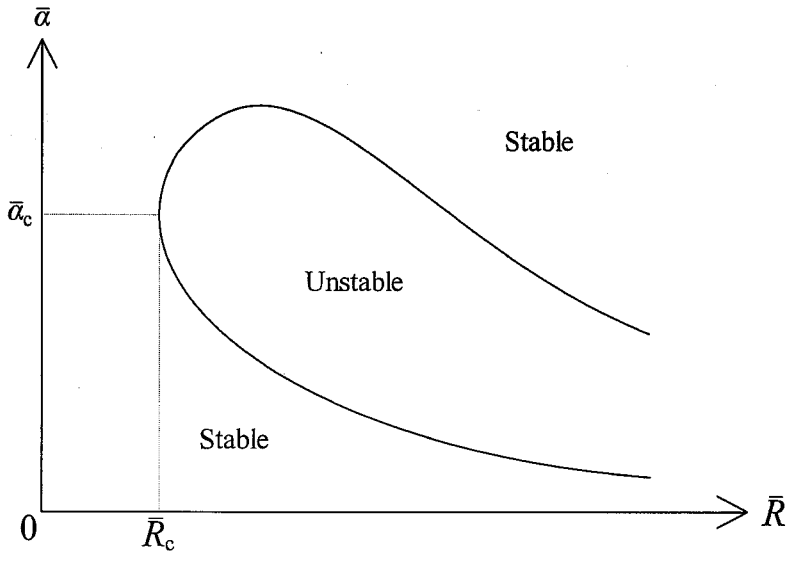


Figure 1.1: Sketch of a typical neutral curve of instability in the $(\bar{R}, \bar{\alpha})$-plane.

where $U_{\min} = \min\big(U(y) : y_1 \leqslant y \leqslant y_2\big)$ and $U_{\max} = \max\big(U(y) : y_1 \leqslant y \leqslant y_2\big)$. Equation (1.1.10) is known as *Howard's semicircle theorem*, and is an upper bound on the growth rate of an unstable mode. This bound was improved by Hickernell (1985).

Viscous instability

An important parameter characterising viscous flows is the Reynolds number, defined as

$$R = \frac{VL}{\nu} \tag{1.1.11}$$

where V is a typical velocity, L a typical length scale and ν is the kinematic viscosity of the fluid. This is a key parameter in stability analysis, since, very often, an increase in Reynolds number is accompanied by a decrease in flow stability. It was first introduced by Reynolds (1883) when investigating the transition to turbulence of the flow through a pipe. The laminar flow is exactly parallel, for which the Reynolds number can be regarded as a true parameter, where we can set (for example) V to be the speed of the fluid through the centre of the pipe and L the pipe radius. Laminar flow is found for $R < R_c$ and turbulence for $R > R_c$, where R_c is called the critical Reynolds number.

When viscosity is included, the linearised equations for the perturbation are

$$\nabla \cdot \tilde{\boldsymbol{u}} = 0 \tag{1.1.12}$$

and

$$\Big(\frac{\partial}{\partial t}+U\frac{\partial}{\partial x}\Big)\tilde{\boldsymbol{u}}+\frac{\mathrm{d}U}{\mathrm{d}y}\tilde{v}\mathbf{i}=-\nabla\tilde{p}+\frac{1}{R}\nabla^2\tilde{\boldsymbol{u}}. \tag{1.1.13}$$

Following the normal-mode approach in the previous section, writing $\tilde{u}$, $\tilde{v}$, $\tilde{w}$ and $\tilde{p}$ in the form (1.1.5), we obtain

$$\mathrm{i}(\alpha\hat{u}+\beta\hat{w})+\frac{\mathrm{d}\hat{v}}{\mathrm{d}y}=0, \tag{1.1.14}$$

$$\mathrm{i}\alpha(U-c)\hat{u}+\frac{\mathrm{d}U}{\mathrm{d}y}\hat{v}+\mathrm{i}\alpha\hat{p}=\frac{1}{R}\Big(\frac{\mathrm{d}^2}{\mathrm{d}y^2}-(\alpha^2+\beta^2)\Big)\hat{u}, \tag{1.1.15}$$

$$\mathrm{i}\alpha(U-c)\hat{v}+\frac{\mathrm{d}\hat{p}}{\mathrm{d}y}=\frac{1}{R}\Big(\frac{\mathrm{d}^2}{\mathrm{d}y^2}-(\alpha^2+\beta^2)\Big)\hat{v}, \tag{1.1.16}$$

$$\mathrm{i}\alpha(U-c)\hat{w}+\mathrm{i}\beta\hat{p}=\frac{1}{R}\Big(\frac{\mathrm{d}^2}{\mathrm{d}y^2}-(\alpha^2+\beta^2)\Big)\hat{w}. \tag{1.1.17}$$

Performing the Squire transformation, namely equations (1.1.7), (1.1.8) and

$$\bar{R}=\frac{\alpha R}{\bar{\alpha}}, \tag{1.1.18}$$

we can eliminate $\bar{u}$ and $\bar{p}$ in favour of $\hat{v}$ to obtain the fourth-order equation

$$\hat{v}''''-2\bar{\alpha}^2\hat{v}''+\bar{\alpha}^4\hat{v}=\mathrm{i}\bar{\alpha}\bar{R}\big[(U-c)(\hat{v}''-\bar{\alpha}^2\hat{v})-U''\hat{v}\big] \tag{1.1.19}$$

known as the *Orr-Sommerfeld equation* (Orr 1907, Sommerfeld 1908). This equation is often written in streamfunction notation, in which $\hat{v}$ is replaced by ϕ in the above equation, where the streamfunction $\widetilde{\psi}=\phi(y)\mathrm{e}^{\mathrm{i}\bar{\alpha}(x-ct)}$. The Squire transformation is useful since for temporal modes the minimum critical Reynolds number can be obtained by considering two-dimensional modes only. This is known as *Squire's theorem.*

The boundary conditions for a bounded flow would be $\phi(y)=0,\phi'(y)=0$ at $y=y_1,y_2$, and for an unbounded flow $\phi(y)=0,\phi'(y)=0$ at $y=-\infty,\infty$. These conditions correspond to the vanishing of both the normal and tangential velocities respectively at the boundaries. As before, the solutions of the Orr-Sommerfeld equation satisfying the boundary conditions exist only when an eigenvalue relation

$$\mathcal{F}(\bar{\alpha},c,\bar{R})=0$$

is satisfied. Solving this relation, say, in the case of temporal instability, yields a so-called neutral curve in the $(\bar{\alpha},\bar{R})$-plane (on which $c_{\mathrm{i}}(\bar{\alpha},\bar{R})=0$), separating regions of stability and instability (see figure 1.1). In particular, there exists a minimum value of the Reynolds number R_{c} below which the flow in question (for example

boundary-layer or plane Poiseuille flow) is stable to disturbances of any wavenumber. This result is qualitatively consistent with the rigorous result for bounded flows proved by using the energy method (Serrin 1959). This method yields bounds for the Reynolds numbers, R_{E} say, below which the energy of the disturbances decay exponentially in time. Unfortunately, such estimates are much smaller than the value of R_{c} observed in experiments, or predicted by normal-mode theory, and so are of little engineering use. There are also certain flows for which the normal-mode approach predicts the critical Reynolds number to be infinite, such as plane Couette flow and Poiseuille pipe flow. This apparently contradicts experimental observations, but the linear theory is only strictly applicable to *infinitesimal* disturbances. In practice plane Couette flow is unstable to certain types of *finite amplitude* disturbances.

For a weakly non-parallel flow such as the boundary-layer flow past a flat plate, the mean flow depends on the streamwise coordinate x and also consists of a component in the y-direction. To study its stability, one may again perturb the basic flow by introducing a small disturbance to obtain a system of linear PDEs as before. However using the normal-mode approach to obtain a system of linear ODEs is, strictly speaking, no longer valid, due to inhomogeneity in the x-direction. The Orr-Sommerfeld equation is derived on the assumption that the basic flow is both a plane-parallel steady flow and an exact solution of the Navier-Stokes equations. Flows which are quasi-parallel may be treated as *locally* parallel for the purpose of stability analysis, provided that the length scale of the disturbance is small compared to the scale of the basic flow variations. One can adopt the so-called Prandtl's parallel flow approximation, that is: (a) ignore the x-variation and seek normal-mode solutions at each location by freezing the profile; (b) retain the viscous diffusion term. This leads to an Orr-Sommerfeld equation at each location. In the case of the Blasius boundary-layer, the equation was first studied by Tollmien (1929) and Schlichting (1933). By using a successive approximation method, they were able to show that provided the Reynolds number is sufficiently high, then there exist unstable modes, which were later referred to as Tollmien-Schlichting (T-S) waves. Their work was significantly improved and refined by Lin (1945). The theoretical predictions of the instability waves and their characteristics were confirmed by the experiments of Schubauer & Skramstad (1947). The critical Reynolds number predicted was in reasonable agreement with experiment.

The scale separation mentioned above is valid only when the Reynolds number is sufficiently large. Then it follows that the non-parallel effect ignored and the viscous term retained are of the same order, implying that Prandtl's parallel flow

approximation is inconsistent despite its apparent success. A consistent approach which treats the non-parallel flow effect systematically is triple-deck theory (Smith 1979).

1.1.2 Nonlinear instability theory

Linear normal-mode instability theory predicts exponential growth for unstable disturbances. Although this may be observed initially in experiments, disturbances cannot possibly keep amplifying forever. Ultimately the growth rate of the disturbance may decrease and the flow reach a new equilibrium state. Alternatively, the disturbances may breakdown into small-scale motion causing the flow to evolve into a more complex state. In other flows, such as plane Poiseuille flow, disturbances are observed to amplify even in the subcritical regime ($R < R_c$).

We thus need a nonlinear theory to describe the evolution (growth/attenuation) of a disturbance of finite amplitude. Stuart (1960) was one of the pioneers to consider nonlinear effects on flow instability. He formulated what has become known as "classical" *weakly nonlinear* theory, using plane Poiseuille flow as a prototype flow. A key observation is that when the Reynolds number is close to its critical value R_c, the disturbance is slowly evolving so that it can be represented by a slowly modulating travelling wave, whose *amplitude function* A depends nontrivially on time. This fundamental wave interacts with itself to produce harmonic and mean components, which in turn interact with the initial fundamental to generate a fundamental at cubic order. This result in fact follows for any α, R in the vicinity of the neutral curve (figure 1.1). Thus Stuart shows that close to neutrality, the mode undergoes nonlinear evolution even though it has a small amplitude. More precisely, a disturbance with amplitude $\epsilon \ll 1$ will evolve nonlinearly if $(R - R_c)^{-1} \sim \mathcal{O}(\epsilon^2)$, on the time scale ϵ^{-2}. On introducing the slow time variable $\tau = \epsilon^2 t$, a nonlinear amplitude equation

$$\frac{\mathrm{d}A}{\mathrm{d}\tau} = aA + b|A|^2 A \tag{1.1.20}$$

can be derived (where a and b are complex constants), by using a solvability condition for an inhomogeneous Orr-Sommerfeld equation. Equation (1.1.20) is known as a Landau-Stuart equation. Depending on whether $\Re(b) < 0$ or > 0, nonlinearity may have stabilising or destabilising effects.

For nearly parallel flows, local linear instability theory can only be justified mathematically by taking the Reynolds number to be large. This assumption is

particularly crucial when developing self-consistent nonlinear instability theories for nearly parallel flows, because only on this basis can numerous competing physical factors be taken into account in a systematic fashion. As was first realised by Lin (1958), nonlinearity should first appear in the critical layer if viscosity is small. This important idea was further pursued by Benney & Bergeron (1969), Davis (1969) and Haberman (1972). Haberman introduced a parameter

$$\Lambda = \frac{1}{R^{1/3}\epsilon^{1/2}},$$

which was later referred to as the Haberman parameter, to delineate the relative importance of viscous and nonlinear effects. If $\Lambda \gg 1$ viscosity is dominant, whilst if $\Lambda \ll 1$ nonlinearity is dominant. For sufficiently small viscosity (i.e. small Λ), nonlinearity is the physical mechanism to smooth out the singularity at the critical layer. The disturbance in the critical layer is governed by *strongly nonlinear* equations (Benney & Bergeron 1969, Davis 1969) in that nonlinearity enters through the coefficient of the operator. As a result, all harmonics are generated simultaneously. This is in contrast to the weakly nonlinear theory of Stuart's, where nonlinear terms appear as inhomogeneous terms of the linear Orr-Sommerfeld equation, and higher harmonics emerge gradually at higher orders. Benney & Bergeron (1969), Davis (1969) and Haberman (1972) looked for nonlinear neutral eigenmodes, rather than following an initially linear instability mode into nonlinear stages, thus the critical layer is *equilibrium* in nature. The major results of this type of critical layer were reviewed by Maslowe (1986).

Hickernell (1984) followed the growth of an initially small instability mode (Rossby wave) in a rotating shear layer into the nonlinear stage. He included at leading order the *non-equilibrium* effect, i.e. the slow effect associated with the envelope modulation of the travelling wave. For the instability mode considered, the critical layer turned out to be weakly nonlinear.

Goldstein & Leib (1988) considered the nonlinear spatial evolution of an externally excited planar instability wave in a free shear layer. They derived an evolution system which is both strongly nonlinear and non-equilibrium. This system describing the critical-layer dynamics is akin to that derived by Warn & Warn (1978) and Stewartson (1978) for the evolution of a forced Rossby wave. Due to the strongly nonlinear nature, the disturbance in the critical layer rolls up to form concentrated vortices, or "rollers". In the inviscid limit considered, pathologically small-scale motions develop within the critical layer.

Goldstein & Hultgren (1988) introduced a small amount of viscosity into the

critical-layer analysis of Goldstein & Leib (1988), so that both diffusion and nonlinear terms appear at leading order. The effect of viscosity causes the vorticity distribution to diffuse into a more regular pattern than the inviscid limit considered in Goldstein & Leib (1988). The nonlinear non-equilibrium critical layer gradually evolves into a quasi-equilibrium critical layer (with variable "cat's-eye" vorticity), and the initial exponential growth of the instability wave is converted into (slow) algebraic growth. Ultimately the disturbance decays in the final stage of evolution, which is simultaneously affected by mean-flow divergence and (equilibrium) nonlinear critical-layer effects. Hultgren (1992) later extended the analysis of Goldstein & Hultgren (1988) further, by generalising it to an arbitrary mean flow. More significantly, he generalised the streamwise composite solution introduced in Goldstein & Leib (1988) to include viscosity, and performed a careful comparison of his composite solution with experiments. Good quantitative agreement was obtained.

The nature of critical-layer nonlinearity depends crucially on the dimensionality and form of the disturbances under consideration. Wu (1993) showed that for a weakly three-dimensional disturbance with a general spanwise modulation on the length scale of $\mathcal{O}(\epsilon^{-1/5})$, the critical layer is weakly nonlinear. For modulation on the scale $\mathcal{O}(\epsilon^{-1/2})$, the critical layer remains strongly nonlinear, but the vorticity equation is now coupled to an equation for the spanwise velocity (Messiter & Davis 1999). Interestingly, for a pure weakly oblique mode, its critical layer remains strongly nonlinear for a spanwise wavelength up to $\mathcal{O}(\epsilon^{-1/4})$ (Churilov & Shukhman 1995). Overall, as three-dimensionality increases, nonlinear evolution commences "earlier", i.e. at a smaller amplitude, and takes places on a shorter length/time scale.

There have been extensive studies of nonlinear interactions of co-existing normal modes within the non-equilibrium critical layer. Important interactions include resonant-triad interaction (Goldstein & Lee 1992, Wu 1995, 1996), phase-locked interaction (Wu & Stewart 1996) and interaction between pairs of oblique modes which propagate at equal angles but of opposite signs with respect to the streamwise direction (Goldstein & Choi 1989, Wu *et al.* 1993). These interactions cause oblique modes to undergo rapid amplification.

1.2 Compressible flows

The compressibility effect is characterised by the Mach number, defined as

$$M = \frac{V}{a} \tag{1.2.21}$$

where a is a reference speed of sound, which in the case of flows of boundary-layer type, may be taken as the sound speed in the free stream. Like the Reynolds number, the Mach number is an important parameter that controls stability. For the subsonic speed regime ($M < 1$), increasing M usually has a stabilising influence, however in the supersonic regime, M may affect stability in quite a complicated and unexpected way.

1.2.1 Linear instability theory

By following the normal-mode approach, with perturbation pressure

$$\tilde{p} = \hat{p}(y)\mathrm{e}^{\mathrm{i}(\alpha x+\beta z-\alpha ct)},$$

a compressible Rayleigh equation can be derived for $\hat{p}$:

$$\hat{p}'' + \left(\frac{T'}{T} - \frac{2U'}{U-c}\right)\hat{p}' + (\alpha^2+\beta^2)\left(\frac{\alpha^2 M^2(U-c)^2}{(\alpha^2+\beta^2)T} - 1\right)\hat{p} = 0. \tag{1.2.22}$$

Here viscous effects are ignored so as to concentrate on inviscid instability, for which the effect of viscosity in the compressible linear theory is negligible for moderate and larger Reynolds numbers (Mack 1987, Ragab & Wu 1989). Equation (1.2.22) with appropriate boundary conditions for the pressure represents an eigenvalue problem, which can be solved to obtain an eigenvalue (dispersion) relation.

By the (Squire-like) transformation

$$\bar{\alpha}^2 = \alpha^2+\beta^2, \quad \bar{\alpha}\bar{M} = \alpha M, \quad \bar{\alpha}\bar{p} = \alpha\hat{p}, \tag{1.2.23}$$

equation (1.2.22) can be reduced to a form equivalent to that for two-dimensional disturbances, namely

$$\bar{p}'' + \left(\frac{T'}{T} - \frac{2U'}{U-c}\right)\bar{p}' + \bar{\alpha}^2\left(\frac{M^2(U-c)^2}{T} - 1\right)\bar{p} = 0. \tag{1.2.24}$$

However it does not follow from this transformation that two-dimensional modes are more unstable than three-dimensional modes.

The inviscid compressible linear theory for shear flows (both free and wall bounded) was first formulated by Lees & Lin (1946). They showed that a necessary condition for a shear flow to be inviscidly unstable is for the base-flow profiles to have a generalised inflection point, i.e.

$$\left(\frac{U'}{T}\right)' = 0, \tag{1.2.25}$$

where a prime denotes differentiation with respect to the transverse coordinate. A critical level coinciding with a generalised inflection point is called a *regular* critical level, otherwise it is called a *singular* critical level.

A significant consequence of including compressibility is that there usually exists a multitude of instability modes at high Mach numbers. Extensive computational work has been carried out to identify these modes. For boundary layers, the major results are documented in the report by Mack (1984); see also the references therein. For small Mach numbers, the only instability is essentially the usual T-S instability modes, but modified by compressibility so that the short-wavelength modes become predominantly inviscid. They are often referred to as the first modes, and the oblique modes can have large growth rates. For larger Mach numbers, in addition to the first modes, higher modes, known as Mack modes (Mack 1984), emerge. However the growth rates of the third and higher modes are very small and thus they are of little relevance for transition. The second modes are more unstable when two-dimensional, and for the insulated wall they are the dominant instability for $M > 5$.

The instability modes are classified, according to the characteristics of their eigenfunctions $\bar{p}$, as "vortical" or "acoustic". The latter is interpreted as acoustic disturbances being reflected between the wall and the relative sonic line in the boundary layer, because the eigenfunction concentrates in that region. This distinction is actually somewhat blurred for moderate Mach numbers. In the asymptotically large-Mach-number limit, they acquire different asymptotic structures. The vortical modes are trapped in the so-called "temperature adjustment layer" near the outer reach of the boundary layer, and the instability is controlled by the temperature gradient in this region, relatively unaffected by the velocity profile (Smith & Brown 1990). In contrast, acoustic modes extend to the entire boundary layer and are influenced by the global distribution of both the velocity and temperature profiles (Cowley & Hall 1990, Blackaby *et al.* 1993).

Instability modes may also be classified according to their propagation speeds relative to the free-stream velocity. If the relative velocity is smaller/larger than the free-stream sound speed, the mode is called a subsonic/supersonic mode. For a subsonic mode, the pressure $\bar{p}$ attenuates exponentially in the free stream. Lees

& Lin (1946) showed that subsonic neutral modes must have phase speeds given by $c = U(y_c)$, where y_c is the point at which equation (1.2.25) is satisfied. Thus for a subsonic neutral mode the critical level is regular. Supersonic modes exist at sufficiently high Mach numbers. The eigenfunction of a *growing* supersonic mode still attenuates exponentially but in an oscillatory manner for large y. However, for a *neutral* supersonic mode, $\bar{p}$ does not vanish but remains bounded in the free stream. These modes are of significance because they may radiate highly directional Mach waves to the far field (Tam & Burton 1984, Wu 2005).

As with boundary layers, linear instability of free shear layers (mixing layers) has been extensively studied. Since the mean profiles depend on β_U and β_T, the free-stream velocity and temperature ratios respectively, the stability is not fully controlled by the (fast) free-stream Mach number M. It has been suggested (Bogdanoff 1983, Papamoschou & Roshko 1988) that the combined effect of β_U, β_T and compressibility can be characterised by a single parameter, the convective Mach number, which for a mixing layer of a single species is defined as

$$M_c = (U_1 - U_2)/(a_1 + a_2), \tag{1.2.26}$$

where a_1 and a_2 denote the sound speeds of the fast and slow streams. Note that M_c may be less than unity even if $M > 1$.

For convenience of analysis and/or calculations, the velocity and/or temperature profiles of the base flow are often taken to be somewhat ad hoc models, rather than exact solutions to the appropriate governing equations (steady Navier-Stokes or boundary-layer equations). Lessen *et al.* (1965, 1966) considered the temporal instability of compressible mixing layers to two- and three-dimensional disturbances. The velocity profile used was that of Lock (1951), but the temperature profile was obtained by assuming that the flow is isoenergetic, so that the temperature of the stagnation gas is much higher than that of the moving gas. They found that oblique modes may be more unstable than planar modes. Blumen (1970), Blumen *et al.* (1975) and Drazin & Davey (1977) considered temporal stability of a mixing layer modelled by a hyperbolic tangent velocity profile and a uniform temperature distribution. They found that the shear layer is unstable to two-dimensional disturbances however large the Mach number is. They recognised the existence of up to three unstable modes at large Mach numbers. For the case of two counter-flowing streams with equal speed, one of the modes is stationary whilst the other two have equal but opposite phase velocities. Jackson & Grosch (1989) carried out a comprehensive analysis of spatial stability for a hyperbolic tangent profile and a temperature pro-

file given by Crocco's relation. They found that subsonic modes exist at relatively low Mach numbers. When the Mach number exceeds a critical value, two groups of unstable modes come into existence, one of which are supersonic with respect to the slow stream whilst the other supersonic relative to the fast stream. Modes which are supersonic with respect to both streams have not been found and probably do not exist. Their calculations of growth rates indicate that two-dimensional subsonic modes are most unstable at relatively low Mach numbers. At sufficiently high Mach numbers, the most unstable modes are oblique waves, consistent with the conclusions from earlier and subsequent temporal instability analyses (e.g. Lessen *et al.* 1965, 1966, Sandham & Reynolds 1991). The most unstable oblique modes may be subsonic or supersonic with respect to one of the free streams, depending on the Mach number and temperature ratio. In general, increasing the Mach number renders the flow less unstable.

Jackson & Grosch (1991) compared the instability results of various velocity and temperature profiles, and found that the qualitative instability properties remain the same, but some quantitative differences are present as expected. They also assessed the effect of the ratio of the free-stream temperatures, and noted that the instability characteristics are quite sensitive to this parameter. Ragab & Wu (1989) investigated the viscous effect on linear instability, and found that viscosity slightly reduces the growth rate. When the Reynolds number (based on the local shear layer thickness) exceeds 1000, the inviscid approximation is sufficiently accurate.

As in the case of boundary layers (Smith & Brown 1990), the instability problem of a free shear layer in the $M \gg 1$ limit is amenable to asymptotic analysis. Balsa & Goldstein (1990) formulated a high-Mach-number asymptotic linear theory, and compared the asymptotic predictions with numerical results, in particular those of Jackson & Grosch (1988) (which also appear in Jackson & Grosch 1989). Good agreement was observed for Mach numbers $M \geqslant 10$. Interestingly, they showed that the most unstable temporal mode is two-dimensional for asymptotically large $M \gg 1$. This suggests that only over a finite range of Mach number are the oblique modes the most unstable. The corresponding asymptotic theory for a compressible plane wake was given by Papageorgiou (1991). The resulting eigenvalue problem turns out to be the same in all these studies despite different flows being considered. That a generic problem arises in the limit $M \gg 1$ is due to the fact that instability modes are trapped in a thin layer, which means that the overall profiles of the base flow become unimportant at leading-order approximation.

To conclude this section, we summarise the main findings of the existing linear

instability calculations of mixing layers as follows:

1. The overall instability weakens as compressibility (i.e. the Mach number), increases.

2. For small to moderate Mach numbers, the dominant instability corresponds to two-dimensional subsonic modes.

3. As the Mach number exceeds a critical value, the fastest growing disturbances are oblique modes, which may be subsonic or supersonic with respect to one of the free streams.

Finally, it may be noted that there have been numerous studies of compressible mixing layers in more complex settings, where several instability mechanisms operate simultaneously. For instance, Grosch & Jackson (1991) and Lu & Lele (1993) analysed linear instability of three-dimensional or skewed mixing layers, in which the instability is substantially altered by the presence of a cross-flow component. Owen *et al.* (1997, 1998) investigated curved mixing layers, where centrifugal instability is in action.

1.2.2 Nonlinear instability theory

Nonlinear instability of a compressible free shear layer was considered in Goldstein & Leib (1989). They studied the evolution of a single oblique instability wave, which propagates at an arbitrary angle θ to the streamwise direction. Their analysis applies equally to a planar instability wave ($\theta = 0$). The instability wave is taken to be a subsonic mode, for which the critical layer corresponds to a generalised inflection point and hence the leading-order eigenfunction for the pressure is free from logarithmic singularity. The dominant critical-layer nonlinearity is associated with a pole at leading order in the temperature perturbation, making nonlinearity appear sooner than in the incompressible case. As a result, nonlinearity operates in a weakly nonlinear fashion in a similar way to Stuart (1960), that is, nonlinear terms appear successively as inhomogeneous terms at higher orders. By analyzing these weakly nonlinear interactions within the critical layer, a nonlinear evolution equation for the amplitude can be derived. Unlike the classical Landau equation, however, the evolution equation now contains a *non-local* cubic nonlinear term. This is due to the non-equilibrium effect being included at leading order in the critical-layer equations. Numerical results were computed for both inviscid and viscous (Chapman's viscosity

law) critical layers. In the inviscid limit, the amplitude always develops a singularity at a finite distance downstream. For a sufficient amount of viscosity, the amplitude evolves into an equilibrium state. Leib (1991) subsequently extended the analysis of Goldstein & Leib (1989) to include supersonic modes, for which the critical level is singular. He included viscosity and gave numerical results for four different velocity profiles. He found that cooling the low speed stream and decreasing the Mach number has a destabilising influence on the nonlinear evolution of the subsonic modes, as is the case for the linear theory. However for supersonic modes it is possible for the opposite effect to occur – for example cooling the low-speed stream is stabilising for the (slow) supersonic mode for Mach numbers up to about five. Unlike the strong nonlinearity for an incompressible shear layer (Goldstein & Leib 1988), weakly nonlinear theory of this kind cannot describe the phenomenon of vortex roll-up. The theory is unsatisfactory because in the moderately compressible (i.e. $M = \mathcal{O}(1)$) mixing layer, vortex roll-up remains the most significant feature during the transition to turbulence.

Another relevant theoretical work is that of Goldstein & Wundrow (1990), who considered the spatial instability of a planar acoustic mode in a hypersonic boundary layer. The mode has a vanishingly small growth rate so that the flow contains a well-defined critical layer. They derived an inviscid strongly nonlinear system similar to that for the incompressible case, but with an extra coupled energy equation. Their results show that the singularity found in Goldstein & Leib (1989) is not reached, owing to the strong vorticity roll-up, however nonlinearity does cause the growth rates to increase initially. Further downstream the growth rates decrease and subsequently oscillate (violently) about zero.

Leib & Lee (1995) considered the nonlinear spatial evolution of a pair of oblique modes in a supersonic boundary layer. Nonlinearity appears much earlier than with a single oblique wave, and the critical layer turns out to be weakly nonlinear. Some key interactions among co-existing modes have been considered in Al-Salman (2002).

There has been some work which applies the classical version of weakly nonlinear theory to compressible shear layers. As with incompressible shear layers, this type of approach is problematic as it inevitably leads to inconsistent treatment of nonlinear, non-equilibrium and non-parallel flow effects. For instance, Ladeinde & Wu (2002) attempted to use this approach to study the nonlinear development of the most unstable instability mode, for which no critical layer exists. They derived a Landau equation, but this result was flawed because the authors erroneously imposed a solvability condition, which is not required at all for a non-neutral mode.

1.3 Instability and transition of the compressible mixing layer: practical relevance and experimental studies

During the three or four decades following the pioneering work of Lees & Lin (1946), the compressible mixing layer was studied primarily as a simple prototype flow to understand a fundamental instability. In the last few decades, there has been a resurgence of research on mixing layers, especially on supersonic mixing layers, driven by their practical relevance to developing scramjet engines which are proposed to provide propulsion for high speed aircraft (Curran 1996). The projected engine uses an air-breathing technique and combustion takes place at supersonic speeds between the initially non-premixed reactants. A major technical obstacle is the extremely short time available for the fuel and oxidizer to sufficiently mix in a combustor of restricted length. Effective mixing is crucial to overcome this difficulty. A compressible mixing layer provides the simplest conceptual model in which relevant mixing processes can be investigated.

A full mathematical characterisation of mixing at the molecular level is a great challenge. Fortunately, mixing properties are intrinsically linked to several discernable and inter-related characteristics of the mixing layer, such as the mean spreading rate of the layer thickness, instability, and the resulting fluctuations at various scales. Thus studies of these aspects usually offer key insights into mixing.

In the incompressible regime, dominant unstable waves, which arise from inviscid Kelvin-Helmholtz (i.e. Rayleigh) instability, roll up under the nonlinear effect to form concentrated spanwise vortices, or "rollers". At the locations of repeated vortex pairing, the shear-layer thickness increases abruptly (Ho & Huerre 1984). The most striking feature is that predominantly two-dimensional large-scale coherent structures exist also in the fully turbulent state (Brown & Roshko 1974) and undergo pairing (Winant & Browand 1974). These structures are probably controlled by the inherent instability of the background flow (Liu 1989). Their presence implies that the conventional concept of gradient diffusion for turbulent mixing is not applicable. A model which takes into account the large-scale structures was proposed by Broadwell & Breidenthal (1982), and was found to give significantly different predictions from diffusion models.

Experiments have long established that the spreading rate of a compressible mixing layer is smaller than that of its incompressible counterpart with the same

velocity and density ratios (e.g. Brown & Roshko 1974, Bogdanoff 1984, Chinzei *et al.* 1986, Papamoschou & Roshko 1988). This has been attributed to the reduction of linear growth rates of instability waves when compressibility is increased, and the fact that in supersonic flow, disturbances cannot propagate upstream, whereas in the subsonic regime, a disturbance is "felt" throughout the flow field. Bogdanoff (1984) and Papamoschou & Roshko (1988) suggested that the reduction in the spreading rate with respect to the incompressible limit can be characterized by a single parameter, the convective Mach number M_c (equation (1.2.26)), which incorporates compressibility, velocity and density ratios. This has been confirmed by extensive experimental data (e.g. Clemens & Mungal 1995, Miller *et al.* 1998). The maximum growth rates of instability waves have also been found to collapse in the same manner (e.g. Ragab & Wu 1989, Jackson & Grosch 1990).

Large-scale coherent structures remain a focus of interest in the compressible regime. By employing various flow visualization techniques, such as Schlieren imaging, PLIF (planar laser-induced fluorescence), Mie and/or Rayleigh scattering as well as PIV (particle image velocimetry), experiments reveal that for $M_c < 0.6$, the dominant coherent structures are spanwise-oriented rollers of Brown-Roshko type (Clemens & Mungal 1995, Elliott *et al.* 1995, Urban & Mungal 2001, Olsen & Dutton 2003). Three-dimensionality starts to feature for larger values of M_c. When $M_c > 0.86$, roll-up or rollers can hardly be detected (Elliott *et al.* 1995) though large-scale motions with some degree of coherency are observed. In the highly compressible regime (e.g. $M_c = 1.7$), the dominant feature is streamwise vortical structures, which radiate strong Mach waves (Rossmann *et al.* 2002), indicating that supersonic modes become the predominant instability.

A number of experiments have yielded detailed measurements of relevant statistical quantities. It is found that transverse and spanwise turbulence intensity decrease markedly with M_c, but that streamwise intensity remains constant or decreases slightly (Urban & Mungal 2001). The anisotropy of turbulent stress appears to be affected by compressibility (Barre *et al.* 1994), but different experiments have not yet been able to establish a consistent trend.

In most practical applications (such as scramjet engines), flows are chemically reacting. The heat released therefore affects, through density change, the flow motion, which in turn influences mixing and hence chemical reaction. There have been a few experimental studies to examine this complicated coupling. At relatively low speeds or low heat release, two-dimensional large-scale structures still dominate the mixing process (Mungal & Dimotakis 1984, Masutani & Bowman 1986). However

there are several unexpected results in the high-compressibility regime ($M_c > 0.6$). For example Miller *et al.* (1998) conducted three experiments, two for low convective Mach numbers ($M_c = 0.32, 0.35$) and one for a high convective Mach number ($M_c = 0.70$). They observed *enhanced* combustion in the high compressibility case.

Gutmark *et al.* (1995) reviewed a range of mixing enhancement techniques by passive and active means. The former include altering the trailing edge of the splitter plate (e.g. to a lobed shape) to generate streamwise vorticity, use of a wall-mounted cavity to maintain flow-acoustic resonance, and deployment of trailing-edge devices to create skew mixing layers. Watanabe & Mungal (2005) recently reported effective enhancement by placing triangular roughness elements of sub-boundary-layer size along the trailing edge. Active control consists of excitation using glow discharge and injection through wall-mounted ramps. It is interesting to note that most of these techniques rely on manipulation of the flow instability and the related coherent structures.

There have been several direct numerical simulations (DNS) of transition and turbulence in the compressible mixing layer. Sandham & Reynods (1991) performed *temporal* simulations of transition initiated by a pair of oblique modes with spanwise wavenumbers $\pm\beta$. This scenario is important because the oblique modes are more unstable and modes in pairs start to experience enhanced nonlinear development at much smaller amplitudes than has otherwise been suggested by the theoretical result of Leib & Lee (1995). Consistent with the theoretical expectation, the simulations show that oblique pairs can grow out of initially random perturbations. No shocks or Mach-wave radiation occurred in the simulation, presumably because at $M_c = 1.05$, the oblique modes are subsonic. A fully developed turbulent compressible mixing layer was simulated by Vreman *et al.* (1996), again in a temporal evolution setting. Ragab & Sheen (1991) simulated nonlinear *spatial* evolution of supersonic modes in two dimensions, for which Mach-wave radiation was found to be a prominent feature. Spatial simulations of mixing-layer transition initiated by three-dimensional supersonic modes do not appear to have been conducted. McMurtry *et al.* (1989) carried out a three-dimensional, time-dependent direct numerical study of the effect of compressibility on a chemically reacting mixing layer, in which heat release and hydrodynamics are fully coupled. They found that moderate heat release inhibits the mixing-layer spreading, slows the roll-up of large-scale structures and shifts their wavelengths to larger scales. The resulting entrainment of reactants is reduced, and accordingly the amount of product formed decreases as compared with the case where heat release is ignored. Spatial nonlinear instability was investigated by Day

et al. (2001) by using PSE (parabolised stability equations).

It should be noted that DNS has been possible only for Reynolds numbers much smaller than those in experiments. In the case of reacting flows, the Damköhler numbers were artificially reduced in order to avoid the difficulty of resolving extremely thin reaction zones. Due to these limitations, the numerical results are mostly of qualitative validity, and there is a great need to develop theoretical approaches by taking the advantage of large Reynolds and Damköhler numbers.

1.4 Scope of the present study

As was noted earlier, there currently exist two distinct nonlinear instability theories for mixing layers: a strongly nonlinear critical-layer theory in the incompressible regime, and a weakly nonlinear critical-layer theory in the compressible regime with $M = \mathcal{O}(1)$. The two theories have no overlap. From the mathematical viewpoint, it is certainly desirable to unify the two theories by considering a distinguished intermediate regime in which the flow is weakly compressible. This is the first goal of the study.

Existing theories fail to account for the experimental observation that in the fully compressible regime with $M = \mathcal{O}(1)$ (including low supersonic speeds $M > 1$), mixing layers continue to behave in more or less the same manner as in the incompressible regime, i.e. characterized by large-scale, predominantly two-dimensional "rollers". A more ambitious goal of this thesis is to develop a theory which can capture this hallmark behaviour of mixing-layer transition. This is important because "rollers" *per se* play a crucial role in the entrainment and mixing of the two streams, which would be fuel and oxidizer in a combustion setting. Moreover, an appropriate characterization of the large-scale vortices is a prerequisite for investigating their subsequent breakdown into small-scale motions.

In the next chapter (chapter 2) we formulate the instability problem for a compressible mixing layer perturbed by a travelling-wave disturbance whose amplitude is slowly modulating in both space and time. We then analyse the inviscid linear outer flow in the main part of the shear layer, and derive the asymptotic behaviour of the solution as the critical layer is approached, highlighting in particular the nature of singularities, which ultimately determine the nonlinear dynamics within the critical layer.

In chapter 3, we consider the non-equilibrium, viscous, strongly nonlinear critical layer contained within the mixing layer, for the weakly compressible regime $M =$

$\mathcal{O}(\epsilon^{1/4})$. This is the distinguished scaling which unifies the incompressible ($M = 0$) strongly nonlinear theory (Goldstein & Leib 1988, Goldstein & Hultgren 1988) and the weakly nonlinear theory for $M = \mathcal{O}(1)$ Mach number flow (Goldstein & Leib 1989, Leib 1991). The resulting evolution system consists of an amplitude equation coupled with equations governing the development of vorticity and temperature within the critical layer. The strongly nonlinear nature of the system means that it is capable of describing vortex roll-up.

In chapter 4, we present further extensions of the theory to the fully compressible regime with $M = \mathcal{O}(1)$. An extension is made for certain velocity profiles (e.g. tanh profile), where it is possible that $T_c' = 0$ even for $M = \mathcal{O}(1)$. In this case, the weakly nonlinear theory of Goldstein & Leib (1989) and Leib (1991) actually degenerates to linear theory. We will demonstrate the appropriate scaling leading to strongly nonlinear critical-layer dynamics when $T_c' = 0$ and $M = \mathcal{O}(1)$. The vorticity and temperature evolution equations both have to be modified to take into account the effect associated with $\mathcal{O}(1)$ Mach number.

A second extension is based on the observation that T_c' is numerically small for practical profiles (e.g. Lock profile) even when $M = \mathcal{O}(1)$. We then assume that $T_c' = \mathcal{O}(\epsilon^{1/2})$, so as to include the compressible nonlinear effect associated with the singularity in the temperature perturbation, whilst retaining the strongly nonlinear nature. It turns out that the appropriate evolution equations for the vorticity and temperature in the critical layer can be obtained by synthesizing those in chapter 3 (for $M = \mathcal{O}(\epsilon^{1/4})$ and $T_c' = \mathcal{O}(\epsilon^{1/2})$) and chapter 4 (for $T_c' = 0$ and $M = \mathcal{O}(1)$), to obtain a composite system.

The composite system, on one hand, reduces trivially to that of Goldstein & Leib (1988) in the incompressible limit. On the other hand, it is further shown that the amplitude equation for $M = \mathcal{O}(1)$ in the weakly nonlinear theory of Goldstein & Leib (1989) and Leib (1991) can be derived from the present strongly nonlinear system by considering an appropriate limit. We thus demonstrate that our final system represents a composite theory that is uniformly valid for all $0 \leqslant M \sim \mathcal{O}(1)$.

In chapter 5, the strongly nonlinear evolution system is solved numerically, and relevant solutions are presented and discussed. It is shown in particular that for typical flow parameters, the disturbance does roll-up to form roller structures, as has been observed in experiments. It is also demonstrated that for some parameters, the weakly and strongly nonlinear predictions are found to be in good agreement, although for most parameters, this is generally not the case.

The formulation to be developed in chapters 2–4 actually describes the nonlinear

evolution of a *wavetrain*. In chapter 6, this observation allows for a framework to study sideband instability, which involves the nonlinear interaction of two or three modes with frequencies close to each other. Typical theoretical results are presented along with a discussion. Finally, in chapter 7 some main conclusions are drawn, and further work suggested.

Chapter 2

Formulation & Outer Flow

2.1 Problem specification and governing equations

Consider two compressible streams separated by a splitter plate (figure 2.1). The velocities of the oncoming streams are denoted by U_1, U_2, and temperatures by T_1, T_2 respectively. Let x and y be coordinates parallel and normal to the splitter plate respectively. The origin of this (x, y)-coordinate system will be specified later. Let t denote the time variable. The two-dimensional compressible Navier-Stokes equations governing this flow are

$$\frac{D\rho}{Dt} + \rho\Big(\frac{\partial u}{\partial x} + \frac{\partial v}{\partial y}\Big) = 0, \tag{2.1.1}$$

$$\rho\frac{Du}{Dt} = -\frac{\partial p}{\partial x} + \frac{\partial}{\partial x}\Big[\mu\Big(2\frac{\partial u}{\partial x} - \frac{2}{3}\Big(\frac{\partial u}{\partial x} + \frac{\partial v}{\partial y}\Big)\Big)\Big] + \frac{\partial}{\partial y}\Big[\mu\Big(\frac{\partial u}{\partial y} + \frac{\partial v}{\partial x}\Big)\Big], \tag{2.1.2}$$

$$\rho\frac{Dv}{Dt} = -\frac{\partial p}{\partial y} + \frac{\partial}{\partial y}\Big[\mu\Big(2\frac{\partial v}{\partial y} - \frac{2}{3}\Big(\frac{\partial u}{\partial x} + \frac{\partial v}{\partial y}\Big)\Big)\Big] + \frac{\partial}{\partial x}\Big[\mu\Big(\frac{\partial u}{\partial y} + \frac{\partial v}{\partial x}\Big)\Big], \tag{2.1.3}$$

and

$$\begin{aligned}\rho c_p\frac{DT}{Dt} = {} & \frac{\partial}{\partial x}\Big(k\frac{\partial T}{\partial x}\Big) + \frac{\partial}{\partial y}\Big(k\frac{\partial T}{\partial y}\Big) + \beta T\frac{Dp}{Dt} + \mu\Big\{2\Big[\Big(\frac{\partial u}{\partial x}\Big)^2 + \Big(\frac{\partial v}{\partial y}\Big)^2\Big] \\ & + \Big(\frac{\partial v}{\partial x} + \frac{\partial u}{\partial y}\Big)^2 - \frac{2}{3}\Big(\frac{\partial u}{\partial x} + \frac{\partial v}{\partial y}\Big)^2\Big\},\end{aligned} \tag{2.1.4}$$

where u and v are the velocities in the streamwise and transverse directions respectively, T is the absolute temperature, p is the pressure, ρ is the density, μ is the

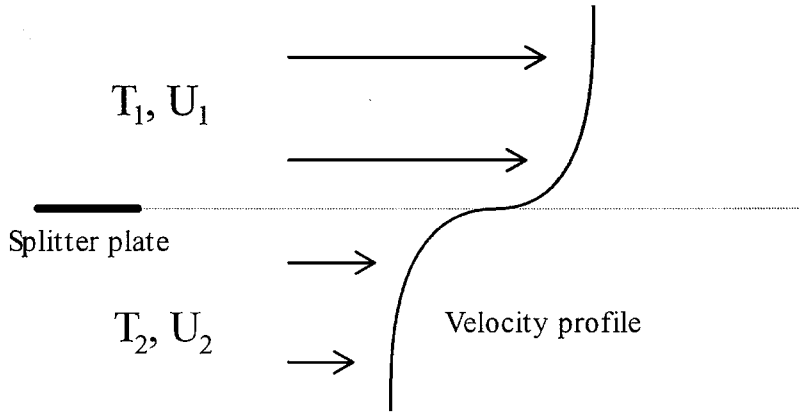


Figure 2.1: Sketch of the flow configuration. Downstream of the splitter plate, a free shear layer forms between the two streams.

viscosity coefficient, c_p is the isobaric specific heat capacity, k is the coefficient of thermal conductivity, and β is the coefficient of thermal expansion. The differential operator D/Dt is defined as

$$\frac{D}{Dt} \equiv \frac{\partial}{\partial t} + u\frac{\partial}{\partial x} + v\frac{\partial}{\partial y}.$$

For a derivation of these equations with an explanation of the various assumptions used, see for example Schlichting & Gersten (2000). The only notable assumptions here are the neglect of body forces and bulk viscosity.

To close the system, we assume a perfect gas, for which the state equation $p = p(\rho, T)$ is

$$p = \rho \mathcal{R} T \tag{2.1.5}$$

where $\mathcal{R}$ is the gas constant. For a perfect gas, $\mathcal{R} = c_p - c_v$ and $\beta = 1/T$, where c_v is the isovolumetric specific heat capacity. If we further assume a calorifically perfect gas, then c_p and c_v are both constants.

Now introduce non-dimensionalisation by

$$x^* = \frac{x}{l}, \quad y^* = \frac{y}{l}, \quad t^* = \frac{V}{l}t, \quad u^* = \frac{u}{V}, \quad v^* = \frac{v}{V},$$

$$\rho^* = \frac{\rho}{\rho_{\mathrm{R}}}, \quad p^* = \frac{\gamma M^2}{\rho_{\mathrm{R}} V^2}p, \quad T^* = \frac{\gamma M^2 \mathcal{R}}{V^2}T,$$

where * signifies dimensionless quantities, ρ_{R} refers to a reference density, l to a reference length, V to a reference velocity, γ is the ratio of specific heats

$$\gamma = \frac{c_p}{c_v}$$

and M is the Mach number

$$M = \frac{V}{a_{\mathrm{R}}} \tag{2.1.6}$$

with a_{R} being a reference speed of sound. For the mixing layer under consideration, we will choose l to be a typical shear-layer width, V to be the fast stream speed, and a_{R} to be the speed of sound in the fast stream. Since the mean pressure is constant, we choose ρ_{R} such that the non-dimensionalised mean pressure is equal to one.

Substitution of (2.1.5) into (2.1.1)–(2.1.4) to eliminate ρ, followed by performing the non-dimensionalisation outlined above, yields, on dropping *, the non-dimensional Navier-Stokes equations:

$$TDp - pDT + pT\left(\frac{\partial u}{\partial x} + \frac{\partial v}{\partial y}\right) = 0, \tag{2.1.7}$$

$$pDu = -\frac{T}{\gamma M^2}\frac{\partial p}{\partial x} + \frac{T}{R}\left\{\frac{2}{3}\frac{\partial}{\partial x}\left[\mu\left(2\frac{\partial u}{\partial x} - \frac{\partial v}{\partial y}\right)\right] + \frac{\partial}{\partial y}\left[\mu\left(\frac{\partial u}{\partial y} + \frac{\partial v}{\partial x}\right)\right]\right\}, \tag{2.1.8}$$

$$pDv = -\frac{T}{\gamma M^2}\frac{\partial p}{\partial y} + \frac{T}{R}\left\{\frac{2}{3}\frac{\partial}{\partial y}\left[\mu\left(2\frac{\partial v}{\partial y} - \frac{\partial u}{\partial x}\right)\right] + \frac{\partial}{\partial x}\left[\mu\left(\frac{\partial u}{\partial y} + \frac{\partial v}{\partial x}\right)\right]\right\} \tag{2.1.9}$$

and

$$\begin{aligned} pDT = {} & \frac{(\gamma-1)}{\gamma}TDp + \frac{T}{PrR}\left\{\frac{\partial}{\partial x}\left(\mu\frac{\partial T}{\partial x}\right) + \frac{\partial}{\partial y}\left(\mu\frac{\partial T}{\partial y}\right)\right\} \\ & + \frac{(\gamma-1)M^2}{R}T\mu\left\{\frac{4}{3}\left[\left(\frac{\partial u}{\partial x}\right)^2 + \left(\frac{\partial v}{\partial y}\right)^2 - \frac{\partial u}{\partial x}\frac{\partial v}{\partial y}\right] + \left(\frac{\partial v}{\partial x} + \frac{\partial u}{\partial y}\right)^2\right\} \end{aligned} \tag{2.1.10}$$

where

$$D \equiv \frac{\partial}{\partial t} + u\frac{\partial}{\partial x} + v\frac{\partial}{\partial y},$$

$$R = \text{Reynolds number} = \frac{\rho_{\mathrm{R}} V l}{\mu_{\mathrm{R}}}, \tag{2.1.11}$$

and

$$Pr = \text{Prandtl number} = \frac{c_p \mu_{\mathrm{R}}}{k}. \tag{2.1.12}$$

We assume that the viscosity μ is a given function of the temperature T (only), thus the above four equations involve four unknowns, namely pressure p, temperature T,

streamwise velocity u and transverse velocity v. Note that the dimensionless state equation now becomes

$$p = \rho T. \tag{2.1.13}$$

2.2 Basic flow

According to the classical boundary-layer theory, the solution for the unperturbed background flow expands as

$$U_{\mathrm{B}} = \bar{U}_0(\mathcal{X}_2, y) + R^{-1}\bar{U}_1(\mathcal{X}_2, y) + \cdots, \tag{2.2.14}$$

$$V_{\mathrm{B}} = R^{-1}\big(\bar{V}_0(\mathcal{X}_2, y) + R^{-1}\bar{V}_1(\mathcal{X}_2, y) + \cdots\big), \tag{2.2.15}$$

$$P_{\mathrm{B}} = 1 + R^{-1}\bar{P}_1(\mathcal{X}_2, y) + \cdots, \tag{2.2.16}$$

$$\rho_{\mathrm{B}} = \bar{\rho}_0(\mathcal{X}_2, y) + R^{-1}\bar{\rho}_1(\mathcal{X}_2, y) + \cdots, \tag{2.2.17}$$

$$T_{\mathrm{B}} = \bar{T}_0(\mathcal{X}_2, y) + R^{-1}\bar{T}_1(\mathcal{X}_2, y) + \cdots, \tag{2.2.18}$$

$$\mu_{\mathrm{B}} = \bar{\mu}_0(\mathcal{X}_2, y) + R^{-1}\bar{\mu}_1(\mathcal{X}_2, y) + \cdots \tag{2.2.19}$$

where B subscript denotes basic flow quantities, and

$$\mathcal{X}_2 = \frac{x}{R} \tag{2.2.20}$$

represents a slow streamwise variable.

The relevant equations for $\bar{U}_0$, $\bar{V}_0$ and $\bar{T}_0$ are found by substituting (2.2.14)–(2.2.19) into (2.1.7)–(2.1.10). We obtain at leading order,

$$\bar{T}_0\bar{U}_{0\mathcal{X}_2} - \bar{U}_0\bar{T}_{0\mathcal{X}_2} + \bar{T}_0\bar{V}_0' - \bar{V}_0\bar{T}_0' = 0, \tag{2.2.21}$$

$$\bar{U}_0\bar{U}_{0\mathcal{X}_2} + \bar{V}_0\bar{U}_0' = \bar{T}_0(\bar{\mu}_0\bar{U}_0')', \tag{2.2.22}$$

and

$$\bar{U}_0\bar{T}_{0\mathcal{X}_2} + \bar{V}_0\bar{T}_0' = \frac{1}{Pr}\bar{T}_0(\bar{\mu}_0\bar{T}_0')' + (\gamma - 1)M^2\bar{T}_0\bar{\mu}_0\bar{U}_0'^2 \tag{2.2.23}$$

where $\mathcal{X}_2$ subscript denotes partial differentiation with respect to $\mathcal{X}_2$ and a prime denotes partial differentiation with respect to y. We remind the reader that the relation $\bar{\rho}_0\bar{T}_0 = 1$ has been used.

Equations (2.2.21)–(2.2.23) are subjected to boundary conditions

$$\bar{U}_0 \to 1 \quad \text{as} \quad y \to +\infty, \quad \bar{U}_0 \to \beta_U \quad \text{as} \quad y \to -\infty \quad \forall \mathcal{X}_2, \tag{2.2.24}$$

$$\bar{T}_0 \to 1 \quad \text{as} \quad y \to +\infty, \quad \bar{T}_0 \to \beta_T \quad \text{as} \quad y \to -\infty \quad \forall \mathcal{X}_2. \tag{2.2.25}$$

The velocity ratio β_U lies in the range $(0,1)$, since the faster stream velocity is used as a reference velocity. The stream below the shear layer will therefore be moving slower than the stream above. If the temperature ratio $\beta_T < 1$, the slow stream is relatively cold compared to the fast stream, whilst if $\beta_T > 1$, it is relatively hot.

Upon using the Howarth-Dorodnitsyn transformation (Dorodnitsyn 1942, Howarth 1948, Stewartson 1964)

$$\eta = \int_0^y \bar{\rho}_0(\mathcal{X}_2,\tilde{y})\mathrm{d}\tilde{y}, \quad \widehat{V}(\mathcal{X}_2,\eta) = \bar{\rho}_0\bar{V}_0 + \bar{U}_0\int_0^y \bar{\rho}_{0\mathcal{X}_2}(\mathcal{X}_2,\tilde{y})\mathrm{d}\tilde{y} \tag{2.2.26}$$

the mean-flow equations (2.2.21)–(2.2.23) become

$$\bar{U}_{0\mathcal{X}_2} + \widehat{V}_\eta = 0, \tag{2.2.27}$$

$$\bar{U}_0\bar{U}_{0\mathcal{X}_2} + \widehat{V}\bar{U}_{0\eta} = \left(\frac{\bar{\mu}_0}{\bar{T}_0}\bar{U}_{0\eta}\right)_\eta \tag{2.2.28}$$

and

$$\bar{U}_0\bar{T}_{0\mathcal{X}_2} + \widehat{V}\bar{T}_{0\eta} = \frac{1}{Pr}\left(\frac{\bar{\mu}_0}{\bar{T}_0}\bar{T}_{0\eta}\right)_\eta + (\gamma-1)M^2\frac{\bar{\mu}_0}{\bar{T}_0}\bar{U}_{0\eta}^2. \tag{2.2.29}$$

These equations are analogous to the incompressible equations, and thus allow for introduction of a streamfunction ψ via

$$\bar{U}_0 = \frac{\partial\psi}{\partial\eta}, \quad \widehat{V} = -\frac{\partial\psi}{\partial\mathcal{X}_2} \tag{2.2.30}$$

so that the continuity equation (2.2.27) is automatically satisfied. Consideration of a similarity solution of the form

$$\psi = (2\mathcal{X}_2)^{1/2}f(q), \quad \bar{U}_0 = f'(q), \quad \bar{T}_0 = \bar{T}_0(q), \quad q = \frac{\eta}{(2\mathcal{X}_2)^{1/2}} \tag{2.2.31}$$

yields the following pair of ODEs for f and $\bar{T}_0$:

$$\left(\frac{\bar{\mu}_0}{\bar{T}_0}f''\right)' + ff'' = 0, \tag{2.2.32}$$

and

$$\frac{1}{Pr}\left(\frac{\bar{\mu}_0}{\bar{T}_0}\bar{T}_0'\right)' + f\bar{T}_0' + (\gamma-1)M^2\left(\frac{\bar{\mu}_0}{\bar{T}_0}\right)(f'')^2 = 0 \tag{2.2.33}$$

where the primes denote differentiation with respect to the similarity variable q.

Under the assumption of unity Prandtl number, the so-called Crocco relation can be derived from (2.2.31)–(2.2.33):

$$\bar{T}_0 = 1 - (1-\beta_T)\frac{(1-\bar{U}_0)}{(1-\beta_U)} - \frac{1}{2}(\gamma-1)M^2\Big[(\bar{U}_0-1)(\bar{U}_0-\beta_U)\Big]. \tag{2.2.34}$$

Equation (2.2.34) is given in Grosch & Jackson (1991), and is valid for an arbitrary viscosity law $\bar{\mu}_0 = \bar{\mu}_0(\bar{T}_0)$ (see, for example, Stewartson 1964, p44).

For the Chapman law $\bar{\mu}_0 = \bar{T}_0$, the momentum and energy equations (2.2.32) & (2.2.33) decouple, and equation (2.2.32) reduces to

$$f''' + ff'' = 0 \tag{2.2.35}$$

with boundary conditions

$$f' \to 1 \ \text{ as } \ \eta \to +\infty, \qquad f' \to \beta_U \ \text{ as } \ \eta \to -\infty, \qquad f(0) = 0. \tag{2.2.36}$$

The third condition $f(0) = 0$ is equivalent to a specification of the streamfunction, and will not affect the physics of the flow, but only the location of the origin of the coordinate system. Equations (2.2.35) & (2.2.36) are equivalent to the Lock (1951) profile with uniform density and viscosity. They have to be solved numerically since there is no known explicit solution.

To the order of approximation of the subsequent stability analysis, it suffices to specify the velocity $\bar{U}_0$, viscosity $\bar{\mu}_0$ and temperature $\bar{T}_0$ profiles only at the location of interest, x_r say (see Leib 1991, p554). Expanding $\bar{U}_0$ and $\bar{T}_0$ as Taylor series about the location x_r

$$\begin{aligned}
\bar{U}_0(\mathcal{X}_2, y) &= U_0(y) + (\mathcal{X}_2 - x_r)U_{0,1}(y) + (\mathcal{X}_2 - x_r)^2 U_{0,2}(y) + \cdots, \\
\bar{T}_0(\mathcal{X}_2, y) &= T_0(y) + (\mathcal{X}_2 - x_r)T_{0,1}(y) + (\mathcal{X}_2 - x_r)^2 T_{0,2}(y) + \cdots
\end{aligned}$$

we thus require only $U_0(y)$ and $T_0(y)$.

As a common practice in shear layer instability studies, most of our subsequent numerical calculations will focus on the tanh profile,

$$U_0 = \frac{1}{2}\Big(1 + \beta_U + (1 - \beta_U)\tanh(\eta + s)\Big) \tag{2.2.37}$$

where η is now defined as

$$\eta = \int_0^y \rho_0(\tilde{y})\mathrm{d}\tilde{y}, \tag{2.2.38}$$

and s is a constant, representing a shift of coordinate so that the critical level is located at $\eta = 0$. The profile (5.1.5), which is only an approximation to equation (2.2.35), will be described in more detail in chapter 5.

2.3 Perturbations

In order to study the stability, we now perturb the basic flow. The perturbed flow can be written as

$$(p, T, u, v, \mu) = (P_{\mathrm{B}}, T_{\mathrm{B}}, U_{\mathrm{B}}, V_{\mathrm{B}}, \mu_{\mathrm{B}}) + (\gamma M^2 \tilde{p}, \widetilde{T}, \tilde{u}, \tilde{v}, \tilde{\mu}) \tag{2.3.39}$$

where the perturbations $\tilde{p}, \widetilde{T}, \tilde{u}, \tilde{v} \ll 1$ and, by Taylor expansion, $\tilde{\mu} = \mu'(T_{\mathrm{B}})\widetilde{T} + \frac{1}{2}\mu''(T_{\mathrm{B}})\widetilde{T}^2 + \cdots \ll 1$. If the perturbation is a (normal-mode) instability wave, then this wave will amplify as it propagates downstream. Its linear growth rate will gradually reduce as the shear layer thickens, eventually becoming nearly neutral at a location close to the neutral point x_{n}. We will choose x_{r} to be this location. Without loss of generality, we can set $x_{\mathrm{r}} = 0$, so that the origin of the coordinate is near the neutral position. Thus close to the origin, a critical layer emerges. Nonlinear effects may then become important in this layer, whilst the unsteady flow outside the critical layer remains linear. The analysis must therefore be performed for two distinct regions – a linear inviscid outer layer and a nonlinear viscous inner region (i.e. critical layer).

2.4 Outer flow

In the main part of the shear layer, outside the critical layer, the perturbation can be considered inviscid and linear. The inviscid assumption simplifies (2.1.7)–(2.1.10) to

$$\frac{1}{\gamma} Dp + p\Big(\frac{\partial u}{\partial x} + \frac{\partial v}{\partial y}\Big) = 0, \tag{2.4.40}$$

$$pDu + \frac{1}{\gamma M^2} T \frac{\partial p}{\partial x} = 0, \tag{2.4.41}$$

$$pDv + \frac{1}{\gamma M^2} T \frac{\partial p}{\partial y} = 0, \tag{2.4.42}$$

and

$$DT + (\gamma - 1)T\Big(\frac{\partial u}{\partial x} + \frac{\partial v}{\partial y}\Big) = 0. \tag{2.4.43}$$

Suppose that the perturbation is of the travelling wave form

$$\tilde{q} = \epsilon\Big[(A(\mathcal{X}_1, \mathcal{T})\tilde{q}_0(y)\mathrm{e}^{\mathrm{i}\zeta} + \text{c.c.}) + \Delta\tilde{q}_1(\mathcal{X}_1, \mathcal{T}, y, \zeta) + O(\epsilon, \Delta^2) + \cdots\Big] \tag{2.4.44}$$

where $\tilde{q}$ represents any of $\tilde{p}$, $\tilde{u}$, $\tilde{v}$, or $\widetilde{T}$, and $\epsilon \ll 1$. The variable ζ is defined as

$$\zeta = \alpha x - \omega t \tag{2.4.45}$$

which represents a moving coordinate. Both α and $\omega(=\alpha c)$ are real in the vicinity of x_n, where the disturbance evolves nonlinearly. The nonlinear development can be described by introducing an amplitude function $A(\mathcal{X}_1, \mathcal{T})$, which depends on the variables

$$\mathcal{X}_1 = \Delta x, \quad \mathcal{T} = \Delta t \tag{2.4.46}$$

representing slow streamwise and temporal coordinates respectively. The slow temporal and spatial effects are assumed to occur at the same order. The length/time scale on which the amplitude evolves, Δ^{-1}, is to be determined later.

Substitution into (2.4.40)–(2.4.43) yields the following equations at $\mathcal{O}(\epsilon)$

$$\mathrm{i}\alpha(U_0 - c)M^2\tilde{p}_0 + \mathrm{i}\alpha\tilde{u}_0 + \tilde{v}_0' = 0, \tag{2.4.47}$$

$$\mathrm{i}\alpha(U_0 - c)\tilde{u}_0 + U_0'\tilde{v}_0 + \mathrm{i}\alpha T_0\tilde{p}_0 = 0, \tag{2.4.48}$$

$$\mathrm{i}\alpha(U_0 - c)\tilde{v}_0 + T_0\tilde{p}_0' = 0, \tag{2.4.49}$$

and

$$\mathrm{i}\alpha(U_0 - c)\widetilde{T}_0 + T_0'\tilde{v}_0 + (\gamma - 1)T_0(\mathrm{i}\alpha\tilde{u}_0 + \tilde{v}_0') = 0. \tag{2.4.50}$$

From equations (2.4.47)–(2.4.49), by eliminating $\tilde{u}_0$ and $\tilde{v}_0$, we can derive the equation for the pressure perturbation:

$$\mathcal{L}\tilde{p}_0 = 0 \tag{2.4.51}$$

where

$$\mathcal{L} \equiv \frac{\partial^2}{\partial y^2} + \left(\frac{T_0'}{T_0} - 2\frac{U_0'}{(U_0 - c)}\right)\frac{\partial}{\partial y} + \alpha^2\left(\frac{M^2(U_0 - c)^2}{T_0} - 1\right)$$

is the compressible linear Rayleigh operator. For subsonic modes of interest in this study, the boundary conditions for (2.4.51) are $\tilde{p}_0 \to 0$ as $y \to \pm\infty$.

Since (2.4.51) is a linear homogeneous ordinary differential equation with a regular singular point at $y = 0$, we can use the Fröbenius method to find two linearly independent solutions valid near $y = 0$. Firstly note that, assuming that the critical level y_c is located at $y_c = 0$ without loss of generality,

$$(U_0 - c) = yU_c' + \frac{1}{2}y^2U_c'' + \frac{1}{6}y^3U_c''' + \cdots, \tag{2.4.52}$$

$$T_0 = T_c + yT_c' + \frac{1}{2}y^2T_c'' + \cdots, \tag{2.4.53}$$

where $U_c = c$, the phase speed of a neutral mode. The two solutions are thus given by (cf. Leib 1991)

$$\pi_1 = 1 - \frac{1}{2}\alpha^2 y^2 + \frac{1}{3}\alpha^2\Big(\frac{T_c'}{T_c} - \frac{U_c''}{U_c'}\Big)y^3 \ln|y| - \frac{1}{4}\alpha^2\Big(\frac{T_c'}{T_c} - \frac{U_c''}{U_c'}\Big)^2 y^4 \ln|y| + a_4 y^4 + \cdots \tag{2.4.54}$$

and

$$\pi_2 = y^3 - \frac{3}{4}\Big(\frac{T_c'}{T_c} - \frac{U_c''}{U_c'}\Big)y^4 + a_5 y^5 + \cdots \tag{2.4.55}$$

where

$$a_4 = \frac{1}{4}\alpha^2\left\{\frac{T_c''}{T_c} - \frac{2}{3}\frac{U_c'''}{U_c'} - \Big(\frac{T_c'}{T_c}\Big)^2 + \frac{1}{2}\Big(\frac{U_c''}{U_c'}\Big)^2 - \frac{1}{2}\alpha^2 - \frac{U_c'^2 M^2}{T_c} + \frac{11}{12}\Big(\frac{T_c'}{T_c} - \frac{U_c''}{U_c'}\Big)^2\right\}$$

and

$$a_5 = \frac{1}{10}\left\{3\Big(\frac{T_c'}{T_c} - \frac{U_c''}{U_c'}\Big)^2 + 3\Big(\frac{T_c'^2}{T_c^2} - \frac{T_c''}{T_c}\Big) + 2\frac{U_c'''}{U_c'} - \frac{3}{2}\frac{U_c''^2}{U_c'^2} + \alpha^2\right\}.$$

A general solution to the homogeneous equation (2.4.51) may be written as

$$\tilde{p}_0 = \frac{U_c'}{T_c}\left[\tilde{\pi}_1(\alpha; y) + \frac{1}{3}\alpha^2\Big(b_1^{\pm} + \frac{1}{2}\frac{U_c''}{U_c'}\Big)\tilde{\pi}_2(\alpha; y)\right], \tag{2.4.56}$$

for any independent solutions $\tilde{\pi}_1$, $\tilde{\pi}_2$, where $b_1^{\pm}$ refers to constant values above and below the critical level respectively. The (arbitrary) constant expected to be multiplying $\tilde{\pi}_1$ has been absorbed into $A(\mathcal{X}_1, \mathcal{T})$. Near $y = 0$, $\tilde{\pi}_1$ and $\tilde{\pi}_2$ are approximated by π_1 and π_2 respectively.

For neutral modes, the eigenfunction is generally singular. If M is sufficiently large, there exist supersonic modes, for which $T_c'/T_c - U_c''/U_c' \neq 0$ so that $\tilde{p}_0$ is logarithmically singular. Our interest is in the subsonic mode regime, for which the instability modes are associated with the generalised inflection point, i.e.

$$\Big(\frac{U_0'}{T_0}\Big)' = 0. \tag{2.4.57}$$

This was shown by Lees & Lin (1946) to be a necessary condition for the existence of a subsonic neutral mode. Thus for a regular critical level,

$$\frac{T_c'}{T_c} = \frac{U_c''}{U_c'}. \tag{2.4.58}$$

It follows that the logarithmic terms in π_1 and the $\mathcal{O}(y^4)$ term in π_2 vanish. The coefficients a_4 and a_5 simplify to

$$a_4 = \frac{1}{4}\alpha^2\left\{\frac{T_c''}{T_c} - \frac{2}{3}\frac{U_c'''}{U_c'} - \frac{1}{2}\Big(\frac{T_c'}{T_c}\Big)^2 - \frac{1}{2}\alpha^2 - \frac{U_c'^2 M^2}{T_c}\right\}$$

and

$$a_5 = \frac{1}{10}\Big\{ -3\frac{T_c''}{T_c} + \frac{3}{2}\Big(\frac{T_c'}{T_c}\Big)^2 + 2\frac{U_c'''}{U_c'} + \alpha^2 \Big\}.$$

Also it follows that

$$b_1^+ = b_1^- \equiv b_1. \tag{2.4.59}$$

We can easily derive asymptotic solutions for $\tilde{u}_0$, $\tilde{v}_0$ and $\widetilde{T}_0$ by substituting (2.4.56) into (2.4.47)–(2.4.50). They are

$$\tilde{u}_0 = -b_1 - \frac{1}{T_c} e_1 y + \mathcal{O}(y^2), \tag{2.4.60}$$

$$\tilde{v}_0 = -\mathrm{i}\alpha + \mathrm{i}\alpha b_1 y + \frac{\mathrm{i}\alpha}{2T_c}\Big(e_1 - M^2 U_c'^2\Big) y^2 + \mathcal{O}(y^3) \tag{2.4.61}$$

and

$$\widetilde{T}_0 = \frac{T_c'}{U_c'}\frac{1}{y} + \frac{1}{U_c'}\left(T_c'' - T_c' b_1 - \frac{1}{2}\frac{T_c'^2}{T_c} + (\gamma - 1) M^2 U_c'^2\right) + \mathcal{O}(y) \tag{2.4.62}$$

where

$$e_1 = T_c'' + T_c' b_1 - \frac{U_c'''}{U_c'} T_c - \alpha^2 T_c - M^2 U_c'^2.$$

Evidently, the leading order velocities $\tilde{u}_0$, $\tilde{v}_0$ and pressure $\tilde{p}_0$ are regular, but the leading order temperature $\tilde{T}_0$ has a pole singularity if $T_c' \neq 0$.

The second term in (2.4.44) can be expressed as

$$\tilde{q}_1 = \sum_{\substack{m=-\infty \\ m\neq 0}}^{\infty} \tilde{q}_1^{(m)}(\mathcal{X}_1, \mathcal{T}, y) \mathrm{e}^{\mathrm{i}m\zeta}, \quad \tilde{q}_1^{(-m)} = \tilde{q}_1^{(m)*} \tag{2.4.63}$$

where * represents complex conjugate. Thus substitution of (2.4.44) into (2.4.40)–(2.4.43) yields, at $\mathcal{O}(\epsilon\Delta)$, equations (2.4.47)–(2.4.50) for the harmonics $\tilde{q}_1^{(m)}$ ($m \neq 0, \pm 1$), with α replaced by $m\alpha$. Hence the pressure harmonics $\tilde{p}_1^{(m)}$, $m \neq 0, \pm 1$ satisfy equation (2.4.51) with $\alpha \to m\alpha$, and so we have

$$\tilde{p}_1^{(m)} = d_1^{(m)}(\mathcal{X}_1, \mathcal{T}) \tilde{\pi}_1(m\alpha; y) + d_2^{(m)\pm}(\mathcal{X}_1, \mathcal{T}) \tilde{\pi}_2(m\alpha; y). \tag{2.4.64}$$

For the fundamental component ($m = 1$) at $\mathcal{O}(\epsilon\Delta)$, the $\tilde{q}_1^{(1)}$s are governed by the inhomogeneous system

$$\mathrm{i}\alpha(U_0 - c) M^2 \tilde{p}_1^{(1)} + \mathrm{i}\alpha \tilde{u}_1^{(1)} + \tilde{v}_1^{(1)\prime} = -\Big((A_{\mathcal{T}} + U_0 A_{\mathcal{X}_1}) M^2 \tilde{p}_0 + A_{\mathcal{X}_1} \tilde{u}_0\Big) \tag{2.4.65}$$

$$\mathrm{i}\alpha(U_0 - c)\tilde{u}_1^{(1)} + U_0' \tilde{v}_1^{(1)} + \mathrm{i}\alpha T_0 \tilde{p}_1^{(1)} = -\Big((A_{\mathcal{T}} + U_0 A_{\mathcal{X}_1})\tilde{u}_0 + T_0 A_{\mathcal{X}_1} \tilde{p}_0\Big), \tag{2.4.66}$$

$$\mathrm{i}\alpha(U_0 - c)\tilde{v}_1^{(1)} + T_0 \tilde{p}_1^{(1)\prime} = -(A_{\mathcal{T}} + U_0 A_{\mathcal{X}_1})\tilde{v}_0, \tag{2.4.67}$$

and

$$\mathrm{i}\alpha(U_0-c)\widetilde{T}_1^{(1)}+T_0'\tilde{v}_1^{(1)}+(\gamma-1)T_0(\mathrm{i}\alpha\tilde{u}_1^{(1)}+\tilde{v}_1^{(1)'}) = -\Big((A_{\mathcal{T}}+U_0A_{\mathcal{X}_1})\widetilde{T}_0+(\gamma-1)T_0A_{\mathcal{X}_1}\tilde{u}_0\Big) \tag{2.4.68}$$

where the subscripts $\mathcal{T}$ and $\mathcal{X}_1$ denote partial differentiations. Again elimination of $\tilde{u}_1^{(1)}$ and $\tilde{v}_1^{(1)}$ from (2.4.65)–(2.4.67) yields the equation for $\tilde{p}_1^{(1)}$:

$$\mathcal{L}\tilde{p}_1^{(1)} = \frac{2\mathrm{i}}{\alpha}(A_{\mathcal{T}}+cA_{\mathcal{X}_1})\Big(\frac{U_0'}{(U_0-c)^2}\tilde{p}_0'+\frac{\alpha^2M^2(U_0-c)}{T_0}\tilde{p}_0\Big)+2\mathrm{i}\alpha\Big(\frac{M^2(U_0-c)^2}{T_0}-1\Big)A_{\mathcal{X}_1}\tilde{p}_0. \tag{2.4.69}$$

Equation (2.4.69) is an inhomogeneous version of (2.4.51). Thus its solution, valid near $y=0$, is given by

$$\tilde{p}_1^{(1)} = \tilde{p}_{1\mathrm{PS}}^{(1)} + d_1(\mathcal{X}_1,\mathcal{T})\pi_1 + d_2^{\pm}(\mathcal{X}_1,\mathcal{T})\pi_2 \tag{2.4.70}$$

where $\tilde{p}_{1\mathrm{PS}}^{(1)}$ is the particular solution of (2.4.69) found near $y=0$ by seeking a particular solution of the form $\tilde{p}_1^{(1)} = c_1y+c_2y^2+c_{3\mathrm{L}}y^3\ln|y|+c_{4\mathrm{L}}y^4\ln|y|+c_4y^4+\cdots$. We find that

$$\begin{aligned}\tilde{p}_{1\mathrm{PS}}^{(1)} = {}& \frac{\mathrm{i}\alpha}{T_{\mathrm{c}}}(A_{\mathcal{T}}+cA_{\mathcal{X}_1})y+\frac{\mathrm{i}\alpha}{T_{\mathrm{c}}}\Big(U_{\mathrm{c}}'A_{\mathcal{X}_1}-(A_{\mathcal{T}}+cA_{\mathcal{X}_1})\Big(b_1+\frac{1}{2}\frac{T_{\mathrm{c}}'}{T_{\mathrm{c}}}\Big)\Big)y^2\\ &+\frac{1}{3}\frac{\mathrm{i}\alpha}{T_{\mathrm{c}}}(A_{\mathcal{T}}+cA_{\mathcal{X}_1})\Big(\frac{T_{\mathrm{c}}''}{T_{\mathrm{c}}}-\frac{U_{\mathrm{c}}'''}{U_{\mathrm{c}}'}\Big)y^3\ln|y|+\mathcal{O}(y^4\ln|y|).\end{aligned} \tag{2.4.71}$$

The asymptotic solutions for $\tilde{u}_1^{(1)}$, $\tilde{v}_1^{(1)}$ and $\widetilde{T}_1^{(1)}$ are found by substituting (2.4.56) and (2.4.70)–(2.4.62) into (2.4.65)–(2.4.68). We obtain

$$\tilde{u}_1^{(1)} = \frac{\mathrm{i}}{\alpha U_{\mathrm{c}}'}\Big(\frac{U_{\mathrm{c}}'''}{U_{\mathrm{c}}'}-\frac{T_{\mathrm{c}}''}{T_{\mathrm{c}}}\Big)(A_{\mathcal{T}}+cA_{\mathcal{X}_1})\ln|y|+e_2^{\pm}+\mathcal{O}(y\ln|y|), \tag{2.4.72}$$

$$\begin{aligned}\tilde{v}_1^{(1)} = {}& \frac{1}{U_{\mathrm{c}}'}\Big(b_1(A_{\mathcal{T}}+cA_{\mathcal{X}_1})-U_{\mathrm{c}}'A_{\mathcal{X}_1}-\mathrm{i}\alpha d_1T_{\mathrm{c}}\Big)+\frac{1}{U_{\mathrm{c}}'}\Big(\frac{U_{\mathrm{c}}'''}{U_{\mathrm{c}}'}-\frac{T_{\mathrm{c}}''}{T_{\mathrm{c}}}\Big)(A_{\mathcal{T}}+cA_{\mathcal{X}_1})y\ln|y|\\ &+e_3^{\pm}y+\mathcal{O}(y^2\ln|y|)\end{aligned} \tag{2.4.73}$$

and

$$\widetilde{T}_1^{(1)} = \frac{\mathrm{i}}{\alpha}\frac{T_{\mathrm{c}}'}{U_{\mathrm{c}}'^2}\Big(A_{\mathcal{T}}+cA_{\mathcal{X}_1}\Big)\frac{1}{y^2}+\frac{\mathrm{i}}{\alpha U_{\mathrm{c}}'^2}\Big\{\Big(T_{\mathrm{c}}''-\frac{T_{\mathrm{c}}'^2}{T_{\mathrm{c}}}\Big)\Big(A_{\mathcal{T}}+cA_{\mathcal{X}_1}\Big)-\mathrm{i}\alpha T_{\mathrm{c}}'T_{\mathrm{c}}d_1\Big\}\frac{1}{y}+\mathcal{O}(\ln|y|) \tag{2.4.74}$$

where we have put

$$\begin{aligned}e_2^{\pm} = {}& \frac{\mathrm{i}}{\alpha}\Big(-\frac{7}{3}\frac{T_{\mathrm{c}}''}{U_{\mathrm{c}}'T_{\mathrm{c}}}+\frac{11}{6}\frac{U_{\mathrm{c}}'''}{U_{\mathrm{c}}'^2}+\frac{1}{U_{\mathrm{c}}'}\Big(\frac{T_{\mathrm{c}}'}{T_{\mathrm{c}}}\Big)^2+\frac{T_{\mathrm{c}}'}{T_{\mathrm{c}}U_{\mathrm{c}}'}b_1+\frac{1}{2}\alpha^2\frac{1}{U_{\mathrm{c}}'}+2M^2\frac{U_{\mathrm{c}}'}{T_{\mathrm{c}}}\Big)\Big(A_{\mathcal{T}}+cA_{\mathcal{X}_1}\Big)\\ &-\frac{\mathrm{i}}{\alpha}\Big(\frac{T_{\mathrm{c}}'}{T_{\mathrm{c}}}+2b_1\Big)A_{\mathcal{X}_1}+\frac{1}{U_{\mathrm{c}}'}\Big(\frac{1}{2}T_{\mathrm{c}}'d_1-\frac{3T_{\mathrm{c}}}{\alpha^2}d_2^{\pm}\Big)\end{aligned}$$

and

$$e_3^{\pm} = \Big(-\frac{4}{3}\frac{T_c''}{U_c' T_c} + \frac{5}{6}\frac{U_c'''}{U_c'^2} + \frac{1}{U_c'}\Big(\frac{T_c'}{T_c}\Big)^2 + \frac{T_c'}{T_c U_c'} b_1 + \frac{1}{2}\alpha^2 \frac{1}{U_c'} + M^2 \frac{U_c'}{T_c}\Big)\Big(A_{\mathcal{T}} + cA_{\mathcal{X}_1}\Big) - \Big(\frac{T_c'}{T_c} + b_1\Big) A_{\mathcal{X}_1} - \frac{\mathrm{i}\alpha}{U_c'}\Big(\frac{1}{2} T_c' d_1 - \frac{3T_c}{\alpha^2} d_2^{\pm}\Big).$$

In order for equation (2.4.69) to have a solution also satisfying the boundary conditions, a solvability condition must be imposed. This condition can be derived by multiplying (2.4.69) by $\tilde{p}_0 W(y)$ and integrating from $y = -\infty$ to $y = +\infty$, where $W(y)$ is the weight function

$$W(y) = \frac{T_0}{(U_0 - c)^2}. \tag{2.4.75}$$

This gives

$$\int_{-\infty}^{+\infty} \tilde{p}_0 \frac{T_0}{(U_0 - c)^2} \mathcal{L}\tilde{p}_1^{(1)} \mathrm{d}y = 2\mathrm{i}\Big(cJ_1 \frac{\partial A}{\partial \mathcal{X}_1} + J_2 \frac{\partial A}{\partial \mathcal{T}}\Big) \tag{2.4.76}$$

where we have put

$$J_1 = J_2 + \frac{\alpha}{c} J_3, \quad J_2 = \frac{1}{\alpha} K_1 + \alpha M^2 K_2, \quad J_3 = M^2 K_3 - K_4 \tag{2.4.77}$$

with

$$K_1 = \int_{-\infty}^{+\infty} \frac{T_0 U_0'}{(U_0 - c)^4} \tilde{p}_0 \tilde{p}_0' \mathrm{d}y, \qquad K_2 = \int_{-\infty}^{+\infty} \frac{1}{(U_0 - c)} \tilde{p}_0^2 \mathrm{d}y$$
$$K_3 = \int_{-\infty}^{+\infty} \tilde{p}_0^2 \mathrm{d}y, \qquad K_4 = \int_{-\infty}^{+\infty} \frac{T_0}{(U_0 - c)^2} \tilde{p}_0^2 \mathrm{d}y. \tag{2.4.78}$$

Here $\fint_{-\infty}^{+\infty}$ denotes the Cauchy principal value. Using integration by parts twice on the left-hand side of (2.4.76) shows that

$$-\frac{3}{U_c'}(d_2^+ - d_2^-) = 2\mathrm{i}\Big(cJ_1 \frac{\partial A}{\partial \mathcal{X}_1} + J_2 \frac{\partial A}{\partial \mathcal{T}}\Big). \tag{2.4.79}$$

The difference $(d_2^+ - d_2^-)$ is related to the jump in the streamwise velocity by

$$\tilde{u}_1^{(1)}(y = 0+) - \tilde{u}_1^{(1)}(y = 0-) = -3\frac{T_c}{\alpha^2 U_c'}(d_2^+ - d_2^-). \tag{2.4.80}$$

In the next chapter, we will examine the critical layer in order to calculate the velocity jump that is needed to derive the equations governing the amplitude $A(\mathcal{X}_1, \mathcal{T})$. To do this requires matching the inner critical-layer solution to the outer

solution, and so to facilitate this process we reproduce here the outer asymptotic solutions for $\tilde{u}$ and $\tilde{v}$:

$$\tilde{u} \sim \epsilon\Bigg\{\Big[\Big(-b_1 - \frac{1}{T_c}e_1 y + \mathcal{O}(y^2)\Big)Ae^{i\zeta} + \text{c.c.}\Big] + \Delta\Bigg[\Big(\frac{i}{\alpha U_c'}\Big(\frac{U_c'''}{U_c'} - \frac{T_c''}{T_c}\Big)(A_{\mathcal{T}} + cA_{\chi_1})\ln|y| + e_2^{\pm} + \mathcal{O}(y\ln|y|)\Big)e^{i\zeta} + \text{c.c.} + \frac{1}{U_c'}\sum_{\substack{m=-\infty \\ m\neq 0,\pm 1}}^{\infty}\Big\{\Big(\frac{T_c'}{2}d_1^{(m)} - \frac{3T_c}{(m\alpha)^2}d_2^{(m)\pm}\Big) + \mathcal{O}(y)\Big\}e^{im\zeta}\Bigg] + \cdots\Bigg\}, \quad (2.4.81)$$

$$\tilde{v} \sim \epsilon\Bigg\{\Big[\Big(-i\alpha + i\alpha b_1 y + \frac{i\alpha}{2T_c}(e_1 - M^2U_c'^2)y^2 + \mathcal{O}(y^3)\Big)Ae^{i\zeta} + \text{c.c.}\Big] + \Delta\Bigg[\Big(\frac{1}{U_c'}\Big(b_1(A_{\mathcal{T}} + cA_{\chi_1}) - U_c'A_{\chi_1} - i\alpha d_1 T_c\Big) + \frac{1}{U_c'}\Big(\frac{U_c'''}{U_c'} - \frac{T_c''}{T_c}\Big)(A_{\mathcal{T}} + cA_{\chi_1})y\ln|y| + e_3^{\pm}y + \mathcal{O}(y^2\ln|y|)\Big)e^{i\zeta} + \text{c.c.} - i\sum_{\substack{m=-\infty \\ m\neq 0,\pm 1}}^{\infty}\Big\{(m\alpha)\frac{T_c}{U_c'}d_1^{(m)} + \mathcal{O}(y)\Big\}e^{im\zeta}\Bigg] + \cdots\Bigg\}. \quad (2.4.82)$$

In the outer flow we have treated $M = \mathcal{O}(1)$, however the outer flow is also valid for $M \ll \mathcal{O}(1)$. Note also that when $\beta_T = 1$ and $M = 0$, $T_c' = 0$. In this case, the critical-layer nonlinearity is dominated by the logarithmic term in $\tilde{u}_1^{(1)}$ (see (2.4.72)), and its dynamics is governed by the strongly nonlinear theory of Goldstein & Leib (1988). If, however, $\beta_T \neq 1$ and/or $M = \mathcal{O}(1)$, then $T_c' \neq 0$, and the critical-layer nonlinearity is dominated by the pole in $\widetilde{T}_0$ (see (2.4.62)), and so nonlinear effects operate in a weakly nonlinear fashion, as in Goldstein & Leib (1989).

To unify these two theories, we need to consider the weakly compressible limit with Mach number $M \ll \mathcal{O}(1)$. The distinguished scaling for M, which includes the nonlinearity effect of both the velocity and temperature perturbations, is to be determined in the next chapter.

Note that the Crocco relation (2.2.34) shows that we must write

$$1 - \beta_T = \hat{\beta}M^2, \quad \hat{\beta} = \mathcal{O}(1) \quad (2.4.83)$$

so that T_c', T_c'', etc. are all $\mathcal{O}(M^2)$, i.e. the temperature difference across the shear layer must be small.

Chapter 3

Nonlinear Critical Layer

3.1 Scaling arguments

The singular nature of the outer solution at y_c implies that the critical layer has to be analysed separately. In particular, viscosity, nonlinearity and non-equilibrium effects, which are negligible in the main part of the flow, have to be included within the critical layer in order to smooth out the singularity. In this section, we derive the distinguished scaling such that all three of these effects appear at leading order simultaneously. For that purpose, we examine the flow inside the thin critical layer. Let us first define an inner variable

$$Y = \frac{y}{\eta} = \mathcal{O}(1), \tag{3.1.1}$$

where the width $\eta \ll \mathcal{O}(1)$ of the critical layer is to be determined. Now substituting (2.3.39) into (2.1.7)–(2.1.10), and rewriting the equations in terms of Y, we obtain

$$\begin{aligned}(T_{\mathrm{B}}+\widetilde{T})\mathrm{D}_{\mathrm{crit}}(P_{\mathrm{B}}+\gamma M^2\tilde{p}) - (P_{\mathrm{B}}+\gamma M^2\tilde{p})\mathrm{D}_{\mathrm{crit}}(T_{\mathrm{B}}+\widetilde{T}) + (P_{\mathrm{B}}+\gamma M^2\tilde{p})(T_{\mathrm{B}}+\widetilde{T})\\ \times\left[\Big(\alpha\frac{\partial}{\partial\zeta}+\Delta\frac{\partial}{\partial\mathcal{X}_1}+\frac{1}{R}\frac{\partial}{\partial\mathcal{X}_2}\Big)(U_{\mathrm{B}}+\tilde{u})+\eta^{-1}\frac{\partial}{\partial Y}(V_{\mathrm{B}}+\tilde{v})\right]=0,\end{aligned} \tag{3.1.2}$$

$$\begin{aligned}(P_{\mathrm{B}}+\gamma M^2\tilde{p})\mathrm{D}_{\mathrm{crit}}(U_{\mathrm{B}}+\tilde{u}) = -\frac{1}{\gamma M^2}(T_{\mathrm{B}}+\widetilde{T})\Big(\alpha\frac{\partial}{\partial\zeta}+\Delta\frac{\partial}{\partial\mathcal{X}_1}+\frac{1}{R}\frac{\partial}{\partial\mathcal{X}_2}\Big)(P_{\mathrm{B}}+\gamma M^2\tilde{p})\\ +\frac{1}{R}(T_{\mathrm{B}}+\widetilde{T})\Bigg\{\frac{2}{3}\Big(\alpha\frac{\partial}{\partial\zeta}+\Delta\frac{\partial}{\partial\mathcal{X}_1}+\frac{1}{R}\frac{\partial}{\partial\mathcal{X}_2}\Big)\Bigg[(\mu_{\mathrm{B}}+\tilde{\mu})\Big(2\Big(\alpha\frac{\partial}{\partial\zeta}+\Delta\frac{\partial}{\partial\mathcal{X}_1}+\frac{1}{R}\frac{\partial}{\partial\mathcal{X}_2}\Big)\\ \times(U_{\mathrm{B}}+\tilde{u})-\eta^{-1}\frac{\partial}{\partial Y}(V_{\mathrm{B}}+\tilde{v})\Big)\Bigg]+\eta^{-1}\frac{\partial}{\partial Y}\Bigg[(\mu_{\mathrm{B}}+\tilde{\mu})\Big(\eta^{-1}\frac{\partial}{\partial Y}(U_{\mathrm{B}}+\tilde{u})\\ +\Big(\alpha\frac{\partial}{\partial\zeta}+\Delta\frac{\partial}{\partial\mathcal{X}_1}+\frac{1}{R}\frac{\partial}{\partial\mathcal{X}_2}\Big)(V_{\mathrm{B}}+\tilde{v})\Big)\Bigg]\Bigg\},\end{aligned} \tag{3.1.3}$$

$$(P_{\rm B}+\gamma M^2\tilde{p})\mathrm{D}_{\rm crit}(V_{\rm B}+\tilde{v}) = -\frac{1}{\gamma M^2}(T_{\rm B}+\widetilde{T})\eta^{-1}\frac{\partial}{\partial Y}(P_{\rm B}+\gamma M^2\tilde{p}) + \frac{1}{R}(T_{\rm B}+\widetilde{T})$$
$$\times\Bigg\{\frac{2}{3}\eta^{-1}\frac{\partial}{\partial Y}\Bigg[(\mu_{\rm B}+\tilde{\mu})\Bigg(2\eta^{-1}\frac{\partial}{\partial Y}(V_{\rm B}+\tilde{v}) - \Big(\alpha\frac{\partial}{\partial\zeta}+\Delta\frac{\partial}{\partial\mathcal{X}_1}+\frac{1}{R}\frac{\partial}{\partial\mathcal{X}_2}\Big)(U_{\rm B}+\tilde{u})\Bigg)\Bigg]$$
$$+\Big(\alpha\frac{\partial}{\partial\zeta}+\Delta\frac{\partial}{\partial\mathcal{X}_1}+\frac{1}{R}\frac{\partial}{\partial\mathcal{X}_2}\Big)\Bigg[(\mu_{\rm B}+\tilde{\mu})\Bigg(\eta^{-1}\frac{\partial}{\partial Y}(U_{\rm B}+\tilde{u})$$
$$+\Big(\alpha\frac{\partial}{\partial\zeta}+\Delta\frac{\partial}{\partial\mathcal{X}_1}+\frac{1}{R}\frac{\partial}{\partial\mathcal{X}_2}\Big)(V_{\rm B}+\tilde{v})\Bigg)\Bigg]\Bigg\}, \tag{3.1.4}$$

$$(P_{\rm B}+\gamma M^2\tilde{p})\mathrm{D}_{\rm crit}(T_{\rm B}+\widetilde{T}) = \frac{(\gamma-1)}{\gamma}(T_{\rm B}+\widetilde{T})\mathrm{D}_{\rm crit}(P_{\rm B}+\gamma M^2\tilde{p}) + \frac{1}{P_r R}(T_{\rm B}+\widetilde{T})$$
$$\times\Bigg\{\Big(\alpha\frac{\partial}{\partial\zeta}+\Delta\frac{\partial}{\partial\mathcal{X}_1}+\frac{1}{R}\frac{\partial}{\partial\mathcal{X}_2}\Big)\Bigg[(\mu_{\rm B}+\tilde{\mu})\Big(\alpha\frac{\partial}{\partial\zeta}+\Delta\frac{\partial}{\partial\mathcal{X}_1}+\frac{1}{R}\frac{\partial}{\partial\mathcal{X}_2}\Big)(T_{\rm B}+\widetilde{T})\Bigg]$$
$$+\eta^{-1}\frac{\partial}{\partial Y}\Big[(\mu_{\rm B}+\tilde{\mu})\eta^{-1}\frac{\partial}{\partial Y}(T_{\rm B}+\widetilde{T})\Big]\Bigg\} + \frac{(\gamma-1)M^2}{R}(T_{\rm B}+\widetilde{T})(\mu_{\rm B}+\tilde{\mu})$$
$$\times\Bigg\{\frac{4}{3}\Bigg[\Bigg(\Big(\alpha\frac{\partial}{\partial\zeta}+\Delta\frac{\partial}{\partial\mathcal{X}_1}+\frac{1}{R}\frac{\partial}{\partial\mathcal{X}_2}\Big)(U_{\rm B}+\tilde{u})\Bigg)^2 + \Big(\eta^{-1}\frac{\partial}{\partial Y}(V_{\rm B}+\tilde{v})\Big)^2$$
$$-\Bigg(\Big(\alpha\frac{\partial}{\partial\zeta}+\Delta\frac{\partial}{\partial\mathcal{X}_1}+\frac{1}{R}\frac{\partial}{\partial\mathcal{X}_2}\Big)(U_{\rm B}+\tilde{u})\Bigg)\Big(\eta^{-1}\frac{\partial}{\partial Y}(V_{\rm B}+\tilde{v})\Big)\Bigg]$$
$$+\Bigg[\Big(\alpha\frac{\partial}{\partial\zeta}+\Delta\frac{\partial}{\partial\mathcal{X}_1}+\frac{1}{R}\frac{\partial}{\partial\mathcal{X}_2}\Big)(V_{\rm B}+\tilde{v})+\eta^{-1}\frac{\partial}{\partial Y}(U_{\rm B}+\tilde{u})\Bigg]^2\Bigg\}, \tag{3.1.5}$$

where

$$\mathrm{D}_{\rm crit} \equiv \alpha\Big((U_{\rm B}-c)+\tilde{u}\Big)\frac{\partial}{\partial\zeta}+\Delta\frac{\partial}{\partial\mathcal{T}}+\big(U_{\rm B}+\tilde{u}\big)\Big(\Delta\frac{\partial}{\partial\mathcal{X}_1}+\frac{1}{R}\frac{\partial}{\partial\mathcal{X}_2}\Big)+\big(V_{\rm B}+\tilde{v}\big)\eta^{-1}\frac{\partial}{\partial Y}. \tag{3.1.6}$$

In order to determine the width of the critical layer, and the nonlinear evolution space/time scale Δ^{-1}, we consider the nonlinear interaction within the critical layer. Note that (2.4.44) & (2.4.61) imply $\tilde{v}\sim\epsilon$, whereas (2.4.44) & (2.4.62) imply $\widetilde{T}\sim\epsilon M^2/\eta$. The temperature fluctuation is much larger, and is the dominant contribution to the nonlinear effect. We thus consider the balance between the inertial and the "Reynolds stress" terms in the energy equation (3.1.5):

$$(U_{\rm B}-c)\frac{\partial\widetilde{T}}{\partial\zeta}\sim\tilde{v}\frac{1}{\eta}\frac{\partial\widetilde{T}}{\partial Y}. \tag{3.1.7}$$

The quadratic nonlinear term on the right-hand side of (3.1.7) generates harmonics ($\mathrm{e}^{2\mathrm{i}\zeta}$, $\mathrm{e}^{-2\mathrm{i}\zeta}$) and a mean flow distortion term, denoted by $\widetilde{T}_{\rm II}$ say. Since $(U_{\rm B}-c)\sim\eta$,

it follows from (3.1.7) that

$$\widetilde{T}_{\mathrm{II}} \sim \frac{\epsilon^2 M^2}{\eta^3}. \tag{3.1.8}$$

Now consider the following balance in the x-momentum equation (3.1.3):

$$(U_{\mathrm{B}} - c)\frac{\partial \tilde{u}}{\partial \zeta} \sim \widetilde{T}\frac{\partial \tilde{p}}{\partial \zeta}. \tag{3.1.9}$$

The fundamental component of the pressure interacts at the cubic level with the mean temperature distortion $\widetilde{T}_{\mathrm{II}}$ to regenerate the fundamental, $\tilde{u}_{\mathrm{III}}$ say. Note that $\tilde{p} \sim \epsilon$ as is implied by (2.4.44) & (2.4.56). Use of this and (3.1.8)–(3.1.9) yields the order of magnitude of this regenerated fundamental $\mathrm{e}^{\mathrm{i}\zeta}$, namely

$$\tilde{u}_{\mathrm{III}} \sim \frac{\epsilon^3 M^2}{\eta^4}. \tag{3.1.10}$$

Equations (2.4.44) & (2.4.72) show that there exists an $\mathcal{O}(\epsilon\Delta)$ jump in the outer solution for $\tilde{u}$. When the jump in $\tilde{u}_{\mathrm{III}}$ becomes of the same order, i.e. when

$$\epsilon^2 M^2 \sim \Delta\eta^4, \tag{3.1.11}$$

the evolution of the instability mode is affected by nonlinearity.

To include the non-equilibrium effect associated with $\partial/\partial\mathcal{X}_1$ (and $\partial/\partial\mathcal{T}$), we require

$$(U_{\mathrm{B}} - c)\frac{\partial}{\partial \zeta} \sim \Delta\frac{\partial}{\partial \mathcal{X}_1}$$

in (3.1.6), from which it can be deduced that

$$\eta \sim \Delta. \tag{3.1.12}$$

Use of this estimate in the balance (3.1.11) leads to

$$\Delta^5 \sim M^2\epsilon^2. \tag{3.1.13}$$

If the Mach number is chosen to be $\mathcal{O}(1)$, then we recover the weakly nonlinear scaling given in Goldstein & Leib (1989), namely $\eta \sim \Delta \sim \epsilon^{2/5}$. However, the strongly nonlinear scaling (associated with the velocity singularity) given in Goldstein & Leib (1988) is $\Delta \sim \epsilon^{1/2}$. We must keep this scaling intact in order for the resulting nonlinear theory to be able to describe vortex roll-up. Thus it can be concluded that the Mach number $M \sim \epsilon^{1/4}$ is the distinguished scaling in that both temperature and velocity fluctuations contribute to the nonlinearity, and the critical layer dynamics is strongly nonlinear.

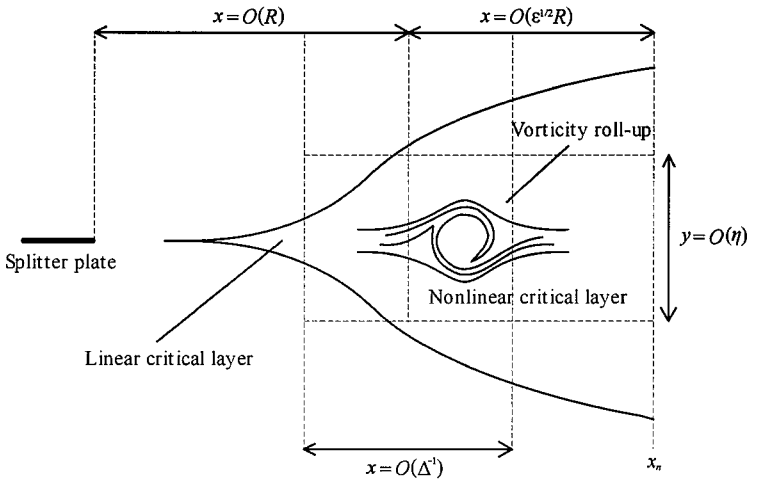


Figure 3.1: Sketch of the flow structure. An instability wave with an amplitude of $\mathcal{O}(\epsilon)$ enters the nonlinear critical layer regime at a distance of $\mathcal{O}(\epsilon^{1/2}R)$ upstream of the neutral position $x_{\rm n}$. The strongly nonlinear evolution occurs on the scale of $\Delta^{-1} \sim \epsilon^{-1/2}$.

Finally, for the viscous effect to be at leading order in the critical layer, we require

$$(U_{\rm B} - c)\frac{\partial \tilde{u}}{\partial \zeta} \sim \frac{1}{R}\frac{1}{\eta^2}\frac{\partial^2 \tilde{u}}{\partial Y^2}$$

which upon using (3.1.12) gives

$$\frac{1}{R} \sim \Delta^3. \tag{3.1.14}$$

Note that if $\Delta \sim \epsilon^{2/5}$ we obtain the viscous scaling in Goldstein & Leib (1989), namely $R \sim \epsilon^{-6/5}$. However with $\Delta \sim \epsilon^{1/2}$ we find that $R \sim \epsilon^{-3/2}$ and so we write

$$\frac{1}{R} = \Lambda\epsilon^{3/2}, \tag{3.1.15}$$

where Λ is an $\mathcal{O}(1)$ parameter (Haberman 1972). Thus, in sum, we set

$$\eta = \epsilon^{1/2}, \tag{3.1.16}$$

$$\Delta = \epsilon^{1/2} \tag{3.1.17}$$

and

$$M = \mathcal{M}\epsilon^{1/4}, \tag{3.1.18}$$

where $\mathcal{M}$ is an $\mathcal{O}(1)$ parameter. The flow structure is illustrated in figure 3.1.

3.2 Critical layer analysis

Under the above assumptions, the solution for the perturbations in the critical layer expands as

$$\tilde{q} = \epsilon\bar{q}_0 + \epsilon^{3/2}(\bar{q}_1 + (\ln\epsilon^{1/2})\bar{q}_{1\mathrm{L}}) + \epsilon^2(\bar{q}_2 + (\ln\epsilon^{1/2})\bar{q}_{2\mathrm{L}}) + \cdots, \tag{3.2.19}$$

where $\tilde{q}$ represents any of $\tilde{p}$, $\tilde{u}$, $\tilde{v}$, or $\widetilde{T}$, and $\bar{q}_i = \bar{q}_i(\zeta, \mathcal{X}_1, \mathcal{T}, Y)$. This expansion is suggested by writing the outer asymptotic solution in terms of Y. Near y_c, the basic temperature and velocity profiles are approximated as

$$T_0 = T_\mathrm{c} + M^2\Big\{\epsilon^{1/2}YT'_{\mathrm{c}M} + \frac{1}{2}\epsilon Y^2T''_{\mathrm{c}M} + \frac{1}{6}\epsilon^{3/2}Y^3T'''_{\mathrm{c}M} + \cdots\Big\}, \tag{3.2.20}$$

$$U_0 = c + \epsilon^{1/2}YU'_\mathrm{c} + \frac{1}{2}M^2\epsilon Y^2U''_{\mathrm{c}M} + \frac{1}{6}\epsilon^{3/2}Y^3U'''_\mathrm{c} + \cdots. \tag{3.2.21}$$

We will also set the Prandtl number Pr to be unity.

By substituting (3.2.19) into (3.1.2)–(3.1.5) and relabelling $\bar{T}_0 \equiv \widehat{T}$ we obtain the following equations at leading order

$$\bar{v}_{0Y} = 0, \tag{3.2.22}$$

$$U'_\mathrm{c}\bar{v}_0 = -\alpha T_\mathrm{c}\bar{p}_{0\zeta}, \tag{3.2.23}$$

$$\bar{p}_{0Y} = 0 \tag{3.2.24}$$

and

$$\alpha U'_\mathrm{c}Y\widehat{T}_\zeta + \widehat{T}_\mathcal{T} + c\widehat{T}_{\mathcal{X}_1} + \bar{v}_0\widehat{T}_Y + \mathcal{M}^2T'_{\mathrm{c}M}\bar{v}_0 = \Lambda T_\mathrm{c}\mu_\mathrm{c}\widehat{T}_{YY}. \tag{3.2.25}$$

Equation (3.2.22) shows that

$$\bar{v}_0 = -\mathrm{i}\alpha A\mathrm{e}^{\mathrm{i}\zeta} + \mathrm{c.c.} \tag{3.2.26}$$

after matching with the outer solution (2.4.61). Similarly equation (3.2.23) shows that

$$\bar{p}_0 = \frac{U'_\mathrm{c}}{T_\mathrm{c}}A\mathrm{e}^{\mathrm{i}\zeta} + \mathrm{c.c.} \tag{3.2.27}$$

after using (3.2.26) and matching with the outer solution (2.4.56). This is consistent with equation (3.2.24). Equation (3.2.25) can be written as

$$L\widehat{T} = \mathrm{i}\alpha\big(A\mathrm{e}^{\mathrm{i}\zeta} - \mathrm{c.c.}\big)\big(\widehat{T}_Y + \mathcal{M}^2T'_{\mathrm{c}M}\big), \tag{3.2.28}$$

where

$$L \equiv \alpha U'_\mathrm{c}Y\frac{\partial}{\partial\zeta} + \frac{\partial}{\partial\mathcal{T}} + c\frac{\partial}{\partial\mathcal{X}_1} - \Lambda T_\mathrm{c}\mu_\mathrm{c}\frac{\partial^2}{\partial Y^2}. \tag{3.2.29}$$

By substituting (3.2.19) into (3.1.2)–(3.1.4) we obtain at second order

$$\alpha\bar{u}_{0\zeta} + \bar{v}_{1Y} = 0, \tag{3.2.30}$$

$$\alpha U_{\rm c}'Y\bar{u}_{0\zeta} + \bar{u}_{0\mathcal{T}} + c\bar{u}_{0\mathcal{X}_1} + \bar{v}_0\bar{u}_{0Y} + U_{\rm c}'\bar{v}_1 = -\alpha T_{\rm c}\bar{p}_{1\zeta} - T_{\rm c}\bar{p}_{0\mathcal{X}_1} + \Lambda T_{\rm c}\mu_{\rm c}\bar{u}_{0YY} \tag{3.2.31}$$

and

$$\bar{p}_{1Y} = 0. \tag{3.2.32}$$

Equation (3.2.32) implies that $\bar{p}_1$ is independent of Y so that it can be expressed as

$$\bar{p}_1 = \sum_{\substack{m=-\infty \\ m\neq 0}}^{\infty} d_1^{(m)}(\mathcal{X}_1, \mathcal{T})\mathrm{e}^{\mathrm{i}m\zeta} \tag{3.2.33}$$

after matching with the outer solution (equations (2.4.64) & (2.4.70)). Now substituting (3.2.26), (3.2.27) & (3.2.33) into (3.2.31), then differentiating with respect to Y, followed by using (3.2.30) yields

$$\alpha U_{\rm c}'Y\bar{u}_{0\zeta Y} + \bar{u}_{0\mathcal{T}Y} + c\bar{u}_{0\mathcal{X}_1 Y} + (-\mathrm{i}\alpha A\mathrm{e}^{\mathrm{i}\zeta} + \text{c.c.})\bar{u}_{0YY} = \Lambda T_{\rm c}\mu_{\rm c}\bar{u}_{0YYY}. \tag{3.2.34}$$

A solution to this equation is $\bar{u}_0 = \bar{u}_0(\mathcal{X}_1, \mathcal{T}, \zeta)$. Matching with the outer solution (2.4.60) shows that

$$\bar{u}_0 = -b_1 A\mathrm{e}^{\mathrm{i}\zeta} + \text{c.c.}. \tag{3.2.35}$$

By substituting (3.2.19) into (3.1.2)–(3.1.4) we obtain at third order

$$\begin{aligned} &- \mathcal{M}^2 T_{{\rm c}M}'\bar{v}_0 - \alpha U_{\rm c}'Y\widehat{T}_\zeta - \widehat{T}_{\mathcal{T}} - c\widehat{T}_{\mathcal{X}_1} - \bar{v}_0\widehat{T}_Y + \alpha T_{\rm c}\bar{u}_{1\zeta} \\ &\quad + T_{\rm c}\bar{u}_{0\mathcal{X}_1} + T_{\rm c}\bar{v}_{2Y} + \mathcal{M}^2 T_{{\rm c}M}'Y\bar{v}_{0Y} + \widehat{T}\bar{v}_{0Y} = 0, \end{aligned} \tag{3.2.36}$$

$$\begin{aligned} &\alpha U_{\rm c}'Y\bar{u}_{1\zeta} + \bar{u}_{1\mathcal{T}} + c\bar{u}_{1\mathcal{X}_1} + YU_{\rm c}'\bar{u}_{0\mathcal{X}_1} + \alpha\bar{u}_0\bar{u}_{0\zeta} + V_{\rm c}\bar{u}_{0Y} + \bar{v}_0\bar{u}_{1Y} + \bar{v}_1\bar{u}_{0Y} \\ &\quad + U_{\rm c}'\bar{v}_2 + \frac{1}{2}U_{\rm c}'''Y^2\bar{v}_0 + \mathcal{M}^2 U_{{\rm c}M}''Y\bar{v}_0 = -\alpha T_{\rm c}\bar{p}_{2\zeta} - T_{\rm c}\bar{p}_{1\mathcal{X}_1} - \alpha\mathcal{M}^2 T_{{\rm c}M}'Y\bar{p}_{0\zeta} \\ &\quad - \alpha\widehat{T}\bar{p}_{0\zeta} + \Lambda\Big(\frac{1}{3}\alpha T_{\rm c}\mu_{\rm c}\bar{v}_{0Y\zeta} + T_{\rm c}\mu_{\rm c}\bar{u}_{1YY} + T_{\rm c}U_{\rm c}'\mu'(T_{\rm c})\widehat{T}_Y\Big) \end{aligned} \tag{3.2.37}$$

and

$$\alpha U_{\rm c}'Y\bar{v}_{0\zeta} + \bar{v}_{0\mathcal{T}} + c\bar{v}_{0\mathcal{X}_1} + \bar{v}_0\bar{v}_{0Y} = -T_{\rm c}\bar{p}_{2Y} - \mathcal{M}^2 T_{{\rm c}M}'Y\bar{p}_{0Y} - \widehat{T}\bar{p}_{0Y} + \frac{4}{3}\Lambda T_{\rm c}\mu_{\rm c}\bar{v}_{0YY}, \tag{3.2.38}$$

where the term $V_{\rm c}$ appearing in equation (3.2.37) is the first term in the Taylor expansion of V_0 about the critical level. Taking the Y-derivative of equation (3.2.37),

followed by using (3.2.36) to eliminate $\alpha\bar{u}_{1\zeta} + \bar{v}_{2Y}$, then taking the ζ-derivative of (3.2.38) to eliminate $\bar{p}_2$, we obtain

$$\alpha U_{\rm c}' Y Q_\zeta + Q_\mathcal{T} + cQ_{\mathcal{X}_1} - \Lambda T_{\rm c}\mu_{\rm c} Q_{YY} + \bar{v}_0 Q_Y + \Lambda U_{\rm c}'\Big(\mu_{\rm c} - T_{\rm c}\mu'(T_{\rm c})\Big)\widehat{T}_{YY}$$
$$= \frac{U_{\rm c}'}{T_{\rm c}}\bar{v}_0\widehat{T}_Y - U_{\rm c}'''Y\bar{v}_0 + \alpha^2 U_{\rm c}' Y\bar{v}_{0\zeta\zeta} + \alpha\bar{v}_{0\mathcal{T}\zeta} + \alpha c\bar{v}_{0\mathcal{X}_1\zeta} \tag{3.2.39}$$

where we have put

$$Q = \bar{u}_{1Y}, \tag{3.2.40}$$

and use has also been made of (2.4.58), (3.2.23) & (3.2.28) to simplify. Taking the Y-derivative of (3.2.36) gives

$$\alpha T_{\rm c} Q_\zeta - \alpha U_{\rm c}' Y\widehat{T}_{\zeta Y} - \alpha U_{\rm c}'\widehat{T}_\zeta - \widehat{T}_{\mathcal{T}Y} - c\widehat{T}_{\mathcal{X}_1 Y} - \bar{v}_0\widehat{T}_{YY} + T_{\rm c}\bar{v}_{2YY} = 0. \tag{3.2.41}$$

Now writing the outer solution for $\tilde{v}$ (see (2.4.82)) in terms of Y and re-ordering, we find at $\mathcal{O}(\epsilon^2)$ that there are regular terms

$$[\tilde{v}] = \Bigg\{ -\frac{\mathrm{i}\alpha}{2}\Big(\alpha^2 + \frac{U_{\rm c}'''}{U_{\rm c}'}\Big)AY^2 + \frac{1}{U_{\rm c}'}\Bigg[\frac{1}{2}(A_\mathcal{T} + cA_{\mathcal{X}_1})\Big(\alpha^2 + \frac{5}{3}\frac{U_{\rm c}'''}{U_{\rm c}'}\Big)$$
$$-b_1 U_{\rm c}' A_{\mathcal{X}_1} + 3\mathrm{i}\frac{T_{\rm c}}{\alpha}d_2^{\pm}\Bigg]Y + d_3\Bigg\}\mathrm{e}^{\mathrm{i}\zeta} + \mathrm{c.c.} \tag{3.2.42}$$

where $d_3(\mathcal{X}_1, \mathcal{T})$ is the $\mathcal{O}(1)$ term in the asymptotic expansion of $\tilde{v}_2^{(1)}$ about the critical level. Now write

$$\bar{v}_2 = \hat{v}_2 + \epsilon^2[\tilde{v}] \tag{3.2.43}$$

and

$$Q = \widehat{Q} + \Bigg[\Big(\alpha^2 + \frac{U_{\rm c}'''}{U_{\rm c}'}\Big)A\mathrm{e}^{\mathrm{i}\zeta} + \mathrm{c.c.}\Bigg]. \tag{3.2.44}$$

Then substitution of (3.2.43) & (3.2.44) into (3.2.41) & (3.2.39) yields

$$\alpha T_{\rm c}\widehat{Q}_\zeta - \alpha U_{\rm c}' Y\widehat{T}_{\zeta Y} - \alpha U_{\rm c}'\widehat{T}_\zeta - \widehat{T}_{\mathcal{T}Y} - c\widehat{T}_{\mathcal{X}_1 Y} - \Big(-\mathrm{i}\alpha A\mathrm{e}^{\mathrm{i}\zeta} + \mathrm{c.c.}\Big)\widehat{T}_{YY} + T_{\rm c}\hat{v}_{2YY} = 0 \tag{3.2.45}$$

and

$$L\widehat{Q} + \Big(-\mathrm{i}\alpha A\mathrm{e}^{\mathrm{i}\zeta} + \mathrm{c.c.}\Big)\Big(\widehat{Q}_Y - \frac{U_{\rm c}'}{T_{\rm c}}\widehat{T}_Y\Big)$$
$$= -\frac{U_{\rm c}'''}{U_{\rm c}'}\Big\{(A_\mathcal{T} + cA_{\mathcal{X}_1})\mathrm{e}^{\mathrm{i}\zeta} + \mathrm{c.c.}\Big\} - \Lambda U_{\rm c}'\Big(\mu_{\rm c} - T_{\rm c}\mu'(T_{\rm c})\Big)\widehat{T}_{YY} \tag{3.2.46}$$

respectively.

The $\mathcal{O}(\epsilon^{3/2})$ outer solution streamwise velocity jump (2.4.80) for the fundamental

component should match with the inner solution streamwise velocity jump. To facilitate this matching we write

$$\widehat{Q} = \sum_{m=-\infty}^{\infty} \widehat{Q}_m(\mathcal{X}_1, \mathcal{T}, Y)\mathrm{e}^{\mathrm{i}m\zeta} \tag{3.2.47}$$

where $\widehat{Q}_{-m} = \widehat{Q}_m^*$, with * denoting complex conjugate. We can pick out the fundamental wave term, $\widehat{Q}_1$, from (3.2.47), by multiplying $\widehat{Q}$ by $\mathrm{e}^{-\mathrm{i}\zeta}$ and integrating over one wavelength as follows

$$\widehat{Q}_1 = \frac{1}{2\pi}\int_0^{2\pi} \widehat{Q}\mathrm{e}^{-\mathrm{i}\zeta}\mathrm{d}\zeta.$$

Thus the matching condition can be expressed as

$$-3\frac{T_\mathrm{c}}{\alpha^2 U_\mathrm{c}'}(d_2^+ - d_2^-) = \int_{-\infty}^{\infty}\left\{\frac{1}{2\pi}\int_0^{2\pi}\widehat{Q}\mathrm{e}^{-\mathrm{i}\zeta}\mathrm{d}\zeta\right\}\mathrm{d}Y. \tag{3.2.48}$$

Similarly, for $m \neq 0, \pm 1$, matching requires

$$-3\frac{T_\mathrm{c}}{(m\alpha)^2 U_\mathrm{c}'}(d_2^{(m)+} - d_2^{(m)-}) = \frac{1}{2\pi}\int_{-\infty}^{\infty}\int_0^{2\pi}\widehat{Q}\mathrm{e}^{-\mathrm{i}m\zeta}\mathrm{d}\zeta\mathrm{d}Y. \tag{3.2.49}$$

Inserting (3.2.48) into the solvability condition (2.4.79), we obtain the evolution equation

$$\fint_{-\infty}^{\infty}\int_0^{2\pi}\widehat{Q}\mathrm{e}^{-\mathrm{i}\zeta}\mathrm{d}\zeta\mathrm{d}Y = 4\pi\mathrm{i}\frac{T_\mathrm{c}}{\alpha^2}\left(cJ_1\frac{\partial A}{\partial \mathcal{X}_1} + J_2\frac{\partial A}{\partial \mathcal{T}}\right). \tag{3.2.50}$$

To summarise, the system to determine the evolution of A consists of the coupled equations (3.2.28), (3.2.46) & (3.2.50) subject to a suitable upstream condition, which is prescribed in the next chapter.

Chapter 4

Extensions to the Fully Compressible Regime

4.1 The case $T_c' \approx 0, M = \mathcal{O}(1)$

The previous chapters focused on the distinguished scaling $M = \mathcal{O}(\epsilon^{1/4})$, for which $T_c' = \mathcal{O}(\epsilon^{1/2})$ in general, and the critical-layer dynamics is strongly nonlinear, governed by equations (3.2.28), (3.2.46) & (3.2.50). We note that for the profile (5.1.5), $T_c' = 0$ when $\beta_T = 1$ even for $M = \mathcal{O}(1)$. In this section, we will show that the critical layer dynamics is also strongly nonlinear, however the evolution equations must be slightly modified.

Suppose that $T_c' = 0$ for $|y| \ll 1$. Then the outer solution (2.4.62) shows that the temperature perturbation at leading order is

$$\widetilde{T}_0 = \frac{1}{U_c'}\left(T_c'' + (\gamma - 1)M^2 U_c'^2\right) + \mathcal{O}(y), \tag{4.1.1}$$

i.e. $\widetilde{T}_0$ is regular. However, the second-order solution (2.4.74) is singular, behaving as

$$\widetilde{T}_1^{(1)} = \frac{\mathrm{i}}{\alpha}\frac{T_c''}{U_c'^2}\left(A_T + cA_{\mathcal{X}_1}\right)\frac{1}{y} + \mathcal{O}(\ln|y|). \tag{4.1.2}$$

Within the critical layer, the leading-order approximation of the energy equation (3.1.5) reads

$$\begin{aligned}\bar{v}_0 Y T_c'' + \alpha U_c' Y \bar{T}_{0\zeta} + \bar{T}_{0T} + c\bar{T}_{0\mathcal{X}_1} + \bar{v}_0 \bar{T}_{0Y} \\ = (\gamma - 1)T_c M^2(\alpha U_c' Y \bar{p}_{0\zeta} + \bar{p}_{0T} + c\bar{p}_{0\mathcal{X}_1} + \bar{v}_0 \bar{p}_{0Y}) \\ + \Lambda T_c \mu_c \bar{T}_{0YY}.\end{aligned} \tag{4.1.3}$$

The solutions $\bar{v}_0$ and $\bar{p}_0$ are still given by equations (3.2.26) & (3.2.27) respectively. Thus after the substitution

$$\widehat{T} = \bar{T}_0 - \left(\frac{T_c''}{U_c'} + (\gamma - 1)M^2 U_c'\right)\left(A\mathrm{e}^{\mathrm{i}\zeta} + \text{c.c.}\right), \tag{4.1.4}$$

we obtain

$$L\widehat{T} = \mathrm{i}\alpha\left(A\mathrm{e}^{\mathrm{i}\zeta} - \text{c.c.}\right)\widehat{T}_Y - \frac{T_c''}{U_c'}\left\{\left(A_\mathcal{T} + cA_{\mathcal{X}_1}\right)\mathrm{e}^{\mathrm{i}\zeta} + \text{c.c.}\right\}. \tag{4.1.5}$$

Note that the right-hand side differs from that of (3.2.28). Further note that

$$\widehat{T} \to \frac{\mathrm{i}}{\alpha}\frac{T_c''}{U_c'^2}\left(A_\mathcal{T} + cA_{\mathcal{X}_1}\right)\frac{1}{Y}\mathrm{e}^{\mathrm{i}\zeta} + \text{c.c.} \quad \text{as} \quad Y \to \pm\infty$$

which matches with the outer solution (4.1.2).

Noting that $\bar{u}_{0Y}$, $\bar{v}_{0Y}$, $\bar{p}_{0Y}$, $\bar{p}_{1Y}$ equal zero, equations (3.2.36), (3.2.37) & (3.2.38) are modified to

$$\begin{aligned}
&\gamma T_c M^2\left(\alpha U_c' Y\bar{p}_{0\zeta} + \bar{p}_{0\mathcal{T}} + c\bar{p}_{0\mathcal{X}_1}\right) - T_c'' Y\bar{v}_0 \\
&\quad -\left(\alpha U_c' Y\bar{T}_{0\zeta} + \bar{T}_{0\mathcal{T}} + c\bar{T}_{0\mathcal{X}_1} + \bar{v}_0\bar{T}_{0Y}\right) + T_c\left(\alpha\bar{u}_{1\zeta} + \bar{u}_{0\mathcal{X}_1} + \bar{v}_{2Y}\right) = 0,
\end{aligned} \tag{4.1.6}$$

$$\begin{aligned}
&\alpha U_c' Y\bar{u}_{1\zeta} + \bar{u}_{1\mathcal{T}} + c\bar{u}_{1\mathcal{X}_1} + YU_c'\bar{u}_{0\mathcal{X}_1} + \alpha\bar{u}_0\bar{u}_{0\zeta} + \bar{v}_0\bar{u}_{1Y} + \gamma M^2 U_c'\bar{p}_0\bar{v}_0 \\
&\quad + U_c'\bar{v}_2 + \frac{1}{2}U_c'''Y^2\bar{v}_0 = -\alpha T_c\bar{p}_{2\zeta} - T_c\bar{p}_{1\mathcal{X}_1} - \frac{1}{2}\alpha T_c''Y^2\bar{p}_{0\zeta} \\
&\quad -\alpha\bar{T}_0\bar{p}_{0\zeta} + \Lambda T_c\left(\mu_c\bar{u}_{1YY} + U_c'\mu'(T_c)\bar{T}_{0Y}\right)
\end{aligned} \tag{4.1.7}$$

and

$$\alpha U_c' Y\bar{v}_{0\zeta} + \bar{v}_{0\mathcal{T}} + c\bar{v}_{0\mathcal{X}_1} = -T_c\bar{p}_{2Y}, \tag{4.1.8}$$

where we have used the fact that since $T_c' = 0$ and (2.4.58) is valid, then $U_c'' = 0$. Taking the Y-derivative of equation (4.1.7), followed by using (4.1.6) to eliminate $\alpha\bar{u}_{1\zeta} + \bar{v}_{2Y}$, then taking the ζ-derivative of (4.1.8) to eliminate $\bar{p}_{2\zeta Y}$, we obtain

$$\begin{aligned}
&LQ_\zeta + \bar{v}_0 Q_Y + \Lambda U_c'(\mu_c - T_c\mu'(T_c))\bar{T}_{0YY} - \frac{U_c'}{T_c}\bar{v}_0\bar{T}_{0Y} \\
&\quad = Y\left(\frac{U_c'}{T_c}T_c'' - U_c'''\right)\bar{v}_0 + \alpha\left(\alpha U_c' Y\bar{v}_{0\zeta\zeta} + \bar{v}_{0\mathcal{T}\zeta} + c\bar{v}_{0\mathcal{X}_1\zeta}\right) \\
&\qquad + U_c' M^2\left(\alpha U_c' Y\bar{p}_{0\zeta} + \bar{p}_{0\mathcal{T}} + c\bar{p}_{0\mathcal{X}_1}\right)
\end{aligned} \tag{4.1.9}$$

where $Q = \bar{u}_{1Y}$ and we have used (3.2.23) & (4.1.3) to simplify. Substitution of

$$\widehat{Q} = Q - \left[\left(\alpha^2 + \frac{U_c'''}{U_c'} - \frac{T_c''}{T_c} + \frac{U_c'^2}{T_c}M^2\right)A\mathrm{e}^{\mathrm{i}\zeta} + \text{c.c.}\right] \tag{4.1.10}$$

into (4.1.9) reduces (4.1.9) to

$$L\widehat{Q}_\zeta - \mathrm{i}\alpha\big(A\mathrm{e}^{\mathrm{i}\zeta} - \mathrm{c.c.}\big)\widehat{Q}_Y = \left(\frac{T_\mathrm{c}''}{T_\mathrm{c}} - \frac{U_\mathrm{c}'''}{U_\mathrm{c}'}\right)\Big\{\big(A_\mathcal{T} + cA_{\mathcal{X}_1}\big)\mathrm{e}^{\mathrm{i}\zeta} + \mathrm{c.c.}\Big\}$$
$$-\mathrm{i}\alpha\frac{U_\mathrm{c}'}{T_\mathrm{c}}\Big(A\mathrm{e}^{\mathrm{i}\zeta} - \mathrm{c.c.}\Big)\widehat{T}_Y - \Lambda U_\mathrm{c}'\Big(\mu_\mathrm{c} - T_\mathrm{c}\mu'(T_\mathrm{c})\Big)\widehat{T}_{YY}. \qquad (4.1.11)$$

The jump condition remains intact, namely

$$\int_{-\infty}^{\infty}\!\!\int_{0}^{2\pi} \widehat{Q}\mathrm{e}^{-\mathrm{i}\zeta}\mathrm{d}\zeta\mathrm{d}Y = 4\pi\mathrm{i}\frac{T_\mathrm{c}}{\alpha^2}\Big(cJ_1\frac{\partial A}{\partial\mathcal{X}_1} + J_2\frac{\partial A}{\partial\mathcal{T}}\Big). \qquad (4.1.12)$$

4.2 Composite theory

Numerical solution of equations (2.2.35) & (2.2.36) indicates that for the Lock profile, when $\beta_\mathcal{T}$ is close to 1, T_c' is numerically quite small, even for $M = \mathcal{O}(1)$. This implies that weakly nonlinear theory based on the scaling $T_\mathrm{c}' = \mathcal{O}(1)$ (Goldstein & Leib 1989, Leib 1991), is unlikely to be accurate. To overcome this difficulty, we tacitly treat T_c' as an independent parameter with $T_\mathrm{c}' = \mathcal{O}(\epsilon^{1/2})$, whilst still treating $M = \mathcal{O}(1)$, so that a strongly nonlinear critical-layer theory may be formulated. This system can be obtained by combining those given in chapter 3 and in the previous section. We thus have

$$L\widehat{T} = \mathrm{i}\alpha\big(A\mathrm{e}^{\mathrm{i}\zeta} - \mathrm{c.c.}\big)\widehat{T}_Y$$
$$+\mathrm{i}\alpha T_{\mathrm{c}M}'\mathcal{M}^2\big(A\mathrm{e}^{\mathrm{i}\zeta} - \mathrm{c.c.}\big) - \frac{T_\mathrm{c}''}{U_\mathrm{c}'}\Big\{\big(A_\mathcal{T} + cA_{\mathcal{X}_1}\big)\mathrm{e}^{\mathrm{i}\zeta} + \mathrm{c.c.}\Big\}, \qquad (4.2.13)$$

$$L\widehat{Q} = \mathrm{i}\alpha\big(A\mathrm{e}^{\mathrm{i}\zeta} - \mathrm{c.c.}\big)\widehat{Q}_Y$$
$$+\left(\frac{T_\mathrm{c}''}{T_\mathrm{c}} - \frac{U_\mathrm{c}'''}{U_\mathrm{c}'}\right)\Big\{\big(A_\mathcal{T} + cA_{\mathcal{X}_1}\big)\mathrm{e}^{\mathrm{i}\zeta} + \mathrm{c.c.}\Big\}$$
$$-\mathrm{i}\alpha\frac{U_\mathrm{c}'}{T_\mathrm{c}}\Big(A\mathrm{e}^{\mathrm{i}\zeta} - \mathrm{c.c.}\Big)\widehat{T}_Y - \Lambda U_\mathrm{c}'\Big(\mu_\mathrm{c} - T_\mathrm{c}\mu'(T_\mathrm{c})\Big)\widehat{T}_{YY} \qquad (4.2.14)$$

and

$$\int_{-\infty}^{\infty}\!\!\int_{0}^{2\pi} \widehat{Q}\mathrm{e}^{-\mathrm{i}\zeta}\mathrm{d}\zeta\mathrm{d}Y = 4\pi\mathrm{i}\frac{T_\mathrm{c}}{\alpha^2}\Big(cJ_1\frac{\partial A}{\partial\mathcal{X}_1} + J_2\frac{\partial A}{\partial\mathcal{T}}\Big), \qquad (4.2.15)$$

where the temperature equation (4.2.13) includes both linear inhomogenous terms involving T_c' and T_c'', and the vorticity equation (4.2.14) includes both linear inhomogeneous terms involving U_c''' and T_c''. We note that:

- For $M = 0$, $T_c' = T_c'' = 0$, and it follows that $\widehat{T} = 0$ so that the system (4.2.13)–(4.2.15) reduces to that of Goldstein & Hultgren (1989).
- For $M = \mathcal{O}(\epsilon^{1/2})$ and $\beta_T \neq 1$, equations (4.2.13)–(4.2.15) reduce to the system (3.2.28), (3.2.46) & (3.2.50).
- If $T_c' = 0$ and $M = \mathcal{O}(1)$, the system (4.2.13)–(4.2.15) simplifies to (4.1.5), (4.1.11) & (4.1.12).

Furthermore, we shall show that in the limit $T_{cM}'\mathcal{M}^2 \to \gg 1$ (either due to $\mathcal{M} \gg 1$ or $|\hat{\beta}| \gg 1$), one may derive the amplitude equation in the weakly nonlinear theory, i.e. the weakly nonlinear system is "contained" in the strongly nonlinear system (4.2.13)–(4.2.15). The latter represents a composite approximation valid for $M = 0$ to $M = \mathcal{O}(1)$ for arbitrary β_T.

We will now turn our attention to the spatial evolution of an unstable disturbance governed by the system (4.2.13)–(4.2.15).

4.3 Decomposition of solution

Whilst the disturbance upstream consists of only a fundamental wave, as it evolves into the nonlinear regime all harmonics are generated at the same order, and so $\widehat{T}$ and $\widehat{Q}$ take the form

$$\widehat{Q} = \sum_{m=-\infty}^{\infty} \widehat{Q}_m(\mathcal{X}_1, \widehat{Y}) \mathrm{e}^{\mathrm{i}m(\zeta+\Omega\mathcal{T})}, \tag{4.3.16}$$

$$\widehat{T} = \sum_{m=-\infty}^{\infty} \widehat{T}_m(\mathcal{X}_1, \widehat{Y}) \mathrm{e}^{\mathrm{i}m(\zeta+\Omega\mathcal{T})}, \tag{4.3.17}$$

where

$$\widehat{Y} = \alpha U_c' Y + \Omega \tag{4.3.18}$$

and $\Omega = (\omega_n - \omega)/\epsilon^{1/2}$ represents a (scaled) deviation of the forcing frequency from the neutral frequency. This corresponds to the case of a single mode forced upstream. The amplitude A takes on the simpler form

$$A(\mathcal{X}_1, \mathcal{T}) = \mathrm{e}^{\mathrm{i}\Omega\mathcal{T}} \widehat{A}(\mathcal{X}_1). \tag{4.3.19}$$

Then equations (4.2.13), (4.2.14) & (4.2.15) become

$$\left(c\frac{\partial}{\partial \mathcal{X}_1} + \mathrm{i}m\widehat{Y}\right)\widehat{T}_m + \mathrm{i}\alpha^2 U_c' \frac{\partial}{\partial \widehat{Y}}\left(\widehat{A}^*\widehat{T}_{m+1} - \widehat{A}\widehat{T}_{m-1}\right) - \Lambda T_c \mu_c \alpha^2 U_c'^2 \frac{\partial^2}{\partial \widehat{Y}^2}\widehat{T}_m$$
$$= -\delta_{m,1}\frac{T_c''}{U_c'}\left(c\frac{\mathrm{d}\widehat{A}}{\mathrm{d}\mathcal{X}_1} + \mathrm{i}\Omega\widehat{A}\right) + \mathrm{i}\delta_{m,1}\alpha\mathcal{M}^2 T_{cM}'\widehat{A}, \tag{4.3.20}$$

$$\left(c\frac{\partial}{\partial\mathcal{X}_1}+\mathrm{i}m\widehat{Y}\right)\widehat{Q}_m+\mathrm{i}\alpha^2U_{\mathrm{c}}'\frac{\partial}{\partial\widehat{Y}}\left(\widehat{A}^*\widehat{Q}_{m+1}-\widehat{A}\widehat{Q}_{m-1}\right)$$
$$-\mathrm{i}\alpha^2\frac{U_{\mathrm{c}}'^2}{T_{\mathrm{c}}}\frac{\partial}{\partial\widehat{Y}}\left(\widehat{A}^*\widehat{T}_{m+1}-\widehat{A}\widehat{T}_{m-1}\right)+\delta_{m,1}\left(\frac{U_{\mathrm{c}}'''}{U_{\mathrm{c}}'}-\frac{T_{\mathrm{c}}''}{T_{\mathrm{c}}}\right)\left(c\frac{\mathrm{d}\widehat{A}}{\mathrm{d}\mathcal{X}_1}+\mathrm{i}\Omega\widehat{A}\right)$$
$$=\Lambda T_{\mathrm{c}}\mu_{\mathrm{c}}\alpha^2U_{\mathrm{c}}'^2\frac{\partial^2}{\partial\widehat{Y}^2}\widehat{Q}_m-\Lambda\alpha^2U_{\mathrm{c}}'^3\left(\mu_{\mathrm{c}}-T_{\mathrm{c}}\mu'(T_{\mathrm{c}})\right)\frac{\partial^2}{\partial\widehat{Y}^2}\widehat{T}_m \quad (4.3.21)$$

and

$$\int_{-\infty}^{\infty}\widehat{Q}_1(\mathcal{X}_1,\widehat{Y})\mathrm{d}\widehat{Y}=2\mathrm{i}\frac{U_{\mathrm{c}}'T_{\mathrm{c}}}{\alpha}\left(cJ_1\frac{\mathrm{d}}{\mathrm{d}\mathcal{X}_1}+\mathrm{i}\Omega J_2\right)\widehat{A} \quad (4.3.22)$$

respectively. We prescribe the initial condition as

$$\widehat{A}(\mathcal{X}_1)\to a\mathrm{e}^{\kappa\mathcal{X}_1}\quad\text{as}\quad\mathcal{X}_1\to-\infty. \quad (4.3.23)$$

where $\Re\{\kappa\}$ is the linear growth rate, and a is a (complex) amplitude parameter.

To remove the parameters $|a|$, $\arg a$ and Ω from equations (4.3.20)–(4.3.23), we now change to the following re-scaled variables (cf. Goldstein & Hultgren 1988)

$$\bar{\mathcal{T}}=\mathcal{T},\quad\bar{\mathcal{X}}=(\alpha\Omega/2)\mathcal{X}_1-x_0,\quad\bar{Y}=(2/\alpha c\Omega)\widehat{Y},\quad\bar{\zeta}=\zeta+\arg a+\bar{\kappa}_{\mathrm{i}}x_0, \quad (4.3.24)$$

$$\bar{A}=(8U_{\mathrm{c}}'/c^2\Omega^2)\widehat{A},\quad\bar{Q}_m=-4(\alpha U_{\mathrm{c}}'^2/c\Omega^2U_{\mathrm{c}}''')\widehat{Q}_m,\quad\bar{T}_m=-4(\alpha U_{\mathrm{c}}'^3/c\Omega^2T_{\mathrm{c}}U_{\mathrm{c}}''')\widehat{T}_m, \quad (4.3.25)$$

$$\bar{\mathcal{M}}^2=-(\alpha U_{\mathrm{c}}'^2|T_{\mathrm{c}M}'|/\Omega T_{\mathrm{c}}U_{\mathrm{c}}''')\mathrm{sgn}(T_{\mathrm{c}}')\mathcal{M}^2,\quad\bar{\Lambda}=8T_{\mathrm{c}}\mu_{\mathrm{c}}(U_{\mathrm{c}}'^2/\alpha c^3\Omega^3)\Lambda, \quad (4.3.26)$$

$$\bar{\kappa}=(2/\alpha\Omega)\kappa, \quad (4.3.27)$$

where $\bar{\kappa}=\bar{\kappa}_{\mathrm{r}}+\mathrm{i}\bar{\kappa}_{\mathrm{i}}$, and x_0 is chosen to be

$$x_0=\frac{1}{\bar{\kappa}_{\mathrm{r}}}\ln\left(\frac{c^2\Omega^2}{8U_{\mathrm{c}}'|a|}\right). \quad (4.3.28)$$

Equations (4.3.20)–(4.3.22) are then re-scaled to

$$\left(\frac{\partial}{\partial\bar{\mathcal{X}}}+\mathrm{i}m\bar{Y}\right)\bar{T}_m+\frac{\mathrm{i}}{2}\frac{\partial}{\partial\bar{Y}}\left(\bar{A}^*\bar{T}_{m+1}-\bar{A}\bar{T}_{m-1}\right)-\bar{\Lambda}\frac{\partial^2\bar{T}_m}{\partial\bar{Y}^2}$$
$$=\delta_{m,1}\left(\mathrm{i}\bar{\mathcal{M}}^2\bar{A}-\sigma\left(\frac{\alpha c}{2}\frac{\mathrm{d}}{\mathrm{d}\bar{\mathcal{X}}}+\mathrm{i}\right)\bar{A}\right), \quad (4.3.29)$$

$$\left(\frac{\partial}{\partial\bar{\mathcal{X}}}+\mathrm{i}m\bar{Y}\right)\bar{Q}_m+\frac{\mathrm{i}}{2}\frac{\partial}{\partial\bar{Y}}\left(\bar{A}^*(\bar{Q}_{m+1}-\bar{T}_{m+1})-\bar{A}(\bar{Q}_{m-1}-\bar{T}_{m-1})\right)$$
$$+\bar{\Lambda}\frac{\partial^2}{\partial\bar{Y}^2}\left(\left(1-T_{\mathrm{c}}\frac{\mu'(T_{\mathrm{c}})}{\mu_{\mathrm{c}}}\right)\bar{T}_m-\bar{Q}_m\right)=\delta_{m,1}(1+\sigma)\left(\frac{\alpha c}{2}\frac{\mathrm{d}\bar{A}}{\mathrm{d}\bar{\mathcal{X}}}+\mathrm{i}\bar{A}\right) \quad (4.3.30)$$

and

$$\int_{-\infty}^{\infty} \bar{Q}_1(\bar{\mathcal{X}},\bar{Y})\mathrm{d}\bar{Y} = -2\mathrm{i}\frac{T_\mathrm{c}U_\mathrm{c}'^2}{\alpha U_\mathrm{c}'''}\left(\frac{\alpha c}{2}J_1\frac{\mathrm{d}}{\mathrm{d}\bar{\mathcal{X}}}+\mathrm{i}J_2\right)\bar{A}, \tag{4.3.31}$$

where

$$\sigma = -U_\mathrm{c}'T_\mathrm{c}''/(T_\mathrm{c}U_\mathrm{c}'''). \tag{4.3.32}$$

The initial condition (4.3.23) becomes

$$\bar{A}(\bar{\mathcal{X}}) \to \mathrm{e}^{\bar{\kappa}\bar{\mathcal{X}}} \quad \text{as} \quad \bar{\mathcal{X}} \to -\infty. \tag{4.3.33}$$

4.4 Upstream linear critical layer

The flow upstream is governed by linear dynamics, with the amplitude given by equation (4.3.33). To determine the linear solutions for the vorticity and temperature, we first drop the nonlinear terms in the critical-layer equations. Thus the energy equation (4.3.29) and vorticity equation (4.3.30) simplify to the linear equations

$$\left\{\left(\frac{\partial}{\partial\bar{\mathcal{X}}}+\mathrm{i}\bar{Y}\right)-\bar{\Lambda}\frac{\partial^2}{\partial\bar{Y}^2}\right\}\bar{T}_1 = \left(\mathrm{i}\bar{\mathcal{M}}^2\bar{A}-\sigma\left(\frac{\alpha c}{2}\frac{\mathrm{d}}{\mathrm{d}\bar{\mathcal{X}}}+\mathrm{i}\right)\bar{A}\right) \tag{4.4.34}$$

and

$$\left\{\left(\frac{\partial}{\partial\bar{\mathcal{X}}}+\mathrm{i}\bar{Y}\right)-\bar{\Lambda}\frac{\partial^2}{\partial\bar{Y}^2}\right\}\bar{Q}_1 = (1+\sigma)\left(\frac{\alpha c}{2}\frac{\mathrm{d}}{\mathrm{d}\bar{\mathcal{X}}}+\mathrm{i}\right)\bar{A}-\bar{\Lambda}\left(1-T_\mathrm{c}\frac{\mu'(T_\mathrm{c})}{\mu_\mathrm{c}}\right)\frac{\partial^2\bar{T}_1}{\partial\bar{Y}^2}. \tag{4.4.35}$$

Since the initial condition (4.3.33) suggests that

$$\bar{T}_1(\bar{\mathcal{X}},\bar{Y}) \to \bar{T}_\mathrm{L}(\bar{Y})\mathrm{e}^{\bar{\kappa}\bar{\mathcal{X}}}, \quad \bar{Q}_1(\bar{\mathcal{X}},\bar{Y}) \to \bar{Q}_\mathrm{L}(\bar{Y})\mathrm{e}^{\bar{\kappa}\bar{\mathcal{X}}} \quad \text{as} \quad \bar{\mathcal{X}} \to -\infty, \tag{4.4.36}$$

we substitute (4.4.36) into (4.4.34) & (4.4.35), which shows that the functions $\bar{T}_\mathrm{L}$ and $\bar{Q}_\mathrm{L}$ satisfy

$$\left\{\left(\bar{\kappa}+\mathrm{i}\bar{Y}\right)-\bar{\Lambda}\frac{\mathrm{d}^2}{\mathrm{d}\bar{Y}^2}\right\}\bar{T}_\mathrm{L} = \mathrm{i}\bar{\mathcal{M}}^2-\sigma\left(\frac{\alpha c}{2}\bar{\kappa}+\mathrm{i}\right) \tag{4.4.37}$$

and

$$\left\{\left(\bar{\kappa}+\mathrm{i}\bar{Y}\right)-\bar{\Lambda}\frac{\mathrm{d}^2}{\mathrm{d}\bar{Y}^2}\right\}\bar{Q}_\mathrm{L} = (1+\sigma)\left(\frac{\alpha c}{2}\bar{\kappa}+\mathrm{i}\right)-\bar{\Lambda}\left(1-T_\mathrm{c}\frac{\mu'(T_\mathrm{c})}{\mu_\mathrm{c}}\right)\frac{\mathrm{d}^2\bar{T}_\mathrm{L}}{\mathrm{d}\bar{Y}^2}. \tag{4.4.38}$$

Equations (4.4.37) & (4.4.38) can be solved by the method of Fourier transform with respect to $\bar{Y}$ to give the linear solutions

$$\bar{T}_{\mathrm{L}}(\bar{Y}) = \left(\mathrm{i}\bar{\mathcal{M}}^2 - \sigma\left(\frac{\alpha c}{2}\bar{\kappa} + \mathrm{i}\right)\right)\int_0^\infty \mathrm{e}^{-\left(\frac{\bar{\Lambda}}{3}\lambda^3 + \bar{\kappa}\lambda + \mathrm{i}\bar{Y}\lambda\right)}\,\mathrm{d}\lambda \tag{4.4.39}$$

and

$$\begin{aligned}\bar{Q}_{\mathrm{L}}(\bar{Y}) = (1+\sigma)\left(\frac{\alpha c}{2}\bar{\kappa} + \mathrm{i}\right)\int_0^\infty \mathrm{e}^{-\left(\frac{\bar{\Lambda}}{3}\lambda^3 + \bar{\kappa}\lambda + \mathrm{i}\bar{Y}\lambda\right)}\,\mathrm{d}\lambda \\ + \frac{\bar{\Lambda}}{3}\left(1 - T_{\mathrm{c}}\frac{\mu'(T_{\mathrm{c}})}{\mu_{\mathrm{c}}}\right)\left(\mathrm{i}\bar{\mathcal{M}}^2 - \sigma\left(\frac{\alpha c}{2}\bar{\kappa} + \mathrm{i}\right)\right)\int_0^\infty \lambda^3 \mathrm{e}^{-\left(\frac{\bar{\Lambda}}{3}\lambda^3 + \bar{\kappa}\lambda + \mathrm{i}\bar{Y}\lambda\right)}\,\mathrm{d}\lambda.\end{aligned} \tag{4.4.40}$$

These particular solutions are in fact the general solutions, since non-zero complementary (Airy) functions are unbounded as $\bar{Y} \to \pm\infty$, making matching with the outer solution impossible and the integral in (4.3.31) divergent (see Appendix A).

Substitution of (4.4.40) into (4.3.31) yields

$$\bar{\kappa} = \frac{2}{\alpha c}\left(2(J_2 - J_1)\frac{T_{\mathrm{c}}U_{\mathrm{c}}'^2}{\pi\alpha U_{\mathrm{c}}'''(1+\sigma) + 2\mathrm{i}T_{\mathrm{c}}U_{\mathrm{c}}'^2 J_1} - \mathrm{i}\right), \tag{4.4.41}$$

from which the linear growth rate $\Re\{\bar{\kappa}\}$ is obtained.

4.5 Weakly nonlinear limit: amplitude equation

In this section, we shall show that for $\bar{\mathcal{M}} \gg 1$, the weakly nonlinear theory can be recovered from the system (4.3.29)–(4.3.31). To facilitate the derivation, we re-introduce Ω as follows

$$\bar{T}^\dagger = \bar{T}, \quad \bar{\mathcal{X}}^\dagger = (1/\Omega)\bar{\mathcal{X}} - x_0^\dagger, \quad \bar{Y}^\dagger = \Omega\bar{Y}, \quad \bar{\zeta}^\dagger = \bar{\zeta} + \bar{\kappa}_{\mathrm{i}}^\dagger x_0^\dagger, \tag{4.5.1}$$

$$\bar{A}^\dagger = \Omega^2\bar{A}, \quad \bar{Q}_m^\dagger = \Omega^2\bar{Q}_m, \quad \bar{T}_m^\dagger = \Omega^2\bar{T}_m, \tag{4.5.2}$$

$$\bar{\mathcal{M}}^{\dagger 2} = \Omega\left|\bar{\mathcal{M}}^2\right|, \quad \bar{\Lambda}^\dagger = \Omega^3\bar{\Lambda}, \quad \bar{\kappa}^\dagger = \Omega\bar{\kappa}, \quad x_0^\dagger = \frac{1}{\bar{\kappa}_{\mathrm{r}}^\dagger}\ln\left(\frac{1}{\Omega^2}\right). \tag{4.5.3}$$

For large $\bar{\mathcal{M}}$, we may ignore the linear inhomogeneous term multiplied by σ in the temperature equation (4.3.29). In this case equations (4.5.1)–(4.5.3) re-scale equations (4.3.29)–(4.3.31) to

$$\left(\frac{\partial}{\partial\bar{\mathcal{X}}^\dagger} + \mathrm{i}m\bar{Y}^\dagger\right)\bar{T}_m^\dagger + \frac{\mathrm{i}}{2}\frac{\partial}{\partial\bar{Y}^\dagger}\left(\bar{A}^{\dagger *}\bar{T}_{m+1}^\dagger - \bar{A}^\dagger\bar{T}_{m-1}^\dagger\right) - \bar{\Lambda}^\dagger\frac{\partial^2\bar{T}_m^\dagger}{\partial\bar{Y}^{\dagger 2}} = \mathrm{i}\delta_{m,1}\mathrm{sgn}(T_{\mathrm{c}}')\bar{\mathcal{M}}^{\dagger 2}\bar{A}^\dagger, \tag{4.5.4}$$

$$\left(\frac{\partial}{\partial\bar{\mathcal{X}}^\dagger}+\mathrm{i}m\bar{Y}^\dagger\right)\bar{Q}_m^\dagger+\frac{\mathrm{i}}{2}\frac{\partial}{\partial\bar{Y}^\dagger}\left(\bar{A}^{\dagger*}(\bar{Q}_{m+1}^\dagger-\bar{T}_{m+1}^\dagger)-\bar{A}^\dagger(\bar{Q}_{m-1}^\dagger-\bar{T}_{m-1}^\dagger)\right)$$
$$+\bar{\Lambda}^\dagger\frac{\partial^2}{\partial\bar{Y}^{\dagger 2}}\left(\left(1-T_\mathrm{c}\frac{\mu'(T_\mathrm{c})}{\mu_\mathrm{c}}\right)\bar{T}_m^\dagger-\bar{Q}_m^\dagger\right)=\delta_{m,1}(1+\sigma)\left(\frac{\alpha c}{2}\frac{\mathrm{d}\bar{A}^\dagger}{\mathrm{d}\bar{\mathcal{X}}^\dagger}+\mathrm{i}\Omega\bar{A}^\dagger\right) \quad (4.5.5)$$

and

$$\oint_{-\infty}^{\infty}\bar{Q}_1^\dagger(\bar{\mathcal{X}}^\dagger,\bar{Y}^\dagger)\mathrm{d}\bar{Y}^\dagger=-2\mathrm{i}\frac{T_\mathrm{c}U_\mathrm{c}'^2}{\alpha U_\mathrm{c}'''}\left(\frac{\alpha c}{2}J_1\frac{\mathrm{d}}{\mathrm{d}\bar{\mathcal{X}}^\dagger}+\mathrm{i}\Omega J_2\right)\bar{A}^\dagger. \quad (4.5.6)$$

The initial condition (4.3.33) is now

$$\bar{A}^\dagger(\bar{\mathcal{X}}^\dagger)\to\mathrm{e}^{\bar{\kappa}^\dagger\bar{\mathcal{X}}^\dagger}\quad\text{as}\quad\bar{\mathcal{X}}^\dagger\to-\infty. \quad (4.5.7)$$

In order to scale $\bar{\mathcal{M}}$ out of the equations (4.5.4)–(4.5.6), we perform the substitutions

$$\widetilde{\mathcal{T}}=\bar{\mathcal{T}}^\dagger,\quad\widetilde{\mathcal{X}}=\bar{\mathcal{M}}^{\dagger(2/5)}\bar{\mathcal{X}}^\dagger,\quad\widetilde{Y}=\bar{\mathcal{M}}^{\dagger(-2/5)}\bar{Y}^\dagger,\quad\widetilde{A}=\bar{A}^\dagger, \quad (4.5.8)$$

$$\widetilde{\Lambda}=\bar{\mathcal{M}}^{\dagger(-6/5)}\bar{\Lambda}^\dagger,\quad\tilde{\kappa}=\bar{\mathcal{M}}^{\dagger(-2/5)}\bar{\kappa}^\dagger,\quad\widetilde{\Omega}=\bar{\mathcal{M}}^{\dagger(-2/5)}\Omega, \quad (4.5.9)$$

and expand $\bar{T}_m^\dagger$ and $\bar{Q}_m^\dagger$ as

$$\bar{T}_m^\dagger=\bar{\mathcal{M}}^{\dagger(8/5)}\left\{\widetilde{T}_m^{(0)}+\bar{\mathcal{M}}^{\dagger(-4/5)}\widetilde{T}_m^{(1)}+\bar{\mathcal{M}}^{\dagger(-8/5)}\widetilde{T}_m^{(2)}+\cdots\right\}, \quad (4.5.10)$$

$$\bar{Q}_m^\dagger=\bar{\mathcal{M}}^{\dagger(8/5)}\left\{\widetilde{Q}_m^{(0)}+\bar{\mathcal{M}}^{\dagger(-4/5)}\widetilde{Q}_m^{(1)}+\bar{\mathcal{M}}^{\dagger(-8/5)}\widetilde{Q}_m^{(2)}+\cdots\right\}. \quad (4.5.11)$$

Inserting these into equations (4.5.4)–(4.5.6), we obtain for $n\geqslant 0$,

$$\left(\frac{\partial}{\partial\widetilde{\mathcal{X}}}+\mathrm{i}m\widetilde{Y}\right)\widetilde{T}_m^{(n)}+\frac{\mathrm{i}}{2}\frac{\partial}{\partial\widetilde{Y}}\left(\widetilde{A}^*\widetilde{T}_{m+1}^{(n-1)}-\widetilde{A}\widetilde{T}_{m-1}^{(n-1)}\right)-\widetilde{\Lambda}\frac{\partial^2\widetilde{T}_m^{(n)}}{\partial\widetilde{Y}^2}=\mathrm{i}\delta_{m,1}\delta_{n+1,1}\mathrm{sgn}(T_\mathrm{c}')\widetilde{A}, \quad (4.5.12)$$

$$\left(\frac{\partial}{\partial\widetilde{\mathcal{X}}}+\mathrm{i}m\widetilde{Y}\right)\widetilde{Q}_m^{(n)}+\frac{\mathrm{i}}{2}\frac{\partial}{\partial\widetilde{Y}}\left(\widetilde{A}^*(\widetilde{Q}_{m+1}^{(n-1)}-\widetilde{T}_{m+1}^{(n-1)})-\widetilde{A}(\widetilde{Q}_{m-1}^{(n-1)}-\widetilde{T}_{m-1}^{(n-1)})\right)$$
$$+\widetilde{\Lambda}\frac{\partial^2}{\partial\widetilde{Y}^2}\left(\left(1-T_\mathrm{c}\frac{\mu'(T_\mathrm{c})}{\mu_\mathrm{c}}\right)\widetilde{T}_m^{(n)}-\widetilde{Q}_m^{(n)}\right)=\delta_{m,1}\delta_{n-1,1}(1+\sigma)\left(\frac{\alpha c}{2}\frac{\mathrm{d}\widetilde{A}}{\mathrm{d}\widetilde{\mathcal{X}}}+\mathrm{i}\widetilde{\Omega}\widetilde{A}\right) \quad (4.5.13)$$

and

$$\oint_{-\infty}^{\infty}\widetilde{Q}_1^{(2)}(\widetilde{\mathcal{X}},\widetilde{Y})\mathrm{d}\widetilde{Y}=-2\mathrm{i}\frac{T_\mathrm{c}U_\mathrm{c}'^2}{\alpha U_\mathrm{c}'''}\left(\frac{\alpha c}{2}J_1\frac{\mathrm{d}}{\mathrm{d}\widetilde{\mathcal{X}}}+\mathrm{i}\widetilde{\Omega}J_2\right)\widetilde{A}, \quad (4.5.14)$$

where $\widetilde{T}_m^{(0)}=\widetilde{Q}_m^{(0)}=0$ for $m\neq-1,1$. The initial condition (4.5.7) becomes

$$\widetilde{A}(\widetilde{\mathcal{X}})\to\mathrm{e}^{\tilde{\kappa}\widetilde{\mathcal{X}}}\quad\text{as}\quad\widetilde{\mathcal{X}}\to-\infty. \quad (4.5.15)$$

The equations to be solved are found step-by-step from (4.5.12) and (4.5.13). They are

$$\left(\frac{\partial}{\partial\widetilde{\mathcal{X}}}+\mathrm{i}\widetilde{Y}\right)\widetilde{T}_1^{(0)}-\widetilde{\Lambda}\frac{\partial^2\widetilde{T}_1^{(0)}}{\partial\widetilde{Y}^2}=\mathrm{isgn}(T_\mathrm{c}')\widetilde{A}, \tag{4.5.16}$$

$$\widetilde{T}_{-1}^{(0)}=\widetilde{T}_1^{(0)*}, \tag{4.5.17}$$

$$\frac{\partial\widetilde{T}_0^{(1)}}{\partial\widetilde{\mathcal{X}}}+\frac{\mathrm{i}}{2}\frac{\partial}{\partial\widetilde{Y}}\left(\widetilde{A}^*\widetilde{T}_1^{(0)}-\widetilde{A}\widetilde{T}_{-1}^{(0)}\right)-\widetilde{\Lambda}\frac{\partial^2\widetilde{T}_0^{(1)}}{\partial\widetilde{Y}^2}=0, \tag{4.5.18}$$

$$\left(\frac{\partial}{\partial\widetilde{\mathcal{X}}}+2\mathrm{i}\widetilde{Y}\right)\widetilde{T}_2^{(1)}+\frac{\mathrm{i}}{2}\frac{\partial}{\partial\widetilde{Y}}\left(-\widetilde{A}\widetilde{T}_1^{(0)}\right)-\widetilde{\Lambda}\frac{\partial^2\widetilde{T}_2^{(1)}}{\partial\widetilde{Y}^2}=0, \tag{4.5.19}$$

$$\left(\frac{\partial}{\partial\widetilde{\mathcal{X}}}+\mathrm{i}\widetilde{Y}\right)\widetilde{T}_1^{(2)}+\frac{\mathrm{i}}{2}\frac{\partial}{\partial\widetilde{Y}}\left(\widetilde{A}^*\widetilde{T}_2^{(1)}-\widetilde{A}\widetilde{T}_0^{(1)}\right)-\widetilde{\Lambda}\frac{\partial^2\widetilde{T}_1^{(2)}}{\partial\widetilde{Y}^2}=0, \tag{4.5.20}$$

$$\left(\frac{\partial}{\partial\widetilde{\mathcal{X}}}+\mathrm{i}\widetilde{Y}\right)\widetilde{Q}_1^{(0)}+\widetilde{\Lambda}\frac{\partial^2}{\partial\widetilde{Y}^2}\left(\left(1-T_\mathrm{c}\frac{\mu'(T_\mathrm{c})}{\mu_\mathrm{c}}\right)\widetilde{T}_1^{(0)}-\widetilde{Q}_1^{(0)}\right)=0, \tag{4.5.21}$$

$$\widetilde{Q}_{-1}^{(0)}=\widetilde{Q}_1^{(0)*}, \tag{4.5.22}$$

$$\begin{aligned}\frac{\partial\widetilde{Q}_0^{(1)}}{\partial\widetilde{\mathcal{X}}}&+\frac{\mathrm{i}}{2}\frac{\partial}{\partial\widetilde{Y}}\left(\widetilde{A}^*(\widetilde{Q}_1^{(0)}-\widetilde{T}_1^{(0)})-\widetilde{A}(\widetilde{Q}_{-1}^{(0)}-\widetilde{T}_{-1}^{(0)})\right)\\&+\widetilde{\Lambda}\frac{\partial^2}{\partial\widetilde{Y}^2}\left(\left(1-T_\mathrm{c}\frac{\mu'(T_\mathrm{c})}{\mu_\mathrm{c}}\right)\widetilde{T}_0^{(1)}-\widetilde{Q}_0^{(1)}\right)=0,\end{aligned} \tag{4.5.23}$$

$$\left(\frac{\partial}{\partial\widetilde{\mathcal{X}}}+2\mathrm{i}\widetilde{Y}\right)\widetilde{Q}_2^{(1)}+\frac{\mathrm{i}}{2}\frac{\partial}{\partial\widetilde{Y}}\left(-\widetilde{A}(\widetilde{Q}_1^{(0)}-\widetilde{T}_1^{(0)})\right)+\widetilde{\Lambda}\frac{\partial^2}{\partial\widetilde{Y}^2}\left(\left(1-T_\mathrm{c}\frac{\mu'(T_\mathrm{c})}{\mu_\mathrm{c}}\right)\widetilde{T}_2^{(1)}-\widetilde{Q}_2^{(1)}\right)=0, \tag{4.5.24}$$

$$\begin{aligned}\left(\frac{\partial}{\partial\widetilde{\mathcal{X}}}+\mathrm{i}\widetilde{Y}\right)\widetilde{Q}_1^{(2)}&+\frac{\mathrm{i}}{2}\frac{\partial}{\partial\widetilde{Y}}\left(\widetilde{A}^*(\widetilde{Q}_2^{(1)}-\widetilde{T}_2^{(1)})-\widetilde{A}(\widetilde{Q}_0^{(1)}-\widetilde{T}_0^{(1)})\right)\\&+\widetilde{\Lambda}\frac{\partial^2}{\partial\widetilde{Y}^2}\left(\left(1-T_\mathrm{c}\frac{\mu'(T_\mathrm{c})}{\mu_\mathrm{c}}\right)\widetilde{T}_1^{(2)}-\widetilde{Q}_1^{(2)}\right)=(1+\sigma)\left(\frac{\alpha c}{2}\frac{\mathrm{d}\widetilde{A}}{\mathrm{d}\widetilde{\mathcal{X}}}+\mathrm{i}\widetilde{\Omega}\widetilde{A}\right),\end{aligned} \tag{4.5.25}$$

where we have used the fact that $\widetilde{T}_{-m}^{(n)}=\widetilde{T}_m^{(n)*}$ and $\widetilde{Q}_{-m}^{(n)}=\widetilde{Q}_m^{(n)*}$.

Using the Fourier transform

$$\widetilde{T}_{m,\mathrm{F}}^{(n)}(\widetilde{\mathcal{X}},\tilde{s})=\int_{-\infty}^{\infty}\widetilde{T}_m^{(n)}(\widetilde{\mathcal{X}},\widetilde{Y})\mathrm{e}^{-\mathrm{i}\tilde{s}\widetilde{Y}}\mathrm{d}\widetilde{Y}$$

and similarly for $\widetilde{Q}_m^{(n)}(\widetilde{\mathcal{X}},\widetilde{Y})$, we can find the Fourier space solutions to equations (4.5.16)–(4.5.25). Some of these solutions will not contribute to the final equation,

since they involve integrals I of the form

$$I = \int_0^\infty H(\tilde{s}-\lambda) f(\tilde{s},\lambda)\mathrm{d}\lambda$$

where H is the Heaviside step function. These integrals are to be evaluated at $\tilde{s}=0$, hence they will all equal zero. We will denote these solutions that do not contribute to the final result by $f_i(\tilde{\mathcal{X}},\tilde{s})$. Also note that it will not be necessary to invert any of the solutions to find their form in the physical space.

The relevant Fourier space solutions to equations (4.5.16)–(4.5.25) are thus

$$\widetilde{T}^{(0)}_{1,\mathrm{F}} = f_0(\widetilde{\mathcal{X}},\tilde{s}), \tag{4.5.26}$$

$$\left(\widetilde{T}^{(0)*}_{1}\right)_{\mathrm{F}} = -2\mathrm{sgn}(T_{\mathrm{c}}')\pi\mathrm{i}\mathrm{e}^{-\frac{1}{3}\widetilde{\Lambda}\tilde{s}^3}\widetilde{A}^*(\widetilde{\mathcal{X}}-\tilde{s})H(\tilde{s}), \tag{4.5.27}$$

$$\widetilde{T}^{(1)}_{0,\mathrm{F}} = \mathrm{sgn}(T_{\mathrm{c}}')\pi\mathrm{i}\tilde{s}\int_0^\infty \mathrm{e}^{-\frac{1}{3}\widetilde{\Lambda}\tilde{s}^2(\tilde{s}+3\lambda)}\widetilde{A}(\widetilde{\mathcal{X}}-\lambda)\widetilde{A}^*(\widetilde{\mathcal{X}}-\tilde{s}-\lambda)H(\tilde{s})\mathrm{d}\lambda + f_1(\widetilde{\mathcal{X}},\tilde{s}), \tag{4.5.28}$$

$$\widetilde{T}^{(1)}_{2,\mathrm{F}} = f_2(\widetilde{\mathcal{X}},\tilde{s}), \tag{4.5.29}$$

$$\widetilde{T}^{(2)}_{1,\mathrm{F}} = -\mathrm{sgn}(T_{\mathrm{c}}')\frac{\pi\mathrm{i}}{2}\int_0^\infty \mathrm{e}^{-\frac{1}{3}\widetilde{\Lambda}(2(\tilde{s}+\lambda)^3-\tilde{s}^3)}\widetilde{A}(\widetilde{\mathcal{X}}-\lambda)(\tilde{s}+\lambda)^2 H(\tilde{s}+\lambda)$$
$$\times\int_0^\infty \mathrm{e}^{-\widetilde{\Lambda}(\tilde{s}+\lambda)^2\mu}\widetilde{A}(\widetilde{\mathcal{X}}-\lambda-\mu)\widetilde{A}^*(\widetilde{\mathcal{X}}-\tilde{s}-2\lambda-\mu)\mathrm{d}\mu\mathrm{d}\lambda + f_3(\widetilde{\mathcal{X}},\tilde{s}), \tag{4.5.30}$$

$$\widetilde{Q}^{(0)}_{1,\mathrm{F}} = f_4(\widetilde{\mathcal{X}},\tilde{s}), \tag{4.5.31}$$

$$\left(\widetilde{Q}^{(0)*}_{1}\right)_{\mathrm{F}} = -\mathrm{sgn}(T_{\mathrm{c}}')\frac{2\pi\mathrm{i}}{3}\left(1-\frac{T_{\mathrm{c}}}{\mu_{\mathrm{c}}}\mu'(T_{\mathrm{c}})\right)\widetilde{\Lambda}\tilde{s}^3\mathrm{e}^{-\frac{1}{3}\widetilde{\Lambda}\tilde{s}^3}H(\tilde{s})\widetilde{A}^*(\widetilde{\mathcal{X}}-\tilde{s}), \tag{4.5.32}$$

$$\widetilde{Q}^{(1)}_{0,\mathrm{F}} = \mathrm{sgn}(T_{\mathrm{c}}')\pi\mathrm{i}\tilde{s}\int_0^\infty \mathrm{e}^{-\frac{1}{3}\widetilde{\Lambda}\tilde{s}^2(\tilde{s}+3\lambda)}\widetilde{A}(\widetilde{\mathcal{X}}-\lambda)\widetilde{A}^*(\widetilde{\mathcal{X}}-\tilde{s}-\lambda)H(\tilde{s})$$
$$\times\left\{\left(1-\frac{T_{\mathrm{c}}}{\mu_{\mathrm{c}}}\mu'(T_{\mathrm{c}})\right)\frac{\widetilde{\Lambda}}{3}\tilde{s}^2(\tilde{s}+3\lambda)-1\right\}\mathrm{d}\lambda + f_5(\widetilde{\mathcal{X}},\tilde{s}), \tag{4.5.33}$$

$$\widetilde{Q}^{(1)}_{2,\mathrm{F}} = f_6(\widetilde{\mathcal{X}},\tilde{s}), \tag{4.5.34}$$

and

$$\begin{aligned}\widetilde{Q}_{1,\mathrm{F}}^{(2)} &= 2\pi \mathrm{e}^{\frac{1}{3}\widetilde{\Lambda}\tilde{s}^3} H(-\tilde{s})\big(1+\sigma\big)\left(\frac{\alpha c}{2}\frac{\mathrm{d}}{\mathrm{d}(\widetilde{\mathcal{X}}+\tilde{s})}+\mathrm{i}\widetilde{\Omega}\right)\widetilde{A}(\widetilde{\mathcal{X}}+\tilde{s}) \\ &\quad +f_7(\widetilde{\mathcal{X}},\tilde{s})+\mathrm{sgn}(T_\mathrm{c}')\pi\mathrm{i}\int_0^\infty (\tilde{s}+\lambda)^2\mathrm{e}^{-\frac{1}{3}\widetilde{\Lambda}\left((\tilde{s}+\lambda)^3-\tilde{s}^3\right)} \\ &\quad \times\Bigg\{\int_0^\infty\left[1-\frac{1}{6}\widetilde{\Lambda}\Big(1-\frac{T_\mathrm{c}}{\mu_\mathrm{c}}\mu'(T_\mathrm{c})\Big)(\tilde{s}+\lambda)^2(\tilde{s}+\lambda+3\mu)\right]\mathrm{e}^{-\frac{1}{3}\widetilde{\Lambda}(\tilde{s}+\lambda)^2(\tilde{s}+\lambda+3\mu)} \\ &\quad \times \widetilde{A}(\widetilde{\mathcal{X}}-\lambda-\mu)\widetilde{A}^*(\widetilde{\mathcal{X}}-\tilde{s}-2\lambda-\mu)H(\tilde{s}+\lambda)\mathrm{d}\mu-\frac{1}{2}\widetilde{\Lambda}\Big(1-\frac{T_\mathrm{c}}{\mu_\mathrm{c}}\mu'(T_\mathrm{c})\Big) \\ &\quad \times\int_0^\infty(\tilde{s}+\lambda+\mu)^2\mathrm{e}^{-\frac{1}{3}\widetilde{\Lambda}\left(2(\tilde{s}+\lambda+\mu)^3-(\tilde{s}+\lambda)^3\right)}\widetilde{A}(\widetilde{\mathcal{X}}-\lambda-\mu)H(\tilde{s}+\lambda+\mu) \\ &\quad \times\int_0^\infty \mathrm{e}^{-\widetilde{\Lambda}(\tilde{s}+\lambda+\mu)\nu}\widetilde{A}(\widetilde{\mathcal{X}}-\lambda-\mu-\nu)\widetilde{A}^*(\widetilde{\mathcal{X}}-\tilde{s}-2\lambda-2\mu-\nu)\mathrm{d}\nu\mathrm{d}\mu\Bigg\}\mathrm{d}\lambda.\end{aligned} \tag{4.5.35}$$

We see that evaluating equation (4.5.35) at $\tilde{s}=0$ gives

$$\begin{aligned}\oint_{-\infty}^{\infty}\widetilde{Q}_1^{(2)}\mathrm{d}\widetilde{Y} &= \widetilde{Q}_{1,\mathrm{F}}^{(2)}(\widetilde{\mathcal{X}},\tilde{s}=0) \\ &= \pi\big(1+\sigma\big)\left(\frac{\alpha c}{2}\frac{\mathrm{d}}{\mathrm{d}\widetilde{\mathcal{X}}}+\mathrm{i}\right)\widetilde{A}(\widetilde{\mathcal{X}})+\mathrm{sgn}(T_\mathrm{c}')\pi\mathrm{i}\int_0^\infty\int_0^\infty \aleph\lambda^2\mathrm{e}^{-\frac{1}{3}\widetilde{\Lambda}(2\lambda+3\mu)\lambda^2}\widetilde{A}(\widetilde{\mathcal{X}}-\lambda) \\ &\quad \times\widetilde{A}(\widetilde{\mathcal{X}}-\lambda-\mu)\widetilde{A}^*(\widetilde{\mathcal{X}}-2\lambda-\mu)\mathrm{d}\mu\mathrm{d}\lambda.\end{aligned} \tag{4.5.36}$$

Substituting this into (4.5.14) yields the desired amplitude equation

$$\frac{\mathrm{d}\widetilde{A}}{\mathrm{d}\widetilde{\mathcal{X}}}=\tilde{\kappa}\widetilde{A}+\mathrm{sgn}(T_\mathrm{c}')\mathcal{C}\int_0^\infty\int_0^\infty \aleph\lambda^2\mathrm{e}^{-\frac{1}{3}\widetilde{\Lambda}(2\lambda+3\mu)\lambda^2}\widetilde{A}(\widetilde{\mathcal{X}}-\lambda)\widetilde{A}(\widetilde{\mathcal{X}}-\lambda-\mu)\widetilde{A}^*(\widetilde{\mathcal{X}}-2\lambda-\mu)\mathrm{d}\mu\mathrm{d}\lambda \tag{4.5.37}$$

where

$$\mathcal{C}=\frac{\pi\alpha U_\mathrm{c}'''\tilde{\kappa}}{\pi\alpha U_\mathrm{c}'''(1+\sigma)+2\mathrm{i}T_\mathrm{c}U_\mathrm{c}'^2J_2} \tag{4.5.38}$$

and

$$\aleph=1-\frac{1}{6}\widetilde{\Lambda}\left(1-\frac{T_\mathrm{c}}{\mu_\mathrm{c}}\mu'(T_\mathrm{c})\right)\lambda^2\big(2\lambda+3\mu\big). \tag{4.5.39}$$

Thus we have shown that the weakly nonlinear theory of Goldstein & Leib (1989) and Leib (1991) for $M = \mathcal{O}(1)$ can be recovered as a limiting case of the current strongly nonlinear formulation. Hence we can conclude that the latter theory is valid for all $0 \leqslant M \sim \mathcal{O}(1)$.

Chapter 5

Numerical Solution

The numerical computations to be performed consist of:

1. Solving the eigenvalue problem (2.4.51) with relevant boundary conditions.
2. Solving the nonlinear evolution system (4.3.29)–(4.3.31), including its various limiting forms.

5.1 Solution of eigenvalue problem and evaluation of coefficients

For compressible flows, the velocity and temperature profiles of the base flow are usually expressed in terms of the Howarth-Dorodnitsyn variable (Stewartson 1964, p29)

$$\eta = \int_0^y \rho_0(\tilde{y})\mathrm{d}\tilde{y}. \tag{5.1.1}$$

After change of variable to η, equation (2.4.51) becomes

$$\left\{\frac{\mathrm{d}^2}{\mathrm{d}\eta^2} - \frac{2}{(U_0-c)}\frac{\mathrm{d}U_0}{\mathrm{d}\eta}\frac{\mathrm{d}}{\mathrm{d}\eta} + \alpha^2 T_0\Big(M^2(U_0-c)^2 - T_0\Big)\right\}\tilde{p}_0 = 0. \tag{5.1.2}$$

The transformation

$$G = \frac{1}{\alpha T_0 \tilde{p}_0}\frac{\mathrm{d}\tilde{p}_0}{\mathrm{d}\eta} \tag{5.1.3}$$

converts equation (5.1.2) to a Riccati equation (cf. Jackson & Grosch 1989, equation (2.24))

$$\frac{\mathrm{d}G}{\mathrm{d}\eta} = -\alpha T_0 G^2 + \left(\frac{2}{(U_0-c)}\frac{\mathrm{d}U_0}{\mathrm{d}\eta} - \frac{1}{T_0}\frac{\mathrm{d}T_0}{\mathrm{d}\eta}\right)G + \alpha\Big(T_0 - M^2(U_0-c)^2\Big). \tag{5.1.4}$$

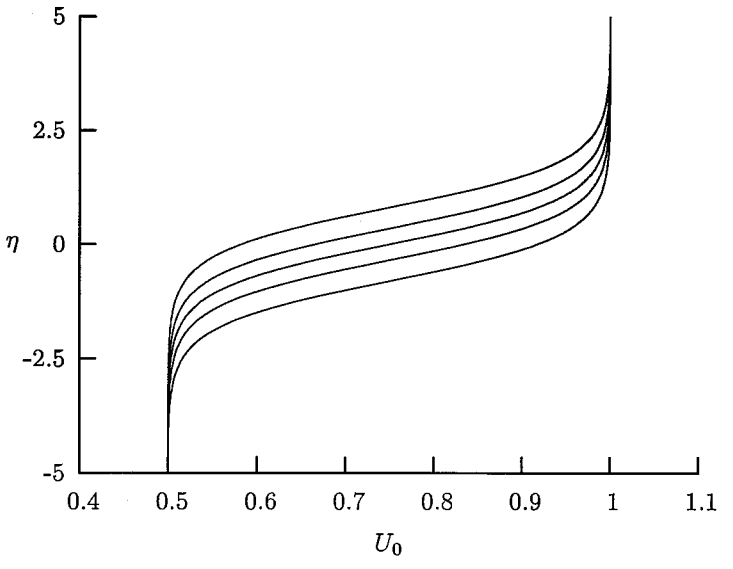


Figure 5.1: Basic velocity profile for $\gamma = 7/5$, $M = 1/2$ and $\beta_U = 1/2$. From top to bottom: $\beta_T = 1/5,\ 1/2,\ 1,\ 2,\ 5$.

For most calculations, we will use the hyperbolic tangent velocity profile

$$U_0 = \frac{1}{2}\Big(1 + \beta_U + (1 - \beta_U)\tanh(\eta + s)\Big) \tag{5.1.5}$$

where s is a shift of coordinate origin so that the critical level is located at $\eta = \eta_c = 0$. Thus s is a root of the cubic equation

$$(\gamma-1)M^2(\beta_U-1)^2\tanh^3(s)+\Big(4(1+\beta_T)-(\gamma-1)M^2(\beta_U-1)^2\Big)\tanh(s)+4(1-\beta_T) = 0 \tag{5.1.6}$$

obtained by solving (2.4.57). The use of the hyperbolic tangent velocity profile as an approximation to the mean velocity has been found only to produce quantitative differences for the subsonic modes in the stability characteristics of the linear theory (Jackson & Grosch 1991) as well as in the nonlinear theory of Leib (1991). Thus we hope that the qualitative structure of the stability properties of the present flow will remain intact through using this profile. Plots of U_0 & T_0 *vs.* η for various β_T are shown in figures 5.1 and 5.2.

For comparison of the tanh profile with the Lock profile, we need to solve (2.2.35)–(2.2.36), which requires knowing the derivatives $f'(0)$ and $f''(0)$. This can be achieved by a "double shooting" approach. A value for $f'(0)$ is guessed and (if possible) $f''(0)$ found by matching to the condition at $+\infty$ using Runge-Kutta.

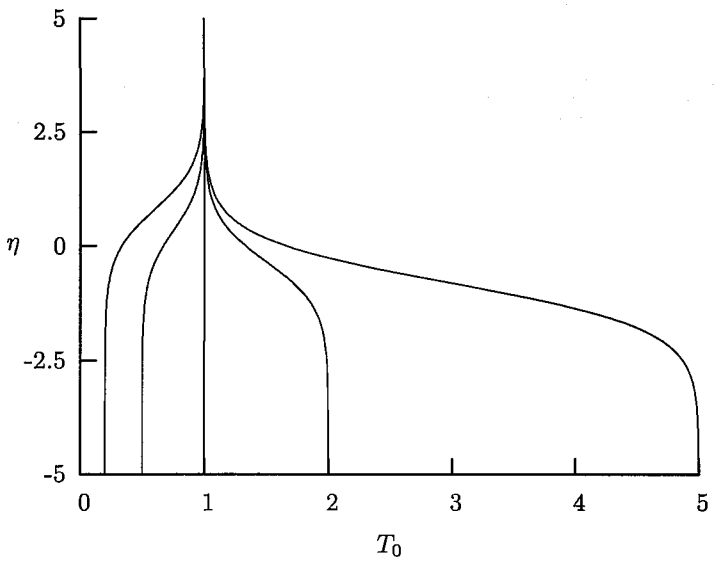


Figure 5.2: Basic temperature profile for $\gamma = 7/5$, $M = 1/2$ and $\beta_U = 1/2$.
From left to right: $\beta_T = 1/5,\ 1/2,\ 1,\ 2,\ 5$.

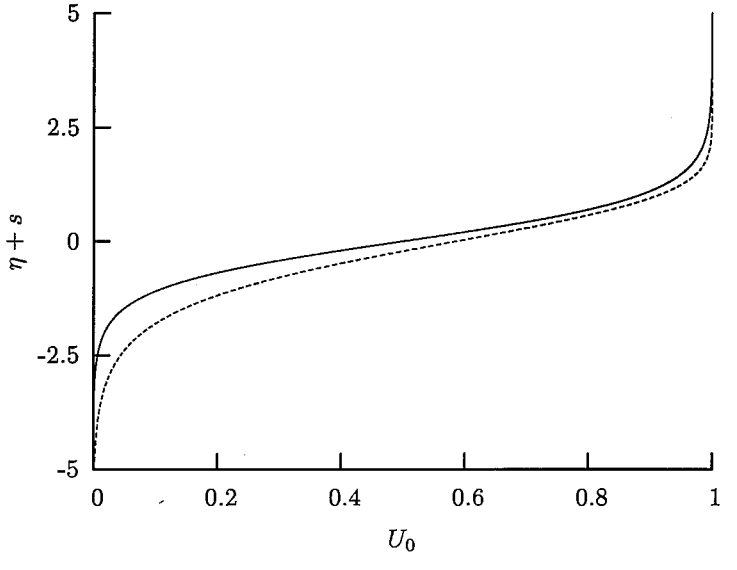


Figure 5.3: Basic velocity profile for $\beta_U = 0$.
Solid line – Tanh profile. Dashed line – Lock profile.

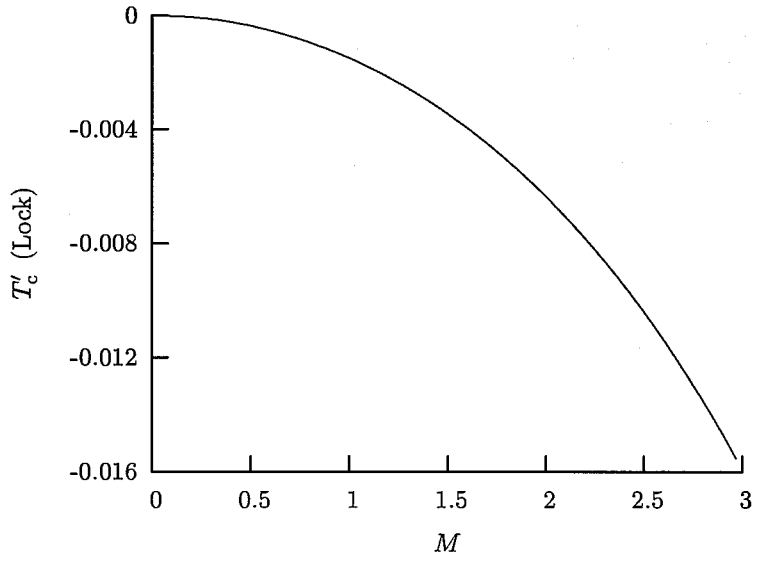


Figure 5.4: T_c' *vs.* M for the Lock profile with $\gamma = 7/5$, $\beta_U = 1/2$ and $\beta_T = 1$.

Using this value of $f''(0)$, $f'(0)$ is then adjusted by matching to the condition at $-\infty$. This process is iterated until the values $f'(0)$ and $f''(0)$ converge to a preset tolerance. U_0 is then calculated by using the $f'(0)$ and $f''(0)$ so found. Figure 5.3 shows a comparison of the tanh and Lock profiles for $\beta_U = 0$. The two are evidently in close resemblance, but there is a noticeable difference.

The generalised inflection point is found by solving (2.4.57). For the tanh profile, we find that $T_c' = 0$ when $\beta_T = 1$ (for all M). In contrast, for the Lock profile, it is found that $T_c' \neq 0$ in general for $\beta_T = 1$. Nevertheless, we can find pairs of values of β_T and M for which T_c' actually equals zero (figure 5.5). This shows the importance of the analysis in chapter 4 for $T_c' = 0$ and $M = \mathcal{O}(1)$. Moreover, as shown in figures 5.4 & 5.5, T_c' is numerically rather small for a range of M and β_T of interest. This motivates the second extension in chapter 4.

Although equation (5.1.6) has three solutions, only one is real provided $M < M_0$, where

$$M_0 = \frac{2}{(1-\beta_U)(\gamma-1)^{1/2}}\left\{1+\beta_T+\frac{3}{2}(1-\beta_T)^{2/3}\left[(1+\beta_T^{1/2})^{2/3}+(1-\beta_T^{1/2})^{2/3}\right]\right\}^{1/2} \tag{5.1.7}$$

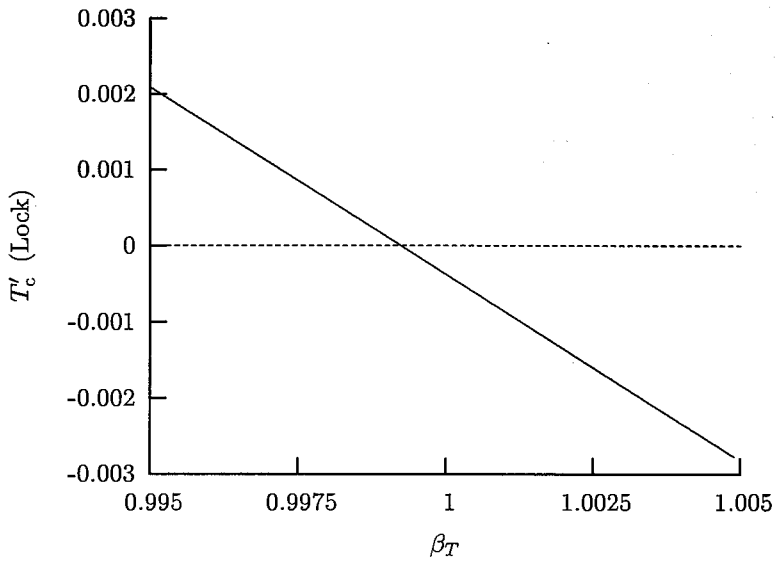


Figure 5.5: T_c' *vs.* β_T for the Lock profile with $\gamma = 7/5$, $\beta_U = 1/2$ and $M = 1/2$.

which is a generalisation of equation (3.6) in Jackson & Grosch (1989) to include β_U. This equation is derived by noting that the discriminant

$$d = \left\{ \frac{1}{27}\left(\frac{4(1+\beta_T)}{(\gamma-1)M^2(\beta_U-1)^2} - 1 \right)^3 + \frac{1}{4}\left(\frac{4(1-\beta_T)}{(\gamma-1)M^2(\beta_U-1)^2} \right)^2 \right\}^{1/2}$$

of (5.1.6) must satisfy $d^2 > 0$ for there to be only one real root of (5.1.6) (see LaFara 1973 p78). M_0 is much larger than the maximum Mach number for neutral subsonic modes (see below).

The neutral phase speed c is given by

$$c = U_0(0) = \frac{1}{2}\Big(1 + \beta_U + (1-\beta_U)\tanh(s)\Big) \tag{5.1.8}$$

and after solving (5.1.6) for s (LaFara 1973 p78), y can be determined explicitly in terms of η upon using (5.1.1) and $\rho_0 T_0 = 1$ to give

$$\begin{aligned} y = {} & \frac{1}{2}(1+\beta_T)\eta + \frac{1}{2}(1-\beta_T)\ln\left(\frac{\cosh(\eta+s)}{\cosh(s)}\right) \\ & + \frac{1}{8}(\gamma-1)M^2(1-\beta_U)^2\big(\tanh(\eta+s) - \tanh(s)\big). \end{aligned} \tag{5.1.9}$$

This variation of y with η is shown in figure 5.6 for various β_T (there is no significant variation with γ, β_U or M).

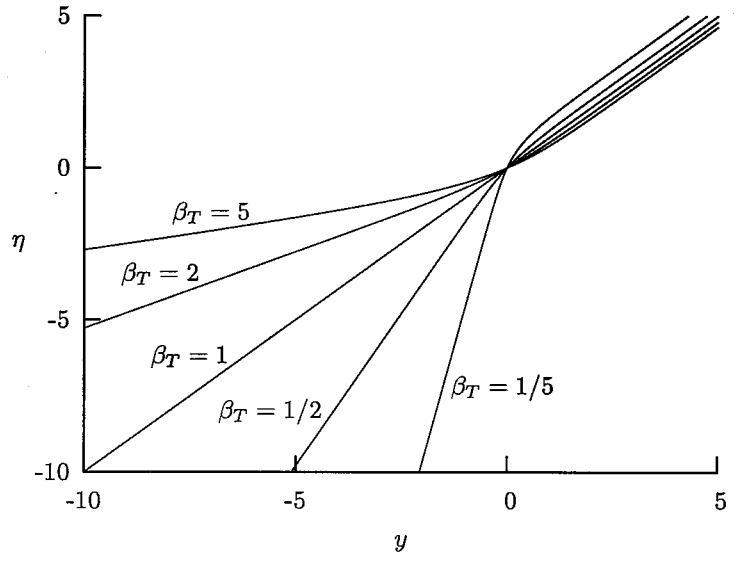


Figure 5.6: η *vs.* y for $\gamma = 7/5$, $M = 1/2$, $\beta_U = 1/2$ and various β_T.

To solve equation (5.1.2), first consider the solution for large η. As $\eta \to +\infty$, $\tilde{p}_0$ and hence G have the asymptotes

$$\tilde{p}_0 \to A^+ e^{t_+\eta} + B^+ e^{-t_+\eta}, \quad G \to \frac{t_+}{\alpha} \frac{(A^+ - B^+ e^{-2t_+\eta})}{(A^+ + B^+ e^{-2t_+\eta})} \tag{5.1.10}$$

respectively, where

$$t_+ = \left(\alpha^2(1 - M^2(1-c)^2)\right)^{1/2} \tag{5.1.11}$$

and A^+, B^+ are constants. For $\tilde{p}_0$ to be bounded as $\eta \to +\infty$, we require $A^+ = 0$.

As $\eta \to -\infty$,

$$\tilde{p}_0 \to A^- e^{t_-\eta} + B^- e^{-t_-\eta}, \quad G \to \frac{1}{\beta_T} \frac{t_-}{\alpha} \frac{(A^- e^{2t_-\eta} - B^-)}{(A^- e^{2t_-\eta} + B^-)} \tag{5.1.12}$$

where

$$t_- = \left(\beta_T \alpha^2(\beta_T - M^2(\beta_U - c)^2)\right)^{1/2} \tag{5.1.13}$$

and A^-, B^- are constants. For $\tilde{p}_0$ to be bounded as $\eta \to -\infty$, we require $B^- = 0$.

Starting with (5.1.10) (setting $B^+ = 1$ and choosing an $\alpha > 0$), the solution for $\tilde{p}_0$ is integrated numerically using Runge-Kutta to advance the solution to small positive η, where it is then equated with the asymptotic result (2.4.56), which we will represent here as $\hat{\pi}_1^+ + b_1^+ \hat{\pi}_2^+$. Thus

$$p^+_{\text{num}} = c^+_{\text{num}}(\hat{\pi}_1^+ + b_1^+ \hat{\pi}_2^+) \tag{5.1.14}$$

where $c^+_{\rm num}$ is a constant. Taking the η-derivative of (5.1.14) gives us a second equation, allowing us to eliminate $c^+_{\rm num}$ and solve for b^+_1:

$$b^+_1 = \frac{p^{+\prime}_{\rm num}\hat{\pi}^+_1 - p^+_{\rm num}\hat{\pi}^{+\prime}_1}{p^+_{\rm num}\hat{\pi}^{+\prime}_2 - p^{+\prime}_{\rm num}\hat{\pi}^+_2}. \tag{5.1.15}$$

Similarly, starting with (5.1.12) (setting $A^- = 1$), Runge-Kutta is again used to advance $\tilde{p}_0$ to small negative η. We can then again equate with the asymptotic result (2.4.56), which we will represent as $\hat{\pi}^-_1 + b^-_1\hat{\pi}^-_2$. Thus

$$p^-_{\rm num} = c^-_{\rm num}(\hat{\pi}^-_1 + b^-_1\hat{\pi}^-_2) \tag{5.1.16}$$

where $c^-_{\rm num}$ is a constant. Hence

$$b^-_1 = \frac{p^{-\prime}_{\rm num}\hat{\pi}^-_1 - p^-_{\rm num}\hat{\pi}^{-\prime}_1}{p^-_{\rm num}\hat{\pi}^{-\prime}_2 - p^{-\prime}_{\rm num}\hat{\pi}^-_2}. \tag{5.1.17}$$

We require equation (2.4.59) to be satisfied. This occurs only for a particular $\alpha^2 > 0$, which can be found by using the secant method (LaFara 1973 p86) on the above process, treating α (assumed > 0) to be a function of the difference $b_{\rm diff} = b^+_1 - b^-_1$. Plots of α, c and ω versus M are shown in figures 5.7–5.12 for some parameter choices, while plots of p_0 *vs.* η for various parameter values are displayed in figures 5.13–5.15.

The sonic speeds c_+ and c_- (cf. Jackson & Grosch 1989) are found as follows. As $\eta \to +\infty$, if $t_+ = 0$ then equation (5.1.11) shows that $c_+ = 1 - 1/M$. Similarly, as $\eta \to -\infty$, $t_- = 0$ implies $c_- = \beta_U + \beta_T^{1/2}/M$ from equation (5.1.13). From this, we can find the maximum Mach number, $M_{\rm max}$, beyond which the modes are supersonic, by using the secant method on $M = M(c)$ (c as given in equation (5.1.8)), until $c = \min(c_+, c_-)$. Plots of $M_{\rm max}$ against β_U and β_T are shown in figure 5.16. It is important to note that $1 < M_{\rm max} < M_0$, and also that both subsonic and supersonic modes may exist for a small range of Mach number near $M_{\rm max}$ (as shown, for example, in figure 7(a) of Jackson & Grosch 1989).

To calculate J_2 and J_3 in (2.4.77), consider K_1 in (2.4.78), i.e.

$$K_1 = \int\!\!\!\!\!\!-_{-\infty}^{\infty} F(y)\mathrm{d}y, \quad \text{with} \quad F(y) = \frac{T_0 U_0'}{(U_0 - c)^4}\tilde{p}_0\tilde{p}_0'.$$

The singular integrand has the property

$$F(y) \;\to\; \frac{f_{-3}}{y^3} + \frac{f_{-2}}{y^2} + \frac{f_{-1}}{y} + \mathcal{O}(1) \quad \text{as} \quad y \to 0,$$

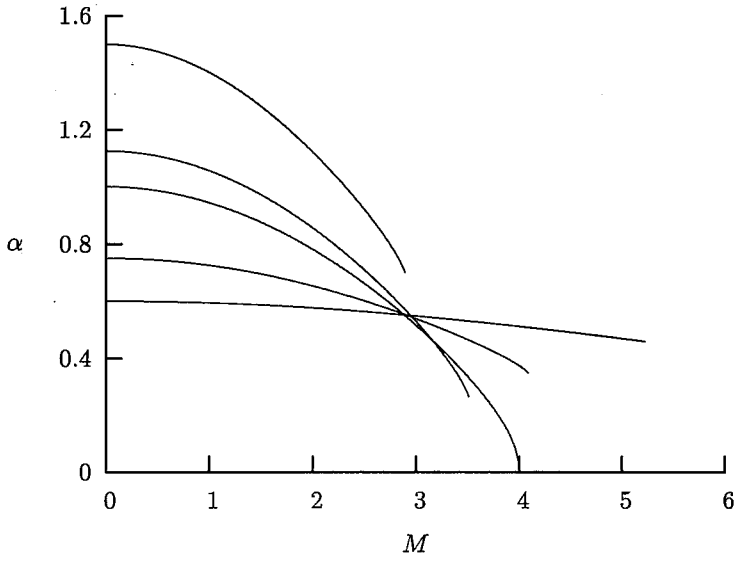


Figure 5.7: Wavenumber α *vs.* Mach number M for $\gamma = 7/5$ and $\beta_U = 1/2$. From top to bottom: $\beta_T = 1/2,\ 4/5,\ 1,\ 2,\ 5$.

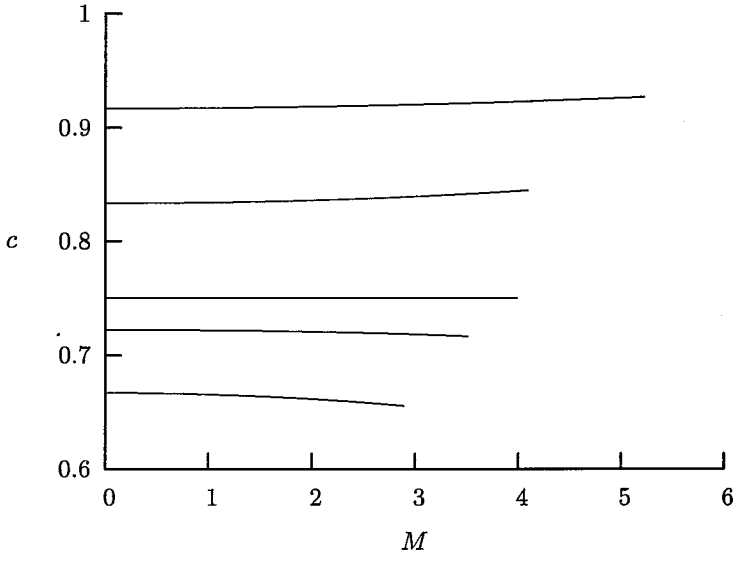


Figure 5.8: Neutral phase speed c *vs.* Mach number M for $\gamma = 7/5$ and $\beta_U = 1/2$. From bottom to top: $\beta_T = 1/2,\ 4/5,\ 1,\ 2,\ 5$.

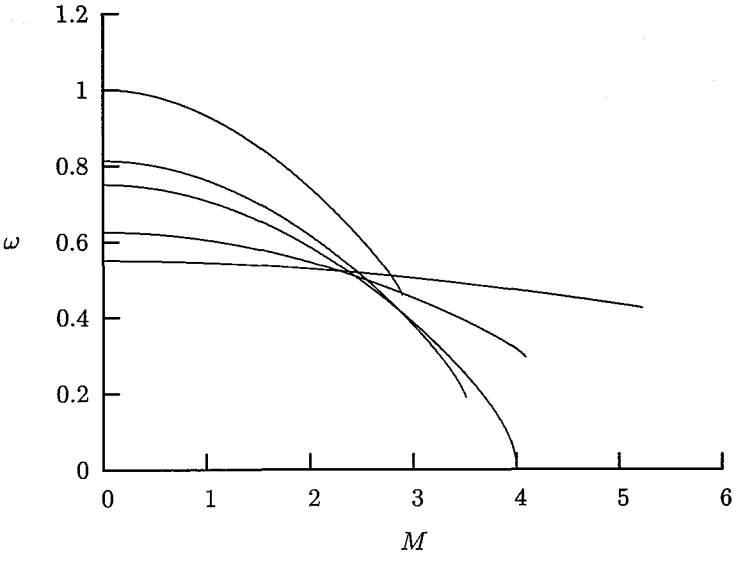


Figure 5.9: Frequency ω *vs.* Mach number M for $\gamma = 7/5$ and $\beta_U = 1/2$. From top to bottom: $\beta_T = 1/2,\ 4/5,\ 1,\ 2,\ 5$.

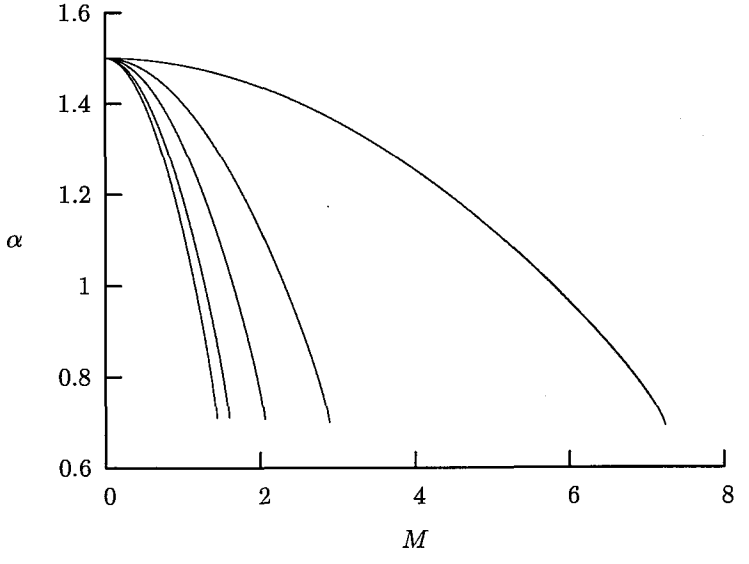


Figure 5.10: Wavenumber α *vs.* Mach number M for $\gamma = 7/5$ and $\beta_T = 1/2$. From left to right: $\beta_U = 0,\ 1/10,\ 3/10,\ 1/2,\ 4/5$.

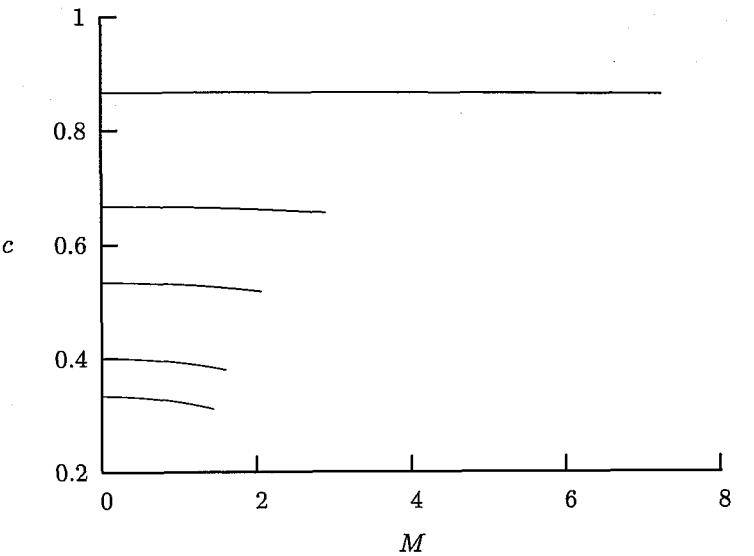


Figure 5.11: Neutral phase speed c *vs.* Mach number M for $\gamma = 7/5$ and $\beta_T = 1/2$. From bottom to top: $\beta_U = 0,\ 1/10,\ 3/10,\ 1/2,\ 4/5$.

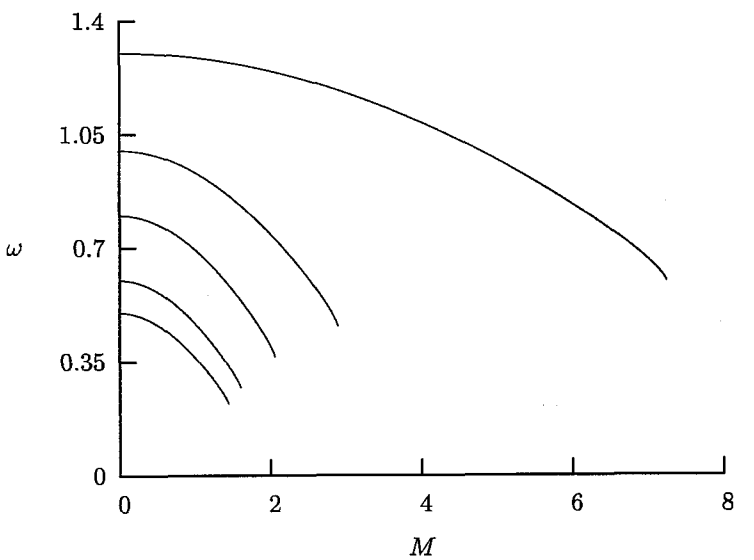


Figure 5.12: Frequency ω *vs.* Mach number M for $\gamma = 7/5$ and $\beta_T = 1/2$. From bottom to top: $\beta_U = 0,\ 1/10,\ 3/10,\ 1/2,\ 4/5$.

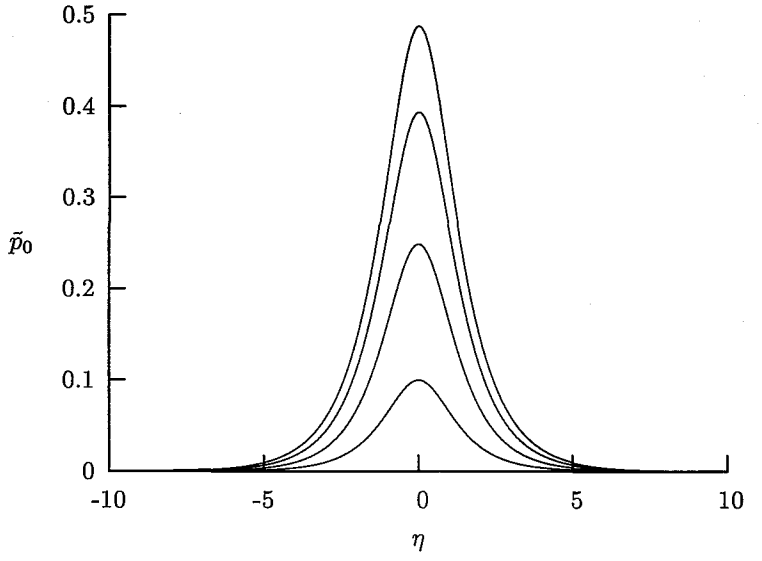


Figure 5.13: $\tilde{p}_0$ *vs.* η for $\gamma = 7/5$, $M = 1/2$ and $\beta_T = 1$.
From top to bottom: $\beta_U = 0$, $1/5$, $1/2$, $4/5$.

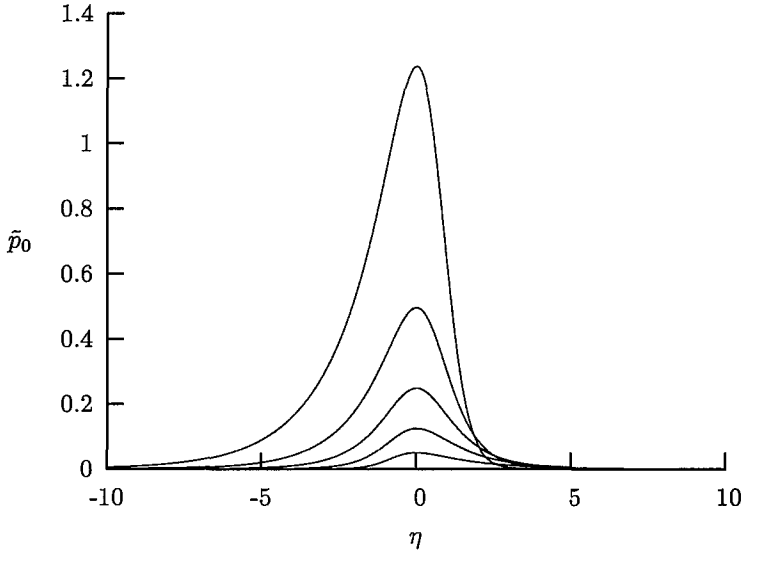


Figure 5.14: $\tilde{p}_0$ *vs.* η for $\gamma = 7/5$, $M = 1/2$ and $\beta_U = 1/2$.
From top to bottom: $\beta_T = 1/5$, $1/2$, 1, 2, 5.

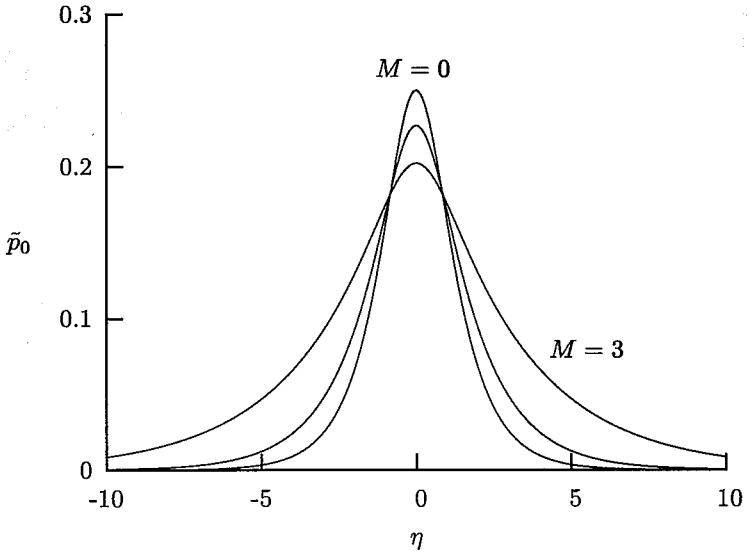


Figure 5.15: $\tilde{p}_0$ *vs.* η for $\gamma = 7/5$, $\beta_U = 1/2$, $\beta_T = 1$, and $M = 0$, 2, 3 ($M_{\max} = 4$).

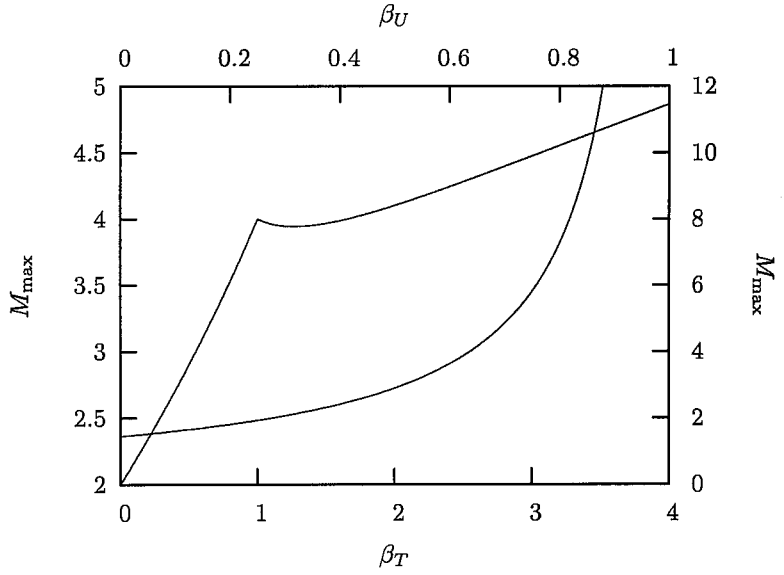


Figure 5.16: Maximum Mach numbers for subsonic modes. Top graph shows variation with β_T for $\gamma = 7/5$, $\beta_U = 1/2$. Bottom graph shows variation with β_U for $\gamma = 7/5$, $\beta_T = 1/2$.

where

$$f_{-3} = -\frac{\alpha^2}{U_c' T_c}, \quad f_{-2} = \frac{\alpha^2}{U_c' T_c}\left(b_1 + \frac{1}{2}\frac{U_c''}{U_c'}\right), \quad f_{-1} = \frac{1}{2}\frac{\alpha^2}{U_c' T_c}\left(\frac{T_c'''}{T_c} - \frac{U_c'''}{U_c'} - 2M^2\frac{U_c'^2}{T_c}\right).$$

For $H \gg 1 \gg \delta$, to evaluate the Hadamard finite part of the integral, we decompose $(-\infty, \infty)$ into $(-H, -\delta)$, $(-\delta, \delta)$ and (δ, H) and evaluate the integral with limits $(-\delta, \delta)$ analytically. Thus

$$\begin{aligned} K_1 &\approx \int_{-H}^{-\delta} F(y)\mathrm{d}y + \oint_{-\delta}^{\delta} \left(\frac{f_{-3}}{y^3} + \frac{f_{-2}}{y^2} + \frac{f_{-1}}{y}\right)\mathrm{d}y + \int_{\delta}^{H} F(y)\mathrm{d}y \\ &= \left\{\int_{-H}^{-\delta} + \int_{\delta}^{H}\right\}\left(F(y) - \frac{f_{-3}}{y^3} - \frac{f_{-2}}{y^2} - \frac{f_{-1}}{y}\right)\mathrm{d}y - 2\frac{f_{-2}}{H} \\ &= \left\{\int_{-H_\eta^-}^{-\delta_\eta^-} + \int_{\delta_\eta^+}^{H_\eta^+}\right\}\left(F(y(\eta)) - \frac{f_{-3}}{y(\eta)^3} - \frac{f_{-2}}{y(\eta)^2} - \frac{f_{-1}}{y(\eta)}\right)T_0(y(\eta))\mathrm{d}\eta - 2\frac{f_{-2}}{H} \end{aligned}$$

where

$$\begin{aligned} y = -\delta \quad &<=> \quad \eta = -\delta_\eta^-, \\ y = \delta \quad &<=> \quad \eta = \delta_\eta^+, \\ y = -H \quad &<=> \quad \eta = -H_\eta^-, \\ y = H \quad &<=> \quad \eta = H_\eta^+. \end{aligned}$$

K_2, K_3 and K_4 are manipulated in a similar fashion. The resulting integrals can then be calculated to a reasonable degree of accuracy using Simpson's rule. Table 5.1 shows how δ affects the accuracy of the constants J_2 and J_3 for chosen parameters $\gamma = 7/5$, $\beta_U = 1/2$, $\beta_T = 1/2$ and $M = 2$.

5.1.1 Viscosity laws

Evaluation of the constants μ_c and $\mu'(T_c)$ appearing in equation (4.3.30) requires specification of the viscosity law. In many calculations, the simple Chapman law

$$\mu = CT \tag{5.1.18}$$

suffices, and this will be used for the majority of the results. The power law

$$\mu = CT^n, \quad n \approx 8/9 \tag{5.1.19}$$

δ	J_2	J_3
0.1	-13.459	3.2215
0.05	-14.202	3.3153
0.025	-14.552	3.3624
0.01	-14.702	3.3907
0.005	-14.739	3.4001
0.0025	-14.758	3.4049
0.001	-14.769	3.4077
0.0005	-14.773	3.4086
0.00025	-14.775	3.4091
0.0001	-14.776	3.4094

Table 5.1: The constants J_2, J_3 for $\gamma = 7/5$, $\beta_U = 1/2$, $\beta_T = 1/2$, $M = 2$ and various δ.

is more accurate, whilst the Sutherland law is

$$\mu = \frac{(1+C)T^{3/2}}{(C+T)} \tag{5.1.20}$$

is most accurate. Since some quantitatively inaccurate assumptions have already been made (such as unity Prandtl number, use of tanh profile), and since we are primarily concerned with the qualitative nature of the flow, the Chapman relation $\mu = T$ will be used unless otherwise stated. The differences between the viscosity laws are shown in figure 5.17.

5.1.2 Upstream linear solutions

The upstream linear solutions for $\bar{T}_1$ and $\bar{Q}_1$ require the calculation of $\bar{\kappa}$ (given by 4.4.41) and the solutions (4.4.39) & (4.4.40). Simpson's rule was used to evaluate the integrals appearing in these expressions. $\bar{T}_\mathrm{L}$ and $\bar{Q}_\mathrm{L}$ are shown for some typical parameters in figures 5.18–5.21.

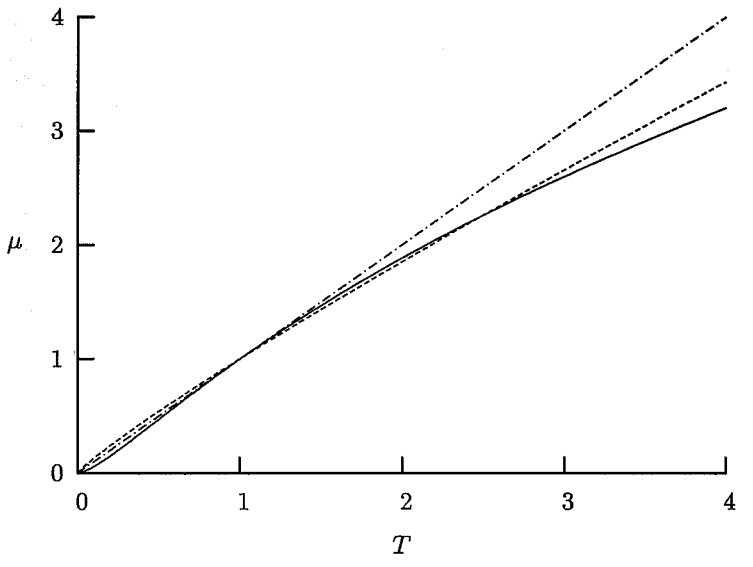


Figure 5.17: Various viscosity laws – (1) $\mu = T$ (dash-dotted line), (2) $\mu = T^{8/9}$ (dashed line), (3) $\mu = \frac{2T^{3/2}}{(1+T)}$ (solid line).

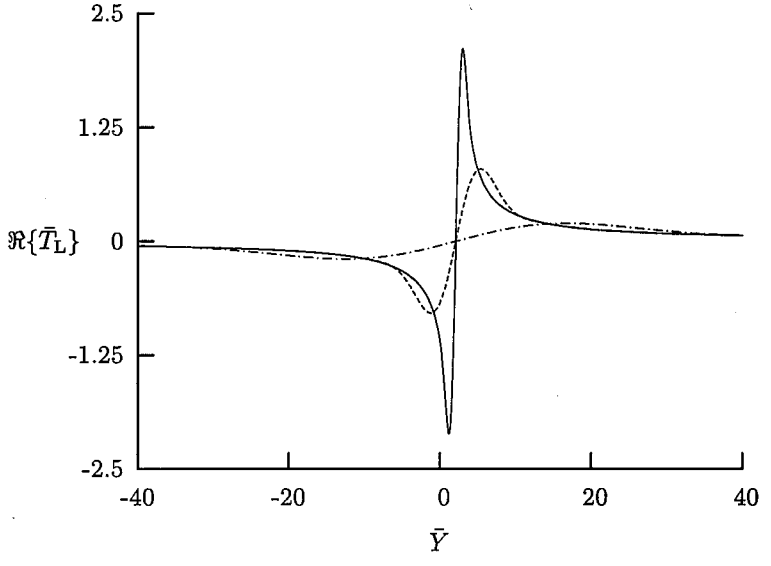


Figure 5.18: $\Re\{\bar{T}_L\}$ *vs.* $\bar{Y}$ for $\gamma = 7/5$, $M = 1/2$, $\beta_U = 1/2$, $\beta_T = 1/2$ and $\widehat{\Lambda} = \Lambda/\Omega^3 = 0.1$ (solid), 10 (dashed), 1000 (dash-dotted).

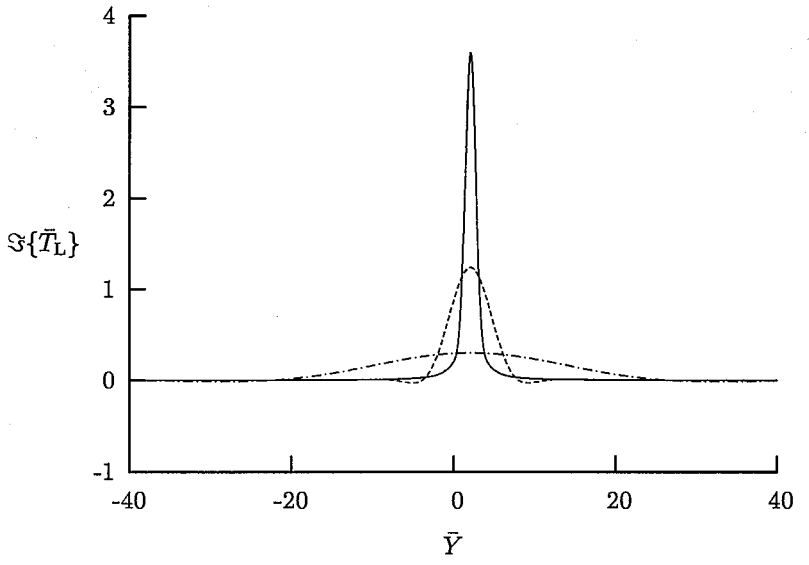


Figure 5.19: $\Im\{\bar{T}_L\}$ *vs.* $\bar{Y}$ for $\gamma = 7/5$, $M = 1/2$, $\beta_U = 1/2$, $\beta_T = 1/2$ and $\widehat{\Lambda} = \Lambda/\Omega^3 = 0.1$ (solid), 10 (dashed), 1000 (dash-dotted).

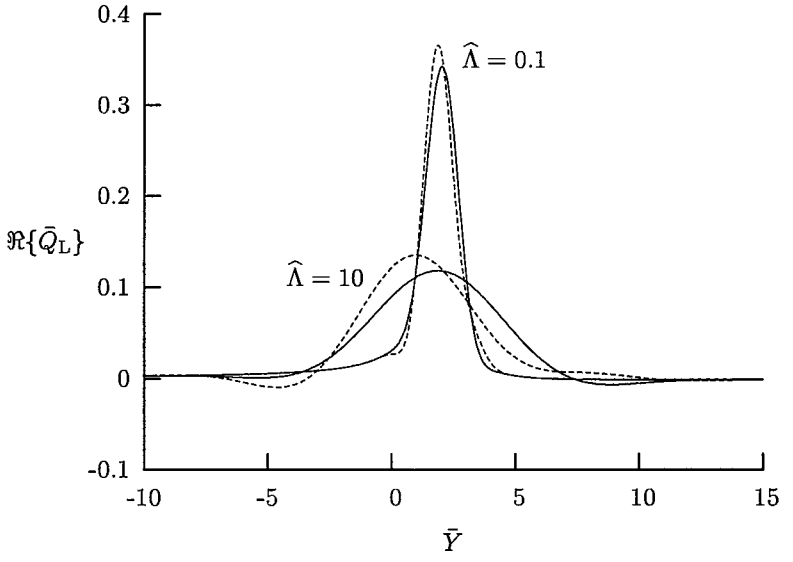


Figure 5.20: $\Re\{\bar{Q}_L\}$ *vs.* $\bar{Y}$ for $\gamma = 7/5$, $M = 1/2$, $\beta_U = 1/2$, $\beta_T = 1/2$ and $\widehat{\Lambda} = \Lambda/\Omega^3 = 10,\ 0.1$. Solid lines – Chapman law $\mu = T$, dashed lines – Sutherland law $\mu = 2T^{3/2}/(1+T)$.

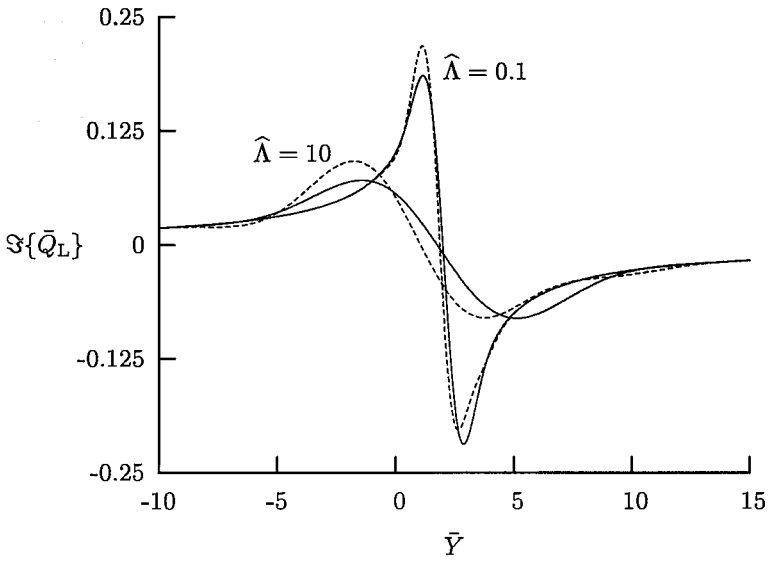


Figure 5.21: $\Im\{\bar{Q}_L\}$ *vs.* $\bar{Y}$ for $\gamma = 7/5$, $M = 1/2$, $\beta_U = 1/2$, $\beta_T = 1/2$ and $\widehat{\Lambda} = \Lambda/\Omega^3 = 10,\ 0.1$. Solid lines – Chapman law $\mu = T$, dashed lines – Sutherland law $\mu = 2T^{3/2}/(1+T)$.

5.2 Nonlinear calculation

5.2.1 Strongly nonlinear evolution system

Numerically solving the nonlinear evolution system requires the boundary conditions on $\bar{T}_m$ and $\bar{Q}_m$ for large $\bar{Y}$. These can be derived by considering the dominant balance for $\bar{Y} \gg 1$. In equation (4.3.29), balancing $\mathrm{i}m\bar{Y}\bar{T}_1$ with the right-hand side shows that

$$\bar{T}_1 \sim \left\{\sigma\left(\mathrm{i}\frac{\alpha c}{2}\frac{\mathrm{d}\bar{A}}{\mathrm{d}\bar{\mathcal{X}}} - \bar{A}\right) + \bar{\mathcal{M}}^2\bar{A}\right\}\frac{1}{\bar{Y}} + \left\{\mathrm{i}\bar{\mathcal{M}}^2\frac{\mathrm{d}\bar{A}}{\mathrm{d}\bar{\mathcal{X}}} - \sigma\left(\frac{\alpha c}{2}\frac{\mathrm{d}^2\bar{A}}{\mathrm{d}\bar{\mathcal{X}}^2} + \mathrm{i}\frac{\mathrm{d}\bar{A}}{\mathrm{d}\bar{\mathcal{X}}}\right)\right\}\frac{1}{\bar{Y}^2} + \mathcal{O}\left(\frac{1}{\bar{Y}^3}\right). \tag{5.2.21}$$

Next, balancing $\partial\bar{T}_0/\partial\bar{\mathcal{X}}$ with $\frac{\mathrm{i}}{2}(\partial/\partial\bar{Y})\left(\bar{A}^*\bar{T}_1 - \bar{A}\bar{T}_{-1}\right)$ demonstrates that

$$\bar{T}_0 \sim -\frac{1}{4}\alpha c\sigma|\bar{A}|^2\frac{1}{\bar{Y}^2} - \bar{\mathcal{M}}^2|\bar{A}|^2\frac{1}{\bar{Y}^3} + \mathcal{O}\left(\frac{\sigma}{\bar{Y}^3}\right) + \mathcal{O}\left(\frac{1}{\bar{Y}^4}\right). \tag{5.2.22}$$

Balancing $2\mathrm{i}\bar{Y}\bar{T}_2$ with $-\frac{\mathrm{i}}{2}\bar{A}\left(\partial\bar{T}_1/\partial\bar{Y}\right)$ shows that

$$\bar{T}_2 \sim -\frac{1}{4}\left\{\sigma\bar{A}\left(\mathrm{i}\frac{\alpha c}{2}\frac{\mathrm{d}\bar{A}}{\mathrm{d}\bar{\mathcal{X}}} - \bar{A}\right) + \bar{\mathcal{M}}^2\bar{A}^2\right\}\frac{1}{\bar{Y}^3} + \mathcal{O}\left(\frac{1}{\bar{Y}^4}\right). \tag{5.2.23}$$

Similarly for equation (4.3.30) we have that

$$\bar{Q}_0 \sim \frac{1}{4}\alpha c(1+2\sigma)|\bar{A}|^2\frac{1}{\bar{Y}^2}+\mathcal{O}\left(\frac{1}{\bar{Y}^3}\right), \tag{5.2.24}$$

$$\bar{Q}_1 \sim (1+\sigma)\left(\bar{A}-\mathrm{i}\frac{\alpha c}{2}\frac{\mathrm{d}\bar{A}}{\mathrm{d}\bar{\mathcal{X}}}\right)\frac{1}{\bar{Y}}+(1+\sigma)\left(\frac{\alpha c}{2}\frac{\mathrm{d}^2\bar{A}}{\mathrm{d}\bar{\mathcal{X}}^2}+\mathrm{i}\frac{\mathrm{d}\bar{A}}{\mathrm{d}\bar{\mathcal{X}}}\right)\frac{1}{\bar{Y}^2}+\mathcal{O}\left(\frac{1}{\bar{Y}^3}\right), \tag{5.2.25}$$

$$\bar{Q}_2 \sim \frac{1}{4}\left\{(1+2\sigma)\bar{A}\left(\mathrm{i}\frac{\alpha c}{2}\frac{\mathrm{d}\bar{A}}{\mathrm{d}\bar{\mathcal{X}}}-\bar{A}\right)+\bar{\mathcal{M}}^2\bar{A}^2\right\}\frac{1}{\bar{Y}^3}+\mathcal{O}\left(\frac{1}{\bar{Y}^4}\right) \tag{5.2.26}$$

as $\bar{Y}\to\pm\infty$. Note also that

$$\bar{T}_m\sim\mathcal{O}\left(\frac{1}{\bar{Y}^{2m-1}}\right),\quad \bar{Q}_m\sim\mathcal{O}\left(\frac{1}{\bar{Y}^{2m-1}}\right)\qquad (m\geqslant 3) \tag{5.2.27}$$

as $\bar{Y}\to\pm\infty$.

To put equation (4.3.31) into a numerically solvable form, we approximate $\int_{-\infty}^{\infty}$ by $\int_{-H}^{H}$ for $H\gg 1$ to give

$$-2\mathrm{i}\frac{T_{\mathrm{c}}U_{\mathrm{c}}'^2}{\alpha U_{\mathrm{c}}'''}\left(\frac{\alpha c}{2}J_1\frac{\mathrm{d}}{\mathrm{d}\bar{\mathcal{X}}}+\mathrm{i}J_2\right)\bar{A}=\int_{-H}^{H}\bar{Q}_1\mathrm{d}\bar{Y}+2(1+\sigma)\left(\frac{\alpha c}{2}\frac{\mathrm{d}^2\bar{A}}{\mathrm{d}\bar{\mathcal{X}}^2}+\mathrm{i}\frac{\mathrm{d}\bar{A}}{\mathrm{d}\bar{\mathcal{X}}}\right)\frac{1}{H}+\mathcal{O}\left(\frac{1}{H^3}\right) \tag{5.2.28}$$

$$=\int_{-H}^{H}\bar{Q}_1\mathrm{d}\bar{Y}+\mathcal{O}\left(\frac{1}{H}\right). \tag{5.2.29}$$

Now differentiate (5.2.29) with respect to $\bar{\mathcal{X}}$ and substitute into (5.2.28) such that $\mathrm{d}^2\bar{A}/\mathrm{d}\bar{\mathcal{X}}^2$ is eliminated. Then using equation (4.3.30) to eliminate $\partial\bar{Q}_1/\partial\bar{\mathcal{X}}$ we obtain

$$\left\{c\left(U_{\mathrm{c}}'^2T_{\mathrm{c}}^2J_1^2+\alpha^2(1+\sigma)^2\frac{U_{\mathrm{c}}'''^2}{U_{\mathrm{c}}'^2}\right)+2(1+\sigma)U_{\mathrm{c}}'''T_{\mathrm{c}}(J_1-J_2)\frac{1}{H}\right\}\frac{\mathrm{d}\bar{A}}{\mathrm{d}\bar{\mathcal{X}}}$$
$$+\frac{2\mathrm{i}}{\alpha}\left\{U_{\mathrm{c}}'^2T_{\mathrm{c}}^2J_1J_2+\alpha^2(1+\sigma)^2\frac{U_{\mathrm{c}}'''^2}{U_{\mathrm{c}}'^2}\right\}\bar{A}=\mathrm{i}U_{\mathrm{c}}'''T_{\mathrm{c}}J_1\int_{-H}^{H}\bar{Q}_1\mathrm{d}\bar{Y}$$
$$+\mathrm{i}\alpha(1+\sigma)\frac{U_{\mathrm{c}}'''^2}{U_{\mathrm{c}}'^2}\frac{1}{H}\int_{-H}^{H}\bar{Y}\bar{Q}_1\mathrm{d}\bar{Y}+\mathcal{O}\left(\frac{1}{H^2}\right). \tag{5.2.30}$$

This process can be repeated once more to give an error of $\mathcal{O}(1/H^3)$, as in Goldstein & Hultgren (1988). Equation (5.2.30) is perfectly adequate however provided H is sufficiently large.

Discretization

For convenience, let us represent equation (5.2.30) as

$$\frac{\mathrm{d}\bar{A}}{\mathrm{d}\bar{\mathcal{X}}} = c_1\bar{A} + c_2 J \tag{5.2.31}$$

where J represents the integral terms. We then discretize equations (5.2.31), (4.3.29) & (4.3.30) into the following predictor-corrector scheme

$$\begin{aligned}
\bar{A}_{i+1}^{(k)} = \bar{A}_i + \frac{l}{24}\Big\{ & 9\big(1-\delta_{k+1,1}\big)\Big[c_1\bar{A}_{i+1}^{(k-1)} + c_2 J_{i+1}^{(k-1)}\Big] \\
& + \Big(55\delta_{k+1,1} + 19\big(1-\delta_{k+1,1}\big)\Big[c_1\bar{A}_i + c_2 J_i\Big] \\
& - \Big(59\delta_{k+1,1} + 5\big(1-\delta_{k+1,1}\big)\Big)\Big[c_1\bar{A}_{i-1} + c_2 J_{i-1}\Big] \\
& + \Big(37\delta_{k+1,1} + \big(1-\delta_{k+1,1}\big)\Big)\Big[c_1\bar{A}_{i-2} + c_2 J_{i-2}\Big] \\
& - 9\delta_{k+1,1}\Big[c_1\bar{A}_{i-3} + c_2 J_{i-3}\Big]\Big\},
\end{aligned} \tag{5.2.32}$$

$$\begin{aligned}
& \left(\frac{\bar{T}_{i+1,j,m}^{(k)} - \bar{T}_{i,j,m}}{l}\right) + \frac{\mathrm{i}mjh}{12}\Big(5\bar{T}_{i+1,j,m}^{(k)} + 8\bar{T}_{i,j,m} - \bar{T}_{i-1,j,m}\Big) \\
& + \frac{\mathrm{i}}{48h}\Big\{5\Big(\delta_{m,1} + \big(1-\delta_{m,1}\big)\big(1-\delta_{k+1,1}\big)\Big)\Big[\bar{A}_{i+1}^{*,(k)}\Big(\bar{T}_{i+1,j+1,m+1}^{(k-1+\delta_{m,1})} - \bar{T}_{i+1,j-1,m+1}^{(k-1+\delta_{m,1})}\Big) \\
& - \bar{A}_{i+1}^{(k)}\Big(\bar{T}_{i+1,j+1,m-1}^{(k-1+\delta_{m,1})} - \bar{T}_{i+1,j-1,m-1}^{(k-1+\delta_{m,1})}\Big)\Big] + \Big(8\delta_{m,1} + \big(1-\delta_{m,1}\big)\big\{8\big(1-\delta_{k+1,1}\big) + 23\delta_{k+1,1}\big\}\Big) \\
& \quad \times\Big[\bar{A}_i^*\Big(\bar{T}_{i,j+1,m+1} - \bar{T}_{i,j-1,m+1}\Big) - \bar{A}_i\Big(\bar{T}_{i,j+1,m-1} - \bar{T}_{i,j-1,m-1}\Big)\Big] \\
& - \Big(\delta_{m,1} + \big(1-\delta_{m,1}\big)\big\{\big(1-\delta_{k+1,1}\big) + 16\delta_{k+1,1}\big\}\Big)\Big[\bar{A}_{i-1}^*\Big(\bar{T}_{i-1,j+1,m+1} - \bar{T}_{i-1,j-1,m+1}\Big) \\
& \quad - \bar{A}_{i-1}\Big(\bar{T}_{i-1,j+1,m-1} - \bar{T}_{i-1,j-1,m-1}\Big)\Big] + 5\big(1-\delta_{m,1}\big)\delta_{k+1,1} \\
& \times\Big[\bar{A}_{i-2}^*\Big(\bar{T}_{i-2,j+1,m+1} - \bar{T}_{i-2,j-1,m+1}\Big) - \bar{A}_{i-2}\Big(\bar{T}_{i-2,j+1,m-1} - \bar{T}_{i-2,j-1,m-1}\Big)\Big]\Big\} \\
& - \frac{\bar{\Lambda}}{12h^2}\Big\{5\Big[\bar{T}_{i+1,j+1,m}^{(k)} - 2\bar{T}_{i+1,j,m}^{(k)} + \bar{T}_{i+1,j-1,m}^{(k)}\Big] + 8\Big[\bar{T}_{i,j+1,m} - 2\bar{T}_{i,j,m} + \bar{T}_{i,j-1,m}\Big] \\
& - \Big[\bar{T}_{i-1,j+1,m} - 2\bar{T}_{i-1,j,m} + \bar{T}_{i-1,j-1,m}\Big]\Big\} = \frac{\delta_{m,1}}{12}\Big\{\mathrm{i}\big(\bar{\mathcal{M}}^2 - \sigma\big)\Big(5\bar{A}_{i+1}^{(k)} + 8\bar{A}_i - \bar{A}_{i-1}\Big) \\
& \quad - \frac{\sigma\alpha c}{24l}\Big(5\Big[25\bar{A}_{i+1}^{(k)} - 48\bar{A}_i + 36\bar{A}_{i-1} - 16\bar{A}_{i-2} + 3\bar{A}_{i-3}\Big] \\
& \quad + 8\Big[25\bar{A}_i - 48\bar{A}_{i-1} + 36\bar{A}_{i-2} - 16\bar{A}_{i-3} + 3\bar{A}_{i-4}\Big] \\
& \quad - \Big[25\bar{A}_{i-1} - 48\bar{A}_{i-2} + 36\bar{A}_{i-3} - 16\bar{A}_{i-4} + 3\bar{A}_{i-5}\Big]\Big)\Big\},
\end{aligned} \tag{5.2.33}$$

$$\left(\frac{\bar{Q}^{(k)}_{i+1,j,m}-\bar{Q}_{i,j,m}}{l}\right)+\frac{\mathrm{i}mjh}{12}\left(5\bar{Q}^{(k)}_{i+1,j,m}+8\bar{Q}_{i,j,m}-\bar{Q}_{i-1,j,m}\right)$$
$$+\frac{\mathrm{i}}{48h}\Big\{5\Big(\delta_{m,1}+(1-\delta_{m,1})(1-\delta_{k+1,1})\Big)\Big[\bar{A}^{*,(k)}_{i+1}\Big(\bar{Q}^{(k-1+\delta_{m,1})}_{i+1,j+1,m+1}+\bar{T}^{(k)}_{i+1,j-1,m+1}$$
$$-\bar{Q}^{(k-1+\delta_{m,1})}_{i+1,j-1,m+1}-\bar{T}^{(k)}_{i+1,j+1,m+1}\Big)-\bar{A}^{(k)}_{i+1}\Big(\bar{Q}^{(k-1+\delta_{m,1})}_{i+1,j+1,m-1}+\bar{T}^{(k)}_{i+1,j-1,m-1}$$
$$-\bar{Q}^{(k-1+\delta_{m,1})}_{i+1,j-1,m-1}-\bar{T}^{(k)}_{i+1,j+1,m-1}\Big)\Big]+\Big(8\delta_{m,1}+(1-\delta_{m,1})\{8(1-\delta_{k+1,1})+23\delta_{k+1,1}\}\Big)$$
$$\times\Big[\bar{A}^{*}_{i}\Big(\bar{Q}_{i,j+1,m+1}+\bar{T}_{i,j-1,m+1}-\bar{Q}_{i,j-1,m+1}-\bar{T}_{i,j+1,m+1}\Big)$$
$$-\bar{A}_{i}\Big(\bar{Q}_{i,j+1,m-1}+\bar{T}_{i,j-1,m-1}-\bar{Q}_{i,j-1,m-1}-\bar{T}_{i,j+1,m-1}\Big)\Big]$$
$$-\Big(\delta_{m,1}+(1-\delta_{m,1})\{(1-\delta_{k+1,1})+16\delta_{k+1,1}\}\Big)\Big[\bar{A}^{*}_{i-1}\Big(\bar{Q}_{i-1,j+1,m+1}+\bar{T}_{i-1,j-1,m+1}$$
$$-\bar{Q}_{i-1,j-1,m+1}-\bar{T}_{i-1,j+1,m+1}\Big)-\bar{A}_{i-1}\Big(\bar{Q}_{i-1,j+1,m-1}+\bar{T}_{i-1,j-1,m-1}$$
$$-\bar{Q}_{i-1,j-1,m-1}-\bar{T}_{i-1,j+1,m-1}\Big)\Big]+5(1-\delta_{m,1})\delta_{k+1,1}\Big[\bar{A}^{*}_{i-2}\Big(\bar{Q}_{i-2,j+1,m+1}+\bar{T}_{i-2,j-1,m+1}$$
$$-\bar{Q}_{i-2,j-1,m+1}-\bar{T}_{i-2,j+1,m+1}\Big)-\bar{A}_{i-2}\Big(\bar{Q}_{i-2,j+1,m-1}+\bar{T}_{i-2,j-1,m-1}$$
$$-\bar{Q}_{i-2,j-1,m-1}-\bar{T}_{i-2,j+1,m-1}\Big)\Big]\Big\}+\frac{\bar{\Lambda}}{12h^2}\Big\{5\Big[\Big(1-T_{\mathrm{c}}\frac{\mu'(T_{\mathrm{c}})}{\mu_{\mathrm{c}}}\Big)$$
$$\times\Big(\bar{T}^{(k)}_{i+1,j+1,m}-2\bar{T}^{(k)}_{i+1,j,m}+\bar{T}^{(k)}_{i+1,j-1,m}\Big)-\Big(\bar{Q}^{(k)}_{i+1,j+1,m}-2\bar{Q}^{(k)}_{i+1,j,m}+\bar{Q}^{(k)}_{i+1,j-1,m}\Big)\Big]$$
$$+8\Big[\Big(1-T_{\mathrm{c}}\frac{\mu'(T_{\mathrm{c}})}{\mu_{\mathrm{c}}}\Big)\Big(\bar{T}_{i,j+1,m}-2\bar{T}_{i,j,m}+\bar{T}_{i,j-1,m}\Big)-\Big(\bar{Q}_{i,j+1,m}-2\bar{Q}_{i,j,m}+\bar{Q}_{i,j-1,m}\Big)\Big]$$
$$-\Big[\Big(1-T_{\mathrm{c}}\frac{\mu'(T_{\mathrm{c}})}{\mu_{\mathrm{c}}}\Big)\Big(\bar{T}_{i-1,j+1,m}-2\bar{T}_{i-1,j,m}+\bar{T}_{i-1,j-1,m}\Big)$$
$$-\Big(\bar{Q}_{i-1,j+1,m}-2\bar{Q}_{i-1,j,m}+\bar{Q}_{i-1,j-1,m}\Big)\Big]\Big\}=\frac{\delta_{m,1}}{12}\Big\{\mathrm{i}\Big(5\bar{A}^{(k)}_{i+1}+8\bar{A}_{i}-\bar{A}_{i-1}\Big)$$
$$+\frac{\alpha c}{24l}\Big(5\Big[25\bar{A}^{(k)}_{i+1}-48\bar{A}_{i}+36\bar{A}_{i-1}-16\bar{A}_{i-2}+3\bar{A}_{i-3}\Big]$$
$$+8\Big[25\bar{A}_{i}-48\bar{A}_{i-1}+36\bar{A}_{i-2}-16\bar{A}_{i-3}+3\bar{A}_{i-4}\Big]$$
$$-\Big[25\bar{A}_{i-1}-48\bar{A}_{i-2}+36\bar{A}_{i-3}-16\bar{A}_{i-4}+3\bar{A}_{i-5}\Big]\Big)\Big\},\tag{5.2.34}$$

where $l=\Delta\bar{\mathcal{X}}$ and $h=\Delta\bar{Y}$ are the step sizes in the streamwise and transverse directions respectively, (il,jh) is the mesh point at $(\bar{\mathcal{X}},\bar{Y})$, $k=0$ represents the predictor step, and $k\geqslant 1$ the k^{th} corrector step. The solution method used here is often referred to as an IMEX method, since some terms are treated in an "IMplicit" fashion and others in an "EXplicit" fashion. The explicit coefficients used for the predictor step are fourth-order Adams-Bashforth in equation (5.2.32) and third-

order Adams-Bashforth in equations (5.2.33) & (5.2.34). The implicit coefficients used for subsequent corrector steps are fourth-order Adams-Moulton in equation (5.2.32) and third-order Adams-Moulton in equations (5.2.33) & (5.2.34). The error of the scheme is $\mathcal{O}(l^3, h^2)$.

The solution begins with the upstream linear solutions (4.3.33) & (4.4.36) at a sufficiently large negative $\bar{\mathcal{X}}$. $\bar{A}^{(0)}_{i+1}$ can then be predicted from equation (5.2.32), using Simpson's rule to evaluate the integrals. The boundary conditions for $\bar{T}^{(0)}_{i+1,J,m}$ and $\bar{Q}^{(0)}_{i+1,J,m}$ (where $J = H/h$) are then computed from (5.2.21)–(5.2.27), using the fourth-order backward difference formulae (James *et al.* 1993)

$$\left.\frac{\mathrm{d}\bar{A}}{\mathrm{d}\bar{\mathcal{X}}}\right|_{i+1} \approx \frac{1}{12l}\Big(25\bar{A}_{i+1} - 48\bar{A}_i + 36\bar{A}_{i-1} - 16\bar{A}_{i-2} + 3\bar{A}_{i-3}\Big), \tag{5.2.35}$$

$$\left.\frac{\mathrm{d}^2\bar{A}}{\mathrm{d}\bar{\mathcal{X}}^2}\right|_{i+1} \approx \frac{1}{12l^2}\Big(45\bar{A}_{i+1} - 154\bar{A}_i + 214\bar{A}_{i-1} - 156\bar{A}_{i-2} + 61\bar{A}_{i-3} - 10\bar{A}_{i-4}\Big) \tag{5.2.36}$$

to approximate the $\bar{A}$ derivatives. Note that equation (5.2.35) has also been used in approximating the $\bar{A}$ derivatives appearing in equations (5.2.33) & (5.2.34).

Next, $\bar{T}^{(0)}_{i+1,j,m}$ is predicted using equation (5.2.33), in the order $m = 0$, 2, 1, 3, $4, \cdots, m_{\max}-1, m_{\max}$, where $m_{\max}$ is the maximum number of Fourier components used for the calculation (and we set $\bar{T}_{m_{\max}+1} = \bar{Q}_{m_{\max}+1} \equiv 0$). This yields tridiagonal matrix equations for $\bar{T}^{(0)}_{i+1,j,m}$, which can be solved by the usual forward-and-back substitution method. To increase computation speed, for $m \geqslant 3$, the $\bar{Y}$ numerically-solved domain was reduced, since for these cases $\bar{Q}_m$ and $\bar{T}_m$ become vanishingly small for large $\bar{Y}$, as seen from equation (5.2.27).

We can next predict $\bar{Q}^{(0)}_{i+1,j,m}$ in essentially the same way as for $\bar{T}^{(0)}_{i+1,j,m}$, and then correct $\bar{A}^{(k)}_{i+1}$, $\bar{T}^{(k)}_{i+1,j,m}$ and $\bar{Q}^{(k)}_{i+1,j,m}$ in sequence in a similar manner. In practice however, due to some terms already treated implicitly in the IMEX method, supplemented with utilising a fine mesh resolution, correction always yielded a negligible improvement in the numerics.

For small $\bar{\Lambda}$, the numerics often exhibited an anomaly near the boundaries, usually for the largest computed harmonic components. To remove this anomaly, the asymptotic solution was used to overwrite the erroneous numerical result near the boundaries.

Several code validation tests were performed, which are summarised in appendix C. In particular, the code was able to reproduce the main results from the incompressible case of Goldstein & Hultgren (1988).

5.2.2 Weakly nonlinear amplitude equation

To solve the weakly nonlinear equation (4.5.37), we firstly make the substitution

$$\widetilde{B}(\widetilde{\mathcal{X}}) = \widetilde{A}(\widetilde{\mathcal{X}})\mathrm{e}^{-\tilde{\kappa}\widetilde{\mathcal{X}}}. \tag{5.2.37}$$

Then equation (4.5.37) becomes

$$\begin{aligned}\frac{\mathrm{d}\widetilde{B}}{\mathrm{d}\widetilde{\mathcal{X}}} = \mathcal{C}\mathrm{e}^{2\tilde{\kappa}_{\mathrm{r}}\widetilde{\mathcal{X}}}\int_0^\infty \aleph\lambda^2\mathrm{e}^{-2(\frac{1}{3}\widetilde{\Lambda}\lambda^3+2\tilde{\kappa}_{\mathrm{r}}\lambda)}\widetilde{B}(\widetilde{\mathcal{X}}-\lambda)\\ \times\int_0^\infty \mathrm{e}^{-(\widetilde{\Lambda}\lambda^2\mu+2\tilde{\kappa}_{\mathrm{r}}\mu)}\widetilde{B}(\widetilde{\mathcal{X}}-\lambda-\mu)\widetilde{B}^*(\widetilde{\mathcal{X}}-2\lambda-\mu)\mathrm{d}\mu\mathrm{d}\lambda\end{aligned} \tag{5.2.38}$$

with initial condition

$$\widetilde{B}(\widetilde{\mathcal{X}}) \to 1 \quad \text{as} \quad \widetilde{\mathcal{X}} \to -\infty. \tag{5.2.39}$$

Equation (5.2.38) was solved numerically by using a fourth-order Adams-Bashforth/ Moulton scheme to advance the solution downstream from the upstream state (5.2.39). Simpson's rule was used to evaluate both integrals, using the linear solution where required. Integration and downstream step sizes were kept equal to simplify solution code.

5.3 Vorticity and temperature within the critical layer

Nonlinear dynamics of the critical layer will be illustrated by suitable contours of vorticity and temperature. The total vorticity within the critical layer is

$$\begin{aligned}\Omega &= -\left(\frac{1}{\epsilon^{1/2}}\frac{\partial u}{\partial Y} - \left(\alpha\frac{\partial v}{\partial\zeta} + \epsilon^{1/2}\frac{\partial v}{\partial\mathcal{X}_1} + \Lambda\epsilon^{3/2}\frac{\partial v}{\partial\mathcal{X}_2}\right)\right)\\ &= -\left(\Omega_0 + \epsilon^{1/2}\Omega_{1/2} + \epsilon\Omega_1 + \cdots\right).\end{aligned} \tag{5.3.40}$$

Equations (2.2.14), (2.2.15), (2.3.39), (3.2.19), (3.2.26), (3.2.35), (3.2.40) & (4.1.10) show that $\Omega_0 = U_{\mathrm{c}}'$, $\Omega_{1/2} = 0$ and

$$\Omega_1 = \frac{1}{2}Y^2U_{\mathrm{c}}''' + Y\frac{U_{\mathrm{c}}'T_{\mathrm{c}M}}{T_{\mathrm{c}}}\mathcal{M}^2 + \Lambda\widehat{U}_{\mathrm{c}}'\mathcal{X}_1 + \widehat{Q} + 2\left(\frac{U_{\mathrm{c}}'''}{U_{\mathrm{c}}'} - \frac{T_{\mathrm{c}}''}{T_{\mathrm{c}}} + \frac{U_{\mathrm{c}}'^2}{T_{\mathrm{c}}}M^2\right)\Re\{A\mathrm{e}^{\mathrm{i}\zeta}\} \tag{5.3.41}$$

where $\Lambda\widehat{U}_c'\mathcal{X}_1$ is the first term proportional to $1/R$ in the Taylor expansion of U_{BY}. This term is a downstream-dependent shift of the contour levels. The vorticity contours in the subsequent figures are plotted in terms of the normalised $\mathcal{O}(\epsilon)$ vorticity

$$\begin{aligned}\bar{\Omega}_1 &= \frac{8U_c''^2}{c^2U_c'''\Omega^2}\Omega_1 - \bar{\Lambda}\frac{2c\widehat{U}_c'}{T_c\mu_cU_c'''}\Big(\bar{\mathcal{X}} + x_0\Big) + 4\frac{\bar{\mathcal{M}}^4}{\alpha^2c^2} - 2\frac{M^2U_c'^3}{T_cU_c'''}\Re\{\bar{A}e^{i\tilde{\zeta}}\} \\ &= \left(\bar{Y} - \frac{2}{\alpha c}\Big(1+\bar{\mathcal{M}}^2\Big)\right)^2 + 2(1+\sigma)\Re\{\bar{A}e^{i\tilde{\zeta}}\} - \frac{2}{\alpha c}\bar{Q}\end{aligned} \tag{5.3.42}$$

where $\tilde{\zeta} = \zeta + \Omega\mathcal{T}$, $\bar{Q} = \sum \bar{Q}_m e^{im\tilde{\zeta}}$ and we have used equations (4.3.24)–(4.3.27).

Similarly, the total temperature within the critical layer is

$$T = \tau_0 + \epsilon^{1/2}\tau_{1/2} + \epsilon\tau_1 + \cdots . \tag{5.3.43}$$

Equations (2.2.18), (2.3.39), (3.2.19) & (4.1.4) show that $\tau_0 = T_c$, $\tau_{1/2} = 0$ and

$$\tau_1 = T_{cM}'\mathcal{M}^2Y + \frac{1}{2}Y^2T_c'' + \widehat{T} + 2\left(\frac{T_c''}{U_c'} + (\gamma-1)M^2U_c'\right)\Re\{Ae^{i\zeta}\}. \tag{5.3.44}$$

The temperature contours in the subsequent figures are plotted in terms of the normalised $\mathcal{O}(\epsilon)$ temperature

$$\begin{aligned}\bar{\tau}_1 &= -\frac{8U_c'^3}{c^2T_cU_c'''\Omega^2}\tau_1 + 4\frac{\bar{\mathcal{M}}^4}{\alpha^2c^2\sigma} + 2\frac{(\gamma-1)U_c'^3M^2}{T_cU_c'''}\Re\{\bar{A}e^{i\tilde{\zeta}}\} \\ &= \sigma\left(\bar{Y} - \frac{2}{\alpha c}\Big(1 - \frac{\bar{\mathcal{M}}^2}{\sigma}\Big)\right)^2 + 2\sigma\Re\{\bar{A}e^{i\tilde{\zeta}}\} + \frac{2}{\alpha c}\bar{T}\end{aligned} \tag{5.3.45}$$

where $\tilde{\zeta} = \zeta + \Omega\mathcal{T}$, $\bar{T} = \sum \bar{T}_m e^{im\tilde{\zeta}}$ and we have used equations (4.3.24)–(4.3.27).

Note that terms proportional to $M^2\Re\{\bar{A}e^{i\tilde{\zeta}}\}$ in (5.3.42) & (5.3.45) are omitted from the contour plots since they lead to masking of the fine structure of the vorticity and temperature roll-up.

5.4 A note on scaling

Let us define

$$\widehat{\Lambda} = \frac{\alpha c^3}{8T_c\mu_cU_c'^2}\bar{\Lambda} = \frac{\Lambda}{\Omega^3} = \frac{1}{\hat{\omega}^3R} \tag{5.4.46}$$

where

$$\hat{\omega} = (\omega_n - \omega). \tag{5.4.47}$$

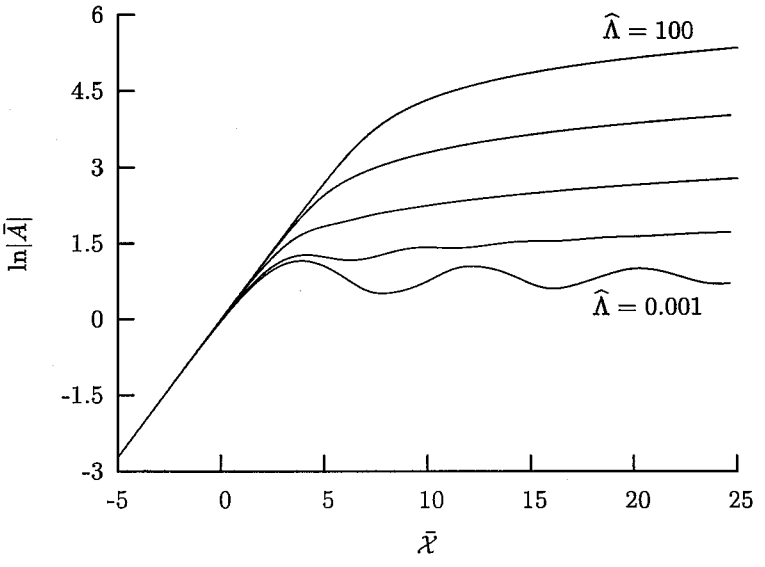


Figure 5.22: Amplitude $\ln|\bar{A}|$ *vs.* $\bar{\mathcal{X}}$ for $\beta_T = 1$, $M = 1/2$ and $\widehat{\Lambda} = 0.001, 0.1, 1, 10, 100$.

This definition is convenient since $\widehat{\Lambda}$ is then directly related to the important physical quantities $\hat{\omega}$ (the deviation from the neutral frequency) and R (the Reynolds number). Also note that

$$\bar{\mathcal{M}}^2 \propto \frac{T'_{cM}\mathcal{M}^2}{\Omega} = \frac{T'_c}{\hat{\omega}}. \tag{5.4.48}$$

So $\bar{\mathcal{M}}^2$ is directly proportional to the important physical quantity T'_c (controlled by the ratio of specific heats γ, Mach number M, temperature ratio β_T, and velocity ratio β_U) and inversely proportional to $\hat{\omega}$.

For the tanh profile, when $\beta_T = 1$, $T'_c = 0$ for all M. After fixing γ, β_U and M, the remaining parameter is the product $\hat{\omega}^3 R$. If $\beta_T \neq 1$ we have $T'_c \neq 0$. Here, if we fix γ, β_U and M, but decrease $\hat{\omega}$, then we increase $|\bar{\mathcal{M}}^2|$. The parameter $|\bar{\mathcal{M}}^2|$ may also be increased by increasing $|\beta_T - 1|$, and less so by increasing M. These observations are worth noting since the validity of the weakly nonlinear theory, formally derived for $|\bar{\mathcal{M}}^2| \gg 1$, can be better related to physical parameters.

5.5 Results

Unless otherwise stated we assume:

- $\gamma = 7/5$, which is close to the ratio for air (≈ 1.401 at 1atm. and 15°C).
- Chapman viscosity law $\mu = T$. This is a reasonable approximation to the dependence on viscosity μ with temperature T. This assumption also yields the Lock profile solution to the mean-flow equations.
- Tanh profile. This is a good approximation to the Lock profile, and allows the profile to be analytically studied (as done earlier in this chapter).
- $\beta_U = 1/2$. This choice for β_U will be explained in a later section, where it will also be demonstrated that β_U does not have a substantial effect on the numerical results.
- $\hat{\omega} = 1/40$. In order for the nearly-neutral mode assumption to remain valid, $\hat{\omega}$ should not be much larger than this value. It should also not be too small, since then the coefficient $\bar{\mathcal{M}}^2$ becomes significantly larger than the other coefficients in equation (4.3.29) (e.g. $\gamma = 7/5$, $\beta_U = 1/2$, $\beta_T = 1/2$, $M = 1/2$ and $\hat{\omega} = 1/40$ gives $\bar{\mathcal{M}}^2 \approx 2.33$, whilst if $\hat{\omega} = 1/4000$, then $\bar{\mathcal{M}}^2 \approx 233$).

This leaves us with three parameters: M, β_T and $\widehat{\Lambda}$. Note that, primarily due to the choice of $\hat{\omega}$, the results to be presented in this section correspond to the cases with moderate $\bar{\mathcal{M}}$, for which the strongly nonlinear theory is required, since the weakly nonlinear theory is not a good approximation. Parameters for which the weakly nonlinear theory is a good approximation are investigated in a later section.

5.5.1 Case I: $\beta_T = 1$, $M = 1/2$

Results for the first case correspond to streams of equal temperature ($\beta_T = 1$) and a relatively low Mach number ($M = 1/2$). Figures 5.22–5.24 show amplitudes, instantaneous growth rates and wavenumber corrections for a range of $\widehat{\Lambda}$. These results are almost identical to the incompressible case of Goldstein & Hultgren (1988) (see appendix C), which is not surprising, since $T_c' = 0$ (for the tanh profile) and M^2 is quite small. We see that for small $\widehat{\Lambda}$, the amplitudes exhibit sinusoidal-like behaviour with oscillating growth rate and wavenumber. Increasing $\widehat{\Lambda}$ suppresses and eventually eliminates the oscillatory behaviour, with an accompanied increase in amplitude magnitude. For all $\widehat{\Lambda}$, the amplitudes continue to grow with growth rates that ultimately tend to zero. The similarity with the results of Goldstein & Hultgren (1988) suggest that the final asymptotic state is close to $|\bar{A}| \sim (\bar{\Lambda}\bar{\mathcal{X}})^{2/3}$. The effect of the Mach number on the final asymptotic state will be shown in Case

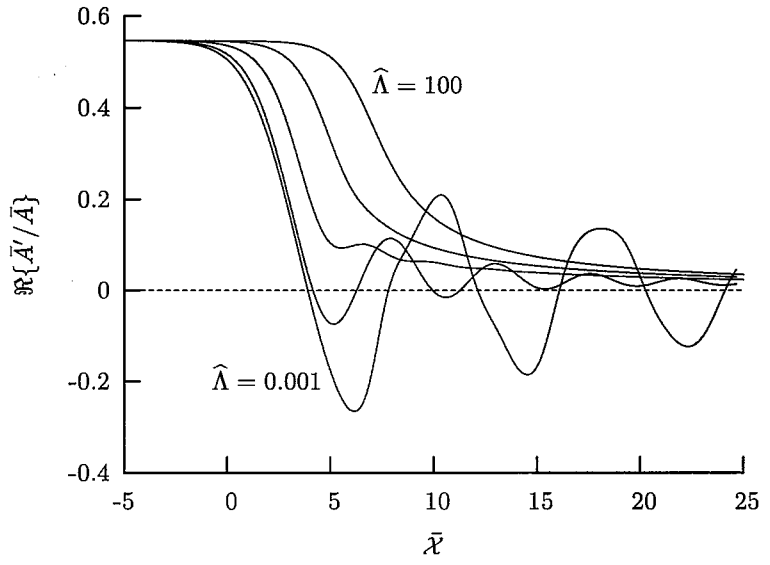


Figure 5.23: Instantaneous growth rate $\Re\{\bar{A}'/\bar{A}\}$ *vs.* $\bar{\mathcal{X}}$ for $\beta_T = 1$, $M = 1/2$ and $\widehat{\Lambda} = 0.001$, 0.1, 1, 10, 100.

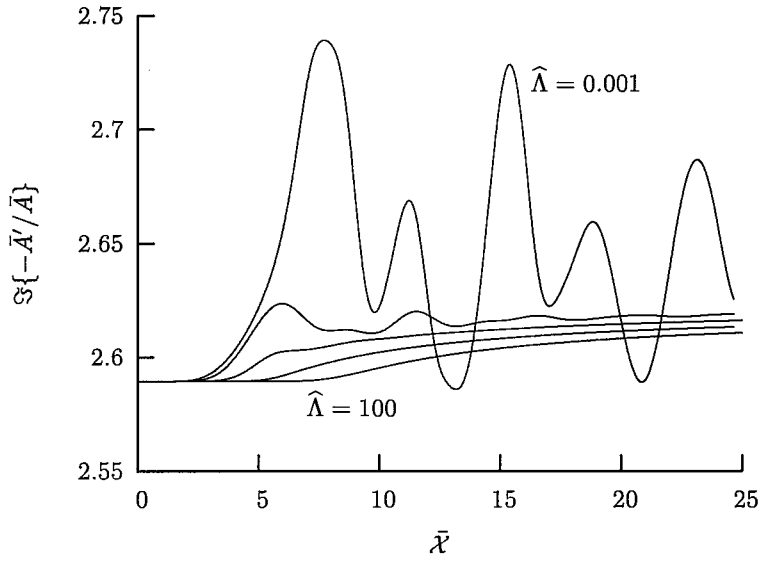


Figure 5.24: Wavenumber correction $\Im\{-\bar{A}'/\bar{A}\}$ *vs.* $\bar{\mathcal{X}}$ for $\beta_T = 1$, $M = 1/2$ and $\widehat{\Lambda} = 0.001$, 0.1, 1, 10, 100.

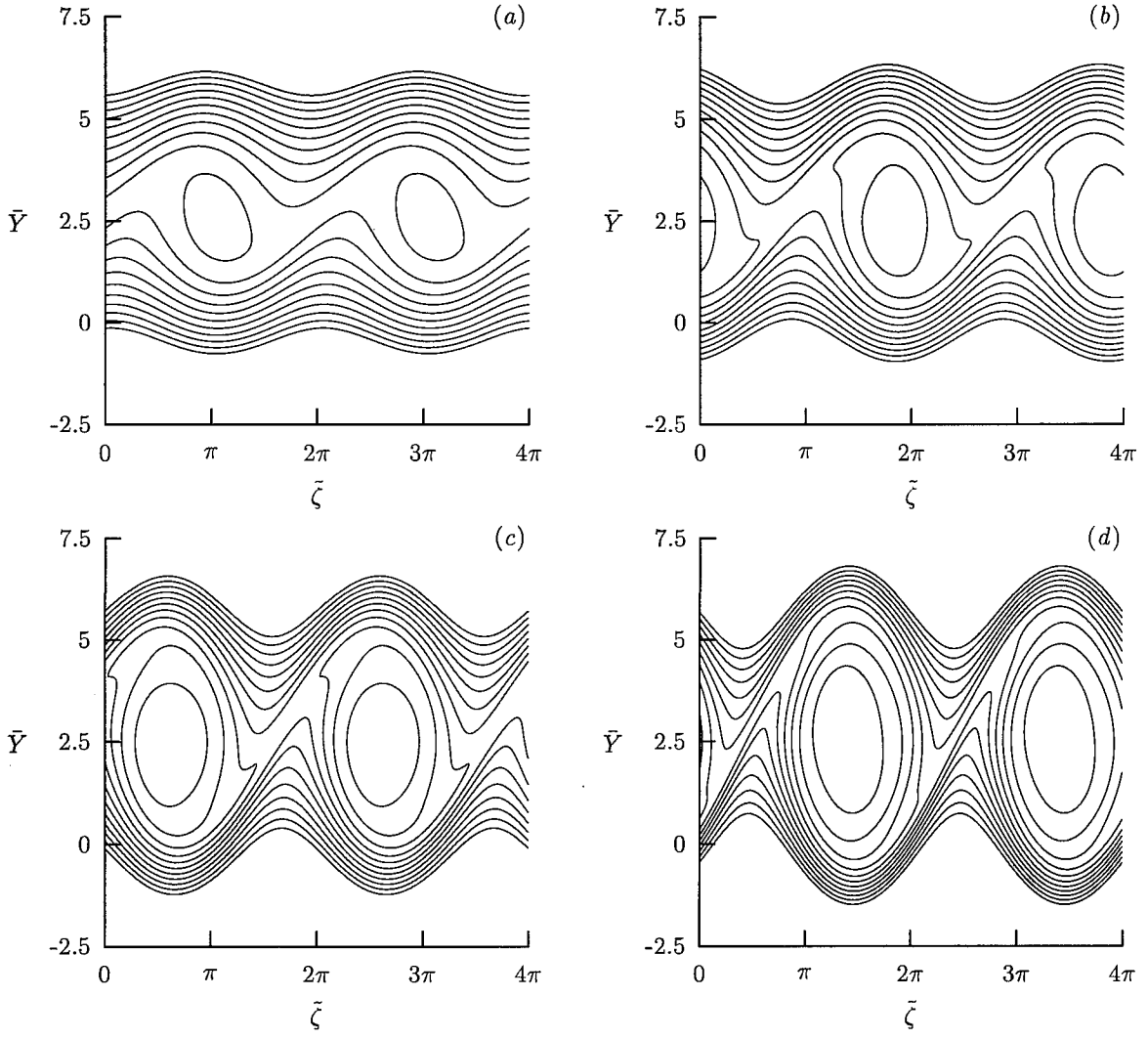


Figure 5.25: Vorticity contours in the $(\tilde{\zeta}, \bar{Y})$-plane for $\beta_T = 1$, $M = 1/2$, $\widehat{\Lambda} = 0.1$ and contour levels 0, 1, 2, ..., 9 and 10: (a) $\bar{\mathcal{X}} = -0.986$; (b) $\bar{\mathcal{X}} = 0.986$; (c) $\bar{\mathcal{X}} = 2.958$; (d) $\bar{\mathcal{X}} = 4.930$.

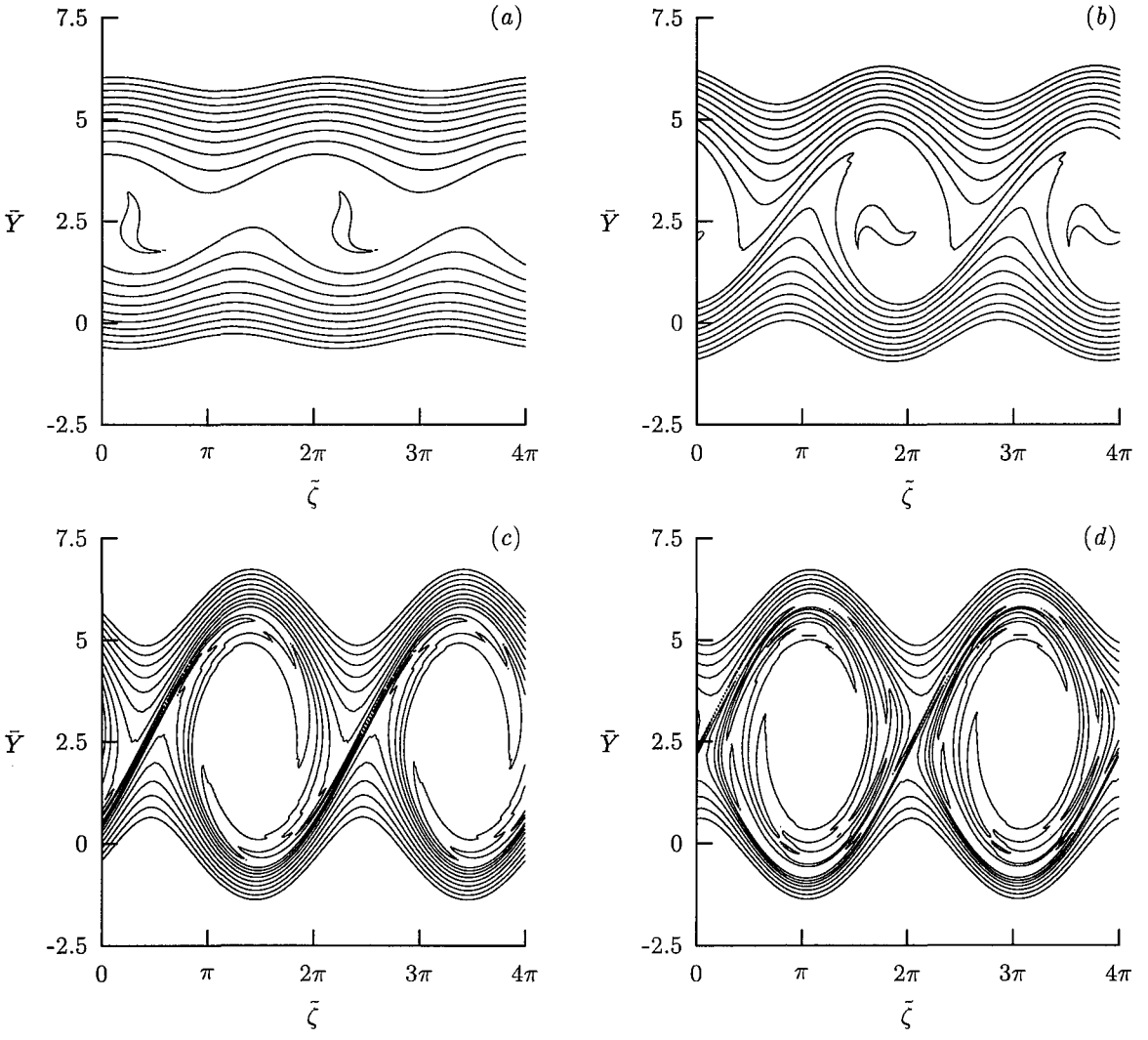


Figure 5.26: Vorticity contours in the $(\tilde{\zeta}, \bar{Y})$-plane for $\beta_T = 1$, $M = 1/2$, $\widehat{\Lambda} = 0.001$ and contour levels 0, 1, 2, ..., 9 and 10: (*a*) $\bar{\mathcal{X}} = -0.986$; (*b*) $\bar{\mathcal{X}} = 0.986$; (*c*) $\bar{\mathcal{X}} = 2.958$; (*d*) $\bar{\mathcal{X}} = 4.930$. (Contour level 0 is omitted from plots (*c*) & (*d*).)

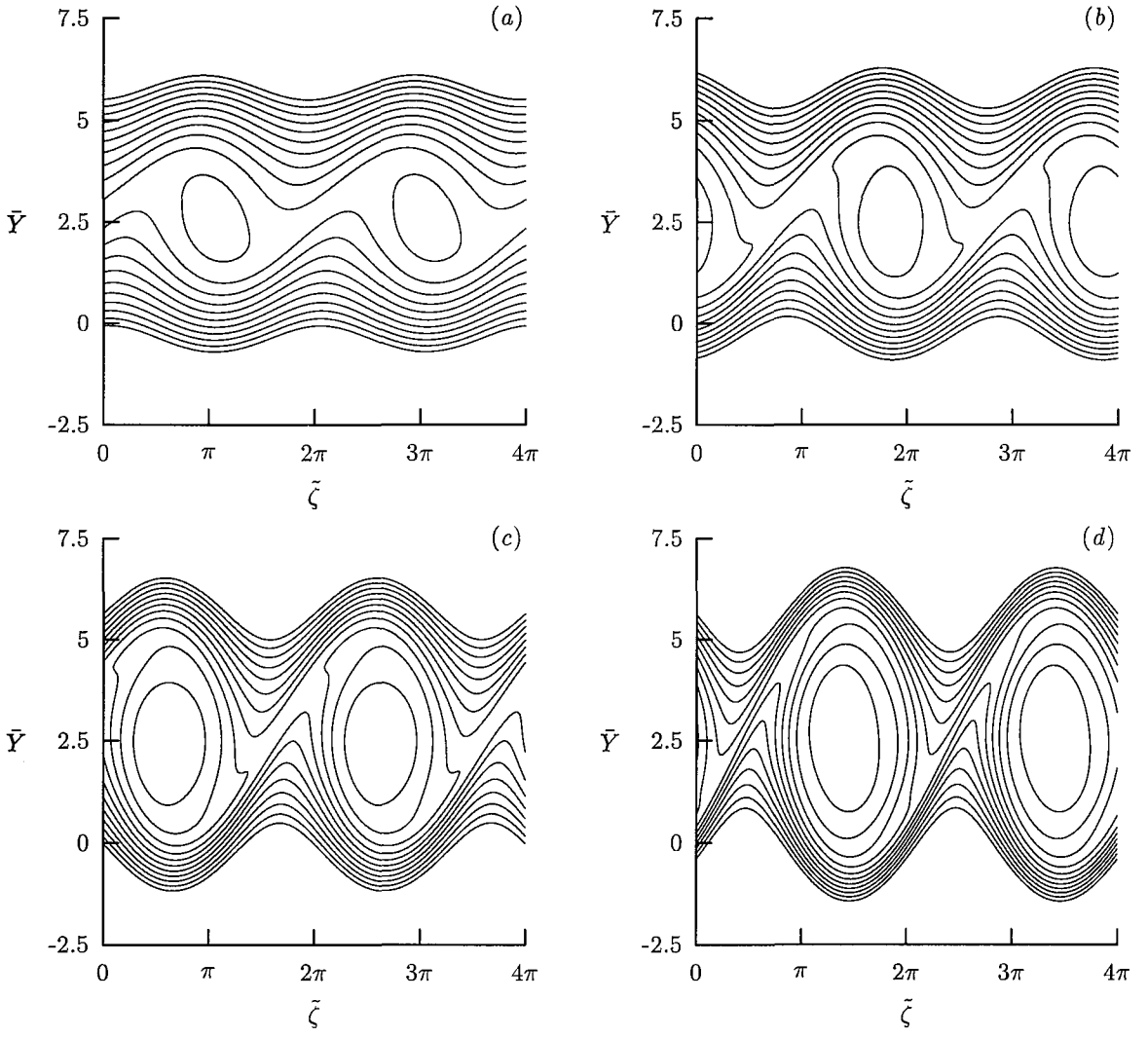


Figure 5.27: Temperature contours in the $(\tilde{\zeta}, \bar{Y})$-plane for $\beta_T = 1$, $M = 1/2$, $\widehat{\Lambda} = 0.1$ and contour levels 0, -0.003, -0.006, ..., -0.027 and -0.030: (a) $\bar{\mathcal{X}} = -0.986$; (b) $\bar{\mathcal{X}} = 0.986$; (c) $\bar{\mathcal{X}} = 2.958$; (d) $\bar{\mathcal{X}} = 4.930$.

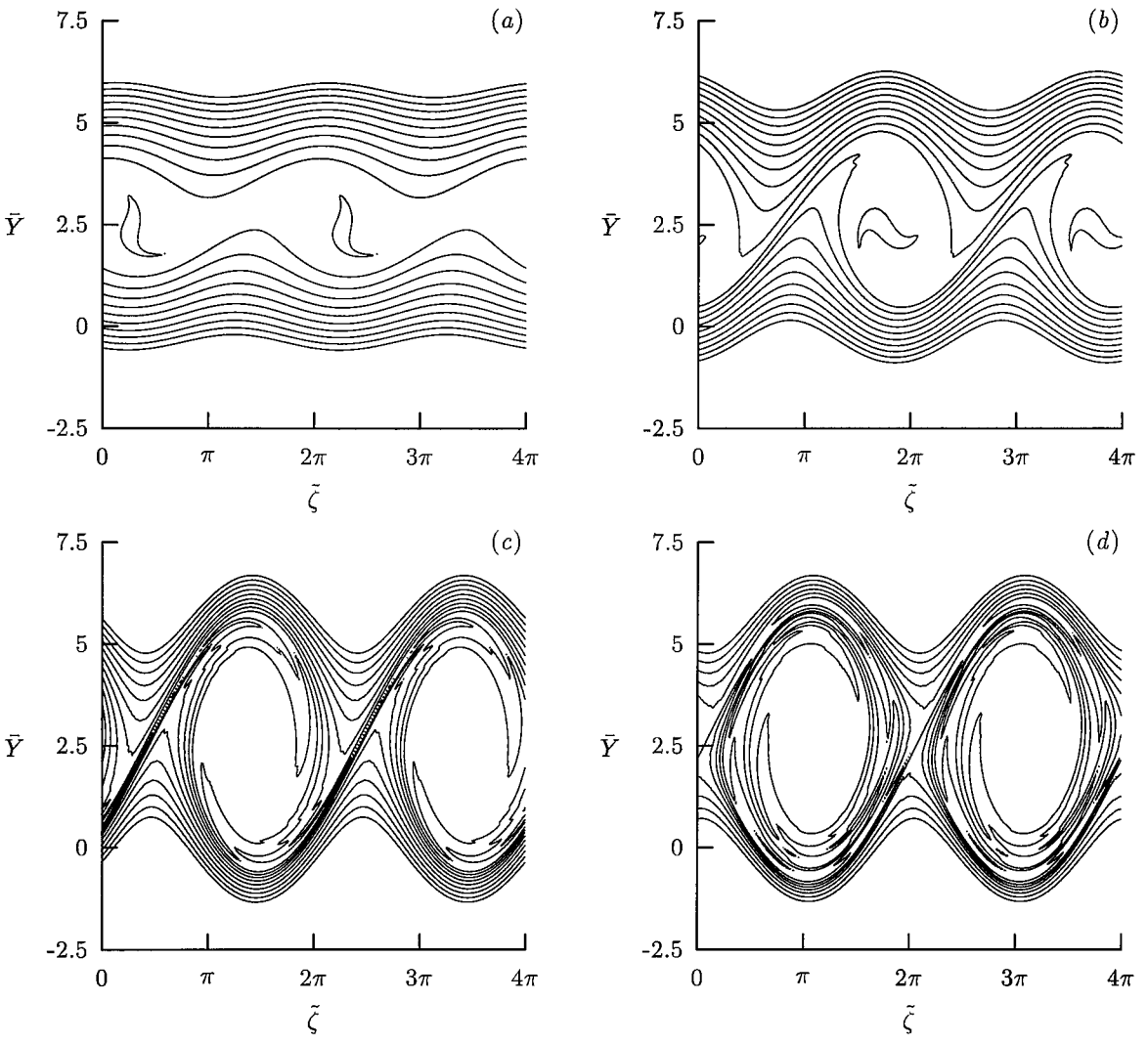


Figure 5.28: Temperature contours in the $(\tilde{\zeta}, \bar{Y})$-plane for $\beta_T = 1$, $M = 1/2$, $\widehat{\Lambda} = 0.001$ and contour levels 0, -0.003, -0.006, ..., -0.027 and -0.030: (*a*) $\bar{\mathcal{X}} = -0.986$; (*b*) $\bar{\mathcal{X}} = 0.986$; (*c*) $\bar{\mathcal{X}} = 2.958$; (*d*) $\bar{\mathcal{X}} = 4.930$. (Contour level 0 is omitted from plots (*c*) & (*d*).)

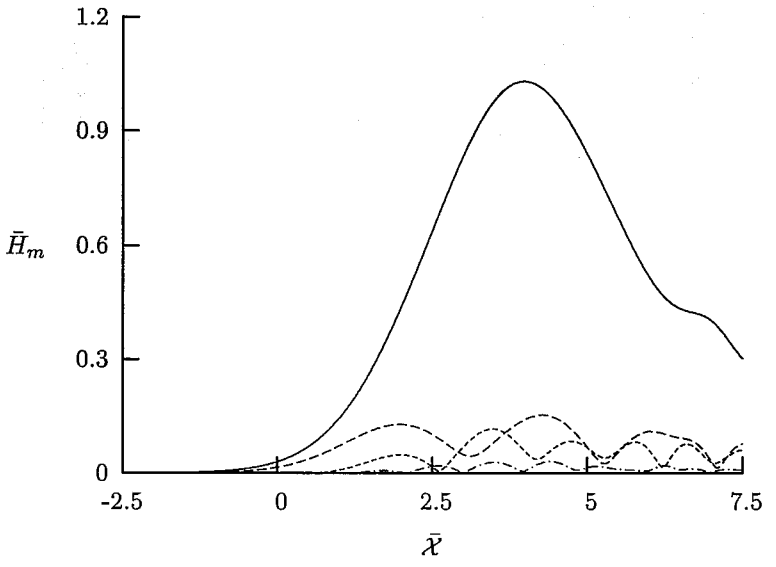


Figure 5.29: Development of higher harmonics, as measured by $\bar{H}_m = \left| \int_{-\infty}^{\infty} \bar{Q}_m \mathrm{d}\bar{Y} \right|$ *vs.* $\bar{\mathcal{X}}$, for $\beta_T = 1$, $M = 1/2$ and $\widehat{\Lambda} = 0.001$: $m = 2$ (solid), $m = 3$ (long-dashed), $m = 5$ (short-dashed) and $m = 10$ (dash-dotted).

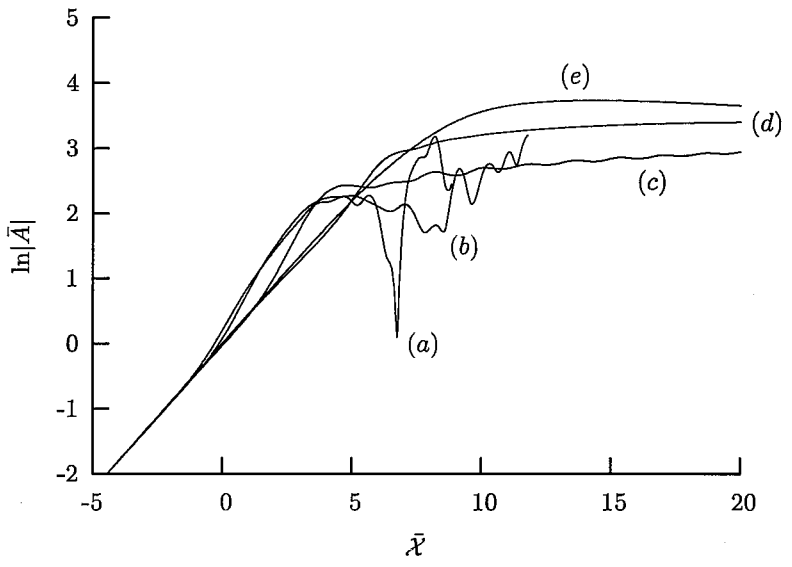


Figure 5.30: Amplitude $\ln|\bar{A}|$ *vs.* $\bar{\mathcal{X}}$ for $\beta_T = 1/2$, $M = 1/2$: (*a*) $\widehat{\Lambda} = 0.001$; (*b*) $\widehat{\Lambda} = 0.1$; (*c*) $\widehat{\Lambda} = 1$; (*d*) $\widehat{\Lambda} = 10$; (*e*) $\widehat{\Lambda} = 100$.

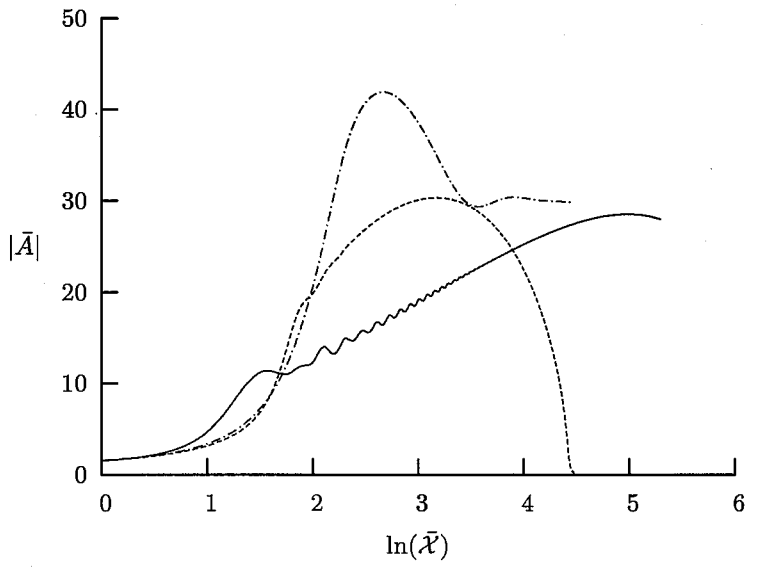


Figure 5.31: Amplitude $|\bar{A}|$ *vs.* $\ln(\bar{\mathcal{X}})$ for $\beta_T = 1/2$, $M = 1/2$: $\widehat{\Lambda} = 1$ (solid); $\widehat{\Lambda} = 10$ (dashed); $\widehat{\Lambda} = 100$ (dash-dotted).

III.

Vorticity roll-up is the most dominant feature of mixing-layer transition. Figure 5.25 shows vorticity contours for $\widehat{\Lambda} = 0.1$. The contours feature a regular Kelvin's cat's eye structure (Kelvin 1880), and there is almost no roll-up for this moderate viscous value ($R = 6.4 \times 10^5$ for $\hat{\omega} = 1/40$). Figure 5.26 shows vorticity contours for a smaller $\widehat{\Lambda} = 0.001$ ($R = 6.4 \times 10^7$ for $\hat{\omega} = 1/40$). In contrast to the previous figure, there is a great degree of roll-up, with mixing occurring mostly along the "braids" where the contours are very close together.

Figures 5.27 & 5.28 show the equivalent temperature contours corresponding to the vorticity contours in figures 5.25 & 5.26. The behaviour of the temperature roll-up is almost identical to that of the vorticity roll-up. This is not surprising – the temperature and vorticity equations (4.3.29) & (4.3.30) are essentially the same, since $\bar{\mathcal{M}} = 0$ and $|\bar{T}_m| \ll |\bar{Q}_m|$.

Physically, roll-up is associated with the development of higher harmonics, which are simultaneously generated by nonlinear interactions. Figure 5.29 shows some of the harmonics for $\widehat{\Lambda} = 0.001$. It can be seen that the first harmonic $m = 2$ has the most significant magnitude, and the first few low harmonics (e.g. $m \leqslant 5$) also retain appreciate amplitudes. Higher harmonics gradually become smaller.

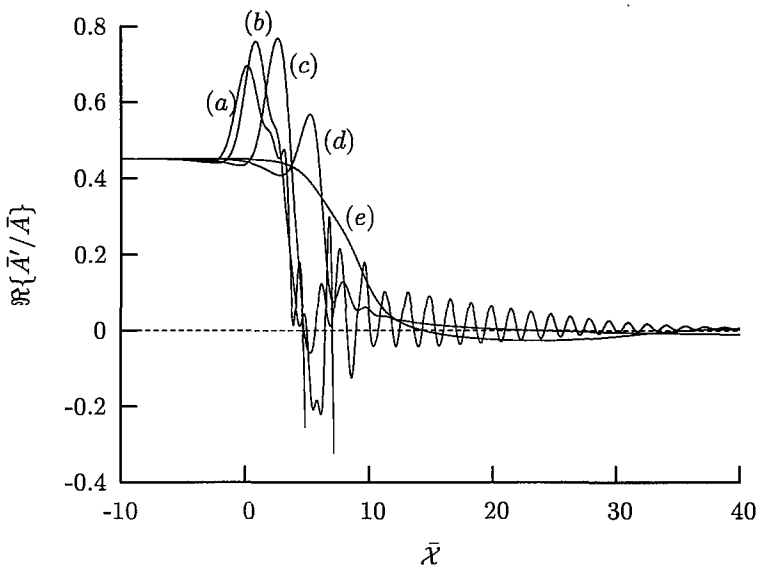


Figure 5.32: Instantaneous growth rate $\Re\{\bar{A}'/\bar{A}\}$ *vs.* $\bar{\mathcal{X}}$ for $\beta_T = 1/2$, $M = 1/2$: (*a*) $\widehat{\Lambda} = 0.001$; (*b*) $\widehat{\Lambda} = 0.1$; (*c*) $\widehat{\Lambda} = 1$; (*d*) $\widehat{\Lambda} = 10$; (*e*) $\widehat{\Lambda} = 100$.

5.5.2 Case II: $\beta_T \neq 1$, $M = 1/2$

Next we consider the case where the two streams have different temperatures, i.e. $\beta_T \neq 1$. The Mach number is kept at $M = 1/2$. Figures 5.30–5.33 show amplitudes, instantaneous growth rates and wavenumber corrections for $\beta_T = 1/2$ and a range of $\widehat{\Lambda}$. In this case $|T_c'| \neq 0$, and consequently these results contrast greatly with those for $\beta_T = 1$.

For small $\widehat{\Lambda}$, the amplitudes exhibit a quite chaotic-like behaviour with growth rates oscillating violently about zero. The initial behaviour is somewhat similar to that found in Goldstein & Wundrow (1990). One major difference from their results is that the growth rates initially decrease before increasing. They presumed that the increase was due to the Bjerknes forces, although this is not likely to be the cause of the (decrease or) increase in the present case. For small $\widehat{\Lambda}$, solutions were unable to be advanced arbitrarily far downstream, unlike those for $\beta_T = 1$, due to pathological development of small-scale structures, which are hard to resolve numerically.

For moderate values of $\widehat{\Lambda}$ ($\widehat{\Lambda} = 1$, 10), solutions could be advanced far downstream. We notice that the amplitudes appear to attenuate or slowly decay. However, for $\widehat{\Lambda} = 10$, much farther downstream the amplitude began to grow again. This strange type of behaviour occurs for other parameters, and is discussed at the

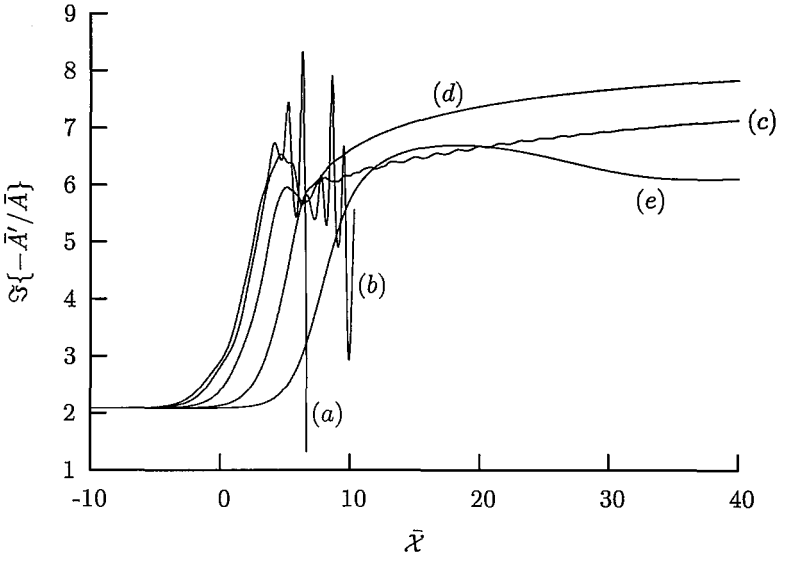


Figure 5.33: Wavenumber correction $\Im\{-\bar{A}'/\bar{A}\}$ *vs.* $\bar{\mathcal{X}}$ for $\beta_T = 1/2$, $M = 1/2$: (*a*) $\widehat{\Lambda} = 0.001$; (*b*) $\widehat{\Lambda} = 0.1$; (*c*) $\widehat{\Lambda} = 1$; (*d*) $\widehat{\Lambda} = 10$; (*e*) $\widehat{\Lambda} = 100$.

end of this chapter. For the largest value of $\widehat{\Lambda}$ considered ($\widehat{\Lambda} = 100$), the amplitude ultimately equilibrates, and this is the only result attaining a clear asymptotic state.

Figure 5.34 shows vorticity contours for $\beta_T = 1/2$ and $\widehat{\Lambda} = 0.1$. Vorticity roll-up is much stronger than for $\beta_T = 1$. Appearance of closed "islands" similar to those found in Goldstein & Wundrow (1990) can initially be seen. Further downstream irregular small-scale development causes contours to break up and form tiny islands or excessive "wiggles". Tests suggested this to be a numerical problem rather than a physical occurrence. As vorticity rolls up, the temperature contours (figure 5.35) also wind up to form tight spirals, indicating a significant degree of mixing. Interestingly, the temperature contours appear rather "regular". It also seems that the temperature roll-up is the "cause" of the vortex roll-up through coupling.

The development of (apparently pathological) small-scale motions becomes much more severe for smaller $\widehat{\Lambda}$, as shown in figure 5.36 for $\widehat{\Lambda} = 0.001$. The contour lines break-up near the cores to give rise to a sharp "banding" effect. Tighter spirals than those for $\widehat{\Lambda} = 0.1$ can be observed, showing an even greater degree of mixing. Figure 5.37 shows the temperature contours for $\widehat{\Lambda} = 0.001$. As for the $\widehat{\Lambda} = 0.1$ case, the temperature contours are more regular than those for the vorticity, and consequently can be reliably presented for distances further downstream. For both values of $\widehat{\Lambda}$, numerical tests showed the larger-scale structure to remain intact, although

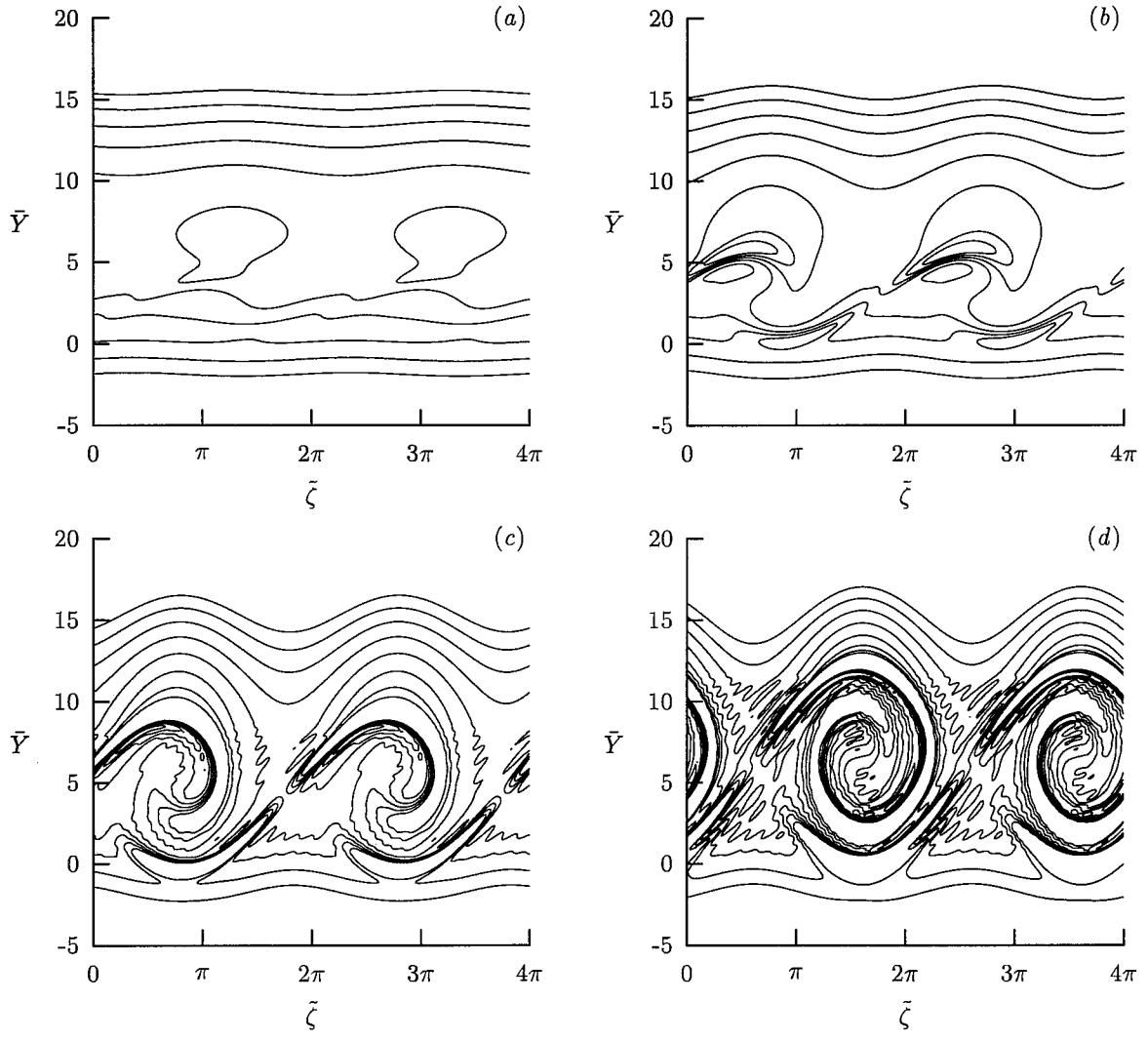


Figure 5.34: Vorticity contours in the $(\tilde{\zeta}, \bar{Y})$-plane for $\beta_T = 1/2$, $M = 1/2$, $\widehat{\Lambda} = 0.1$ and contour levels -30, -15, 0, $\ldots$, 60 and 75: (a) $\bar{\mathcal{X}} = 0$; (b) $\bar{\mathcal{X}} = 1.475$; (c) $\bar{\mathcal{X}} = 2.950$; (d) $\bar{\mathcal{X}} = 4.425$.

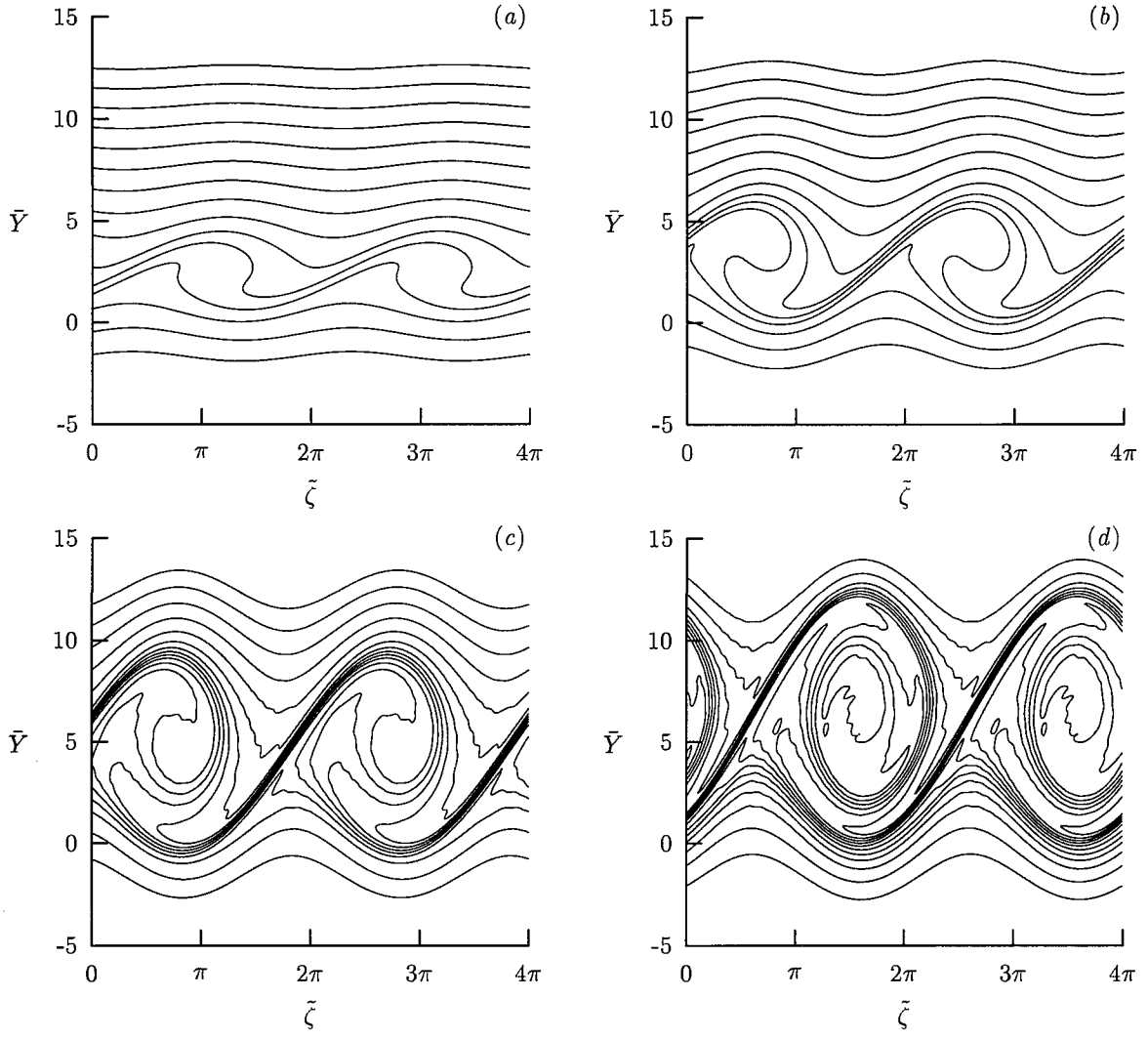


Figure 5.35: Temperature contours in the $(\tilde{\zeta}, \bar{Y})$-plane for $\beta_T = 1/2$, $M = 1/2$, $\widehat{\Lambda} = 0.1$ and contour levels 370, 380, 390, ..., 500 and 510: (a) $\bar{\mathcal{X}} = 0$; (b) $\bar{\mathcal{X}} = 1.475$; (c) $\bar{\mathcal{X}} = 2.950$; (d) $\bar{\mathcal{X}} = 4.425$.

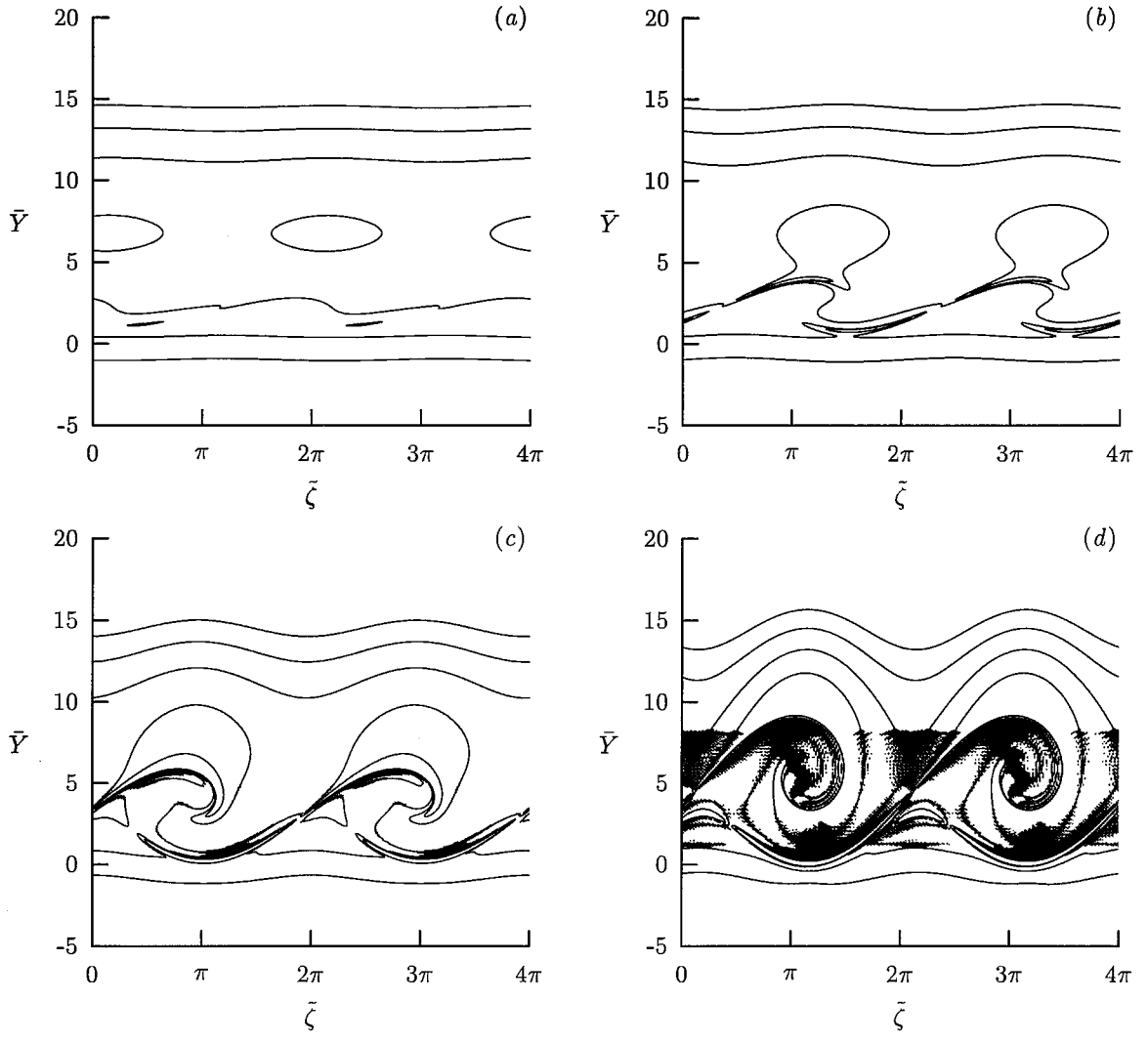


Figure 5.36: Vorticity contours in the $(\tilde{\zeta}, \bar{Y})$-plane for $\beta_T = 1/2$, $M = 1/2$, $\widehat{\Lambda} = 0.001$ and contour levels -20, 0, 20, 40 and 60: (a) $\bar{\mathcal{X}} = -1.475$; (b) $\bar{\mathcal{X}} = 0$; (c) $\bar{\mathcal{X}} = 1.475$; (d) $\bar{\mathcal{X}} = 2.950$. (Contour level -20 is omitted from plot (d).)

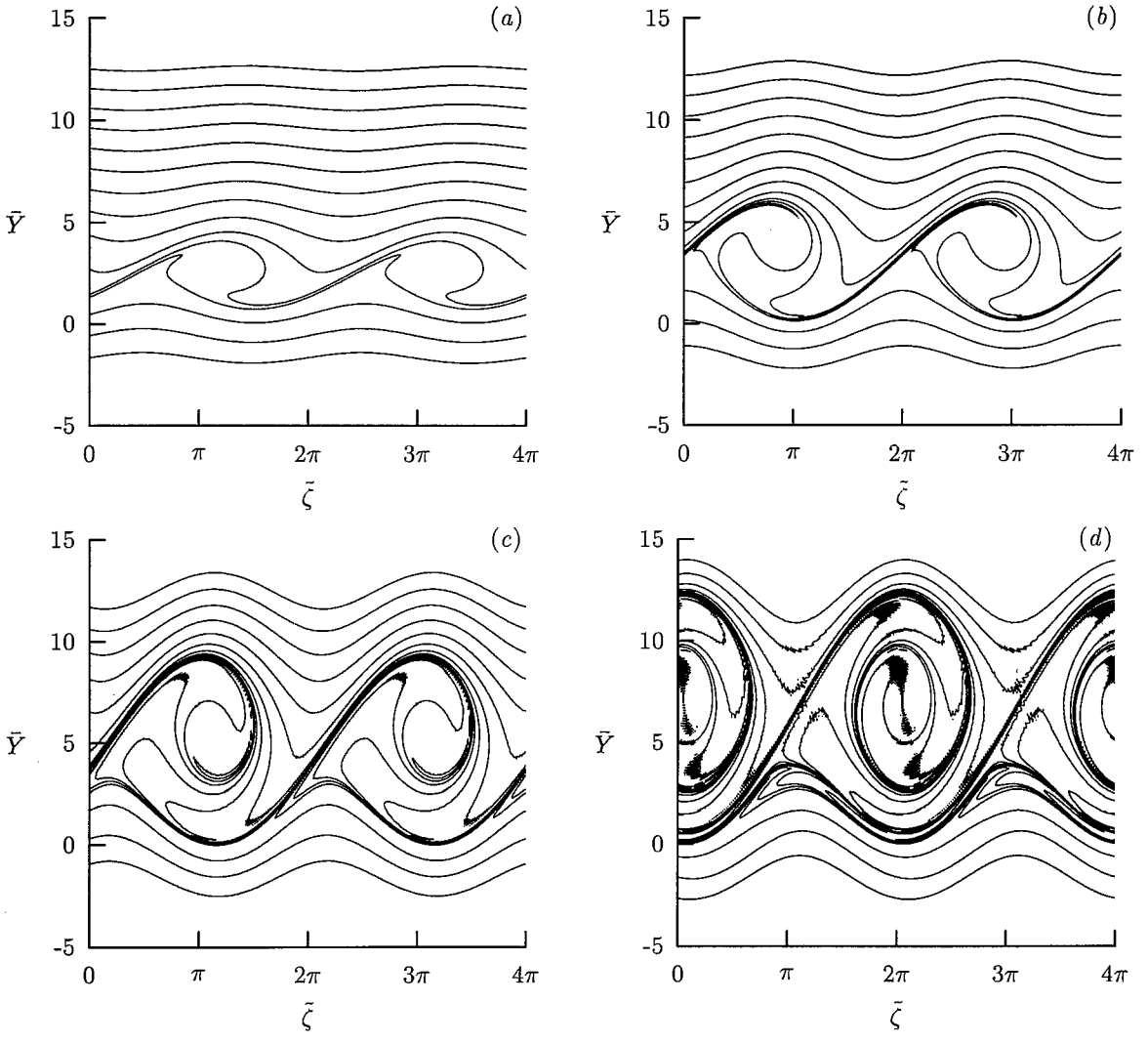


Figure 5.37: Temperature contours in the $(\tilde{\zeta}, \bar{Y})$-plane for $\beta_T = 1/2$, $M = 1/2$, $\widehat{\Lambda} = 0.001$ and contour levels 370, 380, 390, ..., 500 and 510: (a) $\bar{\mathcal{X}} = 0$; (b) $\bar{\mathcal{X}} = 1.475$; (c) $\bar{\mathcal{X}} = 2.950$; (d) $\bar{\mathcal{X}} = 4.425$.

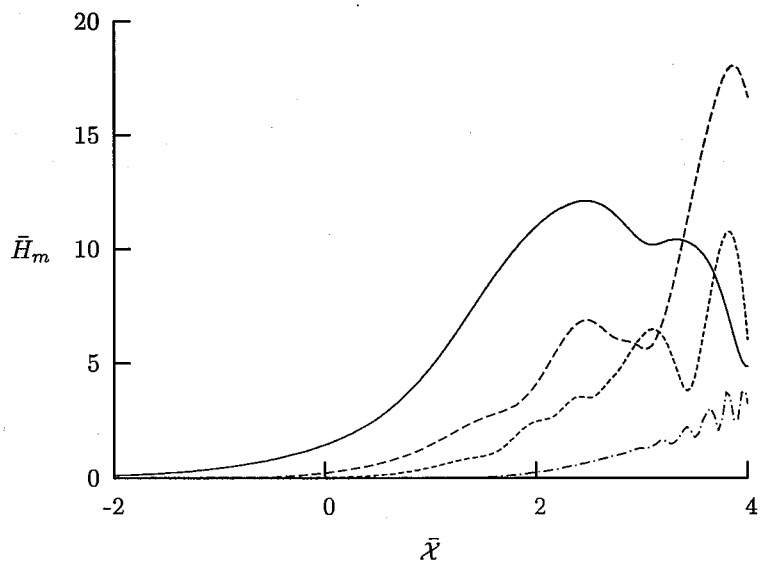


Figure 5.38: Development of higher harmonics, as measured by $\bar{H}_m = \left| \int_{-\infty}^{\infty} \bar{Q}_m \mathrm{d}\bar{Y} \right|$ *vs.* $\bar{\mathcal{X}}$, for $\beta_T = 1/2$, $M = 1/2$ and $\widehat{\Lambda} = 0.001$: $m = 2$ (solid), $m = 5$ (long-dashed), $m = 10$ (short-dashed) and $m = 40$ (dash-dotted).

the small-scales could not be properly resolved.

Figure 5.38 shows the development of some of the harmonics for $\widehat{\Lambda} = 0.001$. In contrast to the $\beta_T = 1$ case, quite a few harmonics are numerically of the same magnitude, with higher harmonics overtaking the lower ones further downstream. It can also be seen that even the largest harmonic considered ($m = 40$) has a substantial amplitude, rather than remaining smaller than the first few harmonics. This was found to occur regardless of the number of Fourier components used (for tests ranging from $m = 5$ to $m = 100$). This suggests increasingly vigorous small-scale motions, which cannot not be adequately resolved by the present spectral method. For sufficiently small-wavelength motions the streamwise diffusion can no longer be ignored even in the critical layer, so they may not even be accommodated by critical-layer theory.

The effect of β_T on the amplitude is rather complicated, depending on $\widehat{\Lambda}$, as shown in figures 5.39–5.42. For moderate to relatively large $\widehat{\Lambda}$ ($\widehat{\Lambda} \geqslant 1$), increasing β_T above unity has a stabilising effect. In particular, for $\widehat{\Lambda} = 10$ the amplitude equilibrates (rather than undergoing (quasi-)algebraic growth as in the case of $\beta_T = 1$), and for $\widehat{\Lambda} = 1$, the amplitude decays. Decreasing β_T below unity has a relatively

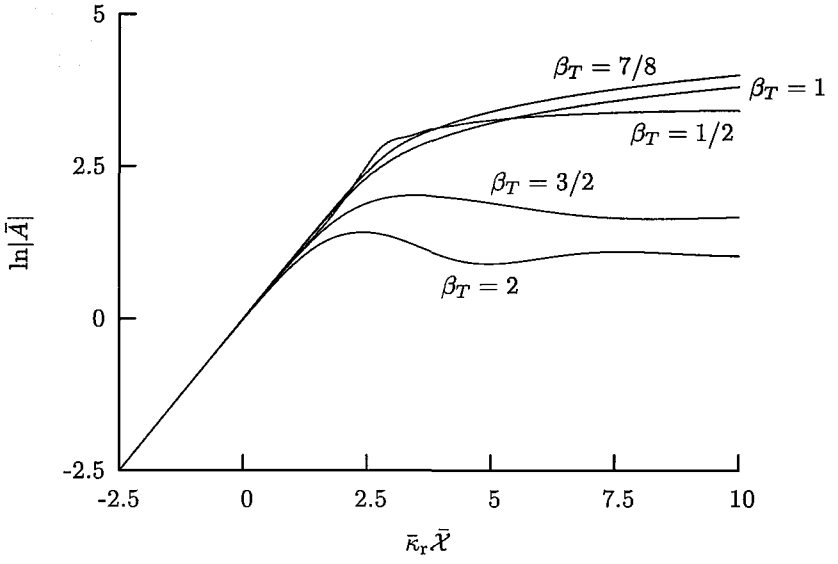


Figure 5.39: Amplitude $\ln|\bar{A}|$ *vs.* $\bar{\kappa}_r\bar{\mathcal{X}}$ for $\widehat{\Lambda} = 10$ and $\beta_T = 1/2,\ 7/8,\ 1,\ 3/2,\ 2$.

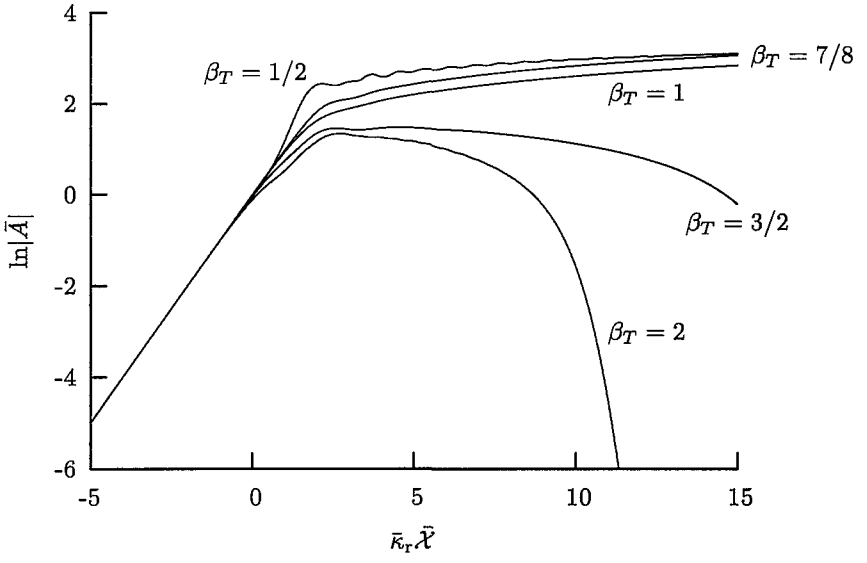


Figure 5.40: Amplitude $\ln|\bar{A}|$ *vs.* $\bar{\kappa}_r\bar{\mathcal{X}}$ for $\widehat{\Lambda} = 1$ and $\beta_T = 1/2,\ 7/8,\ 1,\ 3/2,\ 2$.

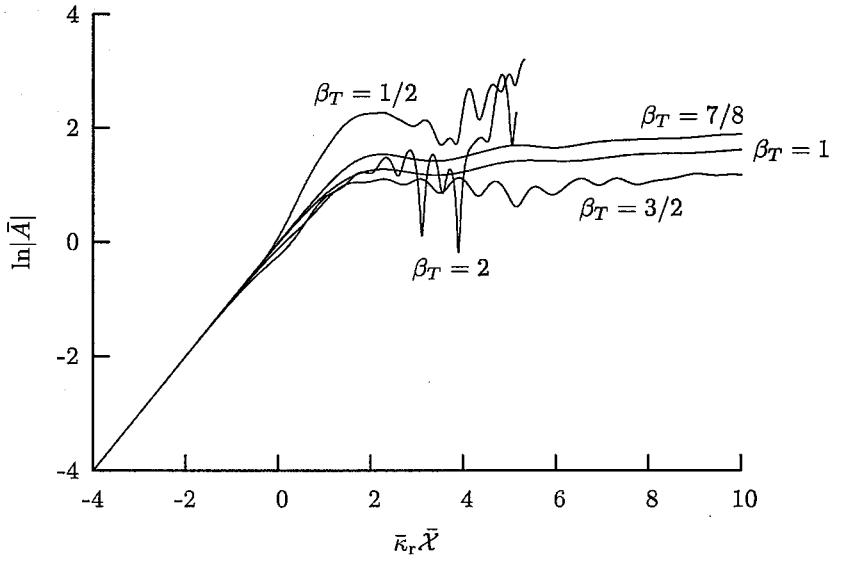


Figure 5.41: Amplitude $\ln|\bar{A}|$ *vs.* $\bar{\kappa}_r\bar{\mathcal{X}}$ for $\widehat{\Lambda} = 0.1$ and $\beta_T = 1/2,\ 7/8,\ 1,\ 3/2,\ 2$.

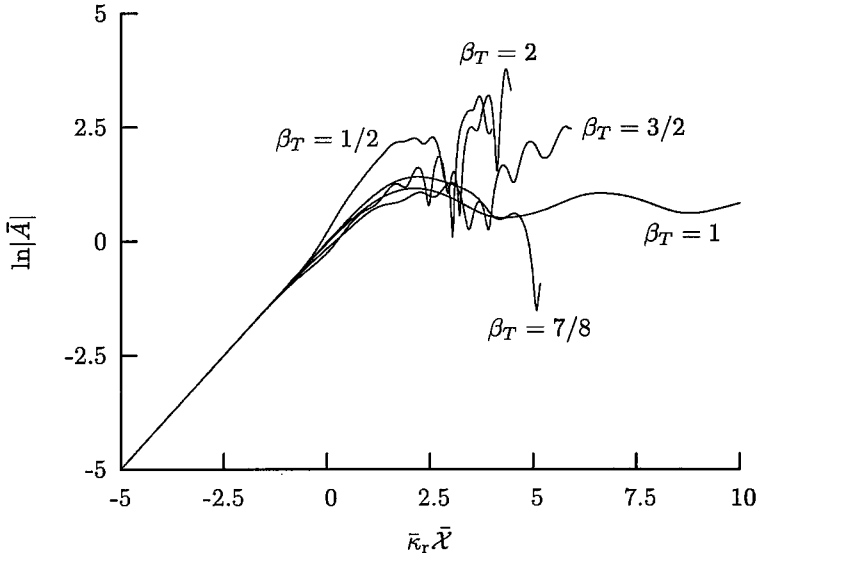


Figure 5.42: Amplitude $\ln|\bar{A}|$ *vs.* $\bar{\kappa}_r\bar{\mathcal{X}}$ for $\widehat{\Lambda} = 0.001$ and $\beta_T = 1/2,\ 7/8,\ 1,\ 3/2,\ 2$.

moderate effect on the amplitude for the streamwise distances shown. For smaller $\widehat{\Lambda}$ ($\widehat{\Lambda} \leqslant 0.1$), both increasing β_T above unity or decreasing β_T below unity causes the amplitude to undergo increasingly complex oscillation (figure 5.42).

Vorticity and temperature contours are shown in figures 5.43 & 5.44 for the case $\widehat{\Lambda} = 0.1$ and $\beta_T = 7/8$. It can be seen that there is slightly less roll-up compared to the $\beta_T = 1/2$ case, but still much more than the $\beta_T = 1$ case. Also the contours do not consist of any irregular wiggles or tiny islands, suggesting that small-scale motions do not develop in this case.

Vorticity and temperature contours are shown in figures 5.45 & 5.46 for $\widehat{\Lambda} = 0.1$ and $\beta_T = 2$, i.e. the slow stream is hotter. Mixing appears to be slightly less strong than that for the "opposite" case $\beta_T = 1/2$, suggesting that mixing would be relatively improved by cooling the slow stream and not the fast stream. The "smooth" contours imply that small-scale motions are resolved, as in the case of $\beta_T = 7/8$.

5.5.3 Case III: $\beta_T = 1$, $M = \mathcal{O}(1)$

In this section we will use slightly different coordinates due to the strong dependence on α with M for $\beta_T = 1$ (see figure 5.7). In particular we replace $\bar{A}$ by $\alpha^2\bar{A}$ and $\bar{\kappa}_T\bar{\mathcal{X}}$ by $\bar{\kappa}_T\bar{\mathcal{X}} + \ln(\alpha^2)$, which removes the dependence of the coordinates on α. This dependence was introduced in the normalisation (4.3.24)–(4.3.27). Thus the new coordinates allow us to determine the effect of Mach number more clearly.

Figures 5.47–5.49 show amplitudes for $\beta_T = 1$ and various M for two different $\widehat{\Lambda}$. The value $M = 3.96$ is chosen since it is 99% of $M_{\max}$, where we recall that $M_{\max}$ is the maximum Mach number for subsonic modes (see figure 5.16). We see that increasing the Mach number has a stabilising effect for $\widehat{\Lambda} = 0.1$, 10, and that for larger Mach numbers the solution is more oscillatory for these two values of $\widehat{\Lambda}$. Recall that in the incompressible case, the amplitude evolves into an asymptotic state $|\bar{A}| \sim (\bar{\Lambda}\bar{\mathcal{X}})^{2/3}$ (Goldstein & Hultgren 1988). In order to see if a similar algebraic growth occurs, calculations for the $\widehat{\Lambda} = 10$ cases have been advanced far downstream, and the results are plotted in figure 5.50. Straight lines of slope 2/3 are approached at large distances, indicating that the algebraic growth law is unchanged. Hence the ultimate asymptotic state does not depend on Mach number for $\beta_T = 1$, except for perhaps a constant multiplying $(\bar{\Lambda}\bar{\mathcal{X}})^{2/3}$.

To assess whether the term involving T_c'' appearing in (4.3.29) & (4.3.30), which is absent for $M \ll \mathcal{O}(1)$, is responsible for the change in amplitude behaviour for larger Mach numbers, or whether the change is due to alterations in the mean flow

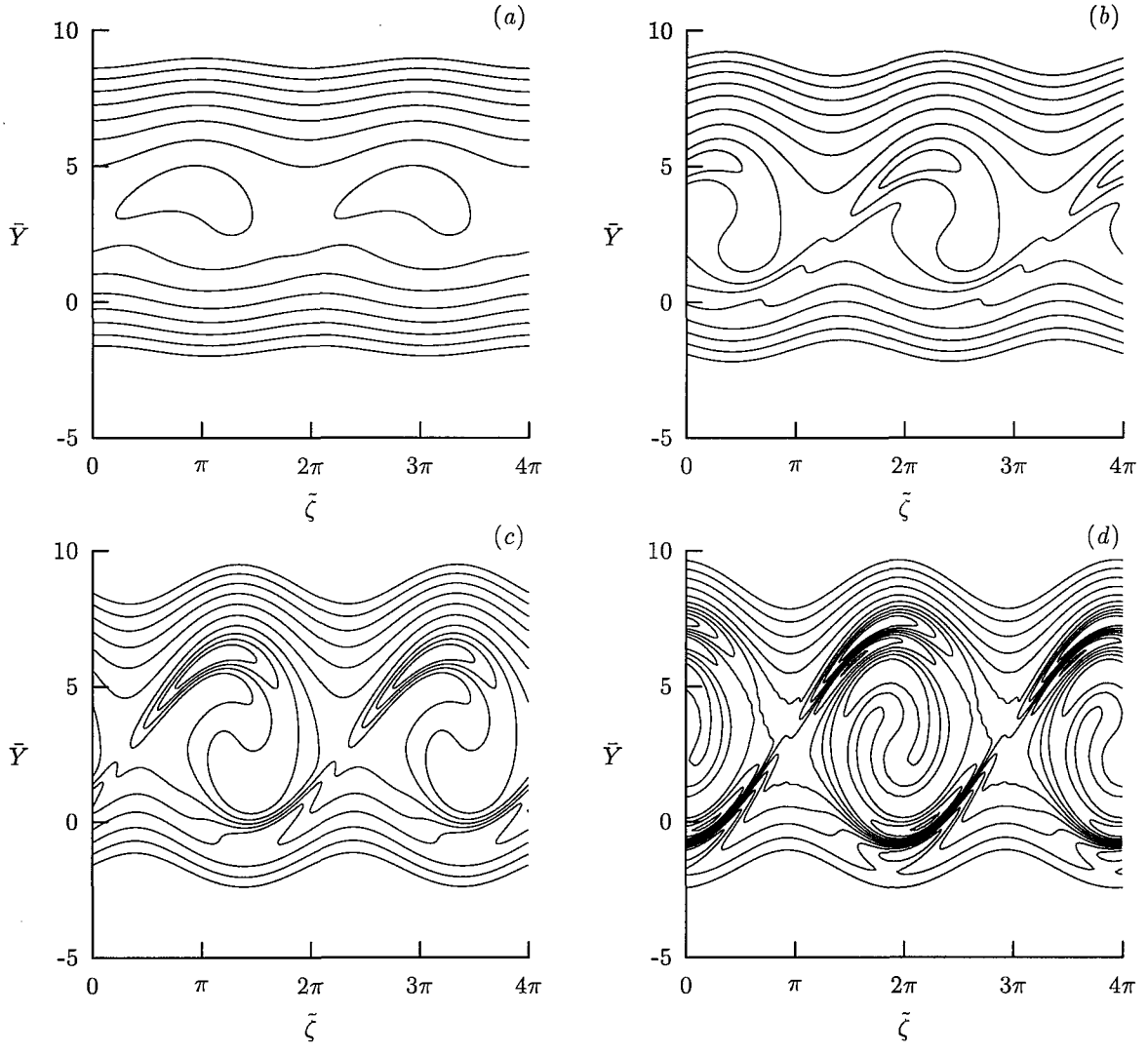


Figure 5.43: Vorticity contours in the $(\tilde{\zeta}, \bar{Y})$-plane for $\beta_T = 7/8$, $M = 1/2$, $\widehat{\Lambda} = 0.1$ and contour levels -8, -4, 0, $\ldots$, 24 and 28: (a) $\bar{\kappa}_{\mathrm{r}}\bar{\mathcal{X}} = 0$; (b) $\bar{\kappa}_{\mathrm{r}}\bar{\mathcal{X}} = 0.861$; (c) $\bar{\kappa}_{\mathrm{r}}\bar{\mathcal{X}} = 1.435$; (d) $\bar{\kappa}_{\mathrm{r}}\bar{\mathcal{X}} = 2.869$.

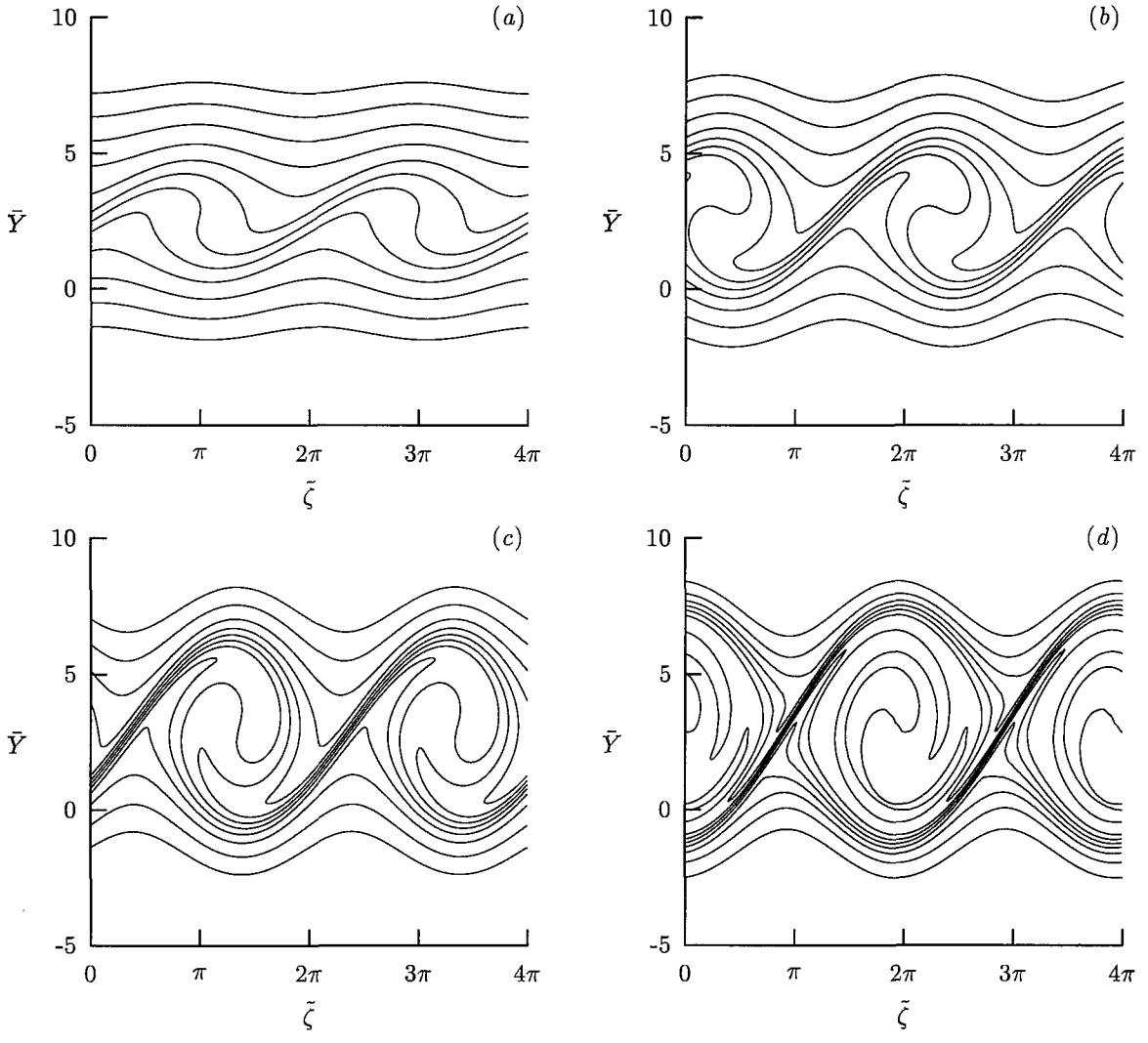


Figure 5.44: Temperature contours in the $(\tilde{\zeta}, \bar{Y})$-plane for $\beta_T = 7/8$, $M = 1/2$, $\widehat{\Lambda} = 0.1$ and contour levels -782.5, -781, -779.5, ..., -767.5 and -766: (*a*) $\bar{\kappa}_{\mathrm{r}}\bar{\mathcal{X}} = 0$; (*b*) $\bar{\kappa}_{\mathrm{r}}\bar{\mathcal{X}} = 0.861$; (*c*) $\bar{\kappa}_{\mathrm{r}}\bar{\mathcal{X}} = 1.435$; (*d*) $\bar{\kappa}_{\mathrm{r}}\bar{\mathcal{X}} = 2.869$.

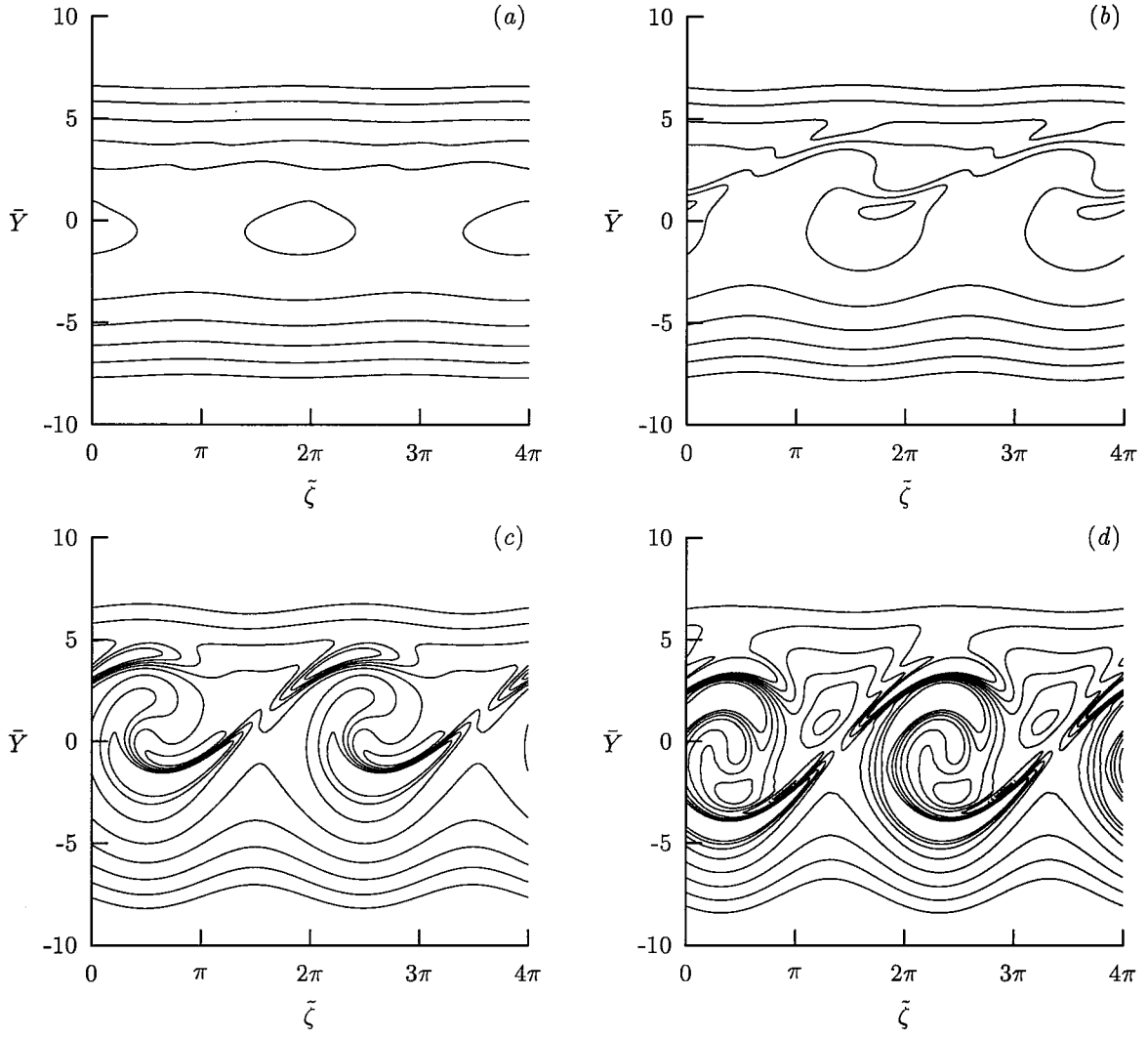


Figure 5.45: Vorticity contours in the $(\tilde{\zeta}, \bar{Y})$-plane for $\beta_T = 2$, $M = 1/2$, $\widehat{\Lambda} = 0.1$ and contour levels -20, -10, 0, $\ldots$, 40 and 50: (a) $\bar{\kappa}_{\mathrm{r}}\bar{\mathcal{X}} = -0.514$; (b) $\bar{\kappa}_{\mathrm{r}}\bar{\mathcal{X}} = 0.514$; (c) $\bar{\kappa}_{\mathrm{r}}\bar{\mathcal{X}} = 1.542$; (d) $\bar{\kappa}_{\mathrm{r}}\bar{\mathcal{X}} = 2.571$.

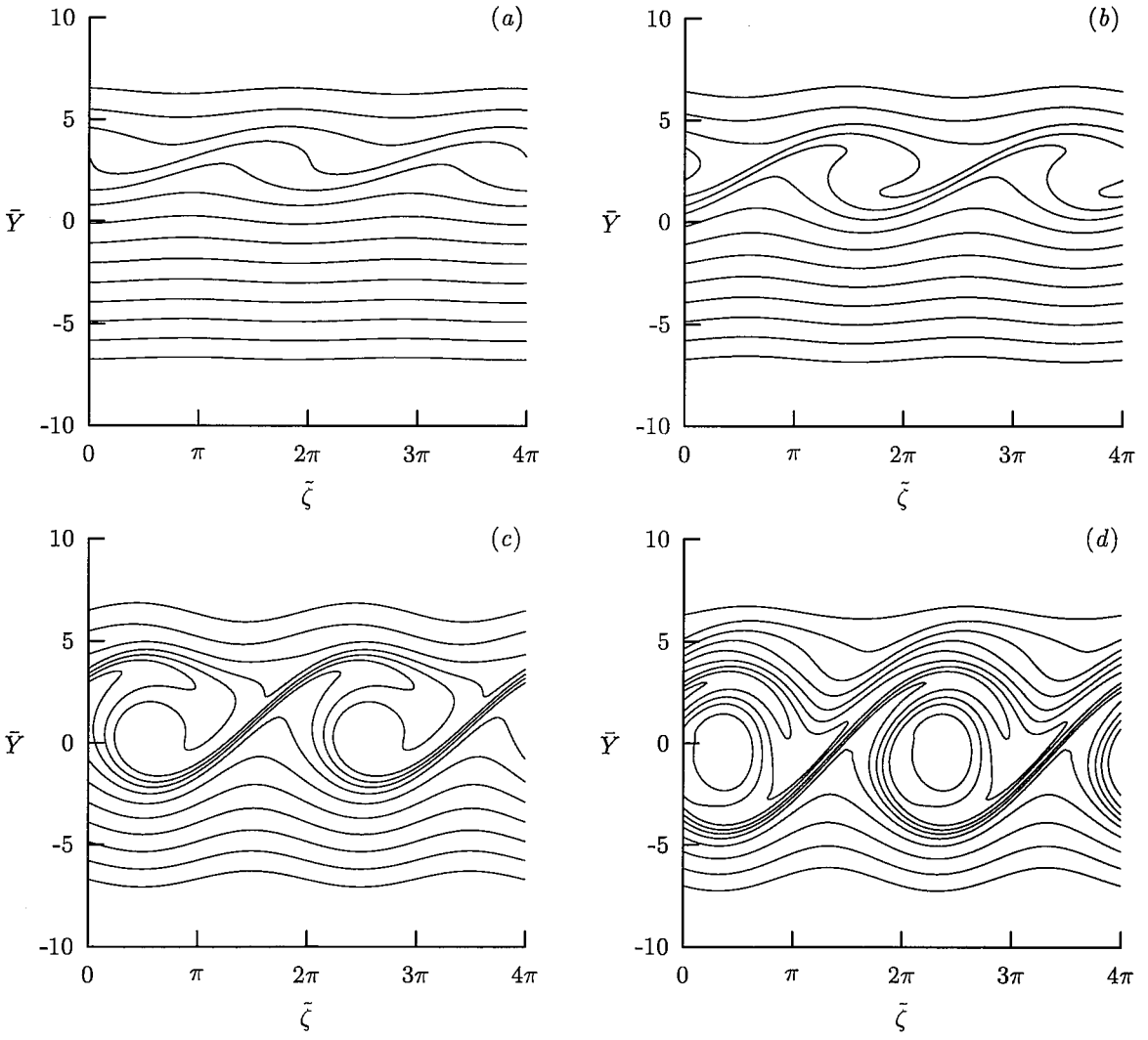


Figure 5.46: Temperature contours in the $(\tilde{\zeta}, \bar{Y})$-plane for $\beta_T = 2$, $M = 1/2$, $\widehat{\Lambda} = 0.1$ and contour levels 226, 234, 242, ..., 322 and 330: (a) $\bar{\kappa}_{\mathrm{r}}\bar{\mathcal{X}} = -0.514$; (b) $\bar{\kappa}_{\mathrm{r}}\bar{\mathcal{X}} = 0.514$; (c) $\bar{\kappa}_{\mathrm{r}}\bar{\mathcal{X}} = 1.542$; (d) $\bar{\kappa}_{\mathrm{r}}\bar{\mathcal{X}} = 2.571$.

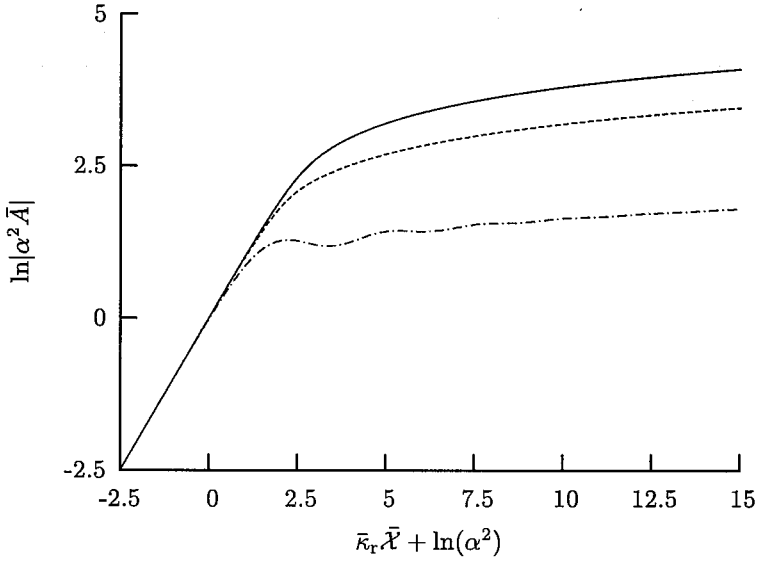


Figure 5.47: Amplitude $\ln|\alpha^2\bar{A}|$ *vs.* $\bar{\kappa}_r\bar{\mathcal{X}} + \ln(\alpha^2)$ for $\beta_T = 1$, $\widehat{\Lambda} = 10$ and $M = 1/10$ (solid), 3 (dashed), 3.96 (dash-dotted).

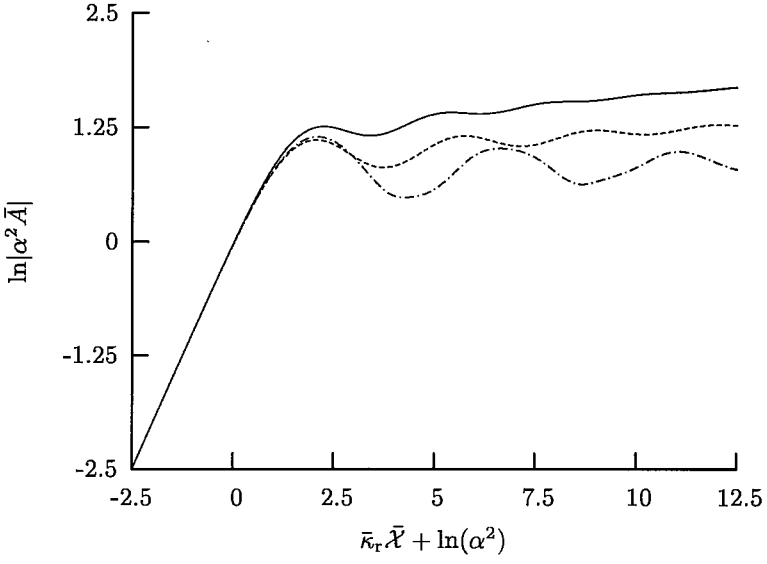


Figure 5.48: Amplitude $\ln|\alpha^2\bar{A}|$ *vs.* $\bar{\kappa}_r\bar{\mathcal{X}} + \ln(\alpha^2)$ for $\beta_T = 1$, $\widehat{\Lambda} = 0.1$ and $M = 1/10$ (solid), 3 (dashed), 3.96 (dash-dotted).

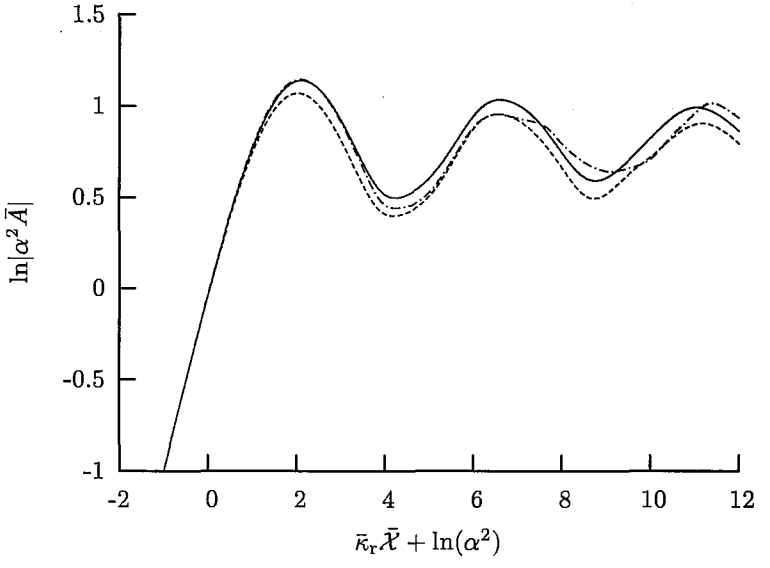


Figure 5.49: Amplitude $\ln|\alpha^2\bar{A}|$ *vs.* $\bar{\kappa}_r\bar{\mathcal{X}} + \ln(\alpha^2)$ for $\beta_T = 1$, $\widehat{\Lambda} = 0.001$ and $M = 1/10$ (solid), 3 (dashed), 3.96 (dash-dotted).

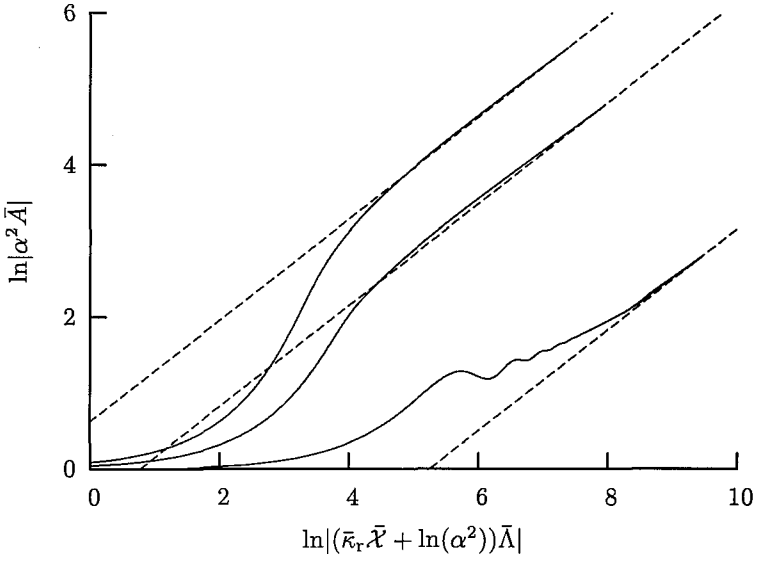


Figure 5.50: Amplitude $\ln|\alpha^2\bar{A}|$ *vs.* $\ln|(\bar{\kappa}_r\bar{\mathcal{X}} + \ln(\alpha^2))\bar{\Lambda}|$ for $\beta_T = 1$, $\widehat{\Lambda} = 10$, and $M = 0$, 3, 3.96. Dashed lines are approximate asymptotes, with slope 2/3.

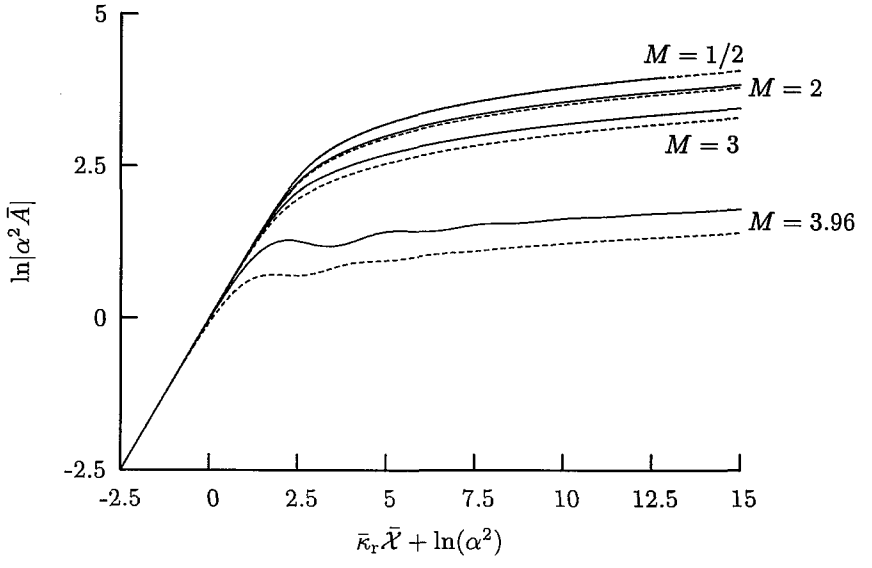


Figure 5.51: Amplitude $\ln|\alpha^2\bar{A}|$ *vs.* $\bar{\kappa}_r\bar{\mathcal{X}} + \ln(\alpha^2)$ for $\beta_T = 1$, $\widehat{\Lambda} = 10$ and various M: $T_c'' \neq 0$ (solid), $T_c'' = 0$ (dashed).

terms such as U_c' and J_1, the evolution equations were also solved by artificially setting $T_c'' = 0$. Figure 5.51 shows the results for $\widehat{\Lambda} = 10$ and $\beta_T = 1$. Obviously, inclusion of the T_c'' term has a rather small effect except for the largest Mach numbers. However, the change in amplitude for larger Mach numbers is primarily due to changes in mean-flow quantities.

Vorticity and temperature contours are shown in figures 5.52 & 5.53 for $M = 3$ and $\widehat{\Lambda} = 0.1$. Both contour plots look similar to those for $\beta_T = 1$ and $M = 1/2$ (cf. figures 5.25 & 5.27). Somewhat surprisingly, for $M = 3.96$ (figures 5.54 & 5.55), we notice a marked increase in roll-up and mixing. This may be explained by examining equations (4.3.20) and (4.3.21). Since α becomes very small as M nears $M_{\max}$, the diffusion coefficient $\Lambda T_c \mu_c \alpha^2 U_c'^2$ becomes much smaller, and consequently larger Mach number solutions exhibit a more inviscid behaviour. The increase in mixing would seem to be at odds with experiments, where there is an observed reduction in mixing for larger Mach number. However we note that the nonlinear coefficient, $i\alpha^2 U_c'$, also becomes small, causing mixing to occur at distances further downstream. Hence there would be an observed reduction in mixing at a fixed streamwise location. In addition, supersonic modes come into play near $M = M_{\max}$ to affect the mixing process, so that experiments performed for Mach numbers close to $M_{\max}$ cannot be reliably compared with the present theory.

As expected, contours for the case $\widehat{\Lambda} = 0.001$ (figures 5.56, 5.57, 5.58 & 5.59) exhibit greater mixing than those for the $\widehat{\Lambda} = 0.1$ case. Loss of small-scale resolution occurs at the last streamwise location in figure 5.58.

5.5.4 Case IV: $\beta_T \neq 1$, $M = \mathcal{O}(1)$

We now examine the effect of Mach number for non-unity β_T. Figures 5.60–5.63 show amplitudes for $\beta_T = 1/2$ and various M for four different $\widehat{\Lambda}$. The value $M = 2.87$ is chosen since it is 99% of $M_{\max}$ (the maximum Mach number for subsonic modes) when $\beta_T = 1/2$. When $\widehat{\Lambda} = 10$, the solutions for $M = 2$ and $M = 2.87$ oscillate about an equilibrium, whilst the $M = 1$ solution decays. Advancing the $M = 1/10$ solution further downstream indicated that it also decayed, but at a very slow rate. For $\widehat{\Lambda} = 1$, the $M = 2.87$ solution rapidly decays. The two other solutions also feature a slow decay upon further advancement of the solution downstream. For this value of $\widehat{\Lambda}$, the Mach number has a pronounced stabilising effect. Results for $\widehat{\Lambda} = 0.1$ and $\widehat{\Lambda} = 0.001$ are very similar. The Mach number initially has a stabilising effect, but thereafter strong oscillations occur, with the amplitude attaining comparable magnitude at all Mach numbers.

Vorticity and temperature contours are shown in figures 5.64 & 5.65 for $\beta_T = 1/2$, $M = 2.87$ and $\widehat{\Lambda} = 0.1$. Roll-up and mixing are the most notable features, which cannot be predicted by weakly nonlinear theory. The contours look very similar to those in figures 5.34 & 5.35, with perhaps a slight reduction in the roll-up.

Figures 5.66–5.69 show amplitudes for $\beta_T = 2$ and various M for four different $\widehat{\Lambda}$. The value $M = 4.06$ corresponds to 99% of $M_{\max}$ for $\beta_T = 2$. The behaviour of the amplitude is somewhat similar to the $\beta_T = 1/2$ case. For $\widehat{\Lambda} = 10$, all the solutions equilibrate. For $\widehat{\Lambda} = 1$, the $M = 1/10$ and $M = 2$ solutions decay, whilst the $M = 4.06$ solution appears to slowly oscillate about an equilibrium. The solutions for $\widehat{\Lambda} = 0.1$ and $\widehat{\Lambda} = 0.001$ are very similar, as they were for the $\beta_T = 1/2$ case, although the Mach number no longer exerts an obvious stabilising effect. The oscillations are also less violent than the $\beta_T = 1/2$ case.

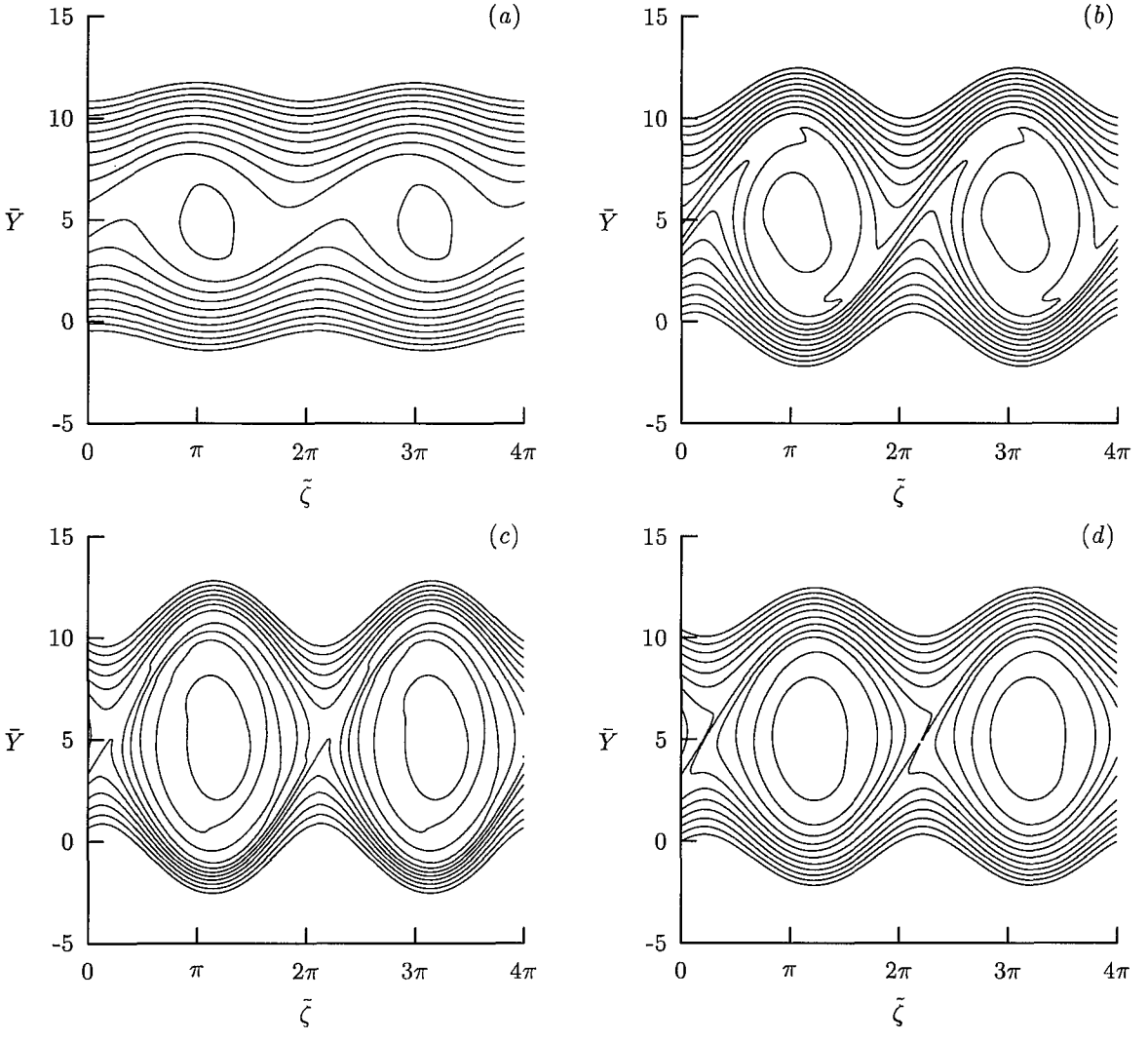


Figure 5.52: Vorticity contours in the $(\tilde{\zeta}, \bar{Y})$-plane for $\beta_T = 1$, $M = 3$, $\widehat{\Lambda} = 0.1$ and contour levels 0, 3.75, 7.5, ..., 33.75 and 37.5: (*a*) $\bar{\kappa}_{\rm r}\bar{\mathcal{X}} + \ln(\alpha^2) = -0.101$; (*b*) $\bar{\kappa}_{\rm r}\bar{\mathcal{X}} + \ln(\alpha^2) = 1.123$; (*c*) $\bar{\kappa}_{\rm r}\bar{\mathcal{X}} + \ln(\alpha^2) = 2.347$; (*d*) $\bar{\kappa}_{\rm r}\bar{\mathcal{X}} + \ln(\alpha^2) = 3.571$.

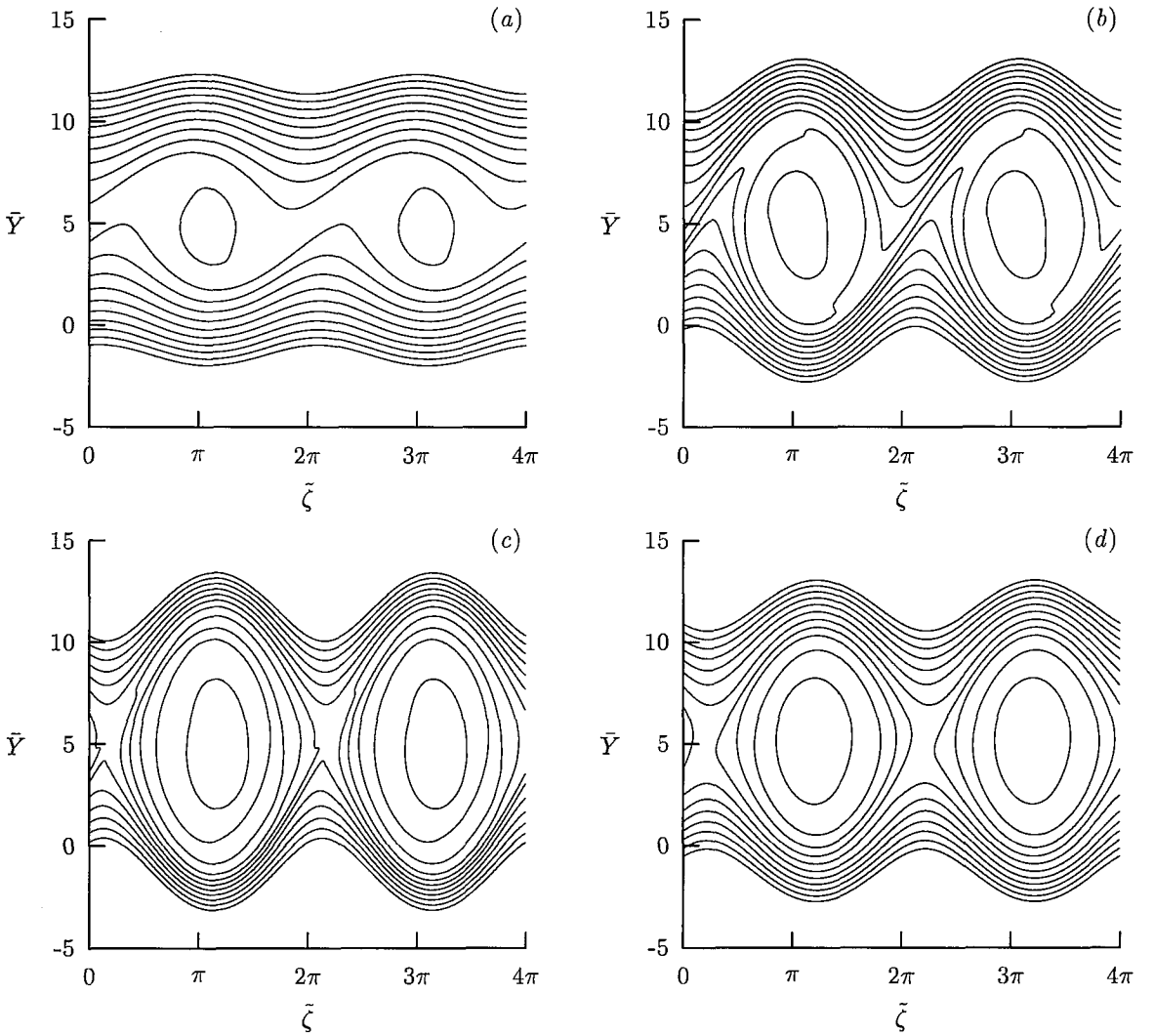


Figure 5.53: Temperature contours in the $(\tilde{\zeta}, \bar{Y})$-plane for $\beta_T = 1$, $M = 3$, $\widehat{\Lambda} = 0.1$ and contour levels -5, -4.5, -4, ..., -0.5 and 0: (*a*) $\bar{\kappa}_{\rm r}\bar{\mathcal{X}} + \ln(\alpha^2) = -0.101$; (*b*) $\bar{\kappa}_{\rm r}\bar{\mathcal{X}} + \ln(\alpha^2) = 1.123$; (*c*) $\bar{\kappa}_{\rm r}\bar{\mathcal{X}} + \ln(\alpha^2) = 2.347$; (*d*) $\bar{\kappa}_{\rm r}\bar{\mathcal{X}} + \ln(\alpha^2) = 3.571$.

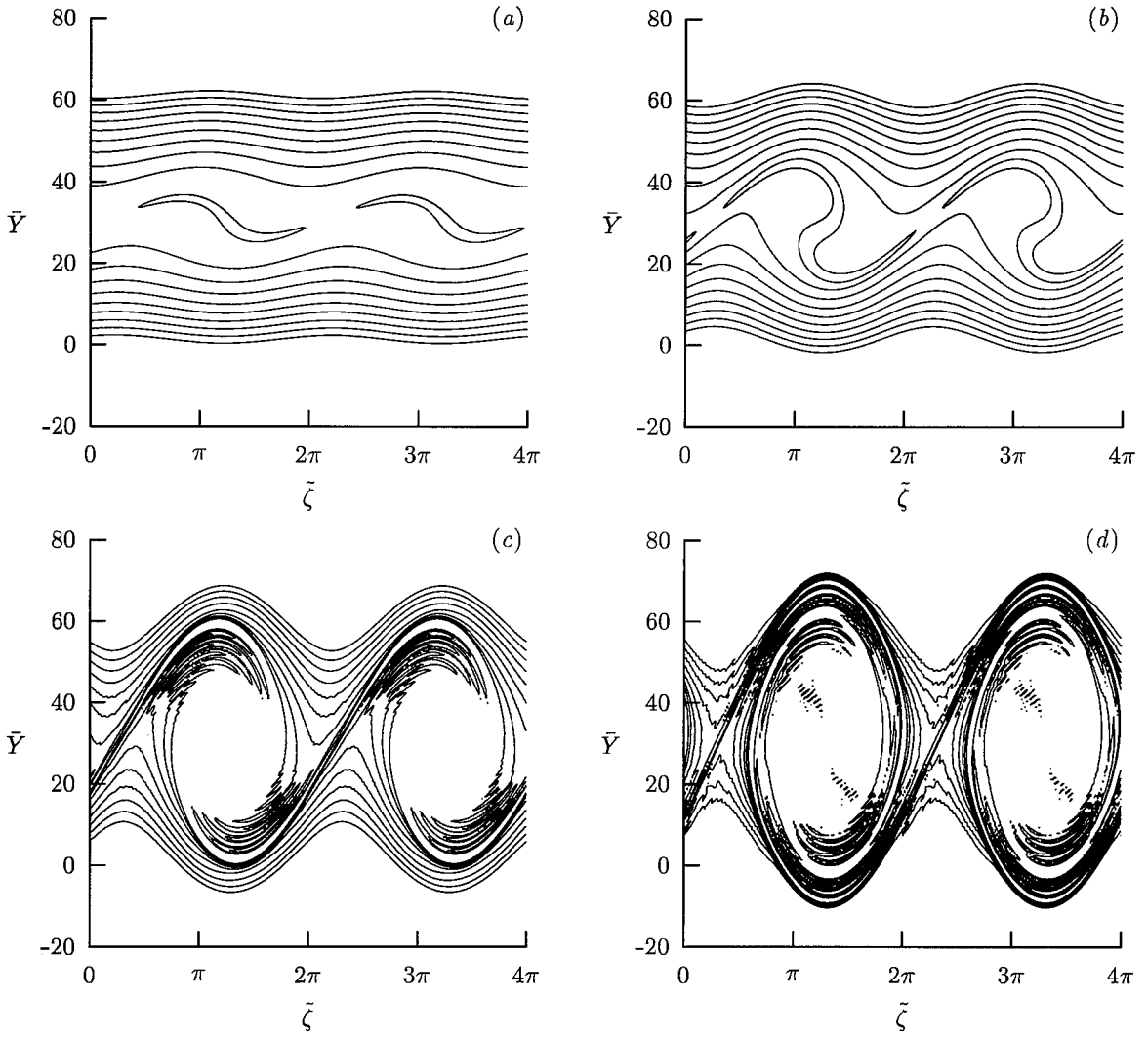


Figure 5.54: Vorticity contours in the $(\tilde{\zeta}, \bar{Y})$-plane for $\beta_T = 1$, $M = 3.96$, $\widehat{\Lambda} = 0.1$ and contour levels 0, 100, 200, ..., 800 and 900: (a) $\bar{\kappa}_{\mathrm{T}}\bar{\mathcal{X}} + \ln(\alpha^2) = -1.350$; (b) $\bar{\kappa}_{\mathrm{T}}\bar{\mathcal{X}} + \ln(\alpha^2) = -0.158$; (c) $\bar{\kappa}_{\mathrm{T}}\bar{\mathcal{X}} + \ln(\alpha^2) = 1.034$; (d) $\bar{\kappa}_{\mathrm{T}}\bar{\mathcal{X}} + \ln(\alpha^2) = 2.225$. (Contour level 0 is omitted from plot (c), contour levels 0 & 100 are omitted from plot (d).)

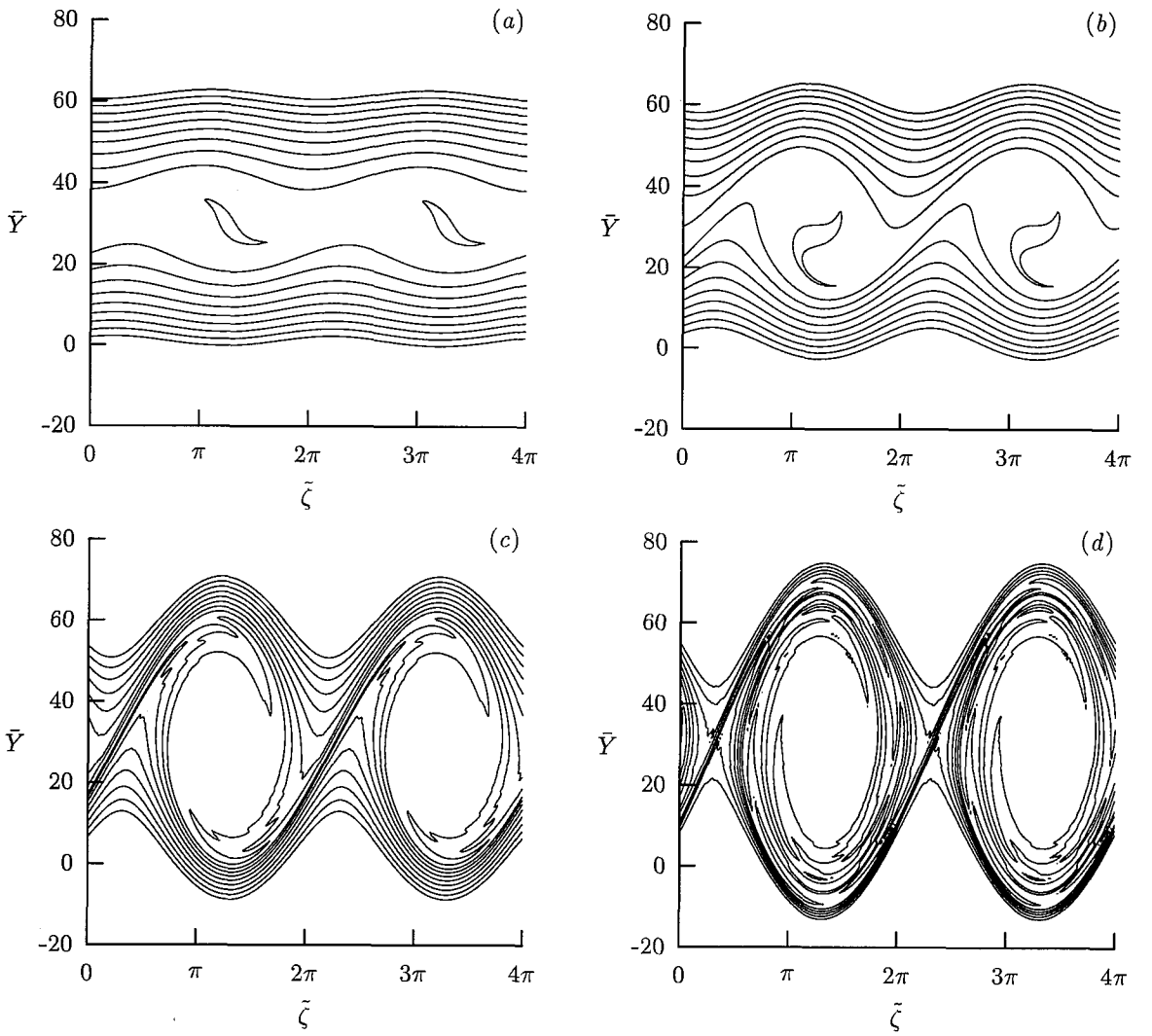


Figure 5.55: Temperature contours in the $(\tilde{\zeta}, \bar{Y})$-plane for $\beta_T = 1$, $M = 3.96$, $\widehat{\Lambda} = 0.1$ and contour levels -180, -160, -140, ..., -20 and 0: (*a*) $\bar{\kappa}_{\rm T}\bar{\mathcal{X}} + \ln(\alpha^2) = -1.350$; (*b*) $\bar{\kappa}_{\rm T}\bar{\mathcal{X}} + \ln(\alpha^2) = -0.158$; (*c*) $\bar{\kappa}_{\rm T}\bar{\mathcal{X}} + \ln(\alpha^2) = 1.034$; (*d*) $\bar{\kappa}_{\rm T}\bar{\mathcal{X}} + \ln(\alpha^2) = 2.225$. (Contour level 0 is omitted from plots (*c*) & (*d*).)

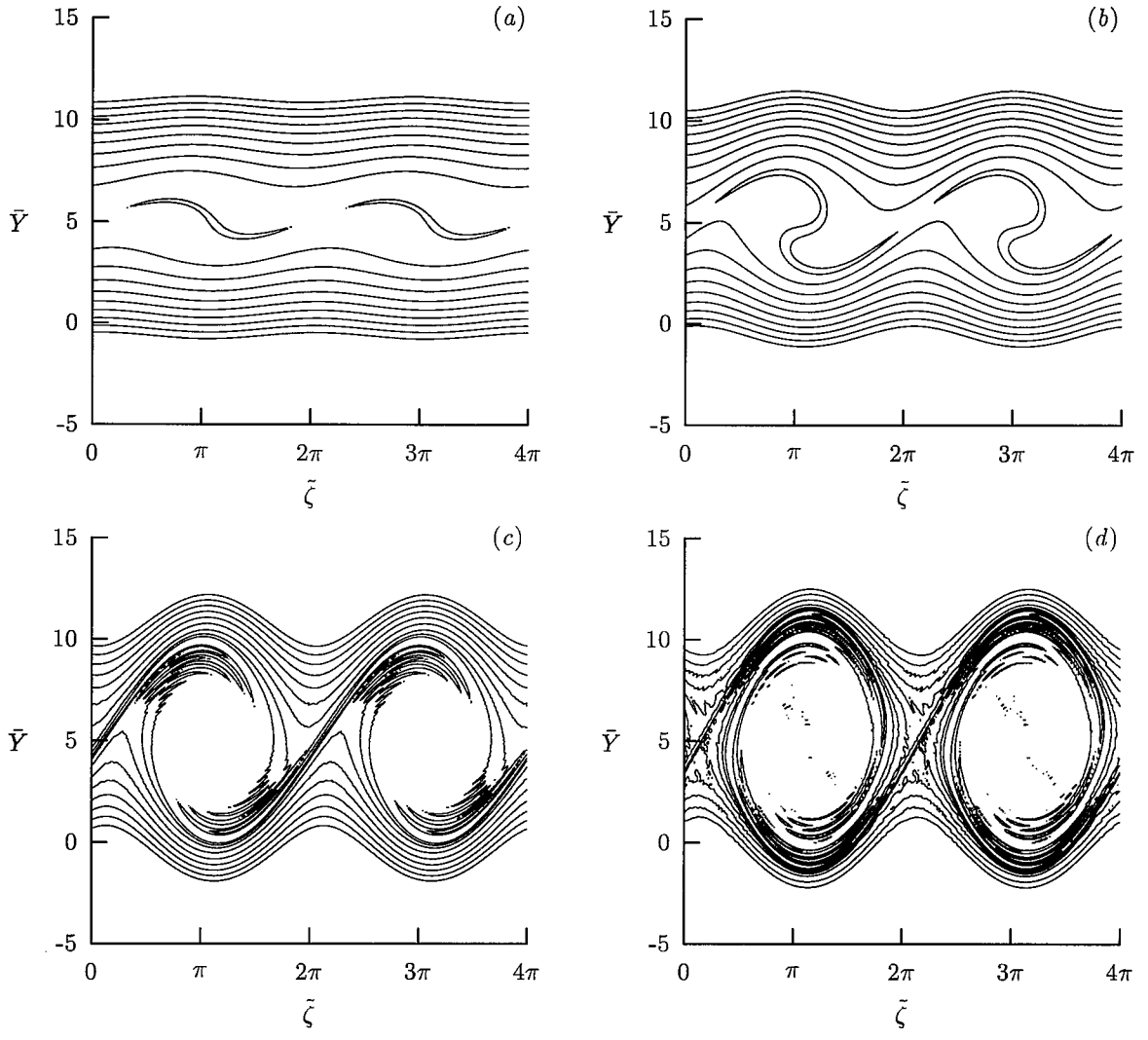


Figure 5.56: Vorticity contours in the $(\tilde{\zeta}, \bar{Y})$-plane for $\beta_T = 1$, $M = 3$, $\widehat{\Lambda} = 0.001$ and contour levels 0, 3.75, 7.5, ..., 30 and 33.75: (a) $\bar{\kappa}_{\mathrm{T}}\bar{\mathcal{X}} + \ln(\alpha^2) = -1.325$; (b) $\bar{\kappa}_{\mathrm{T}}\bar{\mathcal{X}} + \ln(\alpha^2) = -0.101$; (c) $\bar{\kappa}_{\mathrm{T}}\bar{\mathcal{X}} + \ln(\alpha^2) = 1.123$; (d) $\bar{\kappa}_{\mathrm{T}}\bar{\mathcal{X}} + \ln(\alpha^2) = 2.347$. (Contour level 0 is omitted from plot (c), contour levels 0 & 3.75 are omitted from plot (d).)

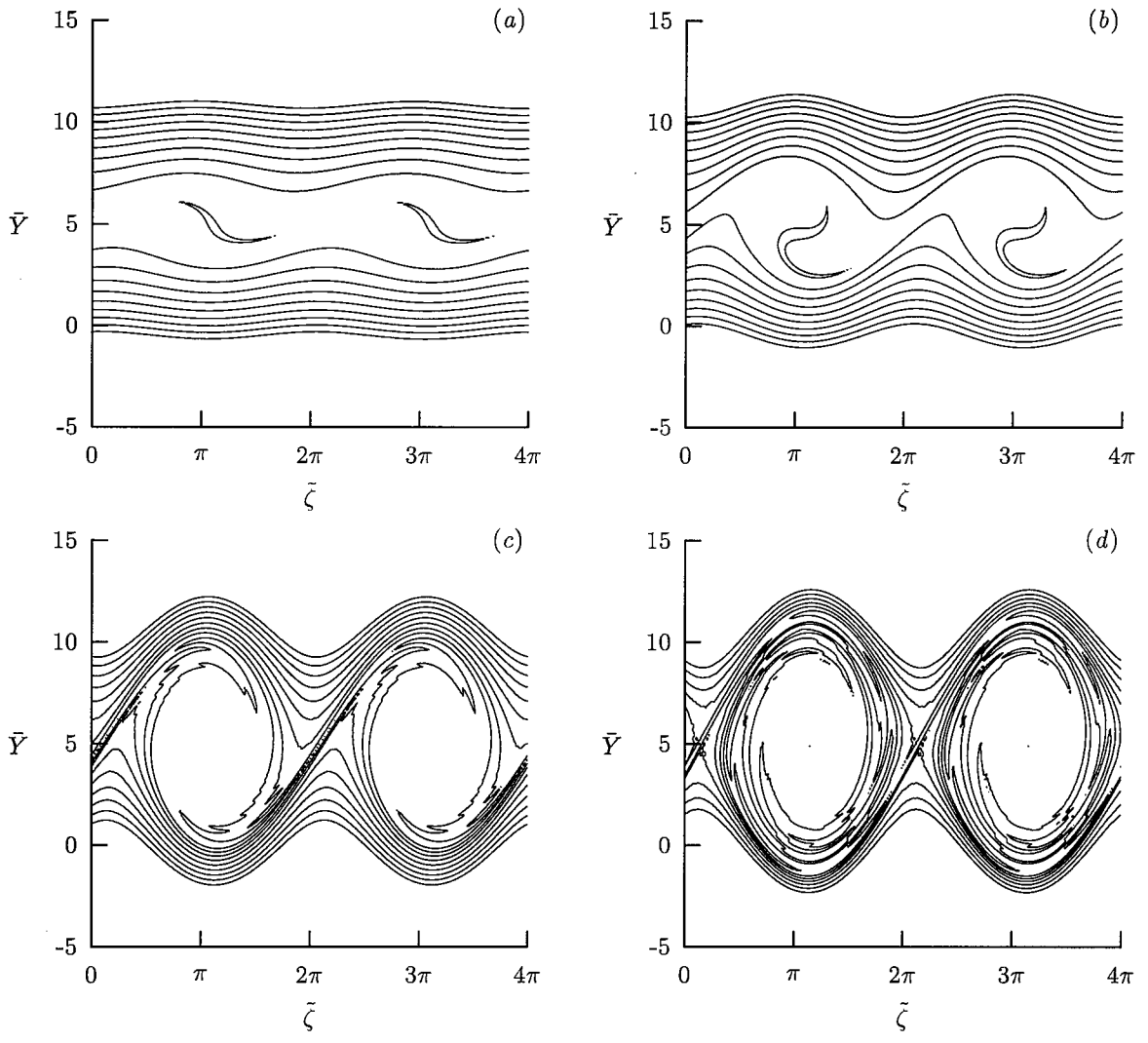


Figure 5.57: Temperature contours in the $(\tilde{\zeta}, \bar{Y})$-plane for $\beta_T = 1$, $M = 3$, $\widehat{\Lambda} = 0.001$ and contour levels -3.6, -3.2, -2.8, ..., -0.4 and 0: (a) $\bar{\kappa}_{\mathrm{r}}\bar{\mathcal{X}} + \ln(\alpha^2) = -1.325$; (b) $\bar{\kappa}_{\mathrm{r}}\bar{\mathcal{X}} + \ln(\alpha^2) = -0.101$; (c) $\bar{\kappa}_{\mathrm{r}}\bar{\mathcal{X}} + \ln(\alpha^2) = 1.123$; (d) $\bar{\kappa}_{\mathrm{r}}\bar{\mathcal{X}} + \ln(\alpha^2) = 2.347$. (Contour level 0 is omitted from plots (c) & (d).)

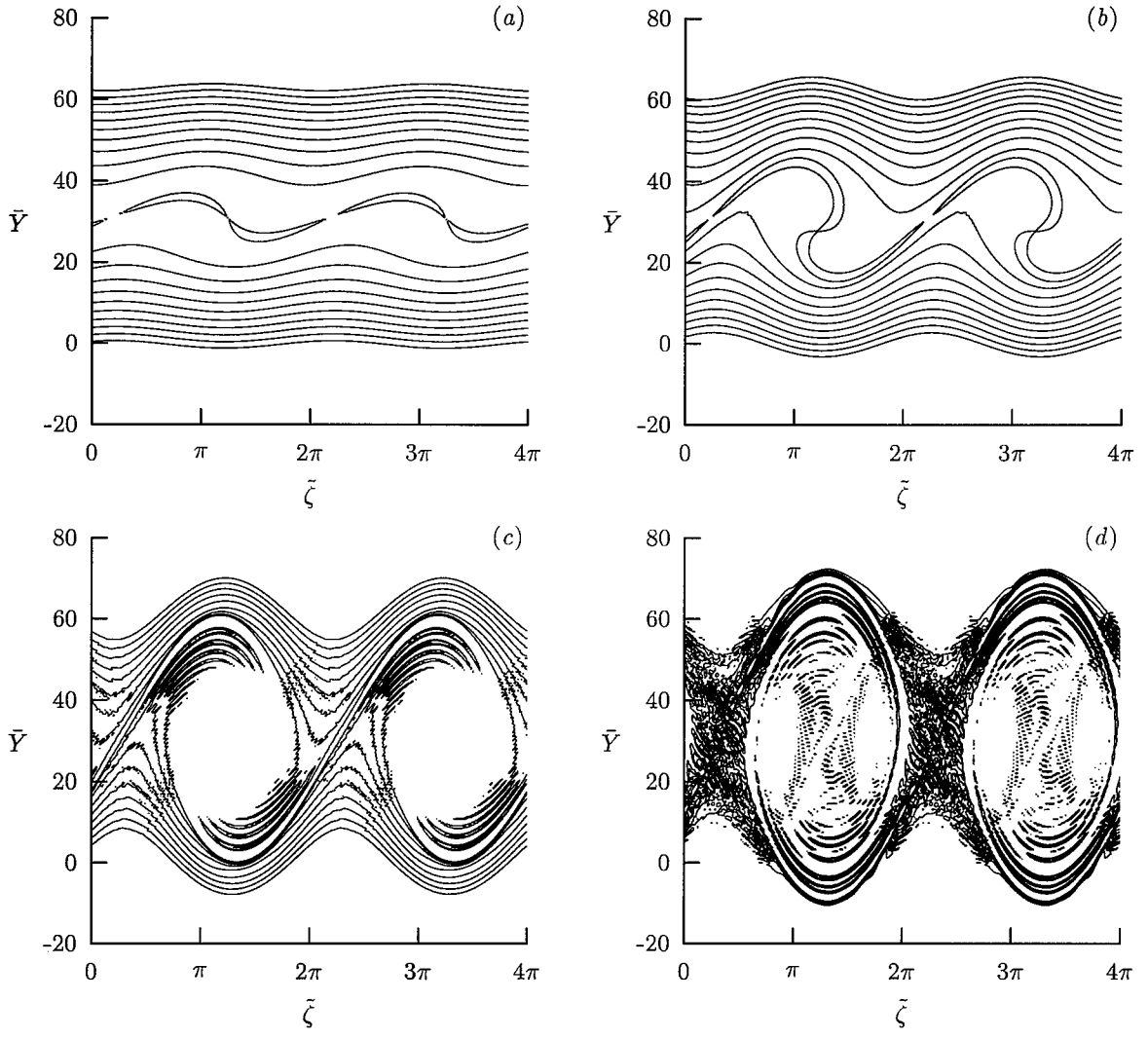


Figure 5.58: Vorticity contours in the $(\tilde{\zeta}, \bar{Y})$-plane for $\beta_T = 1$, $M = 3.96$, $\widehat{\Lambda} = 0.001$ and contour levels 0, 100, 200, ..., 900 and 1000: (a) $\bar{\kappa}_r\bar{\mathcal{X}} + \ln(\alpha^2) = -1.350$; (b) $\bar{\kappa}_r\bar{\mathcal{X}} + \ln(\alpha^2) = -0.158$; (c) $\bar{\kappa}_r\bar{\mathcal{X}} + \ln(\alpha^2) = 1.034$; (d) $\bar{\kappa}_r\bar{\mathcal{X}} + \ln(\alpha^2) = 2.225$. (Contour levels 0 & 100 are omitted from plot (c), contour levels 0, 100, 200 & 300 are omitted from plot (d).)

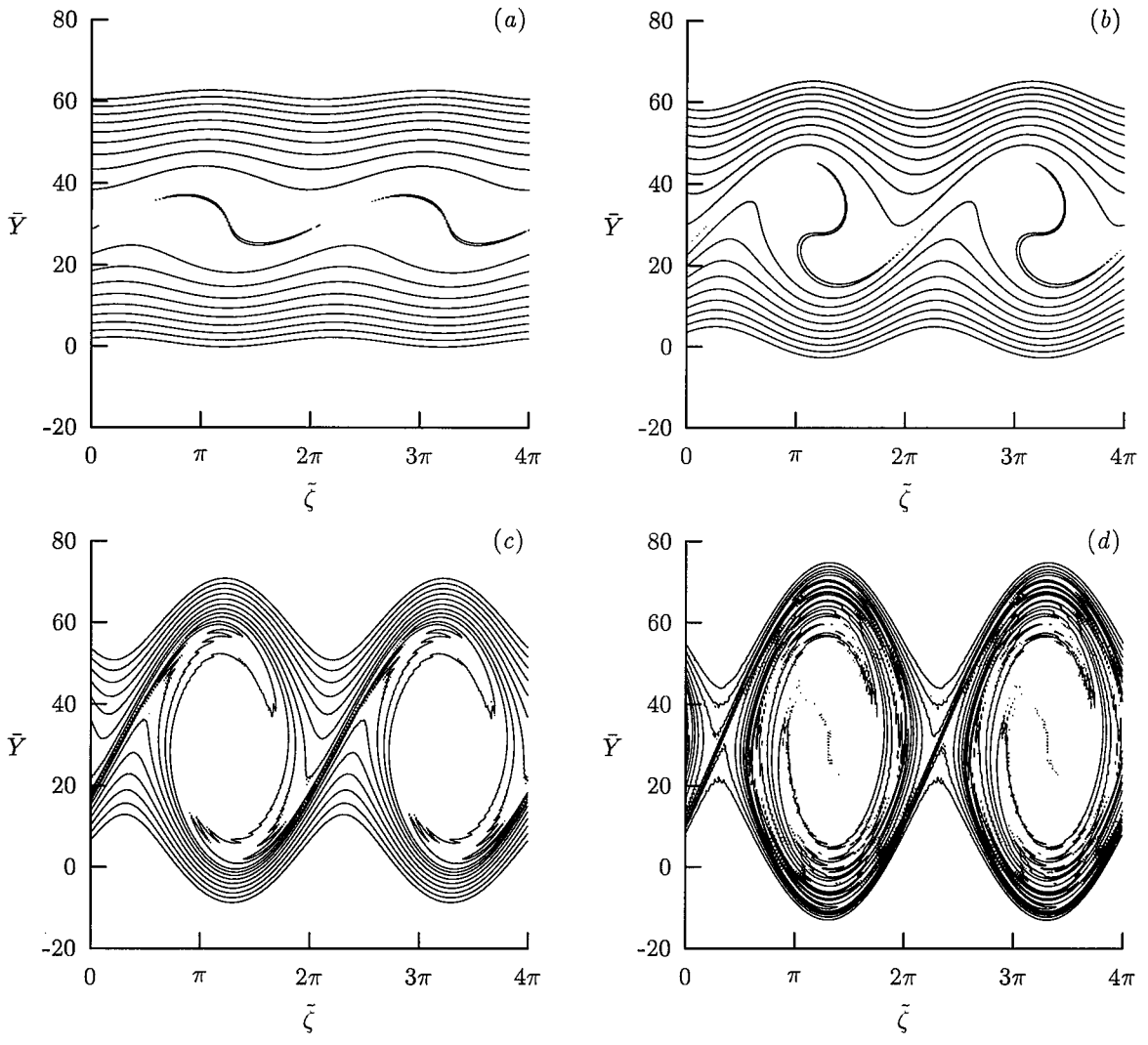


Figure 5.59: Temperature contours in the $(\tilde{\zeta}, \bar{Y})$-plane for $\beta_T = 1$, $M = 3.96$, $\widehat{\Lambda} = 0.001$ and contour levels -180, -160, -140, ..., -20 and 0: (*a*) $\bar{\kappa}_{\rm r}\bar{\mathcal{X}} + \ln(\alpha^2) = -1.350$; (*b*) $\bar{\kappa}_{\rm r}\bar{\mathcal{X}} + \ln(\alpha^2) = -0.158$; (*c*) $\bar{\kappa}_{\rm r}\bar{\mathcal{X}} + \ln(\alpha^2) = 1.034$; (*d*) $\bar{\kappa}_{\rm r}\bar{\mathcal{X}} + \ln(\alpha^2) = 2.225$. (Contour level 0 is omitted from plots (*c*) & (*d*).)

Vorticity and temperature contours are shown in figures 5.70 & 5.71 for $\beta_T = 2$, $M = 4.06$ and $\widehat{\Lambda} = 0.1$. Roll-up and mixing are again present, and the shape of the contours is almost identical to the nearly incompressible case (figures 5.45 & 5.46). Thus it appears that mixing layer dynamics behaves more or less the same as in the nearly incompressible case when β_T is sufficiently different from unity.

We again assess whether the term involving T_c'' appearing in equations (4.3.29) & (4.3.30) is responsible for the change in amplitude behaviour for large Mach numbers. Figure 5.72 shows the results for $\beta_T = 1/2$ and $\widehat{\Lambda} = 10$. We see that inclusion of the term T_c'' in the evolution equations has very little effect for all Mach numbers, in contrast to the $\beta_T = 1$ case. This is not surprising since in the present instance $\bar{\mathcal{M}}^2 \approx 1.41$, $\sigma \approx -0.0367$ and so $\bar{\mathcal{M}}^2 \gg |\sigma|$.

5.6 Effect of β_U

In this section, we briefly examine the effect of the parameter β_U, which has so far been assumed the value of $1/2$, i.e. the slow stream moving at half the speed of the fast stream. The value $1/2$ has been chosen for three reasons. Firstly, mixing layer studies are primarily of interest for those developing high-speed propulsion systems such as scramjet engines. In such systems we must have $\beta_U \geqslant 0$, and moreover $\beta_U \gg 0$, since otherwise burnt gases will remain in the combustion chamber. Secondly, we must avoid parameter space for which the flow is absolutely unstable, since we are considering spatial instability. It is intuitively expected that a sufficiently negative $-1 < \beta_U < 0$ may cause an absolutely unstable flow, however this can occur even for $\beta_U > 0$ if $0 < \beta_T \ll 1$ (Pavithran & Redekopp 1989). Presently, we have assumed that $1/2 < \beta_T < 2$, so that for $\beta_U \geqslant 0$, we expect convective instability. Finally, for values of β_U too close to 1, the flow confiiguration is more like a wake than a mixing layer.

Appendix B shows that the effect of β_U enters through $f(\beta_U) = (1+\beta_U)/(1-\beta_U)$. Figure 5.73 shows $\beta_T = 1$ results for $\beta_U = 0$ ($f(\beta_U) = 1$) and $\beta_U = 1/2$ ($f(\beta_U) = 3$) for two different $\widehat{\Lambda}$. It is seen that β_U has little qualitative effect, however a reduction of β_U (i.e. an increase in shear strength) does cause the amplitude to reach a much larger magnitude. Vorticity contours are shown in figure 5.74 for $\widehat{\Lambda} = 0.1$. We see very little difference between these contours and those of figure 5.25 (for $\beta_U = 1/2$).

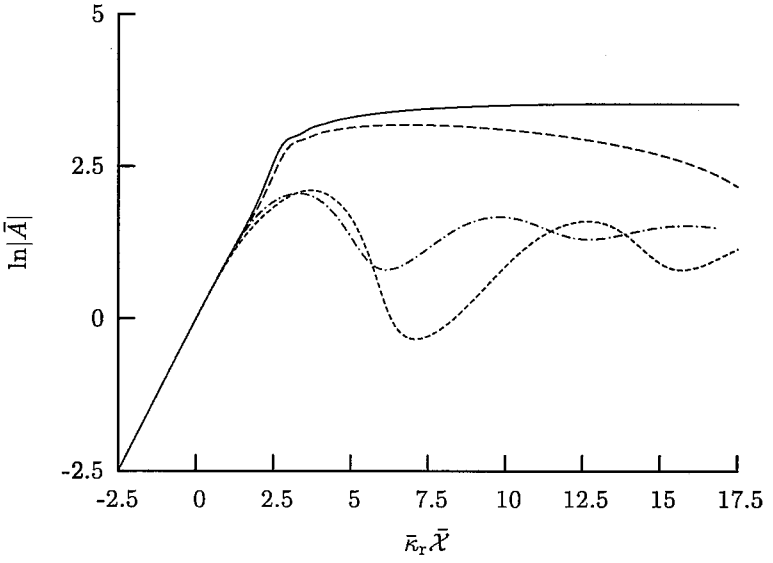


Figure 5.60: Amplitude $\ln|\bar{A}|$ *vs.* $\bar{\kappa}_r\bar{\mathcal{X}}$ for $\beta_T = 1/2$, $\widehat{\Lambda} = 10$ and $M = 1/10$ (solid), 1 (long-dashed), 2 (short-dashed), 2.87 (dash-dotted).

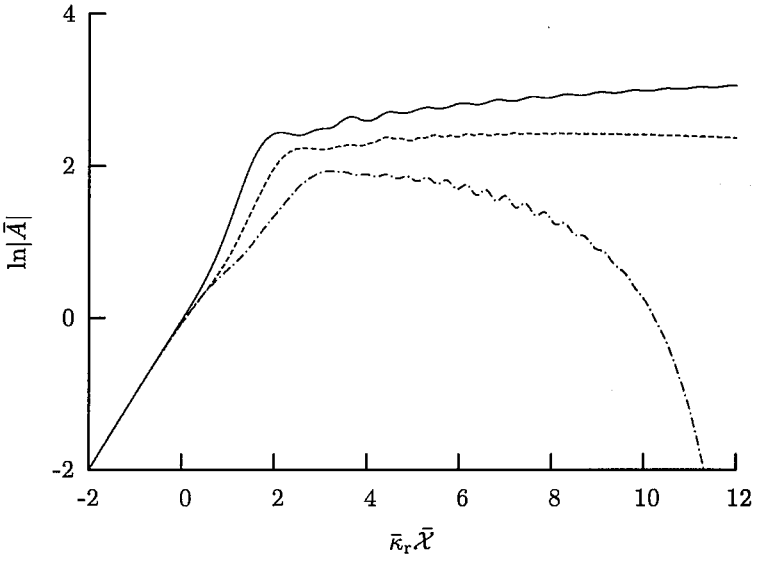


Figure 5.61: Amplitude $\ln|\bar{A}|$ *vs.* $\bar{\kappa}_r\bar{\mathcal{X}}$ for $\beta_T = 1/2$, $\widehat{\Lambda} = 1$ and $M = 1/10$ (solid), 2 (dashed), 2.87 (dash-dotted).

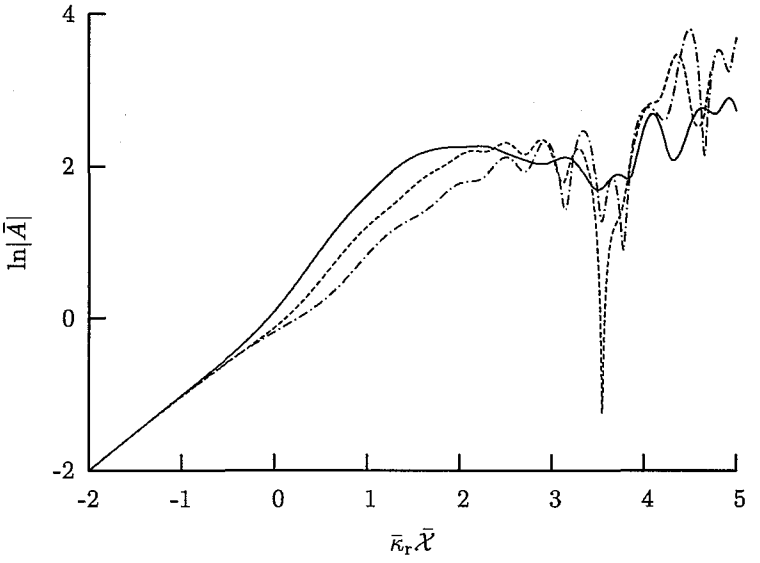


Figure 5.62: Amplitude $\ln|\bar{A}|$ *vs.* $\bar{\kappa}_r\bar{\mathcal{X}}$ for $\beta_T = 1/2$, $\widehat{\Lambda} = 0.1$ and $M = 1/10$ (solid), 2 (dashed), 2.87 (dash-dotted).

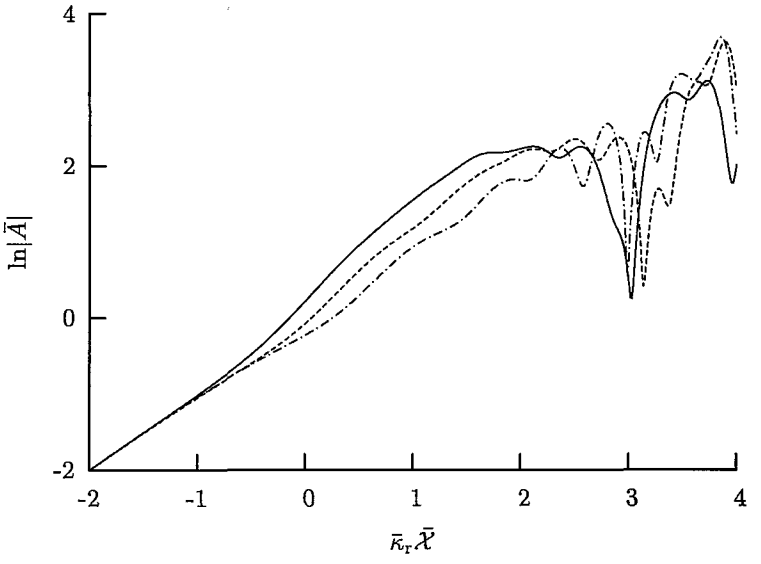


Figure 5.63: Amplitude $\ln|\bar{A}|$ *vs.* $\bar{\kappa}_r\bar{\mathcal{X}}$ for $\beta_T = 1/2$, $\widehat{\Lambda} = 0.001$ and $M = 1/10$ (solid), 2 (dashed), 2.87 (dash-dotted).

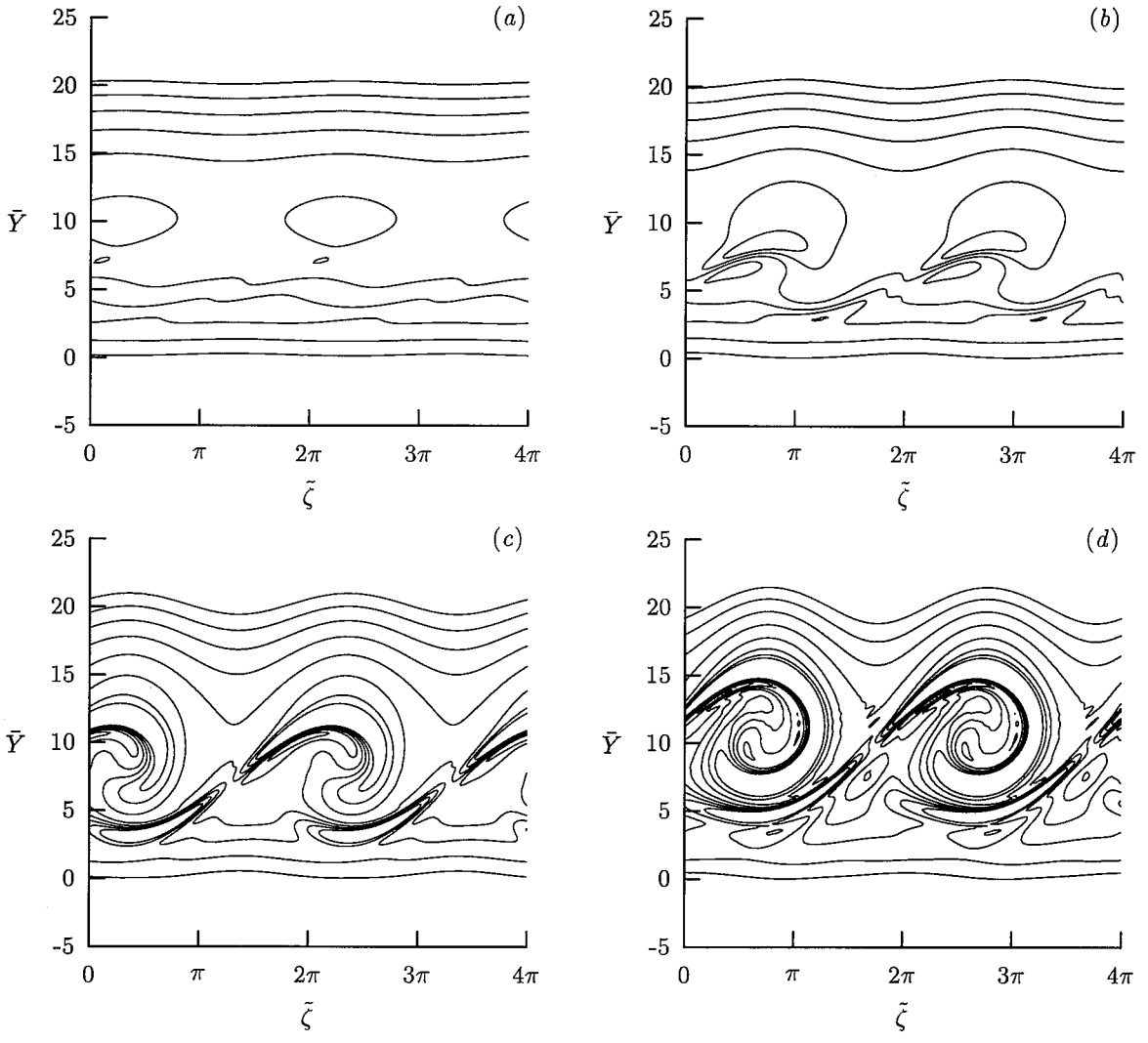


Figure 5.64: Vorticity contours in the $(\tilde{\zeta}, \bar{Y})$-plane for $\beta_T = 1/2$, $M = 2.87$, $\widehat{\Lambda} = 0.1$ and contour levels -40, -20, 0, $\ldots$, 80 and 100: (a) $\bar{\kappa}_{\mathrm{r}}\bar{\mathcal{X}} = 0.451$; (b) $\bar{\kappa}_{\mathrm{r}}\bar{\mathcal{X}} = 1.352$; (c) $\bar{\kappa}_{\mathrm{r}}\bar{\mathcal{X}} = 2.254$; (d) $\bar{\kappa}_{\mathrm{r}}\bar{\mathcal{X}} = 3.156$.

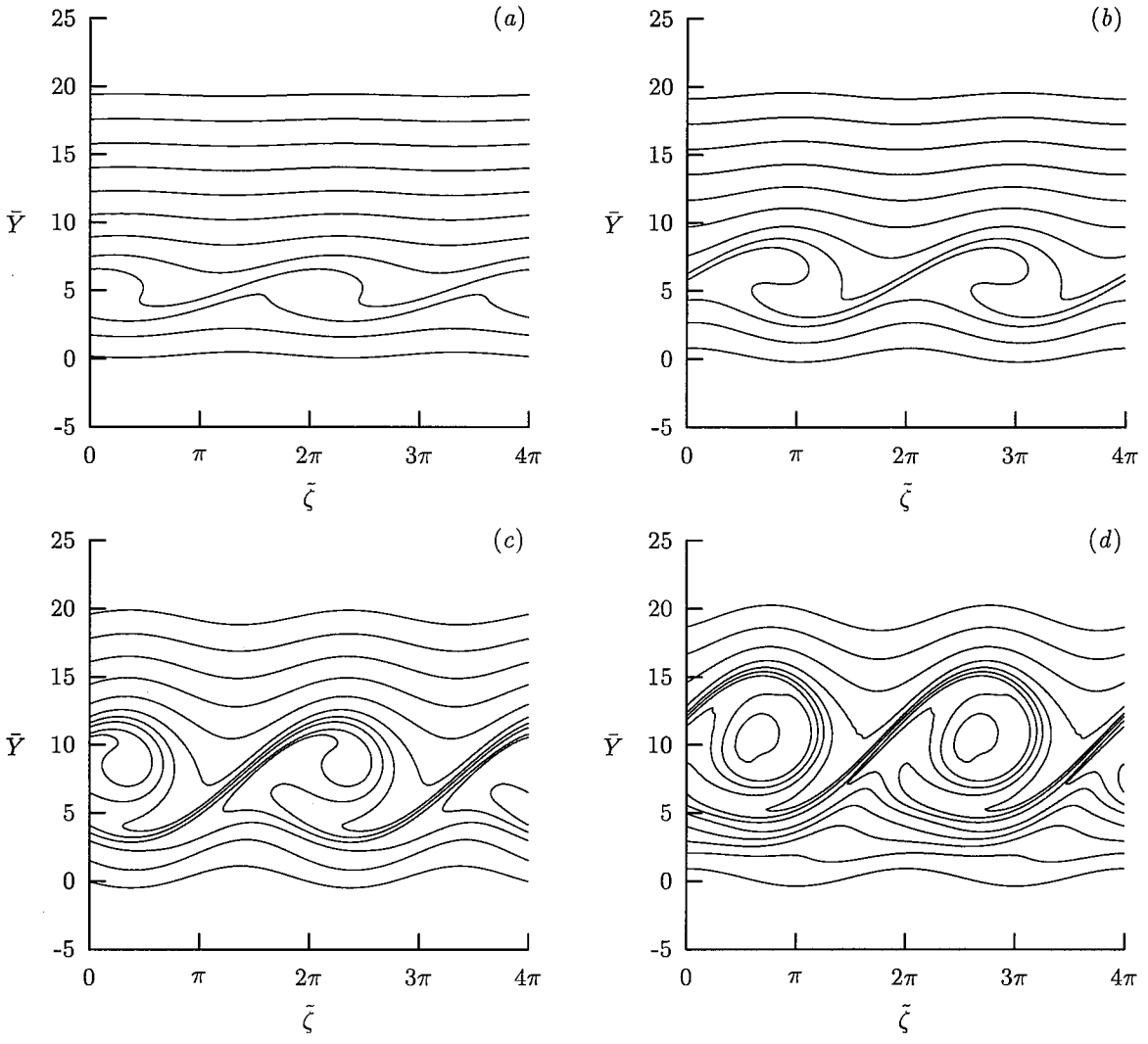


Figure 5.65: Temperature contours in the $(\tilde{\zeta}, \bar{Y})$-plane for $\beta_T = 1/2$, $M = 2.87$, $\widehat{\Lambda} = 0.1$ and contour levels -1020, -1000, -980, $\ldots$, -820 and -800: (a) $\bar{\kappa}_{\mathrm{T}}\bar{\mathcal{X}} = 0.451$; (b) $\bar{\kappa}_{\mathrm{T}}\bar{\mathcal{X}} = 1.352$; (c) $\bar{\kappa}_{\mathrm{T}}\bar{\mathcal{X}} = 2.254$; (d) $\bar{\kappa}_{\mathrm{T}}\bar{\mathcal{X}} = 3.156$.

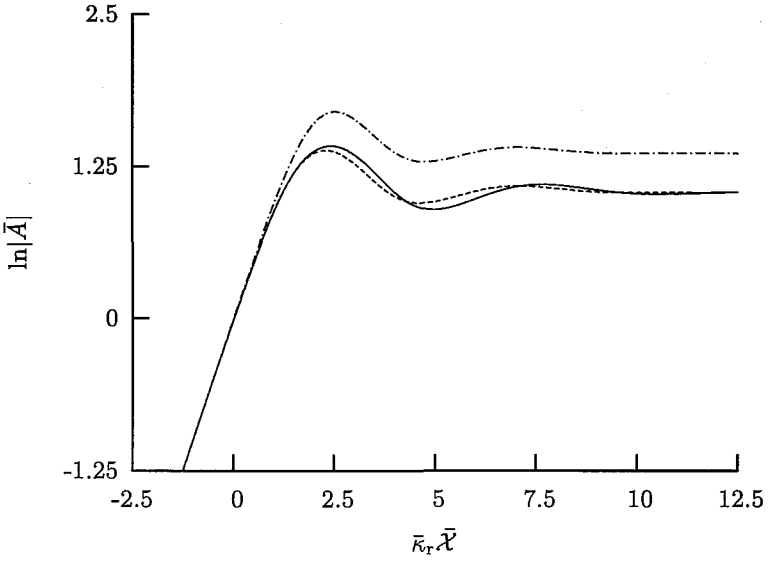


Figure 5.66: Amplitude $\ln|\bar{A}|$ *vs.* $\bar{\kappa}_r\bar{\mathcal{X}}$ for $\beta_T = 2$, $\widehat{\Lambda} = 10$ and $M = 1/10$ (solid), 2 (dashed), 4.06 (dash-dotted).

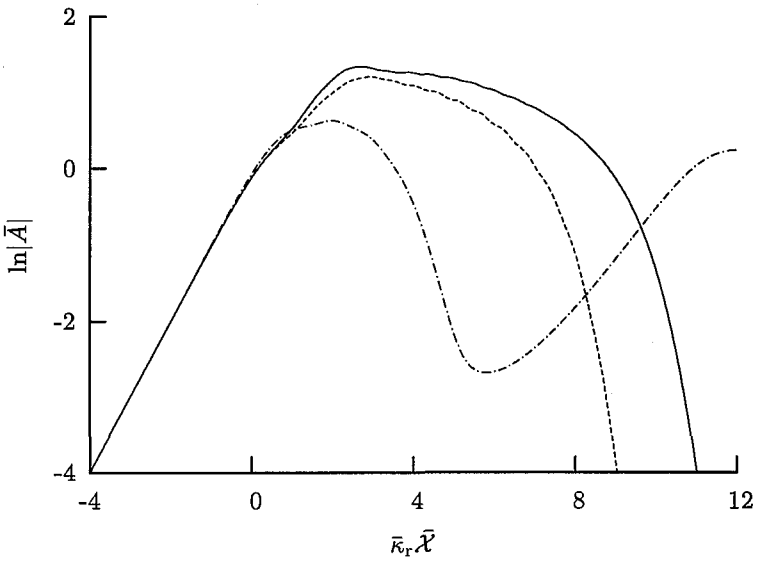


Figure 5.67: Amplitude $\ln|\bar{A}|$ *vs.* $\bar{\kappa}_r\bar{\mathcal{X}}$ for $\beta_T = 2$, $\widehat{\Lambda} = 1$ and $M = 1/10$ (solid), 2 (dashed), 4.06 (dash-dotted).

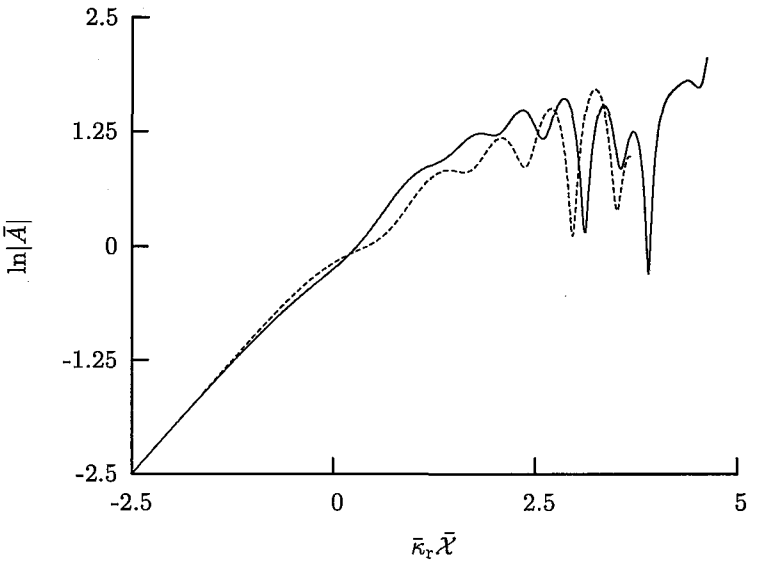


Figure 5.68: Amplitude $\ln|\bar{A}|$ *vs.* $\bar{\kappa}_r\bar{\mathcal{X}}$ for $\beta_T = 2$, $\widehat{\Lambda} = 0.1$ and $M = 1/10$ (solid), 4.06 (dashed).

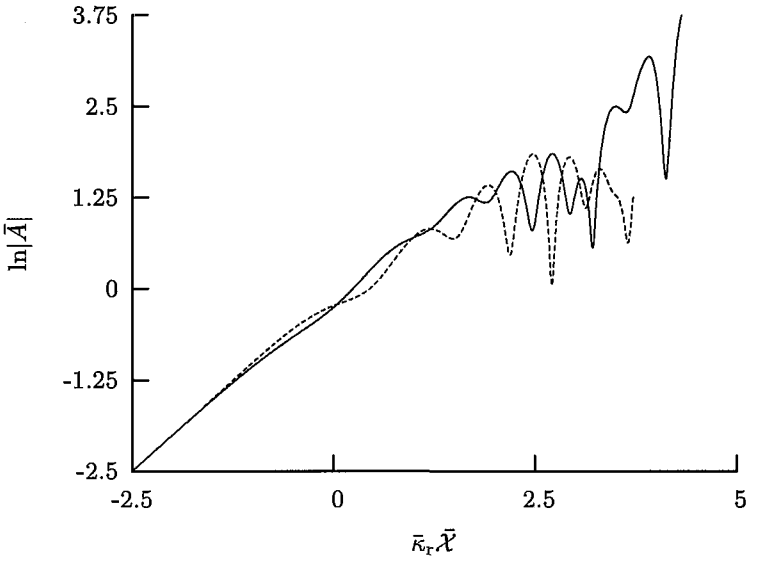


Figure 5.69: Amplitude $\ln|\bar{A}|$ *vs.* $\bar{\kappa}_r\bar{\mathcal{X}}$ for $\beta_T = 2$, $\widehat{\Lambda} = 0.001$ and $M = 1/10$ (solid), 4.06 (dashed).

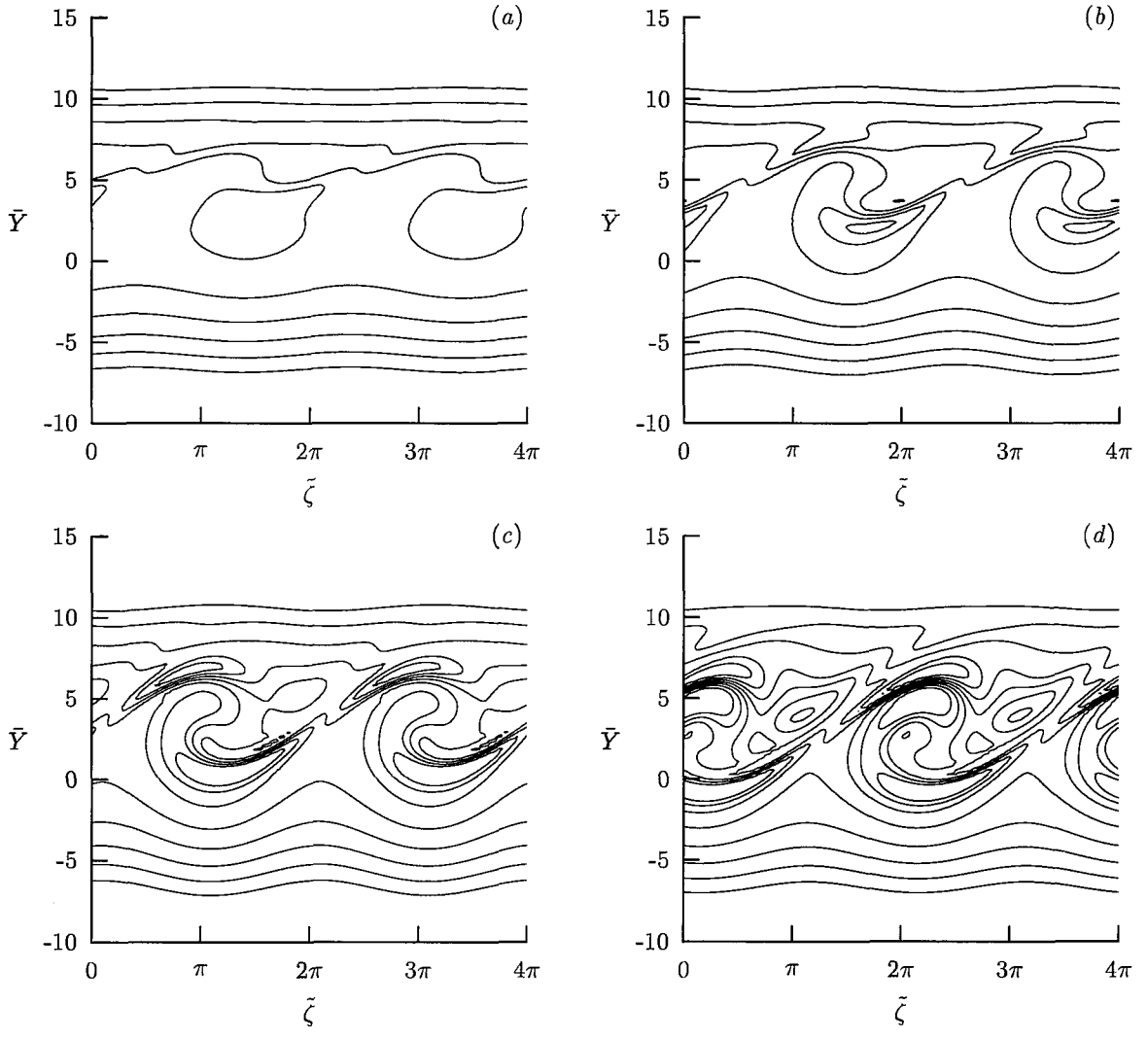


Figure 5.70: Vorticity contours in the $(\tilde{\zeta}, \bar{Y})$-plane for $\beta_T = 2$, $M = 4.06$, $\widehat{\Lambda} = 0.1$ and contour levels -30, -15, 0, $\ldots$, 60 and 75: (a) $\bar{\kappa}_{\mathrm{r}}\bar{\mathcal{X}} = 0.841$; (b) $\bar{\kappa}_{\mathrm{r}}\bar{\mathcal{X}} = 1.682$; (c) $\bar{\kappa}_{\mathrm{r}}\bar{\mathcal{X}} = 2.523$; (d) $\bar{\kappa}_{\mathrm{r}}\bar{\mathcal{X}} = 3.363$.

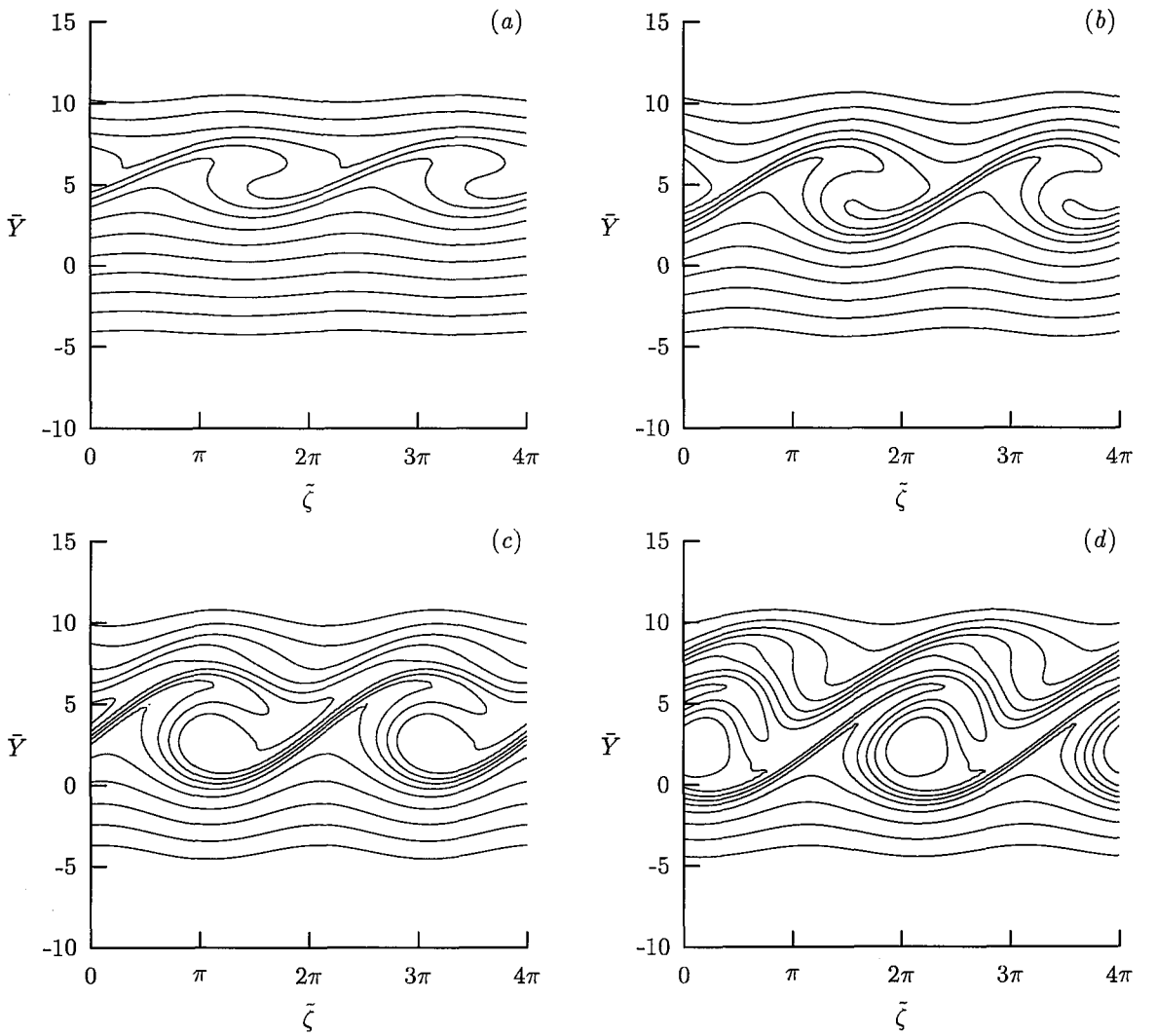


Figure 5.71: Temperature contours in the $(\tilde{\zeta}, \bar{Y})$-plane for $\beta_T = 2$, $M = 4.06$, $\widehat{\Lambda} = 0.1$ and contour levels -620, -610, -600, ..., -500 and -490: (*a*) $\bar{\kappa}_{\rm r}\bar{\mathcal{X}} = 0.841$; (*b*) $\bar{\kappa}_{\rm r}\bar{\mathcal{X}} = 1.682$; (*c*) $\bar{\kappa}_{\rm r}\bar{\mathcal{X}} = 2.523$; (*d*) $\bar{\kappa}_{\rm r}\bar{\mathcal{X}} = 3.363$.

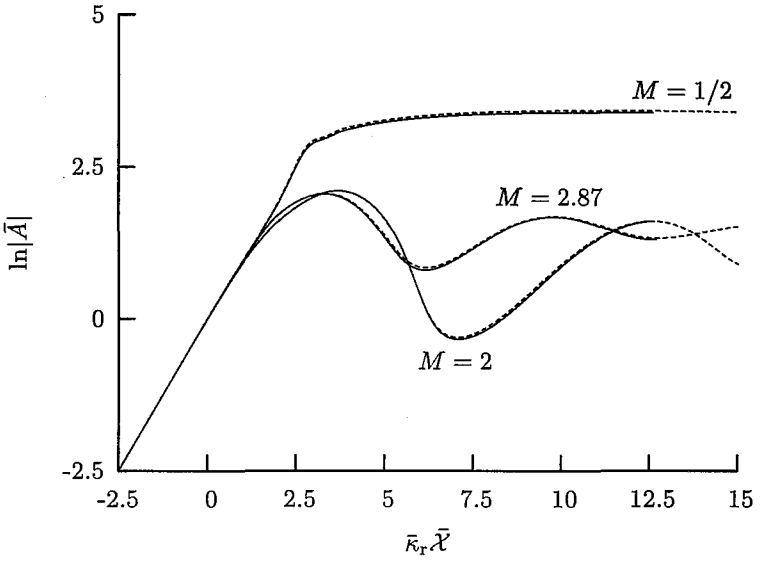


Figure 5.72: Amplitude $\ln|\bar{A}|$ *vs.* $\bar{\kappa}_r\bar{\mathcal{X}}$ for $\beta_T = 1/2$, $\widehat{\Lambda} = 10$ and various M: $T_c'' \neq 0$ (solid), $T_c'' = 0$ (dashed).

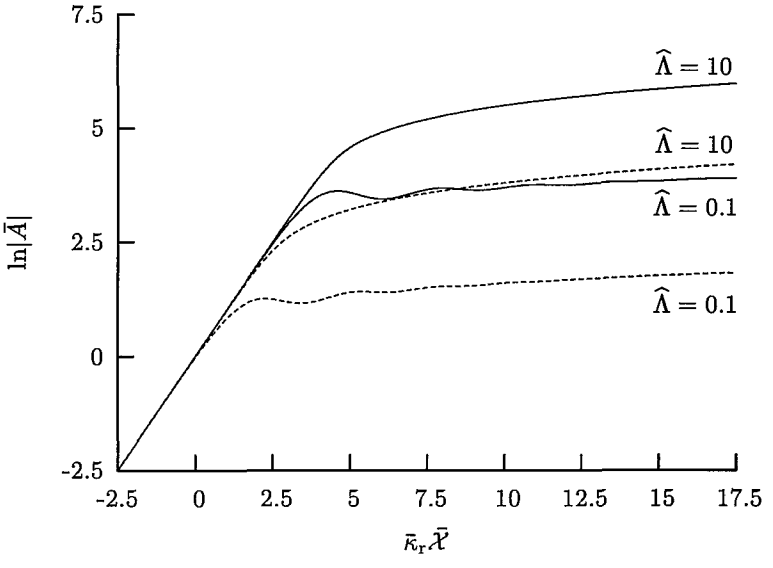


Figure 5.73: Amplitude $\ln|\bar{A}|$ *vs.* $\bar{\kappa}_r\bar{\mathcal{X}}$ for $\beta_T = 1$, $M = 1/10$ and $\beta_U = 0$ (solid), $1/2$ (dashed) for $\widehat{\Lambda} = 10$, 0.1.

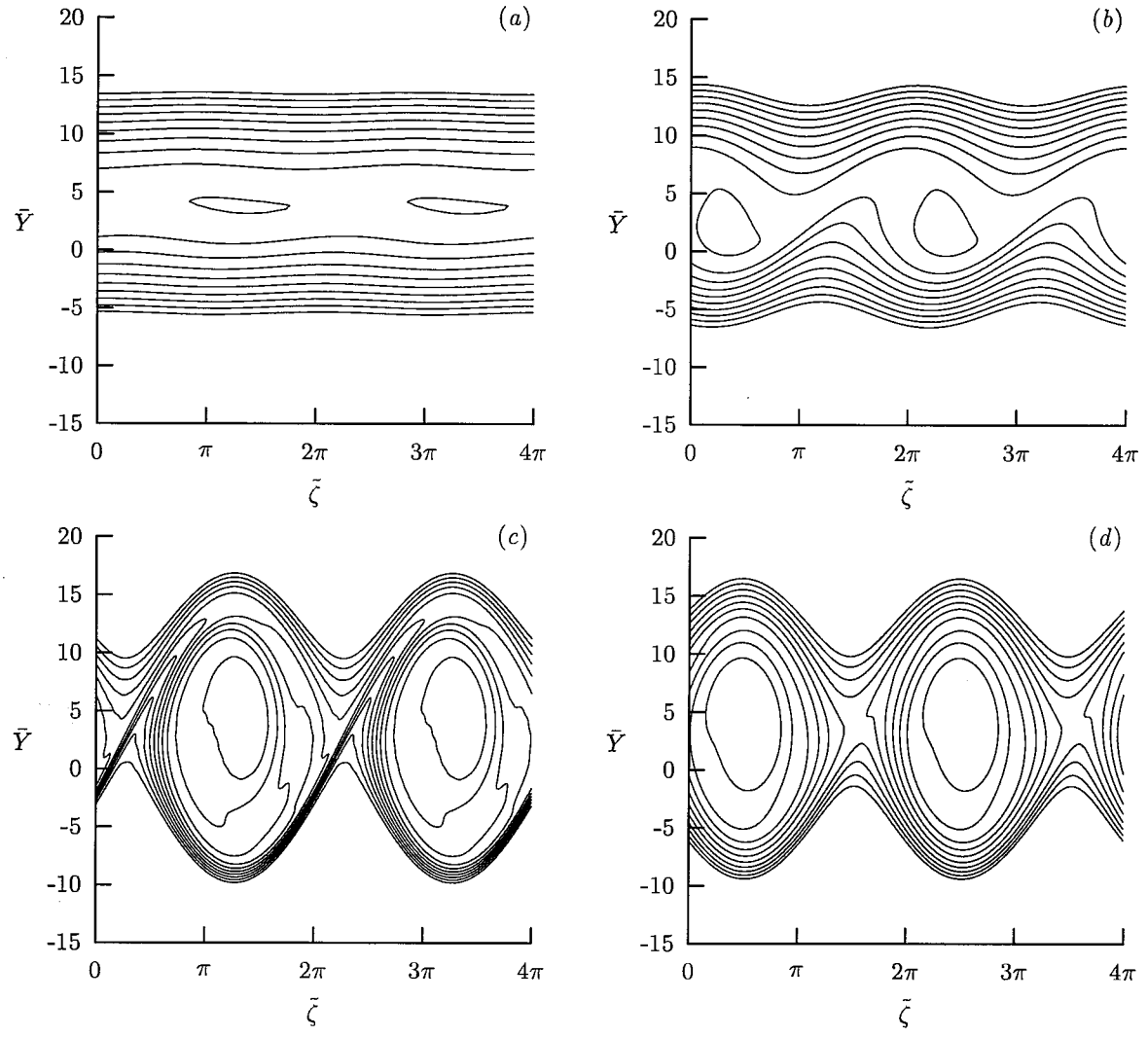


Figure 5.74: Vorticity contours in the $(\tilde{\zeta}, \bar{Y})$-plane for $\beta_U = 0$, $\beta_T = 1$, $M = 1/10$, $\widehat{\Lambda} = 0.1$ and contour levels 0, 10, 20, ..., 80 and 90: (a) $\bar{\kappa}_{\mathrm{r}}\bar{\mathcal{X}} = 0$; (b) $\bar{\kappa}_{\mathrm{r}}\bar{\mathcal{X}} = 2.264$; (c) $\bar{\kappa}_{\mathrm{r}}\bar{\mathcal{X}} = 4.528$; (d) $\bar{\kappa}_{\mathrm{r}}\bar{\mathcal{X}} = 6.792$.

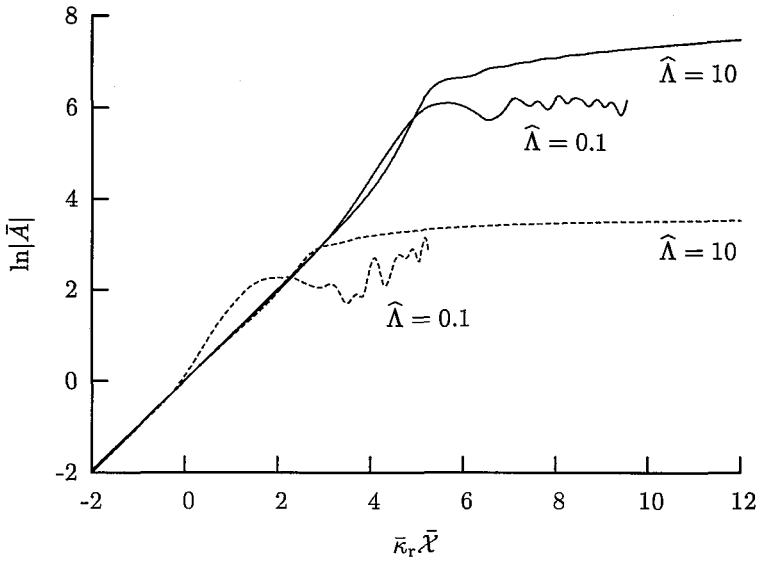


Figure 5.75: Amplitude $\ln|\bar{A}|$ *vs.* $\bar{\kappa}_r\bar{\mathcal{X}}$ for $\beta_T = 1/2$, $M = 1/10$ and $\beta_U = 0$ (solid), $1/2$ (dashed) for $\widehat{\Lambda} = 10$, 0.1.

Figure 5.75 shows $\beta_T = 1/2$ results for $\beta_U = 0$, $\beta_U = 1/2$ and two different $\widehat{\Lambda}$. As for the $\beta_T = 1$ case, β_U has little qualitative effect, but the amplitude reaches a much larger magnitude for smaller β_U. Vorticity contours are shown in figure 5.76 for $\widehat{\Lambda} = 0.1$. On comparing the contours with the $\beta_U = 1/2$ case (figure 5.34), we note that the difference caused by β_U is more appreciable than the comparison for $\beta_T = 1$.

5.7 Effect of base profile

In this section, we compare the results of three different models for the base profile. The first model is the tanh profile with Chapman viscosity law $\mu = T$. This model has been used exclusively in the previous sections, and will be called the Tanh model in this section. The second model is the Lock profile with Chapman viscosity law $\mu = T$, which we will call the Lock1 model. The third model uses the Lock profile with Sutherland viscosity law $\mu = 2T^{3/2}/(1+T)$. We will refer to this as the Lock2 model. Although the solution for the mean flow is not given by the Lock profile for a non-Chapman viscosity law, we nevertheless expect more accurate results by using a more accurate viscosity law. The Prandtl number is kept fixed at unity for

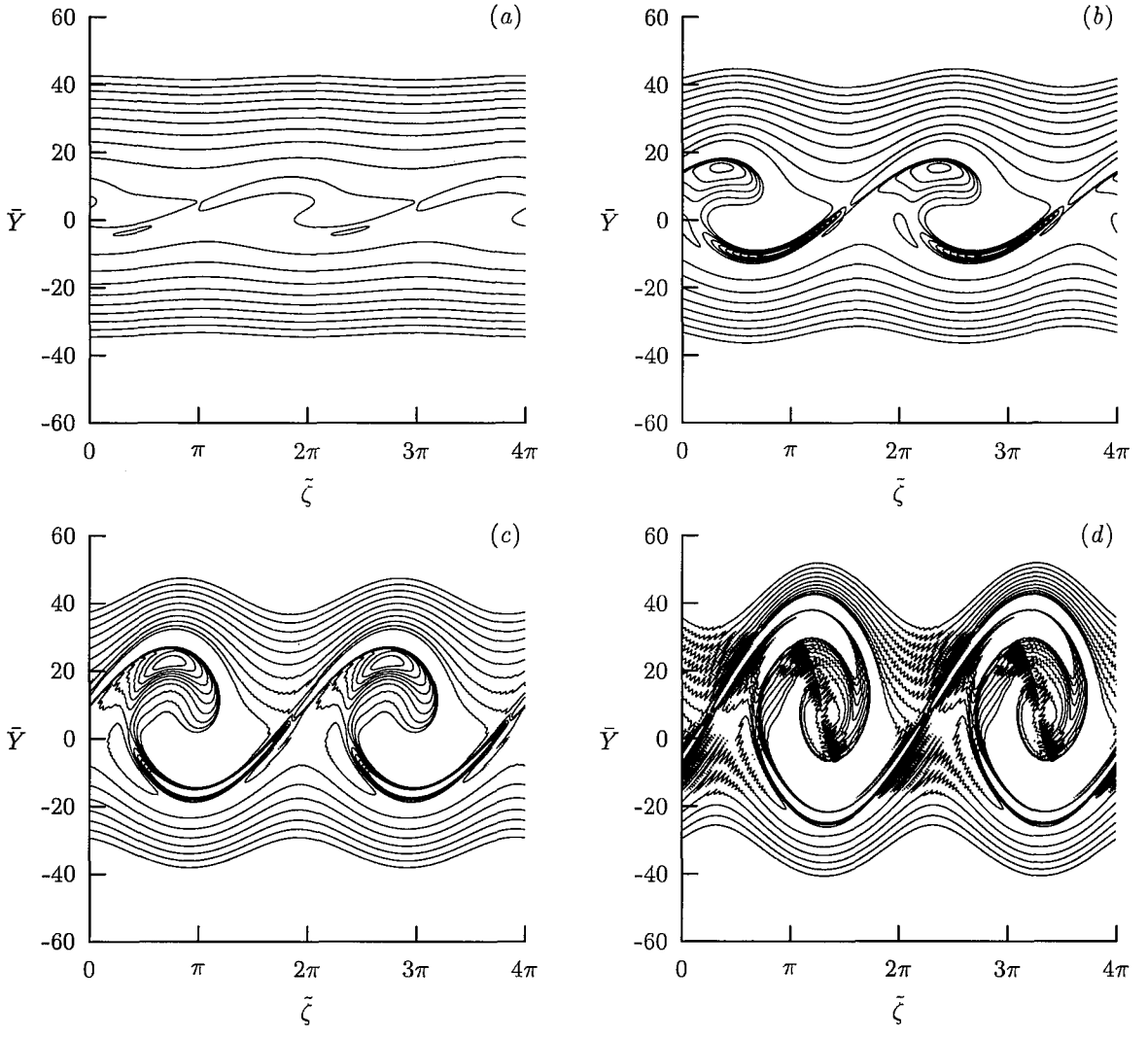


Figure 5.76: Vorticity contours in the $(\tilde{\zeta}, \bar{Y})$-plane for $\beta_U = 0$, $\beta_T = 1/2$, $M = 1/10$, $\widehat{\Lambda} = 0.1$ and contour levels 0, 160, 320, ..., 1280 and 1440: (a) $\bar{\kappa}_{\mathrm{r}}\bar{\mathcal{X}} = 2.956$; (b) $\bar{\kappa}_{\mathrm{r}}\bar{\mathcal{X}} = 3.942$; (c) $\bar{\kappa}_{\mathrm{r}}\bar{\mathcal{X}} = 4.336$; (d) $\bar{\kappa}_{\mathrm{r}}\bar{\mathcal{X}} = 4.730$.

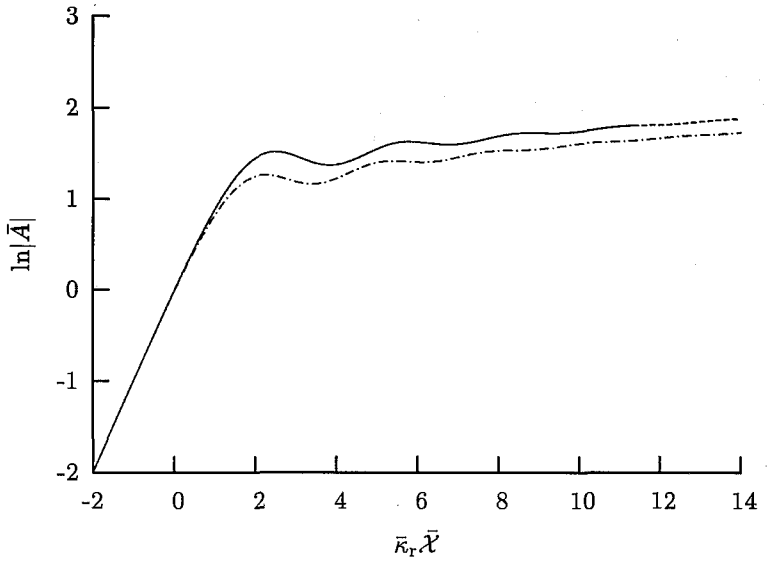


Figure 5.77: Amplitude $\ln|\bar{A}|$ *vs.* $\bar{\kappa}_r\bar{\mathcal{X}}$ for $\beta_U = 1/2$, $\beta_T = 1$, $M = 1/10$, $\hat{\omega} = 1/40$, $\widehat{\Lambda} = 0.1$: Tanh profile (dash-dotted), Lock1 profile (dashed), Lock2 profile (solid).

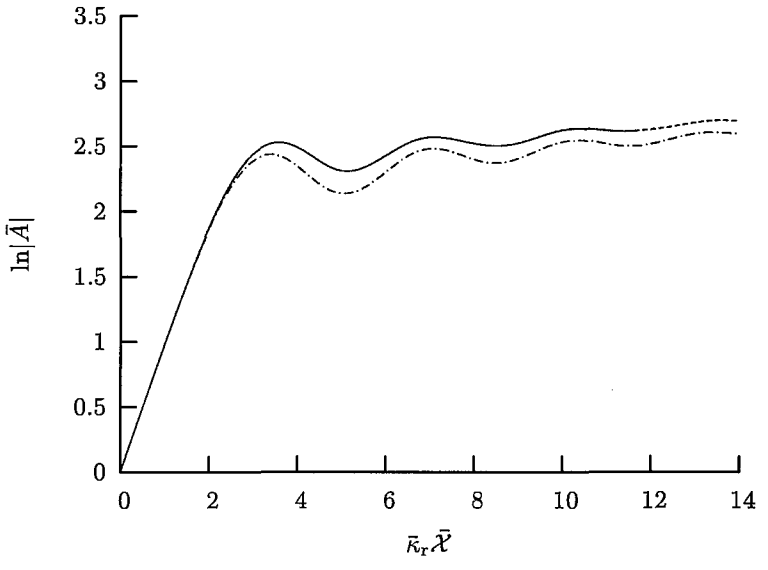


Figure 5.78: Amplitude $\ln|\bar{A}|$ *vs.* $\bar{\kappa}_r\bar{\mathcal{X}}$ for $\beta_U = 1/2$, $\beta_T = 1$, $M = 3$, $\hat{\omega} = 1/40$, $\widehat{\Lambda} = 0.1$: Tanh profile (dash-dotted), Lock1 profile (dashed), Lock2 profile (solid).

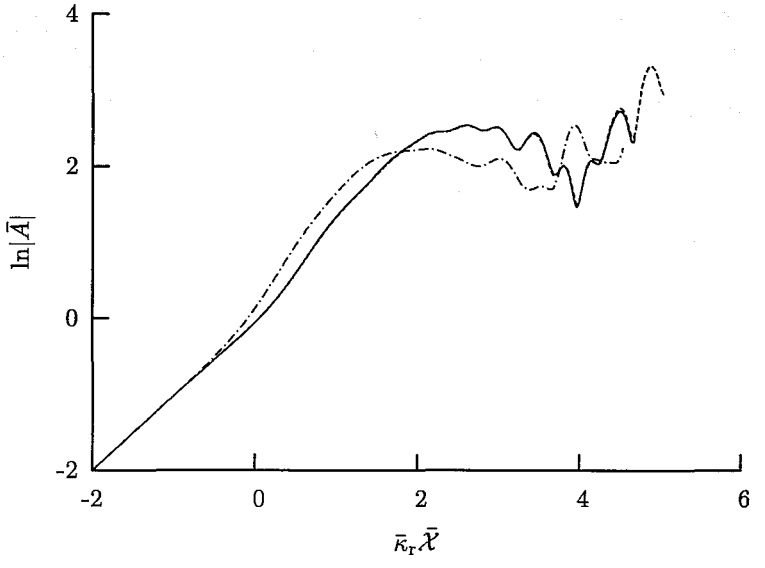


Figure 5.79: Amplitude $\ln|\bar{A}|$ *vs.* $\bar{\kappa}_r\bar{\mathcal{X}}$ for $\beta_U = 1/2$, $\beta_T = 1/2$, $M = 1/10$, $\hat{\omega} = 1/40$, $\widehat{\Lambda} = 0.1$: Tanh profile (dash-dotted), Lock1 profile (dashed), Lock2 profile (solid).

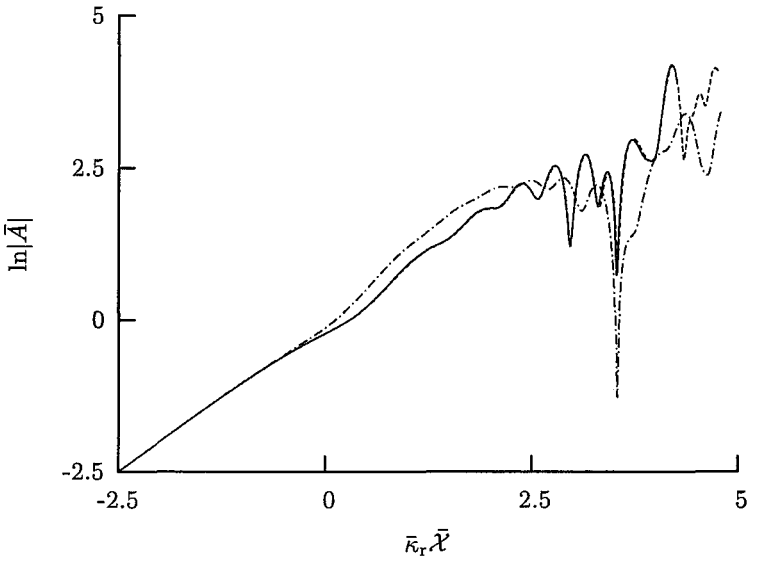


Figure 5.80: Amplitude $\ln|\bar{A}|$ *vs.* $\bar{\kappa}_r\bar{\mathcal{X}}$ for $\beta_U = 1/2$, $\beta_T = 1/2$, $M = 2$, $\hat{\omega} = 1/40$, $\widehat{\Lambda} = 0.1$: Tanh profile (dash-dotted), Lock1 profile (dashed), Lock2 profile (solid).

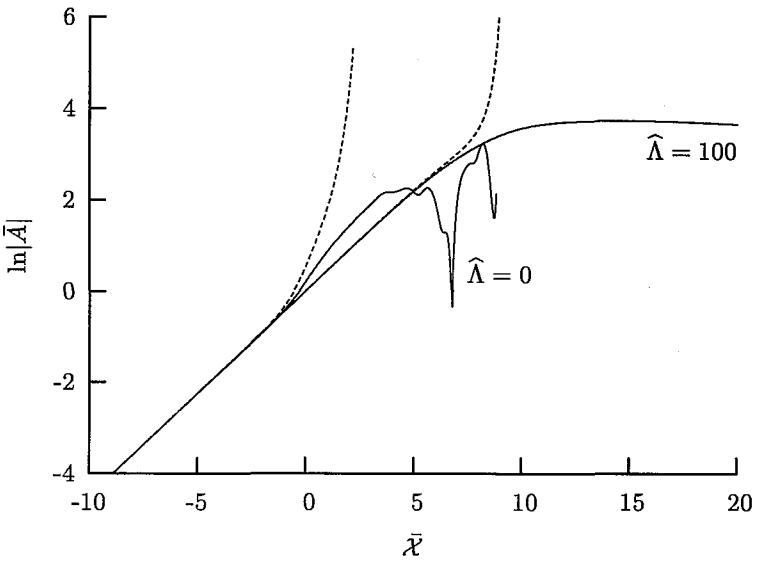


Figure 5.81: Amplitude $\ln|\bar{A}|$ *vs.* $\bar{\mathcal{X}}$ for $\beta_T = 1/2$, $M = 1/2$, $\hat{\omega} = 1/40$ and $\widehat{\Lambda} = 0$, 100. Dashed lines show equivalent weakly nonlinear results.

all three models.

Figure 5.77 shows results for $\beta_T = 1$, $M = 1/10$ and $\widehat{\Lambda} = 0.1$. We see that the Lock1 result gives rise to a slightly larger amplitude than the Tanh result, but exhibits the same general behaviour. There is almost no difference between the Lock1 and Lock2 results. Results in figure 5.78, for a larger Mach number $M = 3$, show a similar difference in behaviour between the three flow models.

Figure 5.79 shows results for $\beta_T = 1/2$, $M = 1/10$ and $\widehat{\Lambda} = 0.1$. In contrast to the $\beta_T = 1$ case, the Lock1 result gives rise, initially, to a slightly smaller amplitude than the Tanh result. Thereafter the two amplitudes oscillate in different irregular manners. As before, there is almost no difference between the Lock1 and Lock2 results. Figure 5.80 shows the results for a larger Mach number $M = 2$. There is a similar difference in behaviour between the three flow models. We thus see that use of the Lock profile seems desirable for obtaining accurate values for the amplitude when $\beta_T \neq 1$.

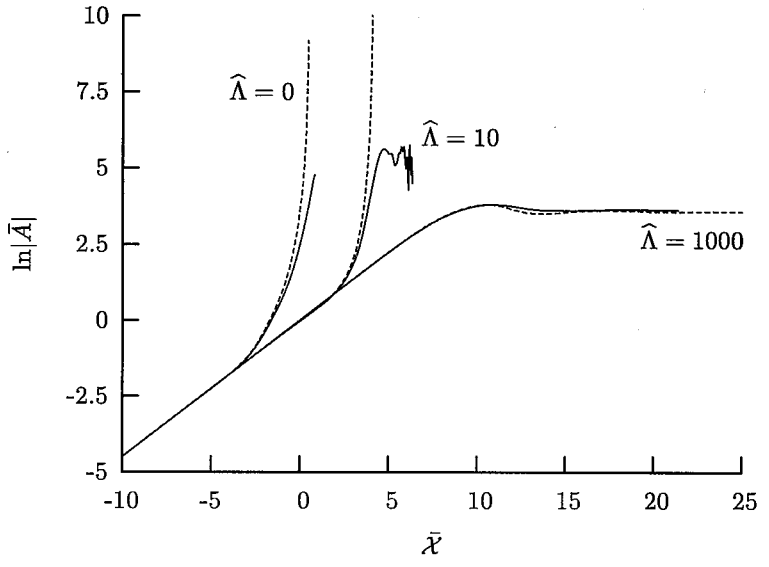


Figure 5.82: Amplitude $\ln|\bar{A}|$ *vs.* $\bar{\mathcal{X}}$ for $\beta_T = 1/2$, $M = 1/2$, $\hat{\omega} = 1/250$ and $\widehat{\Lambda} = 0$, 10, 1000. Dashed lines show equivalent weakly nonlinear results.

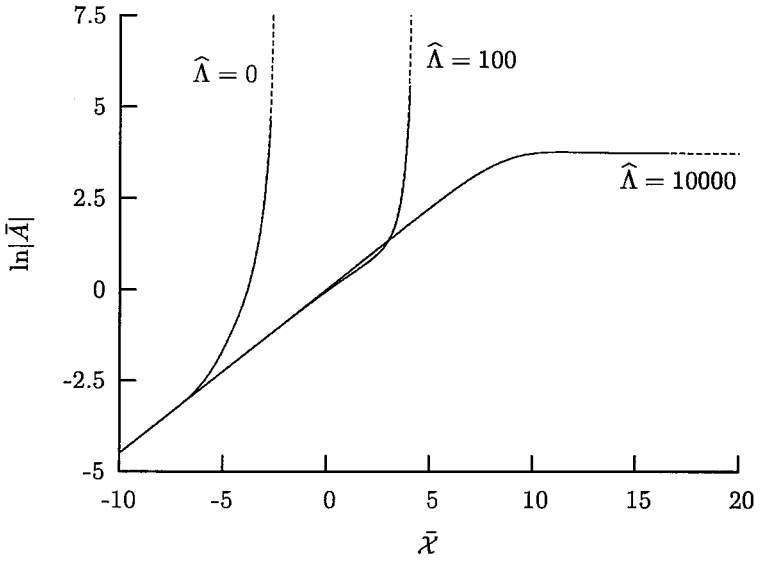


Figure 5.83: Amplitude $\ln|\bar{A}|$ *vs.* $\bar{\mathcal{X}}$ for $\beta_T = 1/2$, $M = 1/2$, $\hat{\omega} = 1/4000$ and $\widehat{\Lambda} = 0$, 100, 10000. Dashed lines show equivalent weakly nonlinear results.

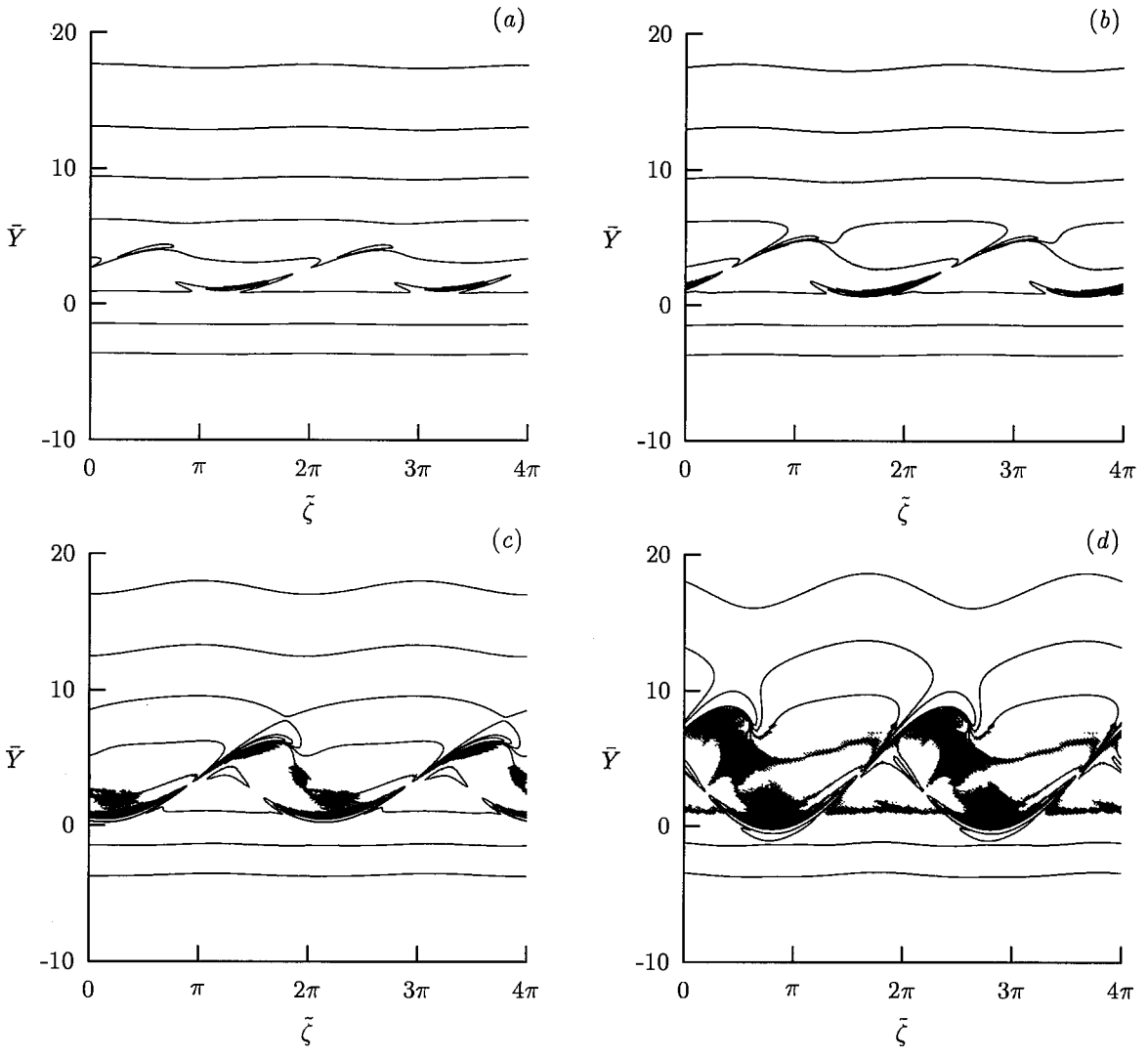


Figure 5.84: Vorticity contours in the $(\tilde{\zeta}, \bar{Y})$-plane for $\beta_T = 1/2$, $M = 1/2$, $\widehat{\Lambda} = 0$, $\hat{\omega} = 1/250$ and contour levels 200, 350, 500, ..., 1100 and 1250: (a) $\bar{\mathcal{X}} = -1.106$; (b) $\bar{\mathcal{X}} = -0.738$; (c) $\bar{\mathcal{X}} = -0.369$; (d) $\bar{\mathcal{X}} = 0$.

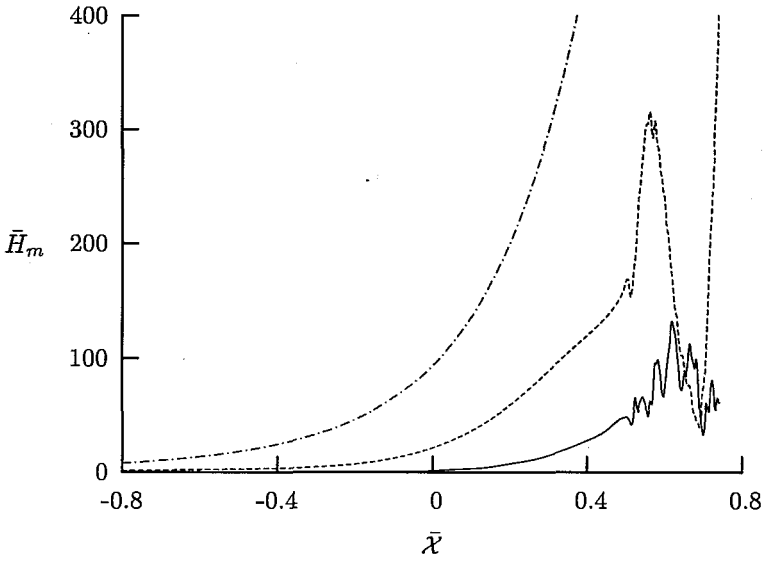


Figure 5.85: Development of higher harmonics, as measured by $\bar{H}_m = \left| \int_{-\infty}^{\infty} \bar{Q}_m d\bar{Y} \right|$ *vs.* $\bar{\mathcal{X}}$, for $\beta_T = 1/2$, $M = 1/2$, $\widehat{\Lambda} = 0$ and $\hat{\omega} = 1/250$: $m = 2$ (dash-dotted), $m = 5$ (dashed), and $m = 20$ (solid).

5.8 Comparisons between strongly and weakly nonlinear predictions

The weakly nonlinear amplitude equation (4.5.37) is derived from the strongly nonlinear formulation, and is of course much easier to solve. We now turn to examine when the weakly nonlinear approximation is valid. It should be mentioned that in previous sections we have concentrated on parameter sets for which the weakly nonlinear theory is not a good approximation, primarily due to the choice of a relatively large $\hat{\omega}$. This will be verified in this section, where we will also see that for most parameters, the weakly nonlinear theory is a poor approximation to the strongly nonlinear theory.

We will first examine the effect of $\hat{\omega}$ for various $\widehat{\Lambda}$. Figures 5.81–5.83 show comparisons for $\beta_T = 1/2$, $M = 1/2$ and $\hat{\omega} = 1/40$, $1/250$, $1/4000$. For $\hat{\omega} = 1/40$, the results from the two theories overlap in the linear regime only (figure 5.81). For $\hat{\omega} = 1/250$, there is an appreciable overlap between the two theories with the degree of the overlap depending on $\widehat{\Lambda}$. For small to moderate $\widehat{\Lambda}$, the weakly nonlinear solutions deviate from the strongly nonlinear solutions to develop a singularity (figure

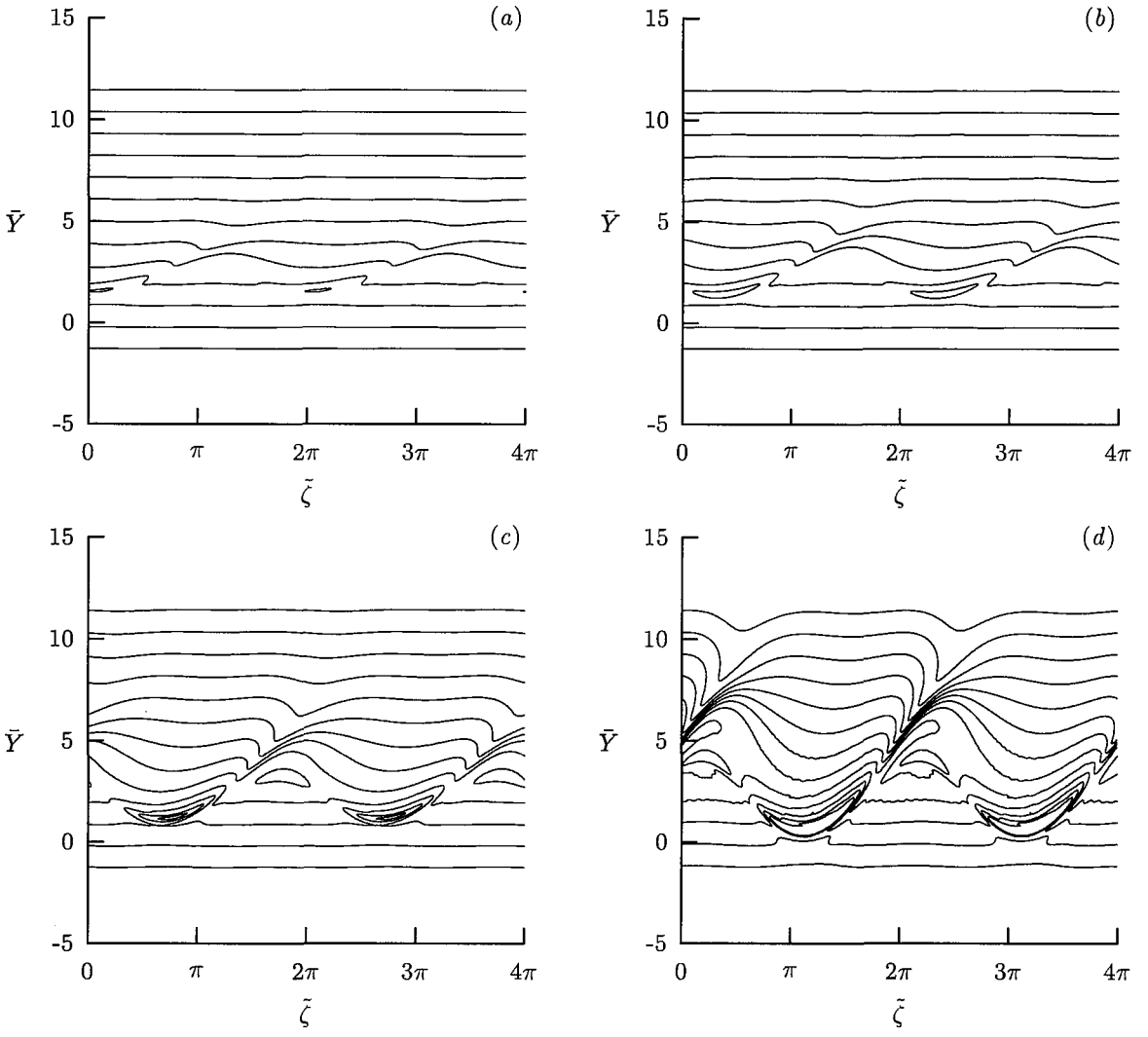


Figure 5.86: Vorticity contours in the $(\tilde{\zeta}, \bar{Y})$-plane for $\beta_T = 1/2$, $M = 1/2$, $\widehat{\Lambda} = 0$, $\hat{\omega} = 1/4000$ and contour levels 2.16×10^5, 2.17×10^5, 2.18×10^5, ..., 2.27×10^5 and 2.28×10^5: (a) $\bar{\mathcal{X}} = -3.503$; (b) $\bar{\mathcal{X}} = -3.319$; (c) $\bar{\mathcal{X}} = -3.135$; (d) $\bar{\mathcal{X}} = -2.950$.

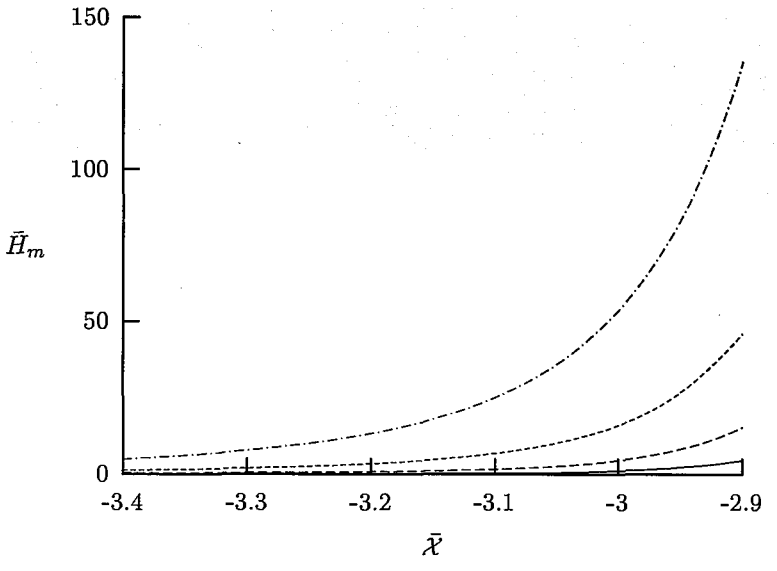


Figure 5.87: Development of higher harmonics, as measured by $\bar{H}_m = \left| \int_{-\infty}^{\infty} \bar{Q}_m \mathrm{d}\bar{Y} \right|$ *vs.* $\bar{\mathcal{X}}$, for $\beta_T = 1/2$, $M = 1/2$, $\widehat{\Lambda} = 0$ and $\hat{\omega} = 1/4000$: $m = 2$ (dash-dotted), $m = 3$ (short-dashed), $m = 4$ (long-dashed) and $m = 5$ (solid).

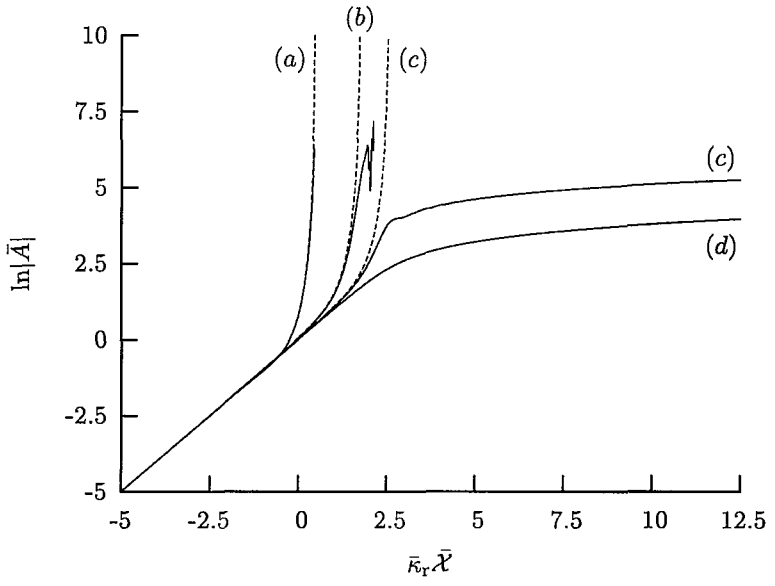


Figure 5.88: Amplitude $\ln|\bar{A}|$ *vs.* $\bar{\kappa}_r\bar{\mathcal{X}}$ for $M = 1/2$, $\hat{\omega} = 1/4000$, $\widehat{\Lambda} = 10$: (*a*) $\beta_T = 1/2$; (*b*) $\beta_T = 0.95$; (*c*) $\beta_T = 0.99$; (*d*) $\beta_T = 1$. Dashed lines show equivalent weakly nonlinear results.

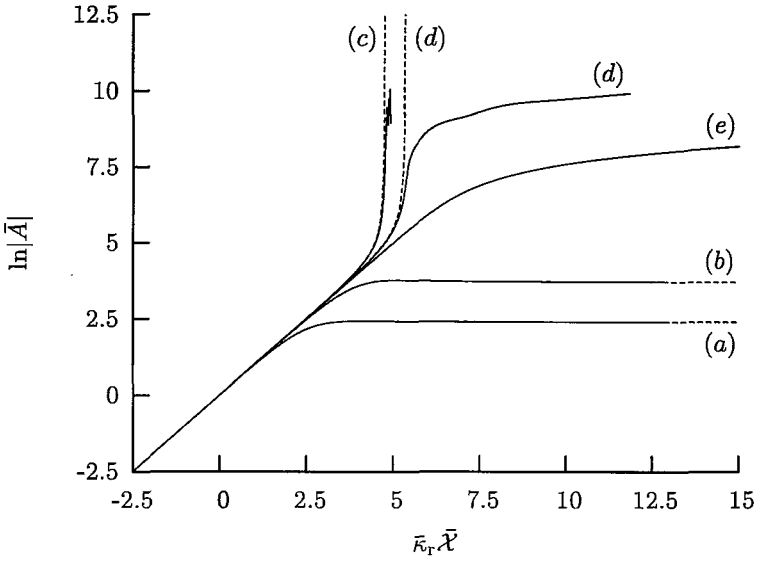


Figure 5.89: Amplitude $\ln|\bar{A}|$ *vs.* $\bar{\kappa}_r\bar{\mathcal{X}}$ for $M = 1/2$, $\hat{\omega} = 1/4000$, $\widehat{\Lambda} = 10^4$: (*a*) $\beta_T = 3/10$; (*b*) $\beta_T = 1/2$; (*c*) $\beta_T = 4/5$; (*d*) $\beta_T = 0.95$; (*e*) $\beta_T = 1$. Dashed lines show equivalent weakly nonlinear results.

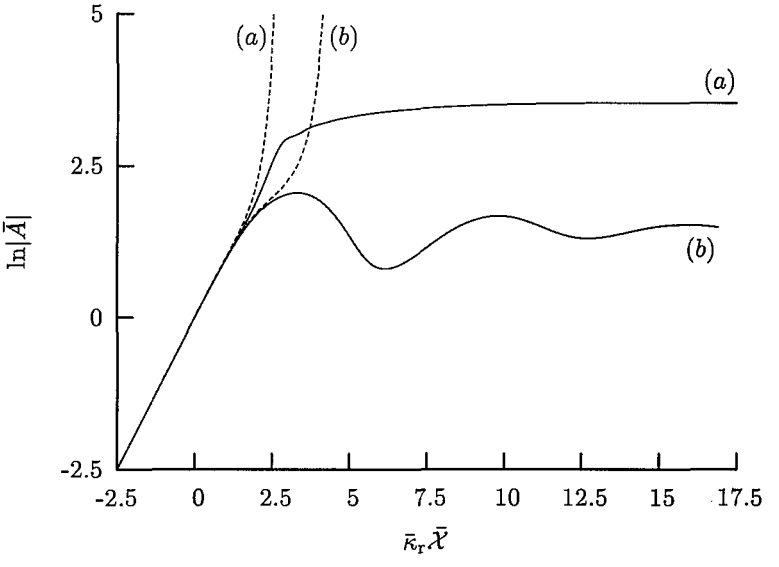


Figure 5.90: Amplitude $\ln|\bar{A}|$ *vs.* $\bar{\kappa}_r\bar{\mathcal{X}}$ for $\hat{\omega} = 1/40$, $\widehat{\Lambda} = 10$, $\beta_T = 1/2$: (*a*) $M = 1/10$; (*b*) $M = 2.87$. Dashed lines show equivalent weakly nonlinear results.

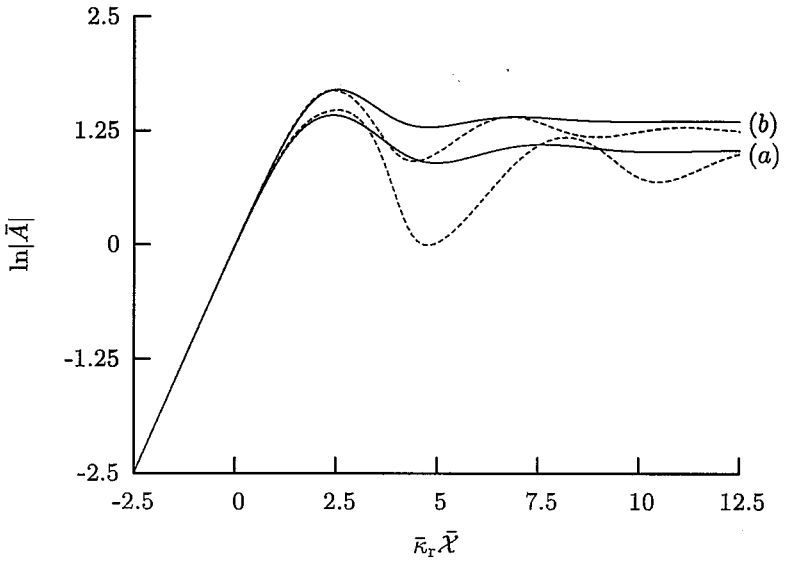


Figure 5.91: Amplitude $\ln|\bar{A}|$ *vs.* $\bar{\kappa}_r\bar{\mathcal{X}}$ for $\hat{\omega} = 1/40$, $\widehat{\Lambda} = 10$, $\beta_T = 2$: (*a*) $M = 1/10$; (*b*) $M = 4.06$. Dashed lines show equivalent weakly nonlinear results.

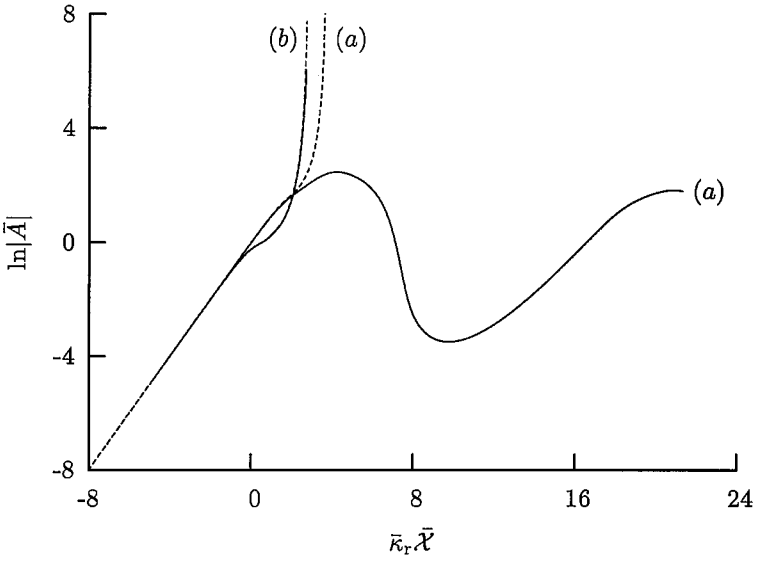


Figure 5.92: Amplitude $\ln|\bar{A}|$ *vs.* $\bar{\kappa}_r\bar{\mathcal{X}}$ for $\hat{\omega} = 1/10^5$, $\widehat{\Lambda} = 10$, $\beta_T = 1$, Lock profile: (*a*) $M = 1/3$; (*b*) $M = 3$. Dashed lines show equivalent weakly nonlinear results.

5.82), whereas for large $\widehat{\Lambda}$, the two solutions are almost identical for all $\bar{\mathcal{X}}$. For $\hat{\omega} = 1/4000$, the two theories essentially give the same results (figure 5.83).

Figure 5.84 shows vorticity contours for $\beta_T = 1/2$, $M = 1/2$, $\widehat{\Lambda} = 0$ and $\hat{\omega} = 1/250$. We see that, for this value of $\hat{\omega}$, the vorticity starts to roll-up in a similar way to the nearly inviscid case for $\hat{\omega} = 1/40$ (figure 5.36). Small-scale development gives rise to a "banding" effect in figure 5.84 (*d*), somewhat similar to that of figure 5.36 (*d*). In figure 5.85, we see that the $m = 2$ harmonic quickly becomes much larger than the higher harmonics, however the higher harmonics are still of appreciable magnitude, and decay slowly with increasing m.

Figure 5.86 shows vorticity contours for $\beta_T = 1/2$, $M = 1/2$, $\widehat{\Lambda} = 0$ and $\hat{\omega} = 1/4000$. For this value of $\hat{\omega}$, we see the vorticity begin to roll-up just before the singularity is reached. Overall though, there is very little roll-up, and noticeably less than the $\hat{\omega} = 1/250$ case. In figure 5.87, we see that successive harmonics are increasingly much smaller. Since this is a requirement of the weakly nonlinear theory, it is not surprising that the weakly nonlinear theory is in good agreement with the strongly nonlinear theory for this set of parameter values.

We will now examine the effect of β_T on the agreement between the two theories. Figures 5.88 & 5.89 show comparisons for $M = 1/2$, $\hat{\omega} = 1/4000$ and various $\beta_T \leqslant 1$ for two different $\widehat{\Lambda}$. The results show that weakly nonlinear theory yields the same result when $1 - \beta_T$ is of sufficient size, e.g. $1 - \beta_T = 1/2$ for $\widehat{\Lambda} = 10$, or $1 - \beta_T = 7/10$ for $\widehat{\Lambda} = 10^4$. For $\widehat{\Lambda} = 10^4$, as β_T is decreased, the solution switches from singular to equilibrium, since the equilibrium criterion is met (Goldstein & Leib 1989).

We finally turn our attention to the effect of Mach number. Figure 5.90 shows comparisons for $\beta_T = 1/2$, $\widehat{\Lambda} = 10$, $\hat{\omega} = 1/40$ and two different Mach numbers. The weakly nonlinear theory is not a good approximation even for the relatively large Mach number $M = 2.87$, despite that it is formally valid for M of order one. Figure 5.91 shows comparisons for $\beta_T = 2$, $\widehat{\Lambda} = 10$, $\hat{\omega} = 1/40$ and two different Mach numbers. In this case, both theories predict the same qualitative feature, but there is a noticeable difference.

Although there is no weakly nonlinear theory for the tanh profile with $\beta_T = 1$, there is such a theory for the Lock profile. Figure 5.92 shows Lock profile amplitudes for $\beta_T = 1$, $\widehat{\Lambda} = 10$, $\hat{\omega} = 1/10^5$ and two different Mach numbers. The weakly nonlinear theory is a good approximation for the larger Mach number $M = 3$, although we note that $\hat{\omega}$ needs to be quite small for this to be the case.

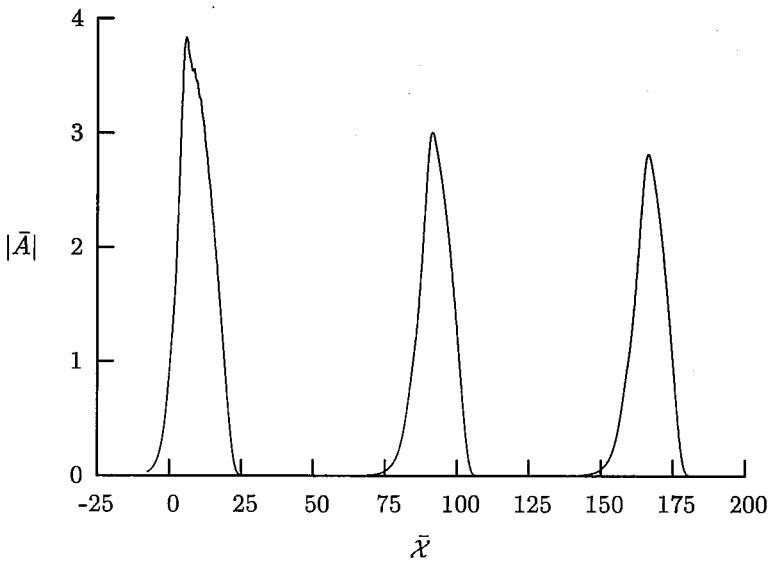


Figure 5.93: Amplitude $|\bar{A}|$ *vs.* $\bar{\mathcal{X}}$, showing annihilation and resurrection. Parameters: $\beta_U = 1/2$, $\beta_T = 2$, $M = 1/10$, $\widehat{\Lambda} = 1$ and $\hat{\omega} = 1/40$.

5.9 Unusual large-$\bar{\mathcal{X}}$ behaviour

As we have seen, the amplitude may exhibit a rich variety of behaviour, such as explosive growth, equilibration, algebraic growth, and violent "chaotic" oscillation. Another interesting behaviour is shown in figure 5.93. The amplitude grows to a local maximum followed by decaying to an almost zero level for an extended period, during which the disturbance is practically annihilated. However, the disturbance re-emerges again, and this cycle of extinction and resurrection repeats itself in quasi-periodic fashion. It should be mentioned that since the amplitude is extremely small during the extinction period, careful resolution checks were carried out before the solution could be accepted. A further note of caution is needed: due to the large streamwise distances involved, other effects, such as the non-parallel nature of the base flow (i.e. the variation of the flow on the slow scale $\mathcal{X}_2$) may become important before the cycle is allowed to repeat itself.

The quasi-periodic cycle of decaying-growing is not uncommon. Several of the solutions for other parameters are found to eventually evolve in this fashion. For many of these solutions, however, the disturbance retains a sizeable level of minimal amplitude rather than going to almost complete annihilation (as displayed in figure 5.93).

Chapter 6

Sideband Instability

6.1 Introduction

The mathematical formulation given in chapters 2–4 actually describes the nonlinear evolution of a modulated *wavetrain*. The numerical calculations have so far been performed for a special situation – the nonlinear development of an initially small-amplitude instability wave of a *single* frequency that is seeded upstream. During the nonlinear stage, all of the harmonics are generated within the critical layer.

In experiments of mixing-layer transition, interactions of instability modes of multiple frequencies play an important role. Two types of interaction have been observed. The first type is the interaction between the dominant fundamental mode and its subharmonic. Through the well-known subharmonic parametric resonance mechanism, the interaction causes a marked increase in subharmonic growth in the late stage (Hajj *et al.* 1992), which in turn leads to vortex pairing. Unfortunately, it has been impossible to investigate this interaction in a simple and self-consistent mathematical framework. The second type is the interaction of two waves with frequencies f_1 and f_2 which are quite close to each other, i.e. $|f_1 - f_2|/f_1 \ll 1$ (Miksad 1973, Sato 1970). The interaction generates various components with combination frequencies $mf_1 + nf_2$ (m, $n \in \mathbb{Z}$), leading to gradual filling of the spectrum and eventually to randomisation. The resulting irregular motion exhibits intermittency and is modulated, at least in the early random stage, by the difference mode $(f_1 - f_2)$, which is found to have an exceptionally large magnitude. Further study was made by Miksad *et al.* (1982), who attempted to interpret the spectral broadening and the associated energy cascade in terms of amplitude and phase modulations. In all of these experiments, the difference between f_1 and f_2 is fairly small (i.e. one component is within the spectral sideband of the other), promoting the authors

to interpret their findings qualitatively in terms of sideband interaction/instability. However, no quantitative mathematical description was provided.

In this chapter, we undertake to develop a theoretical description of the above observations. Specifically, we shall describe, in an appropriate quantitative mathematical framework, the physical concepts of sideband instability, phase and amplitude modulation, which have been put forth or observed by the experimentalist.

Since the frequencies are close to each other, the modes involved share a common carrier wave, and the total disturbance can be represented by a modulated wave whose amplitude function A modulates on long time and length scales. The evolution is governed by the system

$$\begin{aligned}&\alpha U_{\rm c}' Y\widehat{T}_\zeta + \widehat{T}_\mathcal{T} + c\widehat{T}_{\mathcal{X}_1} - \mathrm{i}\alpha\big(A\mathrm{e}^{\mathrm{i}\zeta} - \text{c.c.}\big)\widehat{T}_Y - \Lambda T_{\rm c}\mu_{\rm c}\widehat{T}_{YY}\\ &\qquad = \mathrm{i}\alpha T_{cM}'\mathcal{M}^2\big(A\mathrm{e}^{\mathrm{i}\zeta} - \text{c.c.}\big) - \frac{T_{\rm c}''}{U_{\rm c}'}\Big\{\big(A_\mathcal{T} + cA_{\mathcal{X}_1}\big)\mathrm{e}^{\mathrm{i}\zeta} + \text{c.c.}\Big\},\end{aligned} \tag{6.1.1}$$

$$\begin{aligned}&\alpha U_{\rm c}' Y\widehat{Q}_\zeta + \widehat{Q}_\mathcal{T} + c\widehat{Q}_{\mathcal{X}_1} - \mathrm{i}\alpha\big(A\mathrm{e}^{\mathrm{i}\zeta} - \text{c.c.}\big)\widehat{Q}_Y - \Lambda T_{\rm c}\mu_{\rm c}\widehat{Q}_{YY}\\ &\qquad = \Big(\frac{T_{\rm c}''}{T_{\rm c}} - \frac{U_{\rm c}'''}{U_{\rm c}'}\Big)\Big\{\big(A_\mathcal{T} + cA_{\mathcal{X}_1}\big)\mathrm{e}^{\mathrm{i}\zeta} + \text{c.c.}\Big\}\\ &\qquad\qquad -\mathrm{i}\alpha\frac{U_{\rm c}'}{T_{\rm c}}\Big(A\mathrm{e}^{\mathrm{i}\zeta} - \text{c.c.}\Big)\widehat{T}_Y - \Lambda U_{\rm c}'\big(\mu_{\rm c} - T_{\rm c}\mu'(T_{\rm c})\big)\widehat{T}_{YY}\end{aligned} \tag{6.1.2}$$

and

$$\oint_{-\infty}^{\infty}\int_{0}^{2\pi}\widehat{Q}\mathrm{e}^{-\mathrm{i}\zeta}\mathrm{d}\zeta\mathrm{d}Y = 4\pi\mathrm{i}\frac{T_{\rm c}}{\alpha^2}\Big(cJ_1\frac{\partial A}{\partial\mathcal{X}_1} + J_2\frac{\partial A}{\partial\mathcal{T}}\Big). \tag{6.1.3}$$

The initial perturbation of the sideband form can be represented as

$$A = \delta A^+\mathrm{e}^{\mathrm{i}\Delta\mathcal{T}} + A^{(0)} + \delta A^-\mathrm{e}^{-\mathrm{i}\Delta\mathcal{T}}$$

where we include three modes: the fundamental with amplitude $A^{(0)}$, and two sideband components with amplitudes A^+ and A^-. Here Δ is the scaled difference between their frequencies. The two-frequency excitation is a special case corresponding to either $|A^+|/|A^-| \ll 1$ or $|A^-|/|A^+| \ll 1$ initially. Our interest is in how these initially seeded three (or two) components interact and evolve.

6.2 Linear sideband instability

Firstly, we assume that the fundamental wave is dominant and consider its linear stability to sideband perturbations. Thus $A^{(0)}$ affects the (small) sideband ampli-

tudes $A^{\pm}$, but not vice versa. Let

$$A(\mathcal{X}_1,\mathcal{T}) = A^{(0)}(\mathcal{X}_1,\mathcal{T}) + \delta\big[A^{+}(\mathcal{X}_1,\mathcal{T})\mathrm{e}^{\mathrm{i}\Delta\mathcal{T}} + A^{-}(\mathcal{X}_1,\mathcal{T})\mathrm{e}^{-\mathrm{i}\Delta\mathcal{T}}\big], \tag{6.2.4}$$

where $0<\delta\ll 1$, $0<\Delta=\mathcal{O}(1)$ and $(\Omega-\Delta)>0$. Similarly,

$$\widehat{T}(\mathcal{X}_1,\mathcal{T},Y,\zeta) = \widehat{T}^{(0)}(\mathcal{X}_1,\mathcal{T},Y,\zeta) + \delta\big[\widehat{T}^{+}(\mathcal{X}_1,\mathcal{T},Y,\zeta)\mathrm{e}^{\mathrm{i}\Delta\mathcal{T}} + \widehat{T}^{-}(\mathcal{X}_1,\mathcal{T},Y,\zeta)\mathrm{e}^{-\mathrm{i}\Delta\mathcal{T}}\big], \tag{6.2.5}$$

$$\widehat{Q}(\mathcal{X}_1,\mathcal{T},Y,\zeta) = \widehat{Q}^{(0)}(\mathcal{X}_1,\mathcal{T},Y,\zeta) + \delta\big[\widehat{Q}^{+}(\mathcal{X}_1,\mathcal{T},Y,\zeta)\mathrm{e}^{\mathrm{i}\Delta\mathcal{T}} + \widehat{Q}^{-}(\mathcal{X}_1,\mathcal{T},Y,\zeta)\mathrm{e}^{-\mathrm{i}\Delta\mathcal{T}}\big]. \tag{6.2.6}$$

The fundamental evolves nonlinearly without being affected by the sideband perturbations. Substituting (6.2.4)–(6.2.6) into the critical-layer system (6.1.1)–(6.1.3) yields, at $\mathcal{O}(1)$, equations (6.1.1)–(6.1.3) with $A\to A^{(0)}$, $\widehat{T}\to\widehat{T}^{(0)}$ and $\widehat{Q}\to\widehat{Q}^{(0)}$. At $\mathcal{O}(\delta\mathrm{e}^{\pm\mathrm{i}\Delta\mathcal{T}})$ we obtain the linearized system for the sideband perturbations:

$$\begin{aligned}
&\alpha U_{\mathrm{c}}' Y\widehat{T}^{\pm}_{\zeta} + \widehat{T}^{\pm}_{\mathcal{T}} \pm \mathrm{i}\Delta\widehat{T}^{\pm} + c\widehat{T}^{\pm}_{\mathcal{X}_1} - \mathrm{i}\alpha\Big\{\big(A^{\pm}\mathrm{e}^{\mathrm{i}\zeta} - A^{\mp *}\mathrm{e}^{-\mathrm{i}\zeta}\big)\widehat{T}^{(0)}_{Y} + \big(A^{(0)}\mathrm{e}^{\mathrm{i}\zeta} - A^{(0)*}\mathrm{e}^{-\mathrm{i}\zeta}\big)\widehat{T}^{\pm}_{Y}\Big\} \\
&\quad -\Lambda T_{\mathrm{c}}\mu_{\mathrm{c}}\widehat{T}^{\pm}_{YY} = \mathrm{i}\alpha T_{\mathrm{c}M}'\mathcal{M}^2\big(A^{\pm}\mathrm{e}^{\mathrm{i}\zeta} - A^{\mp *}\mathrm{e}^{-\mathrm{i}\zeta}\big) - \frac{T_{\mathrm{c}}''}{U_{\mathrm{c}}'}\Big\{\big(A^{\pm}_{\mathcal{T}} \pm \mathrm{i}\Delta A^{\pm} + cA^{\pm}_{\mathcal{X}_1}\big)\mathrm{e}^{\mathrm{i}\zeta} \\
&\qquad +\big(A^{\mp *}_{\mathcal{T}} \pm \mathrm{i}\Delta A^{\mp *} + cA^{\mp *}_{\mathcal{X}_1}\big)\mathrm{e}^{-\mathrm{i}\zeta}\Big\},
\end{aligned} \tag{6.2.7}$$

$$\begin{aligned}
&\alpha U_{\mathrm{c}}' Y\widehat{Q}^{\pm}_{\zeta} + \widehat{Q}^{\pm}_{\mathcal{T}} \pm \mathrm{i}\Delta\widehat{Q}^{\pm} + c\widehat{Q}^{\pm}_{\mathcal{X}_1} - \mathrm{i}\alpha\Big\{\big(A^{\pm}\mathrm{e}^{\mathrm{i}\zeta} - A^{\mp *}\mathrm{e}^{-\mathrm{i}\zeta}\big)\widehat{Q}^{(0)}_{Y} + \big(A^{(0)}\mathrm{e}^{\mathrm{i}\zeta} - A^{(0)*}\mathrm{e}^{-\mathrm{i}\zeta}\big)\widehat{Q}^{\pm}_{Y}\Big\} \\
&\quad -\Lambda T_{\mathrm{c}}\mu_{\mathrm{c}}\widehat{Q}^{\pm}_{YY} = \Big(\frac{T_{\mathrm{c}}''}{T_{\mathrm{c}}} - \frac{U_{\mathrm{c}}'''}{U_{\mathrm{c}}'}\Big)\Big\{\big(A^{\pm}_{\mathcal{T}} \pm \mathrm{i}\Delta A^{\pm} + cA^{\pm}_{\mathcal{X}_1}\big)\mathrm{e}^{\mathrm{i}\zeta} + \big(A^{\mp *}_{\mathcal{T}} \pm \mathrm{i}\Delta A^{\mp *} + cA^{\mp *}_{\mathcal{X}_1}\big)\mathrm{e}^{-\mathrm{i}\zeta}\Big\} \\
&\quad -\mathrm{i}\alpha\frac{U_{\mathrm{c}}'}{T_{\mathrm{c}}}\Big\{\big(A^{\pm}\mathrm{e}^{\mathrm{i}\zeta} - A^{\mp *}\mathrm{e}^{-\mathrm{i}\zeta}\big)\widehat{T}^{(0)}_{Y} + \big(A^{(0)}\mathrm{e}^{\mathrm{i}\zeta} - A^{(0)*}\mathrm{e}^{-\mathrm{i}\zeta}\big)\widehat{T}^{\pm}_{Y}\Big\} - \Lambda U_{\mathrm{c}}'\big(\mu_{\mathrm{c}} - T_{\mathrm{c}}\mu'(T_{\mathrm{c}})\big)\widehat{T}^{\pm}_{YY}
\end{aligned} \tag{6.2.8}$$

and

$$\fint_{-\infty}^{\infty}\int_{0}^{2\pi}\widehat{Q}^{\pm}\mathrm{e}^{-\mathrm{i}\zeta}\mathrm{d}\zeta\mathrm{d}Y = 4\pi\mathrm{i}\frac{T_{\mathrm{c}}}{\alpha^2}\Big\{cJ_1\frac{\partial A^{\pm}}{\partial\mathcal{X}_1} + J_2\Big(\frac{\partial A^{\pm}}{\partial\mathcal{T}} \pm \mathrm{i}\Delta A^{\pm}\Big)\Big\}. \tag{6.2.9}$$

Now let

$$\widehat{Y} = \alpha U_{\mathrm{c}}' Y + \Omega, \tag{6.2.10}$$

$$A^{(0)}(\mathcal{X}_1,\mathcal{T}) = \widehat{A}^{(0)}(\mathcal{X}_1)\mathrm{e}^{\mathrm{i}\Omega\mathcal{T}}, \tag{6.2.11}$$

$$\widehat{Q}^{(0)}(\mathcal{X}_1,\mathcal{T},Y,\zeta) = \sum_{m=-\infty}^{\infty}\widehat{Q}^{(0)}_{m}(\mathcal{X}_1,\widehat{Y})\mathrm{e}^{\mathrm{i}m(\zeta+\Omega\mathcal{T})} \tag{6.2.12}$$

and similarly for $\widehat{A}^{\pm}$, $\widehat{Q}^{\pm}$, $\widehat{T}^{(0)}$ and $\widehat{T}^{\pm}$. The system for the fundamental is identical to that solved in chapter 5. The equations for the sideband perturbations for $m \geqslant 0$ are

$$\left(c\frac{\partial}{\partial \mathcal{X}_1} + \mathrm{i}(m\widehat{Y} \pm \Delta)\right)\widehat{T}_m^{\pm} - \Lambda T_\mathrm{c}\mu_\mathrm{c}\alpha^2 U_\mathrm{c}'^2 \frac{\partial^2}{\partial \widehat{Y}^2}\widehat{T}_m^{\pm}$$
$$+ \mathrm{i}\alpha^2 U_\mathrm{c}' \frac{\partial}{\partial \widehat{Y}}\left\{\left(\widehat{A}^{(0)*}\widehat{T}_{m+1}^{\pm} + \widehat{A}^{\mp *}\widehat{T}_{m+1}^{(0)}\right) - \left(\widehat{A}^{(0)}\widehat{T}_{m-1}^{\pm} + \widehat{A}^{\pm}\widehat{T}_{m-1}^{(0)}\right)\right\}$$
$$= \delta_{m,1}\left\{\mathrm{i}\alpha\mathcal{M}^2 T_{\mathrm{c}M}' - \frac{T_\mathrm{c}''}{U_\mathrm{c}'}\left(c\frac{\mathrm{d}}{\mathrm{d}\mathcal{X}_1} + \mathrm{i}(\Omega \pm \Delta)\right)\right\}\widehat{A}^{\pm}, \tag{6.2.13}$$

$$\left(c\frac{\partial}{\partial \mathcal{X}_1} + \mathrm{i}(m\widehat{Y} \pm \Delta)\right)\widehat{Q}_m^{\pm} - \Lambda T_\mathrm{c}\mu_\mathrm{c}\alpha^2 U_\mathrm{c}'^2 \frac{\partial^2}{\partial \widehat{Y}^2}\widehat{Q}_m^{\pm}$$
$$+ \mathrm{i}\alpha^2 U_\mathrm{c}' \frac{\partial}{\partial \widehat{Y}}\left\{\left(\widehat{A}^{(0)*}\widehat{Q}_{m+1}^{\pm} + \widehat{A}^{\mp *}\widehat{Q}_{m+1}^{(0)}\right) - \left(\widehat{A}^{(0)}\widehat{Q}_{m-1}^{\pm} + \widehat{A}^{\pm}\widehat{Q}_{m-1}^{(0)}\right)\right\}$$
$$= \delta_{m,1}\left(\frac{T_\mathrm{c}''}{T_\mathrm{c}} - \frac{U_\mathrm{c}'''}{U_\mathrm{c}'}\right)\left(c\frac{\mathrm{d}}{\mathrm{d}\mathcal{X}_1} + \mathrm{i}(\Omega \pm \Delta)\right)\widehat{A}^{\pm} - \Lambda\alpha^2 U_\mathrm{c}'^3\left(\mu_\mathrm{c} - T_\mathrm{c}\mu'(T_\mathrm{c})\right)\frac{\partial^2}{\partial \widehat{Y}^2}\widehat{T}_m^{\pm}$$
$$+ \mathrm{i}\frac{\alpha^2 U_\mathrm{c}'^2}{T_\mathrm{c}}\frac{\partial}{\partial \widehat{Y}}\left\{\left(\widehat{A}^{(0)*}\widehat{T}_{m+1}^{\pm} + \widehat{A}^{\mp *}\widehat{T}_{m+1}^{(0)}\right) - \left(\widehat{A}^{(0)}\widehat{T}_{m-1}^{\pm} + \widehat{A}^{\pm}\widehat{T}_{m-1}^{(0)}\right)\right\}, \tag{6.2.14}$$

and

$$\int_{-\infty}^{\infty} \widehat{Q}_1^{\pm}(\mathcal{X}_1, \widehat{Y})\mathrm{d}\widehat{Y} = 2\mathrm{i}\frac{U_\mathrm{c}' T_\mathrm{c}}{\alpha}\left(cJ_1\frac{\mathrm{d}}{\mathrm{d}\mathcal{X}_1} + \mathrm{i}(\Omega \pm \Delta)J_2\right)\widehat{A}^{\pm}, \tag{6.2.15}$$

where

$$\widehat{T}_{-m}^{+} = \widehat{T}_m^{-*}, \quad \widehat{Q}_{-m}^{+} = \widehat{Q}_m^{-*} \tag{6.2.16}$$

which follows from the requirement that $\widehat{T}$ and $\widehat{Q}$ must be real. The initial conditions are

$$\widehat{A}^{\pm}(\mathcal{X}_1) \to a^{\pm}\mathrm{e}^{\kappa^{\pm}\mathcal{X}_1} \quad \text{as} \quad \mathcal{X}_1 \to -\infty \tag{6.2.17}$$

where

$$\kappa^{\pm} = \frac{(\Omega \pm \Delta)}{c}\left(2(J_2 - J_1)\frac{T_\mathrm{c}U_\mathrm{c}'^2}{\pi\alpha U_\mathrm{c}'''(1+\sigma) + 2\mathrm{i}T_\mathrm{c}U_\mathrm{c}'^2 J_1} - \mathrm{i}\right). \tag{6.2.18}$$

To remove the parameters Ω, $|a|$, $\arg a$, $|a^+|$ and $\arg a^+$ from the system, we perform renormalisation

$$\bar{\mathcal{T}} = \mathcal{T}, \quad \bar{\mathcal{X}} = (\alpha\Omega/2)\mathcal{X}_1 - x_0, \quad \bar{Y} = (2/\alpha c\Omega)\widehat{Y}, \tag{6.2.19}$$

$$\bar{A} = (8U_\mathrm{c}'/c^2\Omega^2)\widehat{A}^{(0)}, \quad \bar{A}^{\pm} = (1/\hat{a}^+)(8U_\mathrm{c}'/c^2\Omega^2)\widehat{A}^{\pm}, \tag{6.2.20}$$

$$\bar{Q}_m = -4(\alpha U_{\rm c}'^2/c\Omega^2 U_{\rm c}''')\widehat{Q}_m^{(0)}, \quad \bar{Q}_m^{\pm} = -(4/\hat{a}^+)(\alpha U_{\rm c}'^2/c\Omega^2 U_{\rm c}''')\widehat{Q}_m^{\pm}, \tag{6.2.21}$$

$$\bar{T}_m = -4(\alpha U_{\rm c}'^3/c\Omega^2 T_{\rm c} U_{\rm c}''')\widehat{T}_m^{(0)}, \quad \bar{T}_m^{\pm} = -(4/\hat{a}^+)(\alpha U_{\rm c}'^3/c\Omega^2 T_{\rm c} U_{\rm c}''')\widehat{T}_m^{\pm}, \tag{6.2.22}$$

$$\bar{\mathcal{M}}^2 = -(\alpha U_{\rm c}'^2|T'_{{\rm c}M}|/\Omega T_{\rm c} U_{\rm c}''')\mathrm{sgn}(T_{\rm c}')\mathcal{M}^2, \tag{6.2.23}$$

$$\bar{\Lambda} = 8T_{\rm c}\mu_{\rm c}(U_{\rm c}'^2/\alpha c^3\Omega^3)\Lambda, \quad \bar{\Delta} = (2/\alpha c\Omega)\Delta \tag{6.2.24}$$

$$\bar{\kappa} = (2/\alpha\Omega)\kappa, \quad \bar{\kappa}^{\pm} = (2/\alpha\Omega)\kappa^{\pm}, \tag{6.2.25}$$

$$\bar{\zeta} = \zeta + \arg a + \bar{\kappa}_{\rm i} x_0, \quad x_0 = \frac{1}{\bar{\kappa}_{\rm r}}\ln\Big(\frac{c^2\Omega^2}{8U_{\rm c}'|a|}\Big) \tag{6.2.26}$$

where $\bar{\kappa} = \bar{\kappa}_{\rm r} + {\rm i}\bar{\kappa}_{\rm i}$ and

$$\hat{a}^+ = \frac{8U_{\rm c}'}{c^2\Omega^2}|a^+|{\rm e}^{\bar{\kappa}_{\rm r}^+ x_0}{\rm e}^{{\rm i}(\arg a^+ + \bar{\kappa}_{\rm i}^+ x_0)}. \tag{6.2.27}$$

Note that we could have chosen to remove $|a^-|$, $\arg a^-$ instead of $|a^+|$, $\arg a^+$. The normalisation yields equations (4.3.29)–(4.3.31) for the fundamental, and

$$\Big(\frac{\partial}{\partial\bar{\mathcal{X}}} + {\rm i}(m\bar{Y} \pm \bar{\Delta})\Big)\bar{T}_m^{\pm} + \frac{\rm i}{2}\frac{\partial}{\partial\bar{Y}}\Big\{\Big(\bar{A}^*\bar{T}_{m+1}^{\pm} + \bar{A}^{\mp *}\bar{T}_{m+1}\Big) - \Big(\bar{A}\bar{T}_{m-1}^{\pm} + \bar{A}^{\pm}\bar{T}_{m-1}\Big)\Big\}$$
$$- \bar{\Lambda}\frac{\partial^2\bar{T}_m^{\pm}}{\partial\bar{Y}^2} = \delta_{m,1}\Big\{{\rm i}\bar{\mathcal{M}}^2\bar{A}^{\pm} - \sigma\Big(\frac{\alpha c}{2}\frac{\rm d}{{\rm d}\bar{\mathcal{X}}} + {\rm i}\Big(1 \pm \frac{\alpha c}{2}\bar{\Delta}\Big)\Big)\bar{A}^{\pm}\Big\}, \tag{6.2.28}$$

$$\Big(\frac{\partial}{\partial\bar{\mathcal{X}}} + {\rm i}(m\bar{Y} \pm \bar{\Delta})\Big)\bar{Q}_m^{\pm} + \frac{\rm i}{2}\frac{\partial}{\partial\bar{Y}}\Big\{\Big(\bar{A}^*\bar{Q}_{m+1}^{\pm} + \bar{A}^{\mp *}\bar{Q}_{m+1}\Big) - \Big(\bar{A}\bar{Q}_{m-1}^{\pm} + \bar{A}^{\pm}\bar{Q}_{m-1}\Big)\Big\}$$
$$- \bar{\Lambda}\frac{\partial^2\bar{Q}_m^{\pm}}{\partial\bar{Y}^2} = \delta_{m,1}(1+\sigma)\Big(\frac{\alpha c}{2}\frac{\rm d}{{\rm d}\bar{\mathcal{X}}} + {\rm i}\Big(1 \pm \frac{\alpha c}{2}\bar{\Delta}\Big)\Big)\bar{A}^{\pm} - \bar{\Lambda}\Big(1 - T_{\rm c}\frac{\mu'(T_{\rm c})}{\mu_{\rm c}}\Big)\frac{\partial^2\bar{T}_m^{\pm}}{\partial\bar{Y}^2}$$
$$+ \frac{\rm i}{2}\frac{\partial}{\partial\bar{Y}}\Big\{\Big(\bar{A}^*\bar{T}_{m+1}^{\pm} + \bar{A}^{\mp *}\bar{T}_{m+1}\Big) - \Big(\bar{A}\bar{T}_{m-1}^{\pm} + \bar{A}^{\pm}\bar{T}_{m-1}\Big)\Big\}, \tag{6.2.29}$$

and

$$\int_{-\infty}^{\infty}\bar{Q}_1^{\pm}(\bar{\mathcal{X}},\bar{Y}){\rm d}\bar{Y} = -2{\rm i}\frac{T_{\rm c}U_{\rm c}'^2}{\alpha U_{\rm c}'''}\Big(\frac{\alpha c}{2}J_1\frac{\rm d}{{\rm d}\bar{\mathcal{X}}} + {\rm i}\Big(1 \pm \frac{\alpha c}{2}\bar{\Delta}\Big)J_2\Big)\bar{A}^{\pm} \tag{6.2.30}$$

with normalised initial conditions

$$\bar{A}^+ \to {\rm e}^{\bar{\kappa}^+\bar{\mathcal{X}}}, \quad \bar{A}^- \to \bar{a}^-{\rm e}^{\bar{\kappa}^-\bar{\mathcal{X}}} \quad \text{as} \quad \bar{\mathcal{X}} \to -\infty \tag{6.2.31}$$

where

$$\bar{a}^- = |\bar{a}^-|{\rm e}^{{\rm i}\bar{\phi}^-}, \tag{6.2.32}$$

$$|\bar{a}^-| = \frac{|a^-|}{|a^+|}{\rm e}^{(\bar{\kappa}_{\rm r}^- - \bar{\kappa}_{\rm r}^+)x_0} \tag{6.2.33}$$

and

$$\bar{\phi}^- = \arg a^- - \arg a^+ + \bar{\kappa}_{\rm i}^- - \bar{\kappa}_{\rm i}^+. \tag{6.2.34}$$

The boundary conditions on $\bar{T}_m^{\pm}$ and $\bar{Q}_m^{\pm}$ are

$$\begin{aligned}\bar{T}_0^{\pm} \sim\ & -\frac{1}{4}\alpha c\sigma\Big(\bar{A}\bar{A}^{\mp *} + \bar{A}^*\bar{A}^{\pm}\Big)\frac{1}{\bar{Y}^2} - \bar{\mathcal{M}}^2\Big(\bar{A}\bar{A}^{\mp *} + \bar{A}^*\bar{A}^{\pm}\Big)\frac{1}{\bar{Y}^3} \\ & + \mathcal{O}\Big(\frac{\sigma}{\bar{Y}^3}\Big) + \mathcal{O}\Big(\frac{1}{\bar{Y}^4}\Big),\end{aligned} \tag{6.2.35}$$

$$\begin{aligned}\bar{T}_1^{\pm} \sim\ & \left\{\sigma\Big(\mathrm{i}\frac{\alpha c}{2}\frac{\mathrm{d}}{\mathrm{d}\bar{\mathcal{X}}} - \Big(1 \pm \frac{\alpha c}{2}\bar{\Delta}\Big)\Big)\bar{A}^{\pm} + \bar{\mathcal{M}}^2\bar{A}^{\pm}\right\}\frac{1}{\bar{Y}} \\ & + \Big(\frac{\mathrm{d}}{\mathrm{d}\bar{\mathcal{X}}} \pm \mathrm{i}\bar{\Delta}\Big)\left\{\mathrm{i}\bar{\mathcal{M}}^2\bar{A}^{\pm} - \sigma\Big(\frac{\alpha c}{2}\frac{\mathrm{d}}{\mathrm{d}\bar{\mathcal{X}}} + \mathrm{i}\Big(1 \pm \frac{\alpha c}{2}\bar{\Delta}\Big)\Big)\bar{A}^{\pm}\right\}\frac{1}{\bar{Y}^2} \\ & + \mathcal{O}\Big(\frac{1}{\bar{Y}^3}\Big),\end{aligned} \tag{6.2.36}$$

$$\bar{T}_2^{\pm} \sim -\frac{1}{4}\left\{2\bar{\mathcal{M}}^2\bar{A}\bar{A}^{\pm} + \sigma\Big(\mathrm{i}\frac{\alpha c}{2}\frac{\mathrm{d}}{\mathrm{d}\bar{\mathcal{X}}} - \Big(2 \pm \frac{\alpha c}{2}\bar{\Delta}\Big)\Big)\bar{A}\bar{A}^{\pm}\right\}\frac{1}{\bar{Y}^3} + \mathcal{O}\Big(\frac{1}{\bar{Y}^4}\Big), \tag{6.2.37}$$

$$\bar{Q}_0^{\pm} \sim \frac{1}{4}\alpha c(1+2\sigma)\big(\bar{A}\bar{A}^{\mp *} + \bar{A}^*\bar{A}^{\pm}\big)\frac{1}{\bar{Y}^2} + \mathcal{O}\Big(\frac{1}{\bar{Y}^3}\Big), \tag{6.2.38}$$

$$\begin{aligned}\bar{Q}_1^{\pm} \sim\ & \left\{(1+\sigma)\Big(\Big(1 \pm \frac{\alpha c}{2}\bar{\Delta}\Big) - \mathrm{i}\frac{\alpha c}{2}\frac{\mathrm{d}}{\mathrm{d}\bar{\mathcal{X}}}\Big)\bar{A}^{\pm}\right\}\frac{1}{\bar{Y}} \\ & + \Big(\frac{\mathrm{d}}{\mathrm{d}\bar{\mathcal{X}}} \pm \mathrm{i}\bar{\Delta}\Big)\left\{(1+\sigma)\Big(\frac{\alpha c}{2}\frac{\mathrm{d}}{\mathrm{d}\bar{\mathcal{X}}} + \mathrm{i}\Big(1 \pm \frac{\alpha c}{2}\bar{\Delta}\Big)\Big)\bar{A}^{\pm}\right\}\frac{1}{\bar{Y}^2} \\ & + \mathcal{O}\Big(\frac{1}{\bar{Y}^3}\Big),\end{aligned} \tag{6.2.39}$$

$$\bar{Q}_2^{\pm} \sim \frac{1}{4}\left\{2\bar{\mathcal{M}}^2\bar{A}\bar{A}^{\pm} + (1+2\sigma)\Big(\mathrm{i}\frac{\alpha c}{2}\frac{\mathrm{d}}{\mathrm{d}\bar{\mathcal{X}}} - \Big(2 \pm \frac{\alpha c}{2}\bar{\Delta}\Big)\Big)\bar{A}\bar{A}^{\pm}\right\}\frac{1}{\bar{Y}^3} + \mathcal{O}\Big(\frac{1}{\bar{Y}^4}\Big) \tag{6.2.40}$$

and

$$\bar{T}_m^{\pm} \sim \mathcal{O}\Big(\frac{1}{\bar{Y}^{2m-1}}\Big), \quad \bar{Q}_m^{\pm} \sim \mathcal{O}\Big(\frac{1}{\bar{Y}^{2m-1}}\Big) \qquad (m \geqslant 3). \tag{6.2.41}$$

As with equation (5.2.30), the integral in (6.2.30) can be approximated by one over a finite domain, leading to

$$\begin{aligned}
&\left\{c\left(\left(U_c'T_cJ_1\right)^2+\alpha^2(1+\sigma)^2\frac{U_c'''^2}{U_c'^2}\right)\right.\\
&\quad\left.+2(1+\sigma)U_c'''T_c\left(J_1\left(1\pm\alpha c\bar{\Delta}\right)-J_2\left(1\pm\frac{\alpha c}{2}\bar{\Delta}\right)\right)\frac{1}{H}\right\}\frac{\mathrm{d}\bar{A}^{\pm}}{\mathrm{d}\bar{\mathcal{X}}}\\
&\quad+\frac{2\mathrm{i}}{\alpha}\left\{\left(\left(U_c'T_c\right)^2J_1J_2+\alpha^2(1+\sigma)^2\frac{U_c'''^2}{U_c'^2}\right)\left(1\pm\frac{\alpha c}{2}\bar{\Delta}\right)\right.\\
&\qquad\left.\pm\alpha(1+\sigma)T_cU_c'''J_1\bar{\Delta}\left(1\pm\frac{\alpha c}{2}\bar{\Delta}\right)\frac{1}{H}\right\}\bar{A}^{\pm}\\
&\qquad=\mathrm{i}\frac{U_c'''}{U_c'}\left(U_c'T_cJ_1\pm\alpha(1+\sigma)\frac{U_c'''}{U_c'}\frac{\bar{\Delta}}{H}\right)\int_{-H}^{H}\bar{Q}_1^{\pm}\mathrm{d}\bar{Y}\\
&\qquad\quad+\mathrm{i}\alpha(1+\sigma)\frac{U_c'''^2}{U_c'^2}\frac{1}{H}\int_{-H}^{H}\bar{Y}\bar{Q}_1^{\pm}\mathrm{d}\bar{Y}+\mathcal{O}\left(\frac{1}{H^2}\right). \qquad (6.2.42)
\end{aligned}$$

The system is solved by using the same numerical method as described in chapter 5, to compute $\bar{A}$, $\bar{A}^{\pm}$, $\bar{T}_m$, $\bar{T}_m^{\pm}$, $\bar{Q}_m$ and $\bar{Q}_m^{\pm}$ in turn.

6.2.1 Results

In the calculations to be presented, we will fix $\beta_U = 1/2$, $\hat{\omega} = 1/40$ and $\bar{\Delta} = 1/3$. We will use the more physical amplitude parameters a, a^+ and a^- rather than the less intuitive $\bar{a}^-$.

Note that the sideband instability is formulated as an initial-value problem as opposed to the more familiar eigenvalue problem. Sufficiently upstream where $\bar{A}$ is small, the coupling terms in (6.2.28)–(6.2.29) are negligible so that all three waves evolve independently. Thus $\bar{A}^+$ and $\bar{A}^-$ amplify exponentially at their "primary growth rates". The sideband instability is said to be present if either of $\bar{A}^+$ or $\bar{A}^-$ (or both) amplify at a rate larger than their primary growth rate.

Figures 6.1 & 6.2 show the development of $\bar{A}^+$ and $\bar{A}^-$ for two different $\widehat{\Lambda}$ with the initial condition such that $|a^-| \ll |a^+|$. In both cases, once sideband interaction takes place, $\bar{A}^+$ and $\bar{A}^-$ are suppressed. Furthermore, after a transient period both these amplitudes eventually appear to approach quasi-exponential growth, as implied by the parallel (quasi-)straight lines. These lines have a shallower gradient

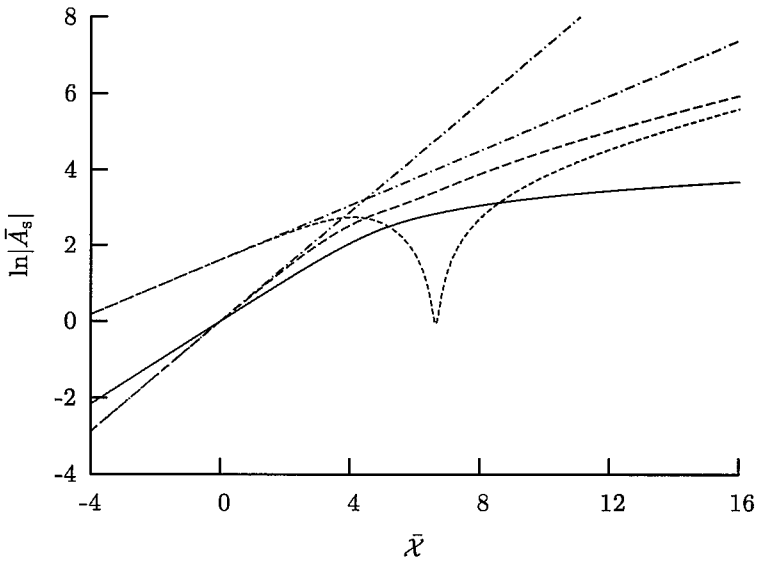


Figure 6.1: Amplitudes $\ln|\bar{A}_s|$ *vs.* $\bar{\mathcal{X}}$ for $\beta_T = 1$, $M = 0$, $\widehat{\Lambda} = 10$ and $a^+ = a = 1$, $a^- = 0.1$. $\bar{A}_s = \bar{A}$ (solid), $\bar{A}_s = \bar{A}^+$ (long-dashed), $\bar{A}_s = \bar{A}^-$ (short-dashed). Dash-dotted lines show the primary growth rates.

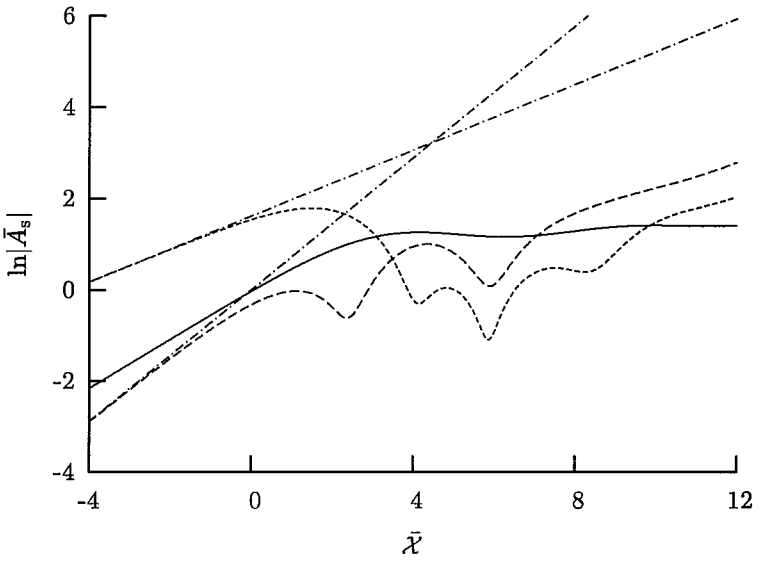


Figure 6.2: Amplitudes $\ln|\bar{A}_s|$ *vs.* $\bar{\mathcal{X}}$ for $\beta_T = 1$, $M = 0$, $\widehat{\Lambda} = 0.1$ and $a^+ = a = 1$, $a^- = 0.1$. $\bar{A}_s = \bar{A}$ (solid), $\bar{A}_s = \bar{A}^+$ (long-dashed), $\bar{A}_s = \bar{A}^-$ (short-dashed). Dash-dotted lines show the primary growth rates.

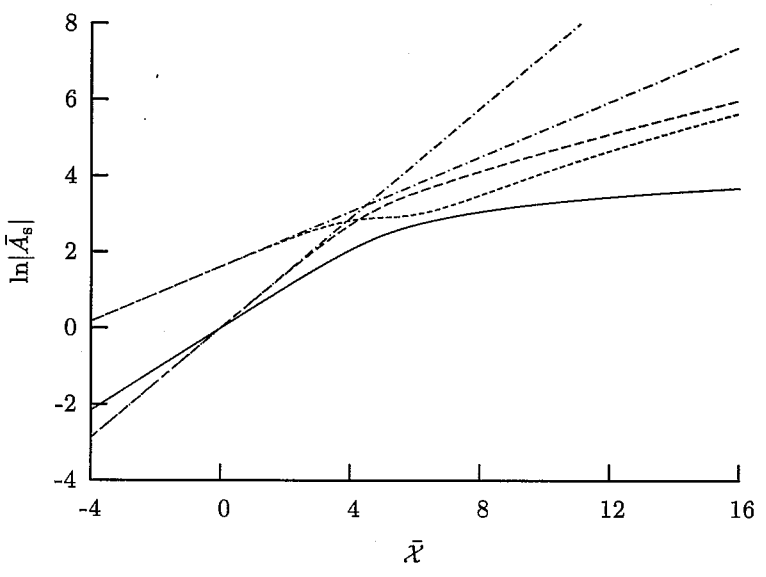


Figure 6.3: Amplitudes $\ln|\bar{A}_s|$ *vs.* $\bar{\mathcal{X}}$ for $\beta_T = 1$, $M = 0$, $\widehat{\Lambda} = 10$ and $a^+ = a = 1$, $a^- = (0.1)\mathrm{i}$. $\bar{A}_s = \bar{A}$ (solid), $\bar{A}_s = \bar{A}^+$ (long-dashed), $\bar{A}_s = \bar{A}^-$ (short-dashed). Dash-dotted lines show the primary growth rates.

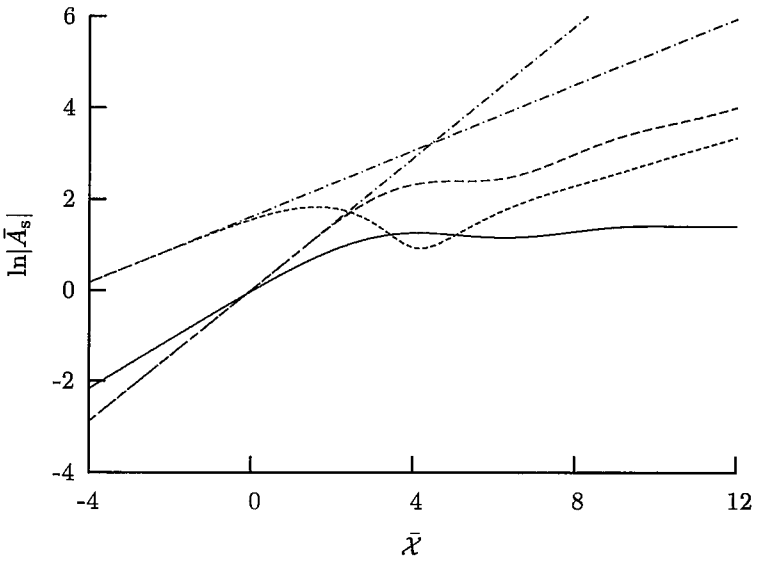


Figure 6.4: Amplitudes $\ln|\bar{A}_s|$ *vs.* $\bar{\mathcal{X}}$ for $\beta_T = 1$, $M = 0$, $\widehat{\Lambda} = 0.1$ and $a^+ = a = 1$, $a^- = (0.1)\mathrm{i}$. $\bar{A}_s = \bar{A}$ (solid), $\bar{A}_s = \bar{A}^+$ (long-dashed), $\bar{A}_s = \bar{A}^-$ (short-dashed). Dash-dotted lines show the primary growth rates.

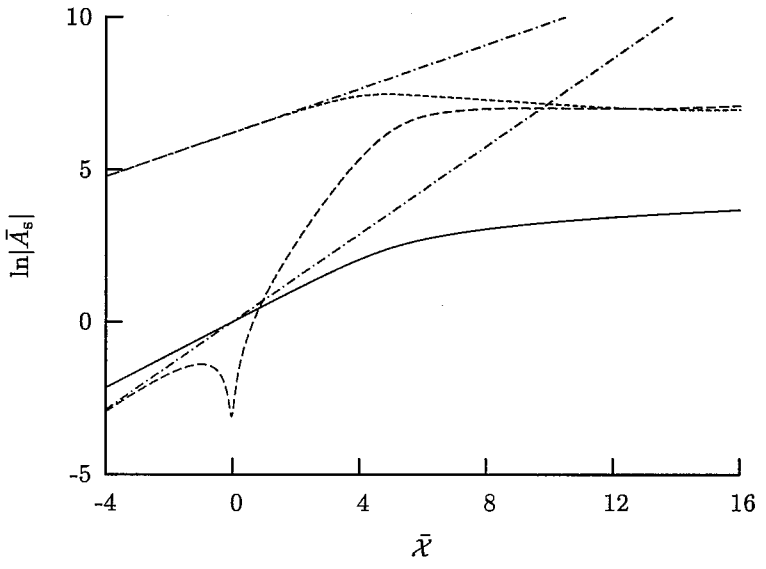


Figure 6.5: Amplitudes $\ln|\bar{A}_s|$ *vs.* $\bar{\mathcal{X}}$ for $\beta_T = 1$, $M = 0$, $\widehat{\Lambda} = 10$ and $a^- = a = 1$, $a^+ = 0.1$. $\bar{A}_s = \bar{A}$ (solid), $\bar{A}_s = \bar{A}^+$ (long-dashed), $\bar{A}_s = \bar{A}^-$ (short-dashed). Dash-dotted lines show the primary growth rates.

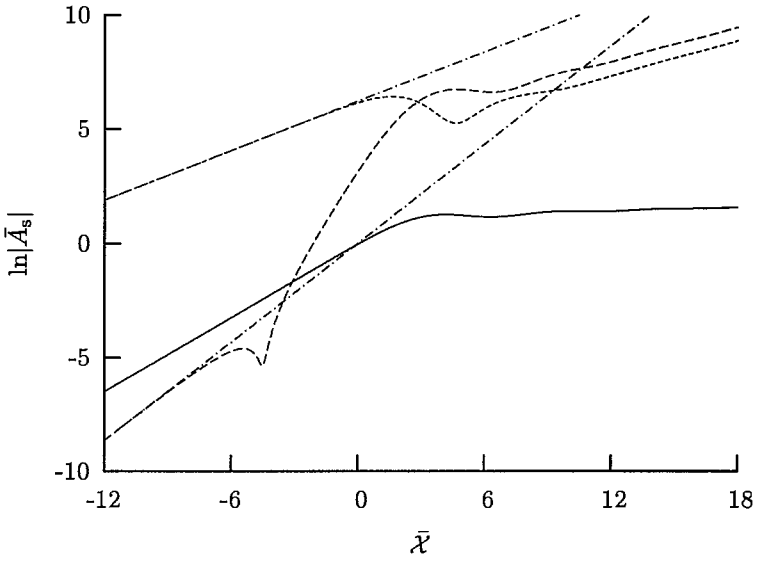


Figure 6.6: Amplitudes $\ln|\bar{A}_s|$ *vs.* $\bar{\mathcal{X}}$ for $\beta_T = 1$, $M = 0$, $\widehat{\Lambda} = 0.1$ and $a^- = a = 1$, $a^+ = 0.1$. $\bar{A}_s = \bar{A}$ (solid), $\bar{A}_s = \bar{A}^+$ (long-dashed), $\bar{A}_s = \bar{A}^-$ (short-dashed). Dash-dotted lines show the primary growth rates.

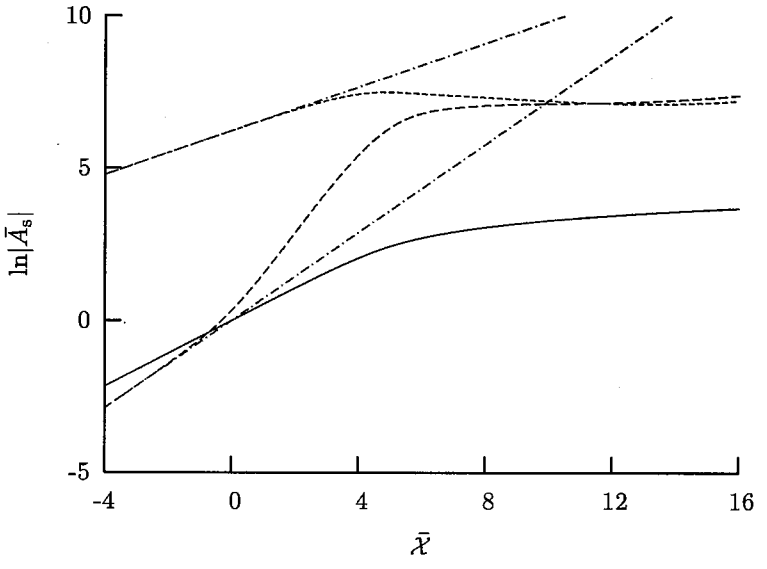


Figure 6.7: Amplitudes $\ln|\bar{A}_s|$ *vs.* $\bar{\mathcal{X}}$ for $\beta_T = 1$, $M = 0$, $\widehat{\Lambda} = 10$ and $a^- = a = 1$, $a^+ = (0.1)\mathrm{i}$. $\bar{A}_s = \bar{A}$ (solid), $\bar{A}_s = \bar{A}^+$ (long-dashed), $\bar{A}_s = \bar{A}^-$ (short-dashed). Dash-dotted lines show the primary growth rates.

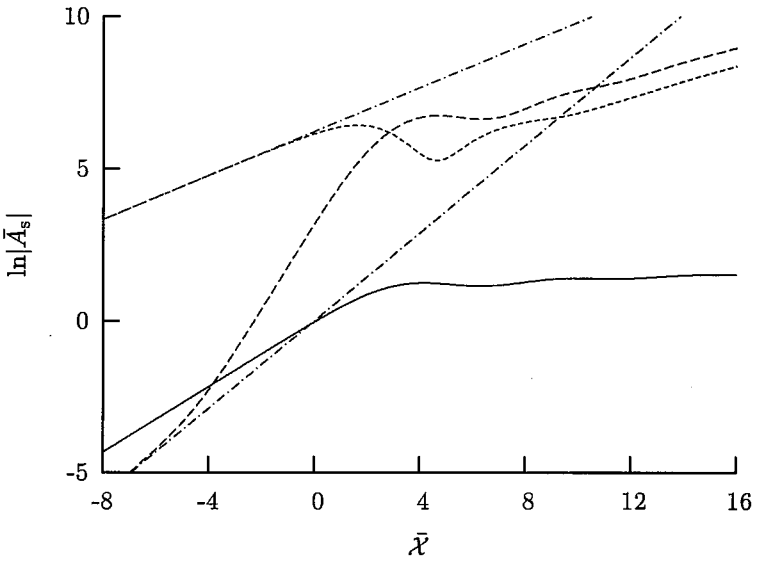


Figure 6.8: Amplitudes $\ln|\bar{A}_s|$ *vs.* $\bar{\mathcal{X}}$ for $\beta_T = 1$, $M = 0$, $\widehat{\Lambda} = 0.1$ and $a^- = a = 1$, $a^+ = (0.1)\mathrm{i}$. $\bar{A}_s = \bar{A}$ (solid), $\bar{A}_s = \bar{A}^+$ (long-dashed), $\bar{A}_s = \bar{A}^-$ (short-dashed). Dash-dotted lines show the primary growth rates.

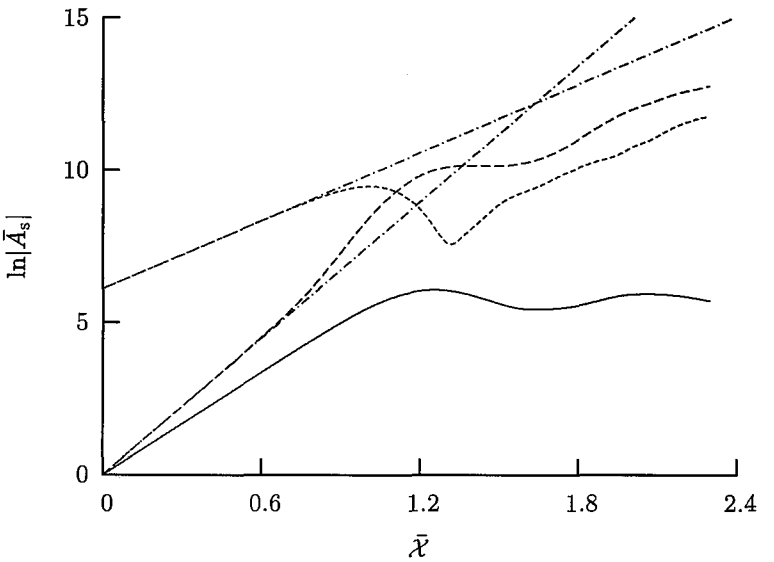


Figure 6.9: Amplitudes $\ln|\bar{A}_s|$ *vs.* $\bar{\mathcal{X}}$ for $\beta_T = 1$, $M = 3.96$, $\widehat{\Lambda} = 0.1$ and $a^- = a = 1$, $a^+ = (0.1)\mathrm{i}$. $\bar{A}_s = \bar{A}$ (solid), $\bar{A}_s = \bar{A}^+$ (long-dashed), $\bar{A}_s = \bar{A}^-$ (short-dashed). Dash-dotted lines show the primary growth rates.

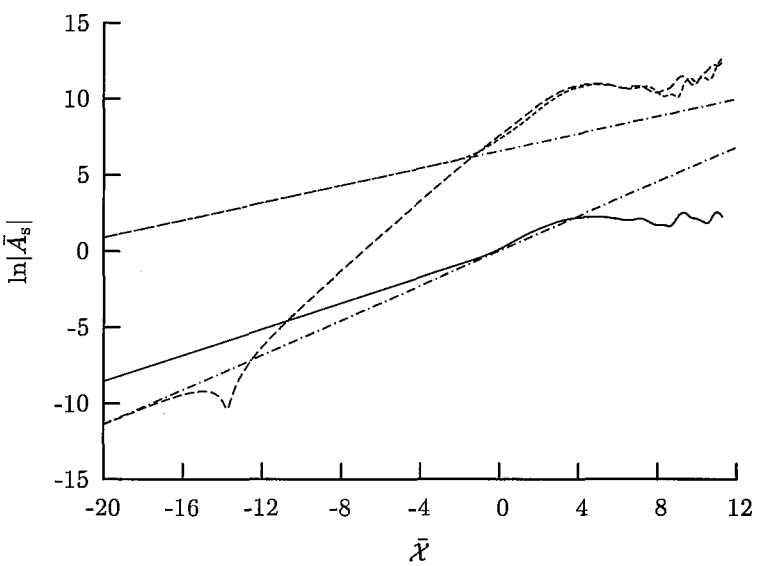


Figure 6.10: Amplitudes $\ln|\bar{A}_s|$ *vs.* $\bar{\mathcal{X}}$ for $\beta_T = 1/2$, $M = 1/2$, $\widehat{\Lambda} = 0.1$ and $a^- = a = 1$, $a^+ = (0.1)\mathrm{i}$. $\bar{A}_s = \bar{A}$ (solid), $\bar{A}_s = \bar{A}^+$ (long-dashed), $\bar{A}_s = \bar{A}^-$ (short-dashed). Dash-dotted lines show the primary growth rates.

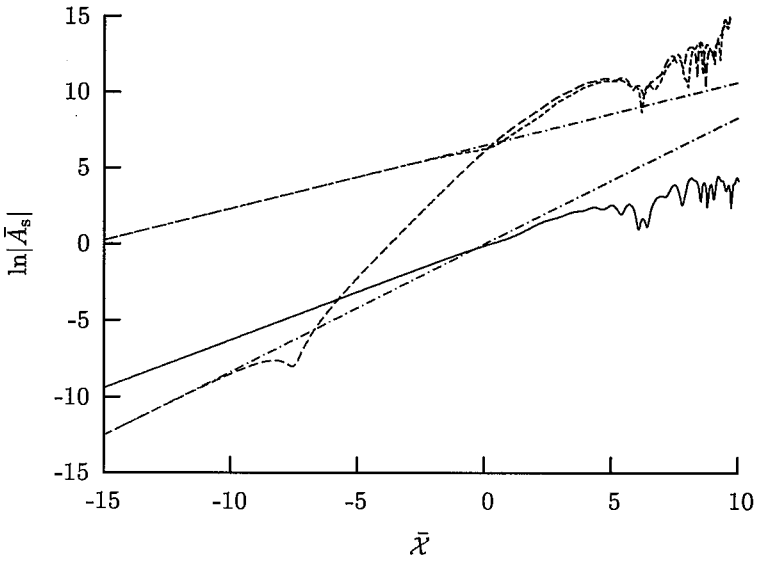


Figure 6.11: Amplitudes $\ln|\bar{A}_s|$ *vs.* $\bar{\mathcal{X}}$ for $\beta_T = 1/2$, $M = 2.87$, $\widehat{\Lambda} = 0.1$ and $a^- = a = 1$, $a^+ = (0.1)\mathrm{i}$. $\bar{A}_s = \bar{A}$ (solid), $\bar{A}_s = \bar{A}^+$ (long-dashed), $\bar{A}_s = \bar{A}^-$ (short-dashed). Dash-dotted lines show the primary growth rates.

than either of their respective primary growth rates. Thus, for the initial condition considered, there appears to be no sideband instability. Figures 6.3 & 6.4 show results when the phase of a^- differs from a^+ by $\pi/2$. We again see suppression and quasi-exponential asymptotes (of similar slope), however less oscillations are present.

Figures 6.5 & 6.6 show results for $|a^+| \ll |a^-|$ and two different $\widehat{\Lambda}$. $\bar{A}^-$ is suppressed in a similar manner to the previous figures. On the other hand, $\bar{A}^+$, after experiencing a local minimum, undergoes a stage of rapid growth, which results in $\bar{A}^+$ attaining a larger amplitude than what could be reached by primary growth. This is an indication of sideband instability. Both $\bar{A}^+$ and $\bar{A}^-$ eventually approach quasi-exponential growth at a rate smaller than the primary growth rates. Therefore if the sideband perturbation remains linear, the overall effect of sideband interaction is stabilising. However, for suitable initial conditions, nonlinearity can come into play following the rapid amplification (see next section), and thus the presence of such a period of rapid amplification can be viewed as supporting the idea that sideband instability operates in mixing-layer transition, as suggested by experiments. Figures 6.7 & 6.8 show results when there is a phase difference of $\pi/2$ between a^+ and a^-. The behaviour is very similar, except that $\bar{A}^+$ no longer

experiences a local minimum.

Figure 6.9 shows results for $\beta_T = 1$, $M = 3.96$, $\widehat{\Lambda} = 0.1$ and $|a^+| \ll |a^-|$, with a $\pi/2$ phase difference between them. Comparing with the $M = 0$ case of figure 6.8, we see that the overall behaviour is similar. There is, however, a much lower initial increase in the growth of $\bar{A}^+$ when $M = 3.96$, which suggests that, for $\beta_T = 1$, increasing M has a stabilising effect.

Figures 6.10 & 6.11 show results for $\beta_T = 1/2$, $\widehat{\Lambda} = 0.1$, and two different Mach numbers $M = 1/2$ and $M = 2.87$. As before, $|a^+| \ll |a^-|$, and there is a $\pi/2$ phase difference between a^+ and a^-. In both cases, $\bar{A}^+$ exhibits the now familiar rapid growth, but, in marked contrast to the results for $\beta_T = 1$, $\bar{A}^-$ also exhibits a stage of fast growth. Further downstream, the amplitudes $\bar{A}^+$ and $\bar{A}^-$ do not tend towards parallel (quasi-)straight line asymptotes. Instead they undergo strong "chaotic" oscillations, similar to that of $\bar{A}$. These oscillations are much more violent for the $M = 2.87$ case.

6.3 Nonlinear evolution of sideband waves

In the linear instability calculations, the amplitude of $\widehat{A}^{(0)}$ was assumed to be much larger than the amplitudes of $\widehat{A}^{\pm}$. This allowed us to formulate a simplified theory examining the influence of $\widehat{A}^{(0)}$ on the development of $\widehat{A}^{\pm}$, but not vice versa. We saw, at least for $\beta_T = 1$, that both $\widehat{A}^{\pm}$ eventually grow faster than $\widehat{A}^{(0)}$ (quasi-exponential *vs.* algebraic growth), and hence a point must be reached where the amplitudes of $\widehat{A}^{\pm}$ are of comparable magnitude to that of $\widehat{A}^{(0)}$. Then the linear assumption must break down, and nonlinear interactions generating terms proportional to $\mathrm{e}^{\mathrm{i}n\Delta}$ ($n \neq -1, 0, 1$) must be considered. Thus to examine the "back" effect of $\widehat{A}^{\pm}$ on $\widehat{A}^{(0)}$, we have to consider the fully nonlinear case, for which the total amplitude can be written as

$$\begin{aligned} A(\mathcal{X}_1, \mathcal{T}) &= \sum_{n=-\infty}^{\infty} \widehat{A}^{(n)}(\mathcal{X}_1)\mathrm{e}^{\mathrm{i}(\Omega+n\Delta)\mathcal{T}} \\ &\approx \sum_{n=-N_{\mathrm{F}}}^{N_{\mathrm{F}}} \widehat{A}^{(n)}(\mathcal{X}_1)\mathrm{e}^{\mathrm{i}(\Omega+n\Delta)\mathcal{T}} \end{aligned} \tag{6.3.43}$$

where $N_{\mathrm{F}} \geqslant 1$ is large. The temperature $\widehat{T}$ is now written as

$$\widehat{T}(\mathcal{X}_1,\mathcal{T},Y,\zeta) = \sum_{n=-\infty}^{\infty}\sum_{m=-\infty}^{\infty}\widehat{T}_m^{(n)}(\mathcal{X}_1,\widehat{Y})\mathrm{e}^{\mathrm{i}(m(\zeta+\Omega\mathcal{T})+n\Delta\mathcal{T})}$$
$$\approx \sum_{n=-N_{\mathrm{F}}}^{N_{\mathrm{F}}}\sum_{m=-M_{\mathrm{F}}}^{M_{\mathrm{F}}}\widehat{T}_m^{(n)}(\mathcal{X}_1,\widehat{Y})\mathrm{e}^{\mathrm{i}(m(\zeta+\Omega\mathcal{T})+n\Delta\mathcal{T})}, \tag{6.3.44}$$

and similarly

$$\widehat{Q}(\mathcal{X}_1,\mathcal{T},Y,\zeta) = \sum_{n=-\infty}^{\infty}\sum_{m=-\infty}^{\infty}\widehat{Q}_m^{(n)}(\mathcal{X}_1,\widehat{Y})\mathrm{e}^{\mathrm{i}(m(\zeta+\Omega\mathcal{T})+n\Delta\mathcal{T})}$$
$$\approx \sum_{n=-N_{\mathrm{F}}}^{N_{\mathrm{F}}}\sum_{m=-M_{\mathrm{F}}}^{M_{\mathrm{F}}}\widehat{Q}_m^{(n)}(\mathcal{X}_1,\widehat{Y})\mathrm{e}^{\mathrm{i}(m(\zeta+\Omega\mathcal{T})+n\Delta\mathcal{T})} \tag{6.3.45}$$

for $\widehat{Q}$, where $M_{\mathrm{F}} \geqslant 1$ is large and $\widehat{Y}$ is given by equation (6.2.10). Substitution of (6.3.43)–(6.3.45) into the critical-layer system (6.1.1)–(6.1.3) produces

$$\left(c\frac{\partial}{\partial\mathcal{X}_1}+\mathrm{i}(m\widehat{Y}+n\Delta)\right)\widehat{T}_m^{(n)} - \mathrm{i}\alpha^2U_{\mathrm{c}}'\left(\widehat{N}_{\mathrm{I},m-1}^{(n)}-\widehat{N}_{\mathrm{II},m+1}^{(n)}\right) - \Lambda T_{\mathrm{c}}\mu_{\mathrm{c}}\alpha^2U_{\mathrm{c}}'^2\frac{\partial^2}{\partial\widehat{Y}^2}\widehat{T}_m^{(n)}$$
$$= \delta_{m,1}\left\{\mathrm{i}\alpha\mathcal{M}^2T_{\mathrm{c}M}' - \frac{T_{\mathrm{c}}''}{U_{\mathrm{c}}'}\left(c\frac{\mathrm{d}}{\mathrm{d}\mathcal{X}_1}+\mathrm{i}(\Omega+n\Delta)\right)\right\}\widehat{A}^{(n)}, \tag{6.3.46}$$

$$\left(c\frac{\partial}{\partial\mathcal{X}_1}+\mathrm{i}(m\widehat{Y}+n\Delta)\right)\widehat{Q}_m^{(n)} - \mathrm{i}\alpha^2U_{\mathrm{c}}'\left(\widehat{N}_{\mathrm{III},m-1}^{(n)}-\widehat{N}_{\mathrm{IV},m+1}^{(n)}\right) - \Lambda T_{\mathrm{c}}\mu_{\mathrm{c}}\alpha^2U_{\mathrm{c}}'^2\frac{\partial^2}{\partial\widehat{Y}^2}\widehat{Q}_m^{(n)}$$
$$= \delta_{m,1}\left(\frac{T_{\mathrm{c}}''}{T_{\mathrm{c}}}-\frac{U_{\mathrm{c}}'''}{U_{\mathrm{c}}'}\right)\left(c\frac{\mathrm{d}}{\mathrm{d}\mathcal{X}_1}+\mathrm{i}(\Omega+n\Delta)\right)\widehat{A}^{(n)} - \Lambda\alpha^2U_{\mathrm{c}}'^3\left(\mu_{\mathrm{c}}-T_{\mathrm{c}}\mu'(T_{\mathrm{c}})\right)\frac{\partial^2}{\partial\widehat{Y}^2}\widehat{T}_m^{(n)}$$
$$-\mathrm{i}\frac{\alpha^2U_{\mathrm{c}}'^2}{T_{\mathrm{c}}}\left(\widehat{N}_{\mathrm{I},m-1}^{(n)}-\widehat{N}_{\mathrm{II},m+1}^{(n)}\right), \tag{6.3.47}$$

and

$$\int_{-\infty}^{\infty}\widehat{Q}_1^{(n)}(\mathcal{X}_1,\widehat{Y})\mathrm{d}\widehat{Y} = 2\mathrm{i}\frac{U_{\mathrm{c}}'T_{\mathrm{c}}}{\alpha}\left(cJ_1\frac{\mathrm{d}}{\mathrm{d}\mathcal{X}_1}+\mathrm{i}(\Omega+n\Delta)J_2\right)\widehat{A}^{(n)} \tag{6.3.48}$$

where

$$\widehat{N}_{\mathrm{I},m-1}^{(n)} = \text{Coefficient of } \mathrm{e}^{\mathrm{i}n\Delta\mathcal{T}} \text{ from } \left(\sum_{-N_{\mathrm{F}}}^{N_{\mathrm{F}}}\widehat{A}^{(n)}\mathrm{e}^{\mathrm{i}n\Delta\mathcal{T}}\right)\left(\sum_{-N_{\mathrm{F}}}^{N_{\mathrm{F}}}\frac{\partial\widehat{T}_{m-1}^{(n)}}{\partial\widehat{Y}}\mathrm{e}^{\mathrm{i}n\Delta\mathcal{T}}\right), \tag{6.3.49}$$

$$\widehat{N}_{\mathrm{II},m+1}^{(n)} = \text{Coefficient of } \mathrm{e}^{\mathrm{i}n\Delta\mathcal{T}} \text{ from } \left(\sum_{-N_{\mathrm{F}}}^{N_{\mathrm{F}}}\widehat{A}^{(-n)*}\mathrm{e}^{\mathrm{i}n\Delta\mathcal{T}}\right)\left(\sum_{-N_{\mathrm{F}}}^{N_{\mathrm{F}}}\frac{\partial\widehat{T}_{m+1}^{(n)}}{\partial\widehat{Y}}\mathrm{e}^{\mathrm{i}n\Delta\mathcal{T}}\right), \tag{6.3.50}$$

$$\widehat{N}^{(n)}_{\mathrm{III},m-1} = \text{Coefficient of } \mathrm{e}^{\mathrm{i}n\Delta\mathcal{T}} \text{ from } \left(\sum_{-N_\mathrm{F}}^{N_\mathrm{F}} \widehat{A}^{(n)}\mathrm{e}^{\mathrm{i}n\Delta\mathcal{T}}\right)\left(\sum_{-N_\mathrm{F}}^{N_\mathrm{F}} \frac{\partial \widehat{Q}^{(n)}_{m-1}}{\partial \widehat{Y}}\mathrm{e}^{\mathrm{i}n\Delta\mathcal{T}}\right), \tag{6.3.51}$$

$$\widehat{N}^{(n)}_{\mathrm{IV},m+1} = \text{Coefficient of } \mathrm{e}^{\mathrm{i}n\Delta\mathcal{T}} \text{ from } \left(\sum_{-N_\mathrm{F}}^{N_\mathrm{F}} \widehat{A}^{(-n)*}\mathrm{e}^{\mathrm{i}n\Delta\mathcal{T}}\right)\left(\sum_{-N_\mathrm{F}}^{N_\mathrm{F}} \frac{\partial \widehat{Q}^{(n)}_{m+1}}{\partial \widehat{Y}}\mathrm{e}^{\mathrm{i}n\Delta\mathcal{T}}\right). \tag{6.3.52}$$

Note that

$$\widehat{T}^{(n)}_{-m} = \widehat{T}^{(-n)*}_{m}, \quad \widehat{Q}^{(n)}_{-m} = \widehat{Q}^{(-n)*}_{m} \tag{6.3.53}$$

in order for $\widehat{T}$ and $\widehat{Q}$ to be real.

Normalisation proceeds as in (6.2.19)–(6.2.26) except that $|a^{\pm}| \to |a^{\pm}|/\delta$,

$$\bar{A}^{(n)} = \left(\frac{8}{\delta_{n+1,1} + (1-\delta_{n+1,1})\hat{a}^{+}}\right)\left(\frac{U_\mathrm{c}'}{(c\Omega)^2}\right)\widehat{A}^{(n)}, \tag{6.3.54}$$

$$\bar{T}^{(n)}_{m} = -\left(\frac{4}{\delta_{n+1,1} + (1-\delta_{n+1,1})\hat{a}^{+}}\right)\left(\frac{\alpha U_\mathrm{c}'^3}{c\Omega^2 T_\mathrm{c} U_\mathrm{c}'''}\right)\widehat{T}^{(n)}_{m}, \tag{6.3.55}$$

$$\bar{Q}^{(n)}_{m} = -\left(\frac{4}{\delta_{n+1,1} + (1-\delta_{n+1,1})\hat{a}^{+}}\right)\left(\frac{\alpha U_\mathrm{c}'^2}{c\Omega^2 U_\mathrm{c}'''}\right)\widehat{Q}^{(n)}_{m}, \tag{6.3.56}$$

$$\bar{N}^{(n)}_{\mathrm{I},m-1} = -\left(\frac{16}{\delta_{n+1,1} + (1-\delta_{n+1,1})\hat{a}^{+}}\right)\left(\frac{\alpha^2 U_\mathrm{c}'^4}{c^2\Omega^3 T_\mathrm{c} U_\mathrm{c}'''}\right)\widehat{N}^{(n)}_{\mathrm{I},m-1}, \tag{6.3.57}$$

$$\bar{N}^{(n)}_{\mathrm{III},m-1} = -\left(\frac{16}{\delta_{n+1,1} + (1-\delta_{n+1,1})\hat{a}^{+}}\right)\left(\frac{\alpha^2 U_\mathrm{c}'^3}{c^2\Omega^3 U_\mathrm{c}'''}\right)\widehat{N}^{(n)}_{\mathrm{III},m-1} \tag{6.3.58}$$

and similarly for $\bar{N}^{(n)}_{\mathrm{II},m+1}$ and $\bar{N}^{(n)}_{\mathrm{IV},m+1}$. Thus the normalised equations are

$$\left(\frac{\partial}{\partial\bar{\mathcal{X}}} + \mathrm{i}(m\bar{Y} + n\bar{\Delta})\right)\bar{T}^{(n)}_{m} + \frac{\mathrm{i}}{2}\left\{\bar{N}^{(n)}_{\mathrm{II},m+1} - \bar{N}^{(n)}_{\mathrm{I},m-1}\right\} - \bar{\Lambda}\frac{\partial^2\bar{T}^{(n)}_{m}}{\partial\bar{Y}^2} = \delta_{m,1}\left\{\mathrm{i}\bar{\mathcal{M}}^2\bar{A}^{(n)} - \sigma\left(\frac{\alpha c}{2}\frac{\mathrm{d}}{\mathrm{d}\bar{\mathcal{X}}} + \mathrm{i}\left(1 + n\frac{\alpha c}{2}\bar{\Delta}\right)\right)\bar{A}^{(n)}\right\}, \tag{6.3.59}$$

$$\left(\frac{\partial}{\partial\bar{\mathcal{X}}} + \mathrm{i}(m\bar{Y} + n\bar{\Delta})\right)\bar{Q}^{(n)}_{m} + \frac{\mathrm{i}}{2}\left\{\bar{N}^{(n)}_{\mathrm{IV},m+1} - \bar{N}^{(n)}_{\mathrm{III},m-1}\right\} - \bar{\Lambda}\frac{\partial^2\bar{Q}^{(n)}_{m}}{\partial\bar{Y}^2}$$
$$= \delta_{m,1}(1+\sigma)\left(\frac{\alpha c}{2}\frac{\mathrm{d}}{\mathrm{d}\bar{\mathcal{X}}} + \mathrm{i}\left(1 + n\frac{\alpha c}{2}\bar{\Delta}\right)\right)\bar{A}^{(n)} - \bar{\Lambda}\left(1 - T_\mathrm{c}\frac{\mu'(T_\mathrm{c})}{\mu_\mathrm{c}}\right)\frac{\partial^2\bar{T}^{(n)}_{m}}{\partial\bar{Y}^2}$$
$$+\frac{\mathrm{i}}{2}\left\{\bar{N}^{(n)}_{\mathrm{II},m+1} - \bar{N}^{(n)}_{\mathrm{I},m-1}\right\}, \tag{6.3.60}$$

and

$$\int_{-\infty}^{\infty} \bar{Q}_1^{(n)} \mathrm{d}\bar{Y} = -2\mathrm{i}\frac{T_c U_c'^2}{\alpha U_c'''}\left(\frac{\alpha c}{2} J_1 \frac{\mathrm{d}}{\mathrm{d}\bar{\mathcal{X}}} + \mathrm{i}\left(1 + n\frac{\alpha c}{2}\bar{\Delta}\right) J_2\right)\bar{A}^{(n)} \tag{6.3.61}$$

with normalised initial conditions as in equations (4.3.33) & (6.2.31). The relevant boundary conditions are

$$\bar{T}_0^{(n)} \sim \frac{\mathrm{i}}{2}\mathrm{e}^{-\mathrm{i}n\bar{\Delta}\bar{\mathcal{X}}} \int_{-\infty}^{\bar{\mathcal{X}}} \left\{\bar{N}_{\mathrm{I},-1}^{(n)} - \bar{N}_{\mathrm{II},1}^{(n)}\right\} \mathrm{e}^{\mathrm{i}n\bar{\Delta}\bar{\mathcal{X}}} \mathrm{d}\bar{\mathcal{X}} + \mathcal{O}\left(\frac{1}{\bar{Y}^3}\right) \tag{6.3.62}$$

$$\begin{aligned}\bar{T}_1^{(n)} \sim{}& \left\{\sigma\left(\mathrm{i}\frac{\alpha c}{2}\frac{\mathrm{d}}{\mathrm{d}\bar{\mathcal{X}}} - \left(1 + n\frac{\alpha c}{2}\bar{\Delta}\right)\right)\bar{A}^{(n)} + \bar{\mathcal{M}}^2\bar{A}^{(n)}\right\}\frac{1}{\bar{Y}} \\ &+ \left(\frac{\mathrm{d}}{\mathrm{d}\bar{\mathcal{X}}} + \mathrm{i}n\bar{\Delta}\right)\left\{\mathrm{i}\bar{\mathcal{M}}^2\bar{A}^{(n)} - \sigma\left(\frac{\alpha c}{2}\frac{\mathrm{d}}{\mathrm{d}\bar{\mathcal{X}}} + \mathrm{i}\left(1 + n\frac{\alpha c}{2}\bar{\Delta}\right)\right)\bar{A}^{(n)}\right\}\frac{1}{\bar{Y}^2} \\ &+ \mathcal{O}\left(\frac{1}{\bar{Y}^3}\right),\end{aligned} \tag{6.3.63}$$

$$\bar{T}_m^{(n)} \sim \frac{1}{2m\bar{Y}}\bar{N}_{\mathrm{I},m-1}^{(n)} + \mathcal{O}\left(\frac{1}{\bar{Y}^{2m}}\right) \qquad (m \geqslant 2), \tag{6.3.64}$$

$$\bar{Q}_0^{(n)} \sim \frac{\mathrm{i}}{2}\mathrm{e}^{-\mathrm{i}n\bar{\Delta}\bar{\mathcal{X}}} \int_{-\infty}^{\bar{\mathcal{X}}} \left\{\bar{N}_{\mathrm{III},-1}^{(n)} + \bar{N}_{\mathrm{II},1}^{(n)} - \bar{N}_{\mathrm{IV},1}^{(n)} - \bar{N}_{\mathrm{I},-1}^{(n)}\right\} \mathrm{e}^{\mathrm{i}n\bar{\Delta}\bar{\mathcal{X}}} \mathrm{d}\bar{\mathcal{X}} + \mathcal{O}\left(\frac{1}{\bar{Y}^3}\right) \tag{6.3.65}$$

$$\begin{aligned}\bar{Q}_1^{(n)} \sim{}& \left\{(1+\sigma)\left(\left(1 + n\frac{\alpha c}{2}\bar{\Delta}\right) - \mathrm{i}\frac{\alpha c}{2}\frac{\mathrm{d}}{\mathrm{d}\bar{\mathcal{X}}}\right)\bar{A}^{(n)}\right\}\frac{1}{\bar{Y}} \\ &+ \left(\frac{\mathrm{d}}{\mathrm{d}\bar{\mathcal{X}}} + \mathrm{i}n\bar{\Delta}\right)\left\{(1+\sigma)\left(\frac{\alpha c}{2}\frac{\mathrm{d}}{\mathrm{d}\bar{\mathcal{X}}} + \mathrm{i}\left(1 + n\frac{\alpha c}{2}\bar{\Delta}\right)\right)\bar{A}^{(n)}\right\}\frac{1}{\bar{Y}^2} \\ &+ \mathcal{O}\left(\frac{1}{\bar{Y}^3}\right),\end{aligned} \tag{6.3.66}$$

$$\bar{Q}_m^{(n)} \sim \frac{1}{2m\bar{Y}}\left\{\bar{N}_{\mathrm{III},m-1}^{(n)} - \bar{N}_{\mathrm{I},m-1}^{(n)}\right\} + \mathcal{O}\left(\frac{1}{\bar{Y}^{2m}}\right) \qquad (m \geqslant 2). \tag{6.3.67}$$

On approximating the integral over a large but finite domain, equation (6.3.61) can be written as

$$\begin{aligned}
&\Bigg\{c\Bigg(\left(U_{\mathrm{c}}'T_{\mathrm{c}}J_1\right)^2+\alpha^2\left(1+\sigma\right)^2\frac{U_{\mathrm{c}}'''^2}{U_{\mathrm{c}}'^2}\Bigg)\\
&\qquad+2\left(1+\sigma\right)U_{\mathrm{c}}'''T_{\mathrm{c}}\Bigg(J_1\left(1+n\alpha c\bar{\Delta}\right)-J_2\Big(1+n\frac{\alpha c}{2}\bar{\Delta}\Big)\Bigg)\frac{1}{H}\Bigg\}\frac{\mathrm{d}\bar{A}^{(n)}}{\mathrm{d}\bar{\mathcal{X}}}\\
&\qquad+\frac{2\mathrm{i}}{\alpha}\Bigg\{\Bigg(\left(U_{\mathrm{c}}'T_{\mathrm{c}}\right)^2J_1J_2+\alpha^2\left(1+\sigma\right)^2\frac{U_{\mathrm{c}}'''^2}{U_{\mathrm{c}}'^2}\Bigg)\Big(1+n\frac{\alpha c}{2}\bar{\Delta}\Big)\\
&\qquad\qquad+n\alpha\left(1+\sigma\right)T_{\mathrm{c}}U_{\mathrm{c}}'''J_1\bar{\Delta}\Big(1+n\frac{\alpha c}{2}\bar{\Delta}\Big)\frac{1}{H}\Bigg\}\bar{A}^{(n)}\\
&\qquad\qquad=\mathrm{i}\frac{U_{\mathrm{c}}'''}{U_{\mathrm{c}}'}\Bigg(U_{\mathrm{c}}'T_{\mathrm{c}}J_1+n\alpha\left(1+\sigma\right)\frac{U_{\mathrm{c}}'''}{U_{\mathrm{c}}'}\frac{\bar{\Delta}}{H}\Bigg)\int_{-H}^{H}\bar{Q}_1^{(n)}\mathrm{d}\bar{Y}\\
&\qquad\qquad\qquad+\mathrm{i}\alpha\left(1+\sigma\right)\frac{U_{\mathrm{c}}'''^2}{U_{\mathrm{c}}'^2}\frac{1}{H}\int_{-H}^{H}\bar{Y}\bar{Q}_1^{(n)}\mathrm{d}\bar{Y}+\mathcal{O}\Big(\frac{1}{H^2}\Big).
\end{aligned}\tag{6.3.68}$$

6.3.1 Results

The nonlinear calculations will be performed for the parameters: $\beta_U = 1/2$, $\beta_T = 1$, $M = 0$, $\hat{\omega} = 1/40$, $\widehat{\Lambda} = 0.1$, $\bar{\Delta} = 1/3$, $\delta = 0.1$, $a = 1$, $a^- = \delta$ and $a^+ = (0.1)\delta\mathrm{i}$. Owing to restrictions of computer time and memory, we set $N_{\mathrm{F}} = 5$ and $M_{\mathrm{F}} = 25$ only. In the following, "linear prediction" will refer to the results obtained by solving equations (6.2.28)–(6.2.30). Note that upstream, we have $\bar{A}^{(-1)} = \delta\bar{A}^-$, $\bar{A}^{(0)} = \bar{A}$ and $\bar{A}^{(1)} = \delta\bar{A}^+$.

Figure 6.12 shows the results for the amplitudes. As expected, the sideband perturbations initially follow linear sideband instability theory whilst the fundamental remains unaltered during the early phase. Ultimately, however, the nonlinear interactions cause all of the amplitudes $\bar{A}^{(-1)}$, $\bar{A}^{(0)}$ and $\bar{A}^{(1)}$ to slowly decay. The moderate attenuation is accompanied by oscillations which are strongest for $\bar{A}^{(1)}$. Such oscillations have actually been observed in experiments (Miksad 1973, Miksad *et al.* 1982) and were found to play an important role in the spectral-broadening and energy redistribution processes. Miksad *et al.* (1982) attempted to explain the observed amplitude and phase modulations using the framework of classical weakly nonlinear theory. It is now generally accepted that their theory cannot be extended/applied to an unbounded shear flow in a mathematically consistent fashion.

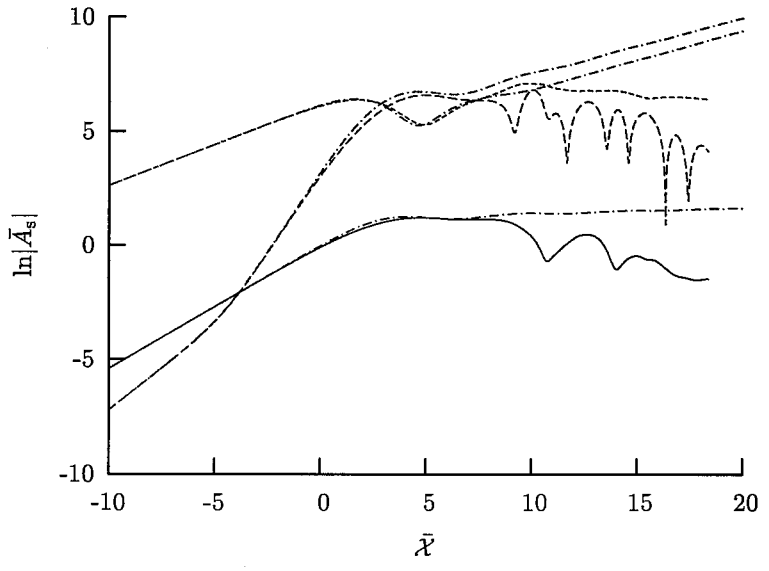


Figure 6.12: Amplitudes $\ln|\bar{A}_s|$ *vs.* $\bar{\mathcal{X}}$ for $\beta_T = 1$, $M = 0$, $\widehat{\Lambda} = 0.1$, $a = 1$, $a^- = \delta$ and $a^+ = (0.1)\delta\mathrm{i}$. $\bar{A}_s = \bar{A}^{(0)}$ (solid), $\bar{A}_s = \bar{A}^{(1)}$ (long-dashed), $\bar{A}_s = \bar{A}^{(-1)}$ (short-dashed). Dash-dotted lines show linear prediction.

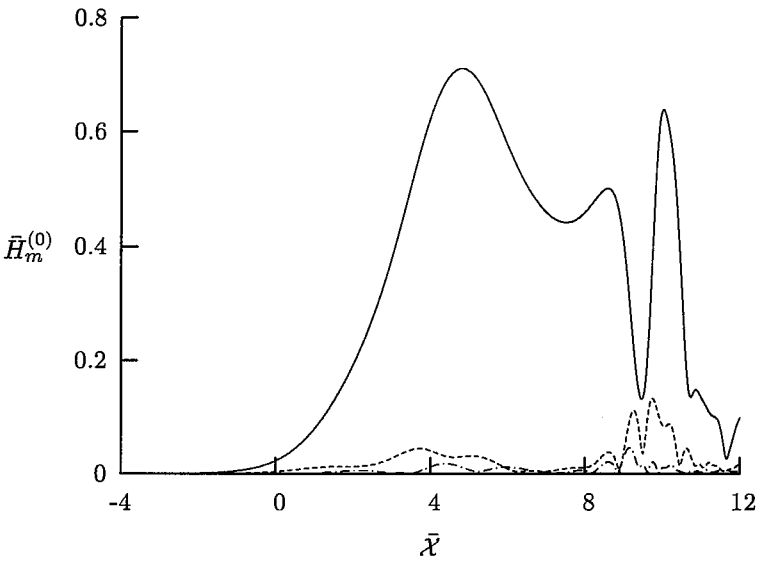


Figure 6.13: Development of higher harmonics, as measured by $\bar{H}_m^{(0)} = \left| \int_{-\infty}^{\infty} \bar{Q}_m^{(0)} \mathrm{d}\bar{Y} \right|$ *vs.* $\bar{\mathcal{X}}$, for $\beta_T = 1$, $M = 0$, $\widehat{\Lambda} = 0.1$, $a = 1$, $a^- = \delta$ and $a^+ = (0.1)\delta\mathrm{i}$: $m = 2$ (solid), $m = 3$ (dashed), $m = 4$ (dash-dotted).

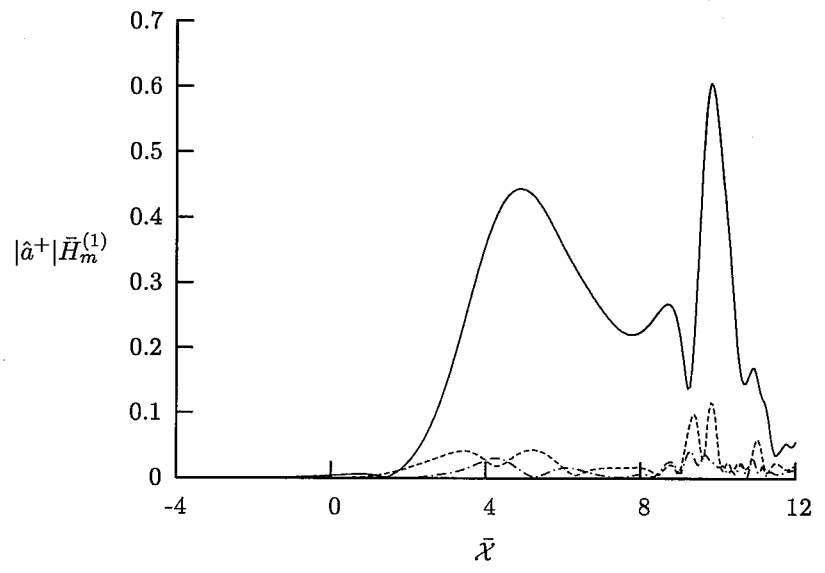


Figure 6.14: Development of higher harmonics, as measured by $\bar{H}_m^{(1)} = \left| \int_{-\infty}^{\infty} \bar{Q}_m^{(1)} \mathrm{d}\bar{Y} \right|$ *vs.* $\bar{\mathcal{X}}$, for $\beta_T = 1$, $M = 0$, $\widehat{\Lambda} = 0.1$, $a = 1$, $a^- = \delta$ and $a^+ = (0.1)\delta$i: $m = 2$ (solid), $m = 3$ (dashed), $m = 4$ (dash-dotted).

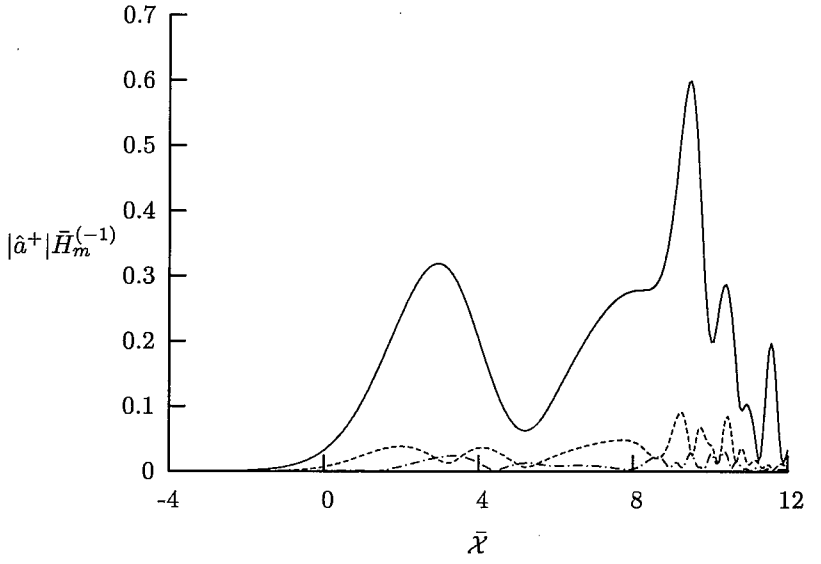


Figure 6.15: Development of higher harmonics, as measured by $\bar{H}_m^{(-1)} = \left| \int_{-\infty}^{\infty} \bar{Q}_m^{(-1)} \mathrm{d}\bar{Y} \right|$ *vs.* $\bar{\mathcal{X}}$, for $\beta_T = 1$, $M = 0$, $\widehat{\Lambda} = 0.1$, $a = 1$, $a^- = \delta$ and $a^+ = (0.1)\delta$i: $m = 2$ (solid), $m = 3$ (dashed), $m = 4$ (dash-dotted).

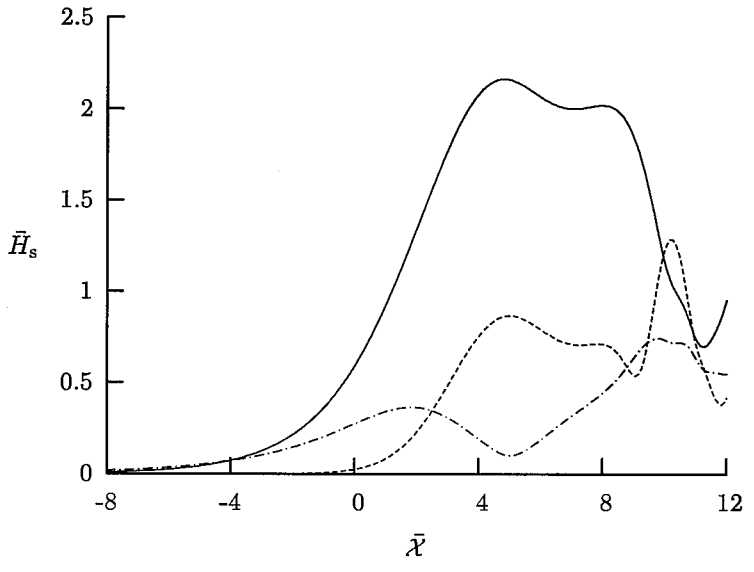


Figure 6.16: $\bar{H}_s$ *vs.* $\bar{\mathcal{X}}$, for $\beta_T = 1$, $M = 0$, $\widehat{\Lambda} = 0.1$, $a = 1$, $a^- = \delta$ and $a^+ = (0.1)\delta i$. $\bar{H}_s = \bar{H}_1^{(0)}$ (solid), $\bar{H}_s = |\hat{a}^+|\bar{H}_1^{(1)}$ (dashed), $\bar{H}_s = |\hat{a}^+|\bar{H}_1^{(-1)}$ (dash-dotted).

The present nonlinear critical-layer theory provides the appropriate mathematical description of the observations.

For perturbations of the sideband form, in addition to exact harmonics, components in their sideband are generated. These can be measured by

$$\bar{H}_m^{(n)} = \left| \int_{-\infty}^{\infty} \bar{Q}_m^{(n)} \mathrm{d}\bar{Y} \right|.$$

The development of the first three exact harmonics, $\bar{H}_m^{(0)}$ ($m = 2$, 3, 4), is displayed in figure 6.13, while the components in their immediate band, $\bar{H}_m^{(\pm 1)}$, are shown in figures 6.14–6.15. For the chosen parameters, the harmonics and their sideband components are dominant, and they all have comparable amplitudes. Figure 6.16 shows the difference between the fundamentals $\bar{H}_1^{(n)}$ ($n = -1$, 0, 1). We notice that $\bar{H}_1^{(1)}$ becomes larger than $\bar{H}_1^{(-1)}$, despite the fact that $\bar{H}_1^{(1)}$ is an order of magnitude smaller than $\bar{H}_1^{(-1)}$ upstream.

To probe the development of the difference-frequency components, in figure 6.17, we plot the distribution of $|\bar{Q}_0^{(0)}|$ (the mean-flow distortion) and the exact harmonics $|\bar{Q}_2^{(0)}|$ at several selected streamwise locations. The mean-flow distortion is much stronger than the harmonics. Figures 6.18–6.19 show the profiles of the difference-frequency components $|\hat{a}^+\bar{Q}_0^{(\pm 1)}|$, and compares them with those of the sideband

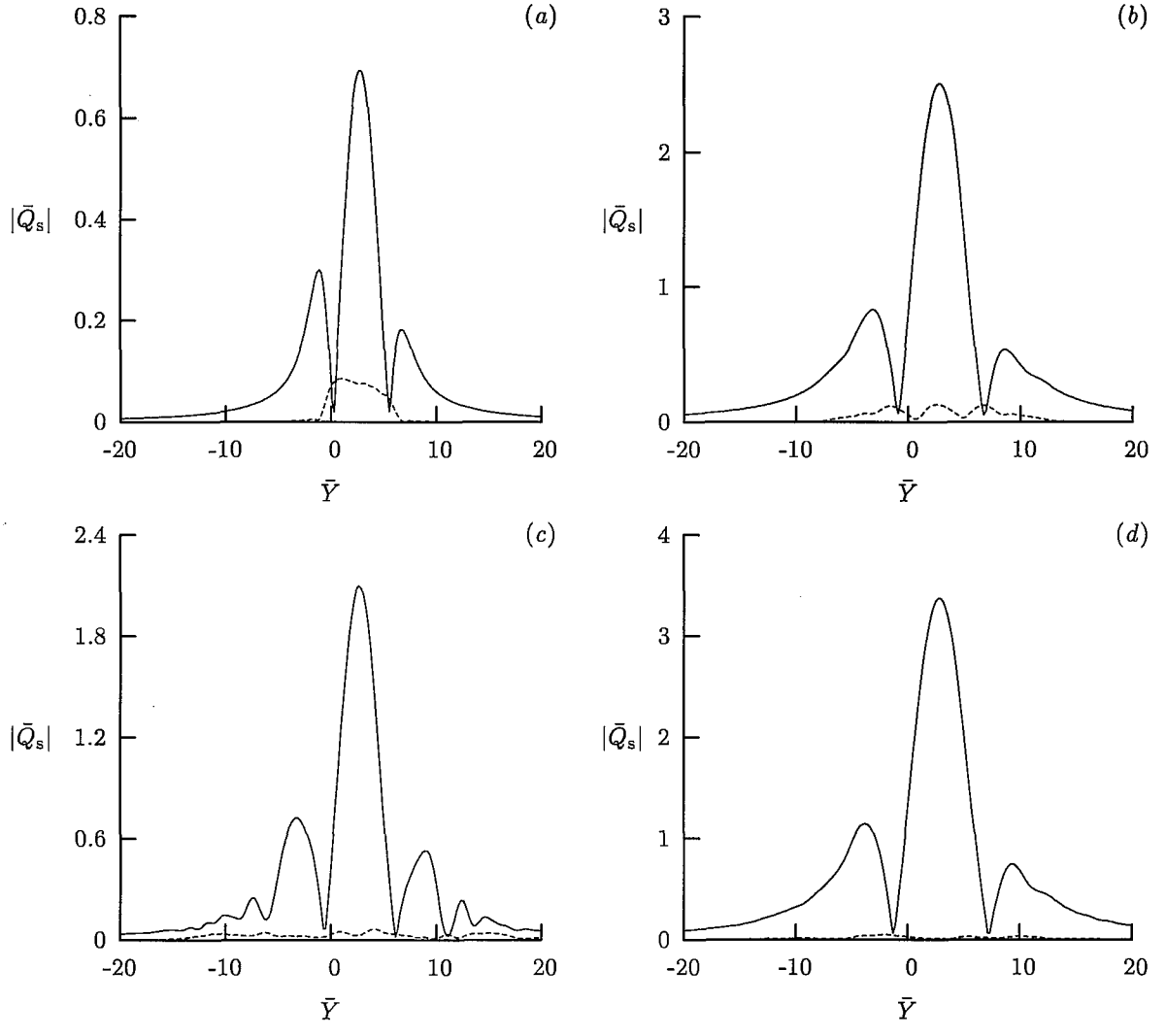


Figure 6.17: $|\bar{Q}_s|$ *vs.* $\bar{Y}$ for $\beta_T = 1$, $M = 0$, $\widehat{\Lambda} = 0.1$, $a = 1$, $a^- = \delta$ and $a^+ = (0.1)\delta$i: $|\bar{Q}_s| = |\bar{Q}_0^{(0)}|$ (solid), $|\bar{Q}_s| = |\bar{Q}_2^{(0)}|$ (dashed). (*a*) $\bar{\mathcal{X}} = 7.85$; (*b*) $\bar{\mathcal{X}} = 9.85$; (*c*) $\bar{\mathcal{X}} = 11.85$; (*d*) $\bar{\mathcal{X}} = 13.85$.

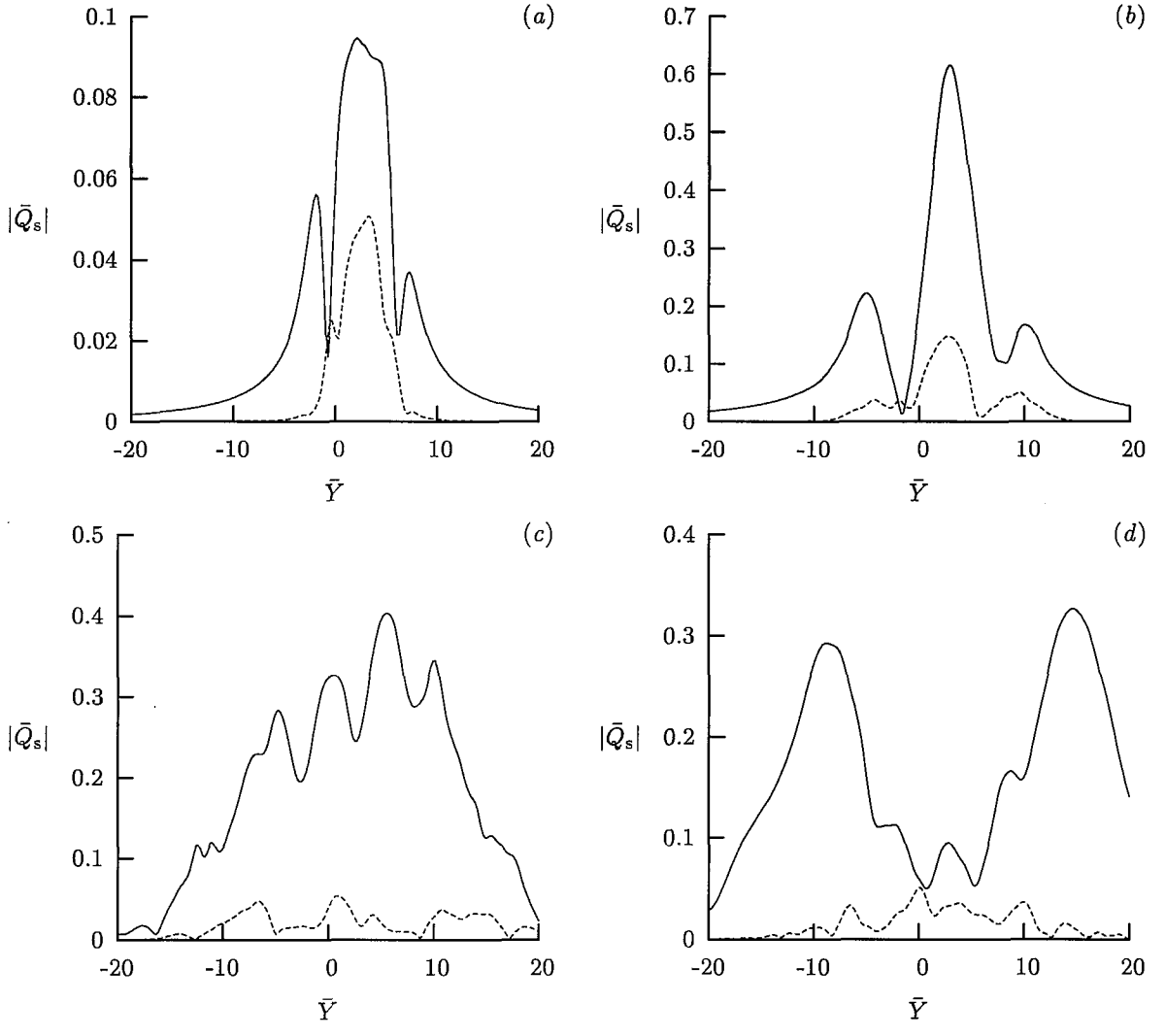


Figure 6.18: $|\bar{Q}_s|$ *vs.* $\bar{Y}$ for $\beta_T = 1$, $M = 0$, $\widehat{\Lambda} = 0.1$, $a = 1$, $a^- = \delta$ and $a^+ = (0.1)\delta$i: $|\bar{Q}_s| = |\hat{a}^+ \bar{Q}_0^{(1)}|$ (solid), $|\bar{Q}_s| = |\hat{a}^+ \bar{Q}_2^{(1)}|$ (dashed). (*a*) $\bar{\mathcal{X}} = 7.85$; (*b*) $\bar{\mathcal{X}} = 9.85$; (*c*) $\bar{\mathcal{X}} = 11.85$; (*d*) $\bar{\mathcal{X}} = 13.85$.

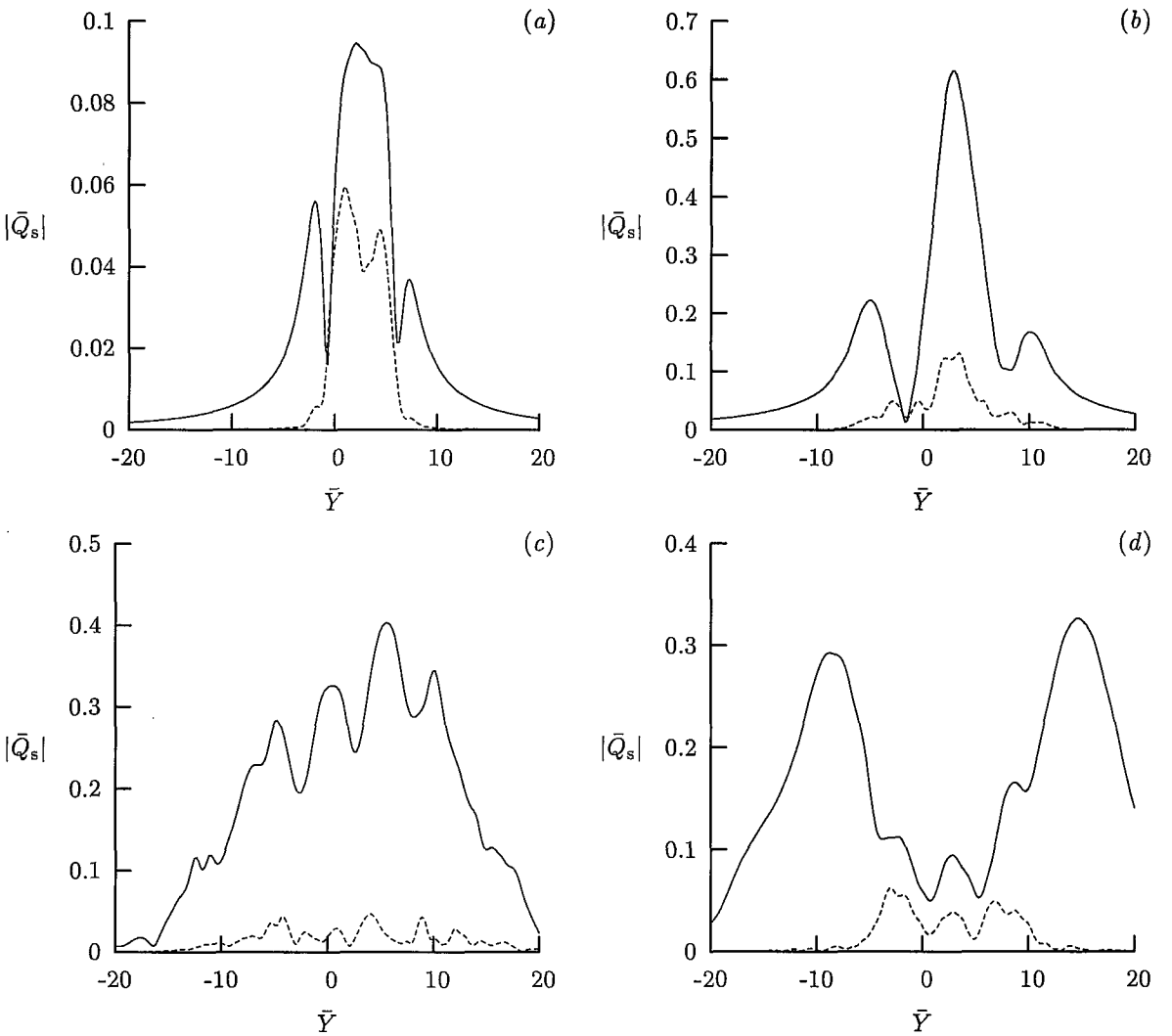


Figure 6.19: $|\bar{Q}_s|$ *vs.* $\bar{Y}$ for $\beta_T = 1$, $M = 0$, $\widehat{\Lambda} = 0.1$, $a = 1$, $a^- = \delta$ and $a^+ = (0.1)\delta$i: $|\bar{Q}_s| = |\hat{a}^+ \bar{Q}_0^{(-1)}|$ (solid), $|\bar{Q}_s| = |\hat{a}^+ \bar{Q}_2^{(-1)}|$ (dashed). (*a*) $\bar{\mathcal{X}} = 7.85$; (*b*) $\bar{\mathcal{X}} = 9.85$; (*c*) $\bar{\mathcal{X}} = 11.85$; (*d*) $\bar{\mathcal{X}} = 13.85$.

harmonics $|\hat{a}^{+}\bar{Q}_2^{(\pm 1)}|$. We notice that the profile of the difference-frequency component undergoes significant deformation. Most interestingly, their amplitude is larger than that of the harmonics by an order of magnitude, even though they are all generated by quadratic interaction of the waves. That the difference-frequency component attains an exceptionally large amplitude is consistent with experimental observation.

6.4 Conclusions

In this chapter, a mathematical description was given for the physical concept of sideband instability that has been put forth by experimentalists for mixing-layer transition. Numerical calculations performed for a disturbance consisting of a dominant fundamental mode and two sideband components revealed that the presence of the latter can substantially affect the development of the disturbance. For suitable initial conditions, the sideband interaction induced rapid amplification of the sideband perturbations, especially in the $\beta_T \neq 1$ case, with the fundamental remaining unaffected.

Continued growth of the sideband components leads to a fully interactive stage. For the case presented (with $\beta_T = 1$ and $M = 0$), the amplitudes underwent significant oscillation. The interaction also generated a difference-frequency mode with a large amplitude. These predictions are in agreement with experimental observations.

Chapter 7

Summary & Further Work

7.1 Summary

In this thesis, we carried out a theoretical investigation of the nonlinear instability of compressible mixing layers. Attention was focused on the regime of small to moderate Mach numbers, where subsonic modes play the dominant role in causing transition. Our primary interest was in predicting the nonlinear evolution of these modes, which required a careful analysis of critical-layer dynamics. By considering a distinguished weakly compressible regime, we presented a theory which "bridges" the strongly and weakly nonlinear critical-layer theories, which are formulated respectively for the incompressible limit and compressible regime with $\mathcal{O}(1)$ Mach numbers. The analysis was then extended to construct a composite theory uniformly valid for all Mach numbers $0 \leqslant M \sim \mathcal{O}(1)$. The theory was able to describe one of the most remarkable phenomenons in mixing-layer transition, namely vortex roll-up. The compressible weakly nonlinear theory, though formally valid for $M = \mathcal{O}(1)$, was found to be a poor approximation for the majority of parameters of interest.

The composite theory provides an efficient tool to study nonlinear instability and transition of mixing layers at high Reynolds numbers, which is still beyond the capability of current DNS. Since the predicted roll-up of vorticity and temperature contours is closely related to the mixing process, the theory allows us to assess how the latter may be affected by various parameters such as the Reynolds number R, the temperature ratio β_T and compressibility as measured by M. Mixing can be enhanced by increasing R, increasing $|\beta_T - 1|$, or a combination of both. Cooling the slow stream ($\beta_T < 1$) was found to enhance mixing relatively more than cooling the fast stream ($\beta_T > 1$).

When $\beta_T \neq 1$, the Mach number M had a relatively moderate effect on mixing. In contrast, when $\beta_T = 1$, the final roll-up (and hence mixing) appears to increase as M is increased, but the process takes a longer streamwise distance to complete. A decrease of velocity ratio β_U (i.e. an increase of overall shear) was found to cause slightly stronger mixing.

The effects of three different base-flow approximations on the development of the amplitude were examined. In general, use of the tanh mean profile approximation showed slight quantitative differences in amplitude behaviour as compared with the more accurate Lock profile. Use of the precise Sutherland viscosity law yielded virtually no improvement in results over use of the less exact Chapman viscosity law. This is consistent with previous stability studies, where use of the tanh profile has been shown to produce the most marked difference (e.g. Jackson & Grosch 1991). However, a *qualitative* difference in solution behaviour arises for the tanh profile, namely that when $\beta_T = 1$, weakly nonlinear theory degenerates to linear theory for all Mach numbers $M < M_{\max}$, as was noted in Leib (1991). Strongly nonlinear critical-layer theory must then be used to describe the dynamics in this case. This demonstrates that caution must be exercised when using the tanh profile for compressible stability studies.

In addition to investigating a single instability mode, nonlinear evolution of disturbances of the sideband form, consisting of a dominant fundamental mode and two other modes with similar frequencies, was considered. A sideband instability problem was formulated in order to put on a quantitative mathematical footing this physical concept, which was proposed by experimentalists some time ago. On assuming that the sideband modes have much smaller amplitudes, their governing equations can be linearised about the fundamental mode in the initial stage. It is found that for suitable initial conditions, one or both of the sideband perturbations undergo rapid amplification, thereby providing the first mathematical evidence of sideband instability.

The continued growth of the sideband modes leads to a second phase, where all three modes are fully interactive. Results were presented for $\beta_U = 1/2$, $\beta_T = 1$, $M = 0$ and moderately large R. It was found that the amplitudes oscillate in a rather irregular fashion, a remarkable phenomenon that has been observed in experiments. It was also found that nonlinear interactions generate a difference-frequency mode with a large amplitude, as has also been discovered empirically. In addition, all of the amplitudes slowly decay.

7.2 Further work

The strongly nonlinear uniformly valid theory presented in this thesis has been shown to capture some key qualitative characteristics of mixing-layer transition, most notably vortex roll-up and amplitude modulation in the case of sideband disturbances. Given the success of the theory in the incompressible limit (Goldstein & Hultgren 1988), it is believed that the present system could be further developed to make quantitative predictions in the fully compressible regime. To that end, it is necessary to lift the restriction of unit Prandtl number (which can be easily done), and more importantly to include the non-parallel flow effect. The theory may then be used to predict the spreading rate of shear-layer thickness under the influence of nonlinear wave interactions.

The present work is valid only for subsonic modes (i.e. M not too large), but it would be interesting to extend it into the large-M regime, for which three-dimensional supersonic modes dominate. This may be achieved by removing the assumption of coincident critical layer and generalised inflection point. One might expect that the weakly nonlinear limit would be an improved approximation for these larger Mach numbers, but a strongly nonlinear theory should be more accurate and provide a more complete description in this region of parameter space.

One of the main motivations for studying shear-layer instability and transition is to understand mixing. In the present case (as in many previous studies), we were only able to infer some qualitative and indirect information from hydrodynamic and thermodynamic aspects of the flow. A fully quantitative characterisation of mixing requires consideration of the transport of a scalar, or more realistically of binary species, in the vortical flow. We note that mixing is an important topic in itself. Much of the existing work assumes simple idealised vortical flow structures, for example regular cat's eye or Stuart's vortices, which do not fully represent developing vortices in true mixing layers. Since the present work has provided a relatively simple framework of describing these vortices, it is now possible to investigate mixing in more realistic models.

For most intended applications, flows are chemically reacting. A prime example is scramjet engines, which involve a chemically reacting mixing layer between fuel and oxidizer streams. To describe the mixing process, one must consider not only how the fluid motion affects the mixing of the chemical species, but also how the chemical reaction of the species affects the fluid motion through heat release. However, the majority of previous theoretical work considers chemical reaction, heat production

and transport in a prescribed hydrodynamical field, i.e., the effect of heat release on the flow is ignored. The present work is intended as a first step towards formulating a fully coupled theory for the two-way interaction described above. Chemical reactions would primarily take place within the critical layer, concentrating in particular in the regions where mixing is most thorough and the temperature is high. The fully interactive system would consist of additional equations for the species mass fractions, coupled to the vortical and temperature equations through heat and mass production. This problem is currently under investigation.

Appendix A

Complementary Solutions of Equations (4.4.37) & (4.4.38)

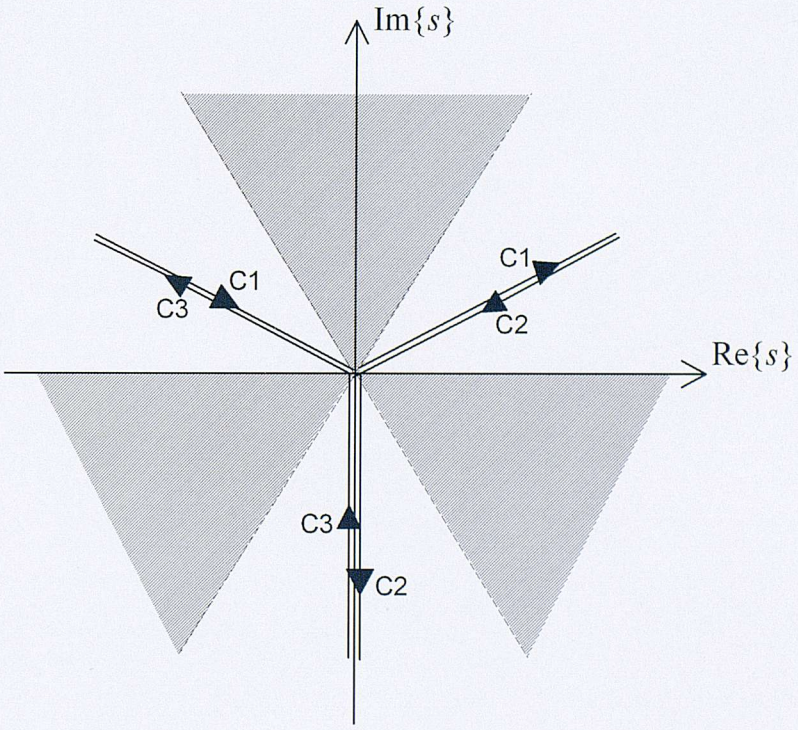


Figure A.1: Airy contours

Consider the solution of

$$\beta \frac{\mathrm{d}^2 \widehat{T}_{\mathrm{L}}}{\mathrm{d}\widehat{Y}^2} - \mathrm{i}\widehat{Y}\widehat{T}_{\mathrm{L}} - c\kappa\widehat{T}_{\mathrm{L}} = 0 \tag{A1}$$

where $\beta = \Lambda T_c \mu_c (\alpha U_c')^2$. Seeking a solution of the form

$$\widehat{T}_L(\widehat{Y}) = \int_C F(s) e^{s\widehat{Y}} ds$$

we obtain

$$\int_C \left\{ \frac{dF}{ds} + i(c\kappa - \beta s^2) F \right\} e^{s\widehat{Y}} ds - \left[F(s) e^{s\widehat{Y}} \right]_C = 0. \tag{A2}$$

We require finding F must be such that the integrand in (A2) is zero. Then, a contour C must be chosen such that the term in square brackets is zero. The function F is clearly

$$F = e^{i(\beta s^3/3 - c\kappa s)}.$$

We need C such that $|e^{i\beta s^3/3}| \to 0$ as $|s| \to \infty$. On writing $s = \rho e^{i\theta}$, it follows that either $0 < \theta < \pi/3$, $2\pi/3 < \theta < \pi$ or $4\pi/3 < \theta < 5\pi/3$. Thus there is some freedom in choice of contours. Here we will use the contours shown in figure A.1. Then three (non-independent) solutions of (A1) are

$$\widehat{T}_{L,i}(\widehat{Y}) = \int_{C_i} F(s) e^{s\widehat{Y}} ds, \qquad i = 1, 2, 3$$

with $\widehat{T}_{L,1} + \widehat{T}_{L,2} + \widehat{T}_{L,3} = 0$.

However, we require the integral of the solution of (A1) across the critical layer to be convergent. No linear combination of the $\widehat{T}_{L,i}$'s achieves this. For example,

$$\int_{-\infty}^{\infty} \widehat{T}_{L,1} d\widehat{Y} = 2 \int_0^{\infty} \frac{(e^{\sqrt{3}t} - e^{-\sqrt{3}t})}{t} \cos(t) dt$$

is divergent. Thus the complementary solution to (4.4.37) must be excluded.

Since the above analysis applies equally to $\widehat{Q}_L$, the complementary solution to (4.4.38) must also be excluded.

Appendix B

Role of β_U in the Critical-layer System

For the mean profile, the parameter β_U may in fact be scaled out. This leads to the benefit that the eigenvalue problem only needs to be solved once for all β_U. The nonlinear evolution system will also be re-scaled to make the dependence on β_U more explicit. Let

$$\widehat{U}^\dagger = \frac{2U_0 - (1+\beta_U)}{(1-\beta_U)}, \quad c^\dagger = \frac{2c - (1+\beta_U)}{(1-\beta_U)}, \tag{B1}$$

$$\widehat{T}^\dagger = T_0, \quad \widehat{M}^\dagger = \frac{1}{2}(1-\beta_U)M. \tag{B2}$$

Then it follows that

$$\widehat{U}^\dagger \to 1 \quad \text{as} \quad y \to +\infty, \qquad \widehat{U}^\dagger \to -1 \quad \text{as} \quad y \to -\infty, \tag{B3}$$

$$\widehat{T}^\dagger \to 1 \quad \text{as} \quad y \to +\infty, \qquad \widehat{T}^\dagger \to \beta_T \quad \text{as} \quad y \to -\infty. \tag{B4}$$

The Crocco relation becomes

$$\widehat{T}^\dagger = 1 - \frac{1}{2}(1-\beta_T)(1-\widehat{U}^\dagger) - \frac{1}{2}(\gamma-1)\widehat{M}^{\dagger 2}\Big[\widehat{U}^{\dagger 2} - 1\Big]. \tag{B5}$$

Now further let

$$x^\dagger = \frac{(1-\beta_U)}{2}x, \quad y^\dagger = \frac{(1-\beta_U)}{2}y, \quad t^\dagger = \frac{(1-\beta_U)c}{2c^\dagger}t, \quad \alpha^\dagger = \frac{2}{(1-\beta_U)}\alpha, \tag{B6}$$

$$\tilde{u}^\dagger = \frac{2}{(1-\beta_U)}\tilde{u}, \quad \tilde{v}^\dagger = \frac{2}{(1-\beta_U)}\tilde{v}, \quad \tilde{p}^\dagger = \frac{4}{(1-\beta_U)^2}\tilde{p}, \quad \widetilde{T}^\dagger = \widetilde{T}. \tag{B7}$$

These scalings give rise to

$$\zeta^\dagger = \alpha^\dagger(x^\dagger - c^\dagger t^\dagger) = \alpha(x-ct) = \zeta \tag{B8}$$

and

$$\widehat{\mathcal{L}}^{\dagger}\tilde{p}_0^{\dagger} = 0 \tag{B9}$$

where

$$\widehat{\mathcal{L}}^{\dagger} \equiv \frac{\partial^2}{\partial y^{\dagger 2}} + \left(\frac{\widehat{T}^{\dagger\prime}}{\widehat{T}^{\dagger}} - 2\frac{\widehat{U}^{\dagger\prime}}{(\widehat{U}^{\dagger} - c^{\dagger})}\right)\frac{\partial}{\partial y^{\dagger}} + \alpha^{\dagger 2}\left(\frac{\widehat{M}^{\dagger 2}(\widehat{U}^{\dagger} - c^{\dagger})^2}{\widehat{T}^{\dagger}} - 1\right),$$

which is independent of β_U. The coefficients J_2 and J_3 appearing in the solvability condition (2.4.76) can be made independent of β_U by writing

$$\widehat{J}_2^{\dagger} = \frac{2}{(1-\beta_U)}J_2, \quad \widehat{J}_3^{\dagger} = \frac{2}{(1-\beta_U)}J_3 \tag{B10}$$

The coefficient combination J_1 is re-written as

$$\widehat{J}_1^{\dagger} = \frac{2}{(1-\beta_U)}J_1 = \widehat{J}_2^{\dagger} + \frac{\alpha^{\dagger}}{c^{\dagger} + f(\beta_U)}\widehat{J}_3^{\dagger} \tag{B11}$$

which is *dependent* on β_U via $f(\beta_U)$, where

$$f(\beta_U) = \frac{(1+\beta_U)}{(1-\beta_U)}. \tag{B12}$$

By scaling the critical-layer equations (4.3.20)–(4.3.23) in the following manner

$$\bar{\bar{T}}^{\dagger} = \mathcal{T}, \quad \bar{\bar{\mathcal{X}}}^{\dagger} = \frac{\Omega}{2c}\mathcal{X}_1 - \bar{\bar{x}}_0, \quad \bar{\bar{Y}}^{\dagger} = \frac{2}{\Omega}\widehat{Y}, \quad \bar{\bar{\zeta}}^{\dagger} = \zeta + \arg a + \bar{\bar{x}}_0\bar{\bar{\kappa}}_{\mathrm{i}}^{\dagger} \tag{B13}$$

$$\bar{\bar{A}}^{\dagger} = \frac{8\alpha^2 U_{\mathrm{c}}'}{\Omega^2}\widehat{A}, \quad \bar{\bar{Q}}_m^{\dagger} = -\frac{4\alpha^2 U_{\mathrm{c}}'^2}{U_{\mathrm{c}}'''\Omega^2}\widehat{Q}_m, \quad \bar{\bar{T}}_m^{\dagger} = -\frac{4\alpha^2 U_{\mathrm{c}}'^3}{T_{\mathrm{c}}U_{\mathrm{c}}'''\Omega^2}\widehat{T}_m, \tag{B14}$$

$$\bar{\bar{\mathcal{M}}}^{\dagger} = -\mathrm{sgn}(T_{\mathrm{c}}')\frac{\alpha U_{\mathrm{c}}'^2|T_{\mathrm{c}M}'|}{T_{\mathrm{c}}U_{\mathrm{c}}'''\Omega}\mathcal{M}^2, \quad \bar{\bar{\Lambda}}^{\dagger} = \frac{8\alpha^2 U_{\mathrm{c}}'^2 T_{\mathrm{c}}\mu_{\mathrm{c}}}{\Omega^3}\Lambda, \tag{B15}$$

$$\bar{\bar{\kappa}}^{\dagger} = \frac{2c}{\Omega}\kappa, \quad \bar{\bar{x}}_0 = \frac{1}{\bar{\bar{\kappa}}_{\mathrm{r}}^{\dagger}}\ln\left(\frac{\Omega^2}{8\alpha^2 U_{\mathrm{c}}'|a|}\right), \tag{B16}$$

we can obtain the system

$$\left(\frac{\partial}{\partial\bar{\bar{\mathcal{X}}}^{\dagger}} + \mathrm{i}m\bar{\bar{Y}}^{\dagger}\right)\bar{\bar{T}}_m^{\dagger} + \frac{\mathrm{i}}{2}\frac{\partial}{\partial\bar{\bar{Y}}^{\dagger}}\left(\bar{\bar{A}}^{\dagger *}\bar{\bar{T}}_{m+1}^{\dagger} - \bar{\bar{A}}^{\dagger}\bar{\bar{T}}_{m-1}^{\dagger}\right) - \bar{\bar{\Lambda}}^{\dagger}\frac{\partial^2\bar{\bar{T}}_m^{\dagger}}{\partial\bar{\bar{Y}}^{\dagger 2}}$$
$$= \delta_{m,1}\left(\mathrm{i}\bar{\bar{\mathcal{M}}}^{\dagger 2}\bar{\bar{A}}^{\dagger} - \sigma_1^{\dagger}\left(\frac{1}{2}\frac{\mathrm{d}\bar{\bar{A}}^{\dagger}}{\mathrm{d}\bar{\bar{\mathcal{X}}}^{\dagger}} + \mathrm{i}\bar{\bar{A}}^{\dagger}\right)\right), \tag{B17}$$

$$\left(\frac{\partial}{\partial\bar{\bar{\mathcal{X}}}^{\dagger}} + \mathrm{i}m\bar{\bar{Y}}^{\dagger}\right)\bar{\bar{Q}}_m^{\dagger} + \frac{\mathrm{i}}{2}\frac{\partial}{\partial\bar{\bar{Y}}^{\dagger}}\left(\bar{\bar{A}}^{\dagger *}(\bar{\bar{Q}}_{m+1}^{\dagger} - \bar{\bar{T}}_{m+1}^{\dagger}) - \bar{\bar{A}}^{\dagger}(\bar{\bar{Q}}_{m-1}^{\dagger} - \bar{\bar{T}}_{m-1}^{\dagger})\right)$$
$$+ \bar{\bar{\Lambda}}^{\dagger}\frac{\partial^2}{\partial\bar{\bar{Y}}^{\dagger 2}}\left(\left(1 - \widehat{T}_{\mathrm{c}}^{\dagger}\frac{\hat{\mu}^{\dagger\prime}(\widehat{T}_{\mathrm{c}}^{\dagger})}{\hat{\mu}_{\mathrm{c}}^{\dagger}}\right)\bar{\bar{T}}_m^{\dagger} - \bar{\bar{Q}}_m^{\dagger}\right) = \delta_{m,1}(1+\sigma_1^{\dagger})\left(\frac{1}{2}\frac{\mathrm{d}\bar{\bar{A}}^{\dagger}}{\mathrm{d}\bar{\bar{\mathcal{X}}}^{\dagger}} + \mathrm{i}\bar{\bar{A}}^{\dagger}\right), \tag{B18}$$

$$\oint_{-\infty}^{\infty} \bar{\bar{Q}}_1^{\dagger}(\bar{\bar{\mathcal{X}}}^{\dagger}, \bar{\bar{Y}}^{\dagger}) \mathrm{d}\bar{\bar{Y}}^{\dagger} = 2\mathrm{i}\sigma_2^{\dagger}\left(\frac{1}{2}\widehat{J}_1^{\dagger}(\beta_U)\frac{\mathrm{d}}{\mathrm{d}\bar{\bar{\mathcal{X}}}^{\dagger}} + \mathrm{i}\widehat{J}_2^{\dagger}\right)\bar{\bar{A}}^{\dagger} \tag{B19}$$

and

$$\bar{\bar{A}}^{\dagger}(\bar{\bar{\mathcal{X}}}^{\dagger}) \to \mathrm{e}^{\bar{\bar{\kappa}}^{\dagger}\bar{\bar{\mathcal{X}}}^{\dagger}} \quad \text{as} \quad \bar{\bar{\mathcal{X}}}^{\dagger} \to -\infty \tag{B20}$$

where

$$\sigma_1^{\dagger} = -\frac{\widehat{U}_{y^{\dagger}\mathrm{c}}^{\dagger}\widehat{T}_{y^{\dagger}y^{\dagger}\mathrm{c}}^{\dagger}}{\widehat{T}_{\mathrm{c}}^{\dagger}\widehat{U}_{y^{\dagger}y^{\dagger}y^{\dagger}\mathrm{c}}^{\dagger}} = -\frac{U_{\mathrm{c}}' T_{\mathrm{c}}''}{T_{\mathrm{c}} U_{\mathrm{c}}'''} = \sigma \tag{B21}$$

and

$$\sigma_2^{\dagger} = -\frac{\widehat{T}_{\mathrm{c}}^{\dagger}\widehat{U}_{y^{\dagger}\mathrm{c}}^{\dagger 2}}{\alpha^{\dagger}\widehat{U}_{y^{\dagger}y^{\dagger}y^{\dagger}\mathrm{c}}^{\dagger}} = -\frac{(1-\beta_U)}{2}\frac{T_{\mathrm{c}} U_{\mathrm{c}}'^2}{\alpha U_{\mathrm{c}}'''}. \tag{B22}$$

Appendix C

Code Validation

In order to validate the numerical code, several checks were performed on the results obtained. These are listed below:

- The linear analytic solution was found to match the numerical solution in the upstream region.
- Selected results obtained in Goldstein & Hultgren (1988) were reproduced (see section below).
- Large $\bar{\mathcal{M}}$ solutions should match the weakly nonlinear solutions, which can be obtained from a simpler amplitude equation. This was verified.
- When $T_c' = 0$ and $T_c'' = 0$, $\bar{T}_m$ should be equivalent to zero, which was found to be the case in solving for $\bar{T}_m$.
- The usual resolution checks have been performed, such as halving streamwise step size l, halving transverse step size h, doubling transverse range H, starting the calculation further upstream (decreasing $\bar{\mathcal{X}}_s$) and adding corrector steps (increasing k) to ensure that none of these produce appreciable difference.
- Doubling the number of Fourier components, m, usually produced no notable improvement in calculating $\bar{A}$. A couple of points need to be explained here. One is that some solutions eventually always became numerically unstable regardless of the number of Fourier components used. The second is that for smaller $\bar{\Lambda}$, solutions benefit from using relatively more Fourier components for the smaller scales present in the vorticity and temperature rollers, but they do not affect the larger-scale structure nor the amplitude $|\bar{A}|$.

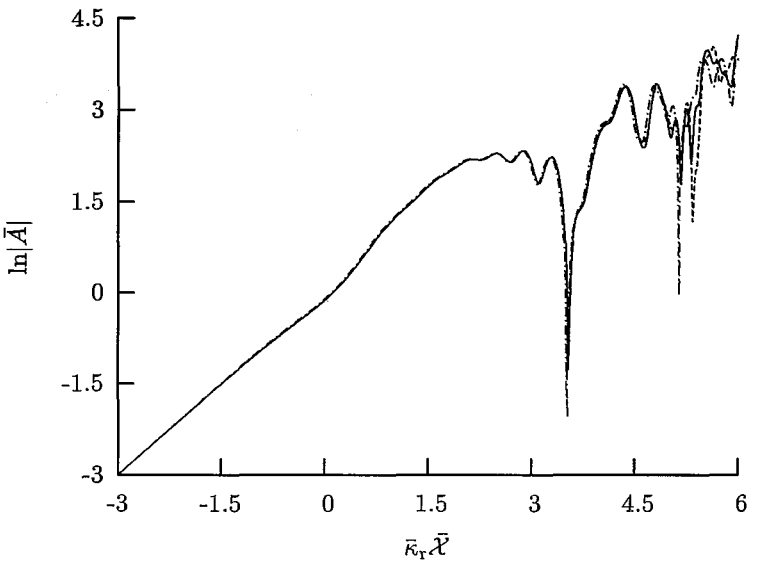


Figure C.1: Resolution check example 1: $\ln|\bar{A}|$ *vs.* $\bar{\kappa}_r\bar{\mathcal{X}}$. The parameters are $\beta_U = 1/2$, $\beta_T = 1/2$, $M = 2$, $\hat{\omega} = 1/40$ and $\hat{\Lambda} = 0.1$. Solid: $\bar{\mathcal{X}}_s$, l, h, H, m. Dashed: $\bar{\mathcal{X}}_s$, l, h, H, $m/2$. Dot-dashed: $\bar{\mathcal{X}}_s/2$, l, h, H, m.

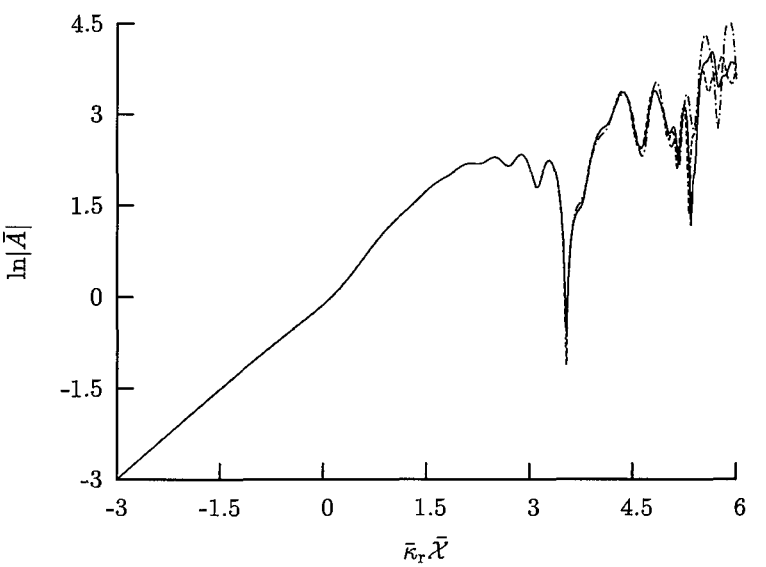


Figure C.2: Resolution check example 2: $\ln|\bar{A}|$ *vs.* $\bar{\kappa}_r\bar{\mathcal{X}}$. The parameters are $\beta_U = 1/2$, $\beta_T = 1/2$, $M = 2$, $\hat{\omega} = 1/40$ and $\hat{\Lambda} = 0.1$. Solid: $\bar{\mathcal{X}}_s$, l, h, H, $m/2$. Dashed: $\bar{\mathcal{X}}_s$, l, h, $H/2$, $m/2$. Dot-dashed: $\bar{\mathcal{X}}_s$, $2l$, $2h$, $H/2$, $m/2$.

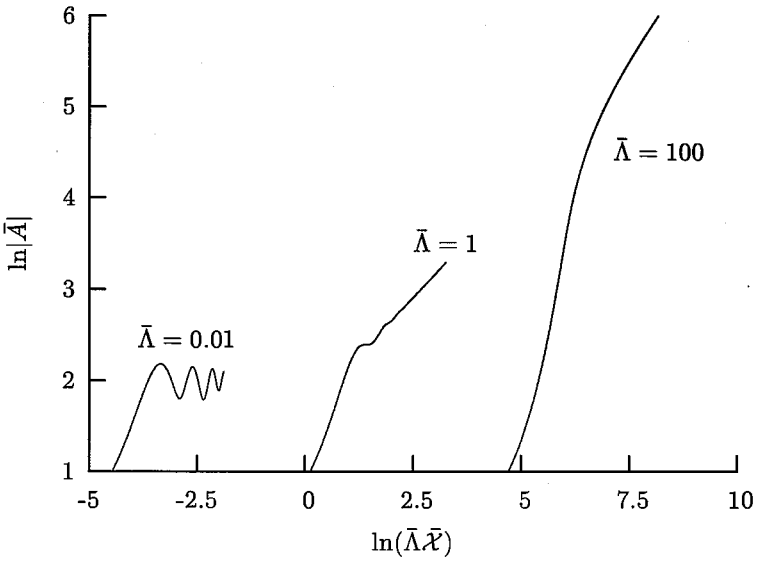


Figure C.3: Nonlinear development of the amplitude: $\ln|\bar{A}|$ *vs.* $\ln(\bar{\Lambda}\bar{\mathcal{X}})$. The parameters are $\bar{U} = 1$, $\beta_T = 1$, $M = 0$ and $\bar{\Lambda} = 0.01$, 1, 100.

Figures C.1 & C.2 show some of the effects of changing the resolution. The amplitude $\ln|\bar{A}|$ is plotted against $\bar{\kappa}_r\bar{\mathcal{X}}$, with chosen parameters $\beta_U = 1/2$, $\beta_T = 1/2$, $M = 2$, $\hat{\omega} = 1/40$ and $\hat{\Lambda} = 0.1$. This graph appears in figure 5.62, where the chosen resolution parameters were $\bar{\mathcal{X}}_s = -10$, $l = 2.5 \times 10^{-4}$, $h = 0.1$, $H = 200$, $m = 24$ and $k = 0$. We see that the solution remains acceptable up to around $\bar{\kappa}_r\bar{\mathcal{X}} = 5$. Increasing k made an undetectable graphical difference to these (and many other) results, and so these graphs have not been included.

Reproduction of Goldstein & Hultgren (1988) results

The principal result of Goldstein & Hultgren (1988), namely their equations (4.2) and (4.3), is the trivial limit $M \to 0$, $\beta_T \to 1$ of equations (4.3.30) and (4.3.31). In order to repeat the calculations, it is necessary to ensure that the relevant parameters are identical.

A slight modification to the basic velocity profile is required. Their profile, $U_{0,\mathrm{GH}}$ say, is related to U_0 through

$$U_{0,\mathrm{GH}} = \bar{U} + \tanh y = \frac{2U_0}{(1-\beta_U)} \tag{C1}$$

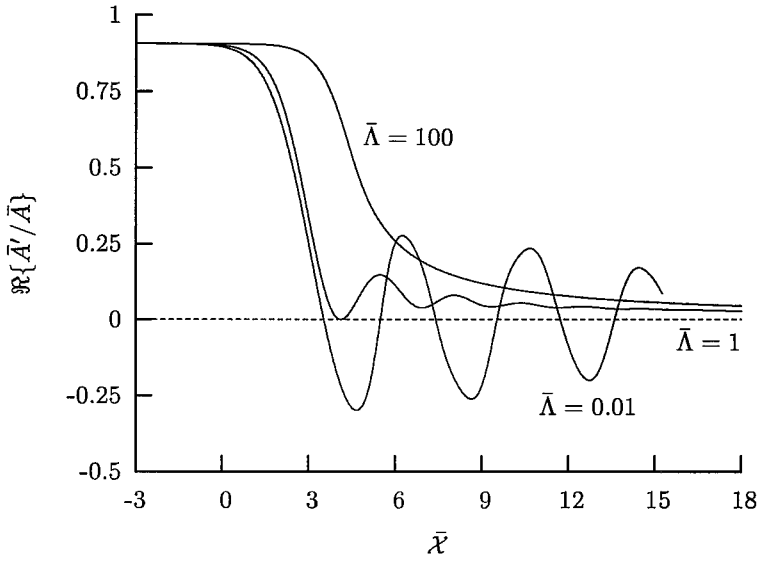


Figure C.4: Instantaneous growth rate $\Re\{\bar{A}'/\bar{A}\}$ *vs.* $\bar{\mathcal{X}}$.
The parameters are $\bar{U} = 1$, $\beta_T = 1$, $M = 0$ and $\bar{\Lambda} = 0.01$, 1, 100.

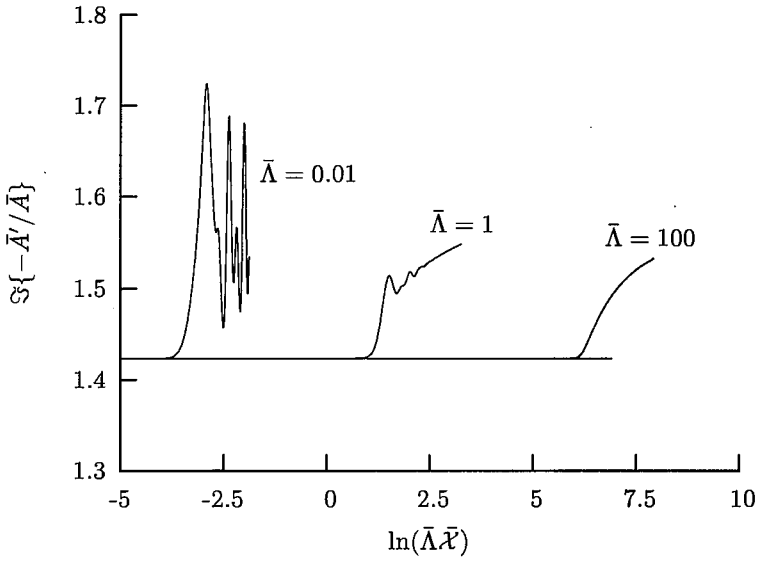


Figure C.5: Wavenumber correction $\Im\{-\bar{A}'/\bar{A}\}$ *vs.* $\ln(\bar{\Lambda}\bar{\mathcal{X}})$.
The parameters are $\bar{U} = 1$, $\beta_T = 1$, $M = 0$ and $\bar{\Lambda} = 0.01$, 1, 100.

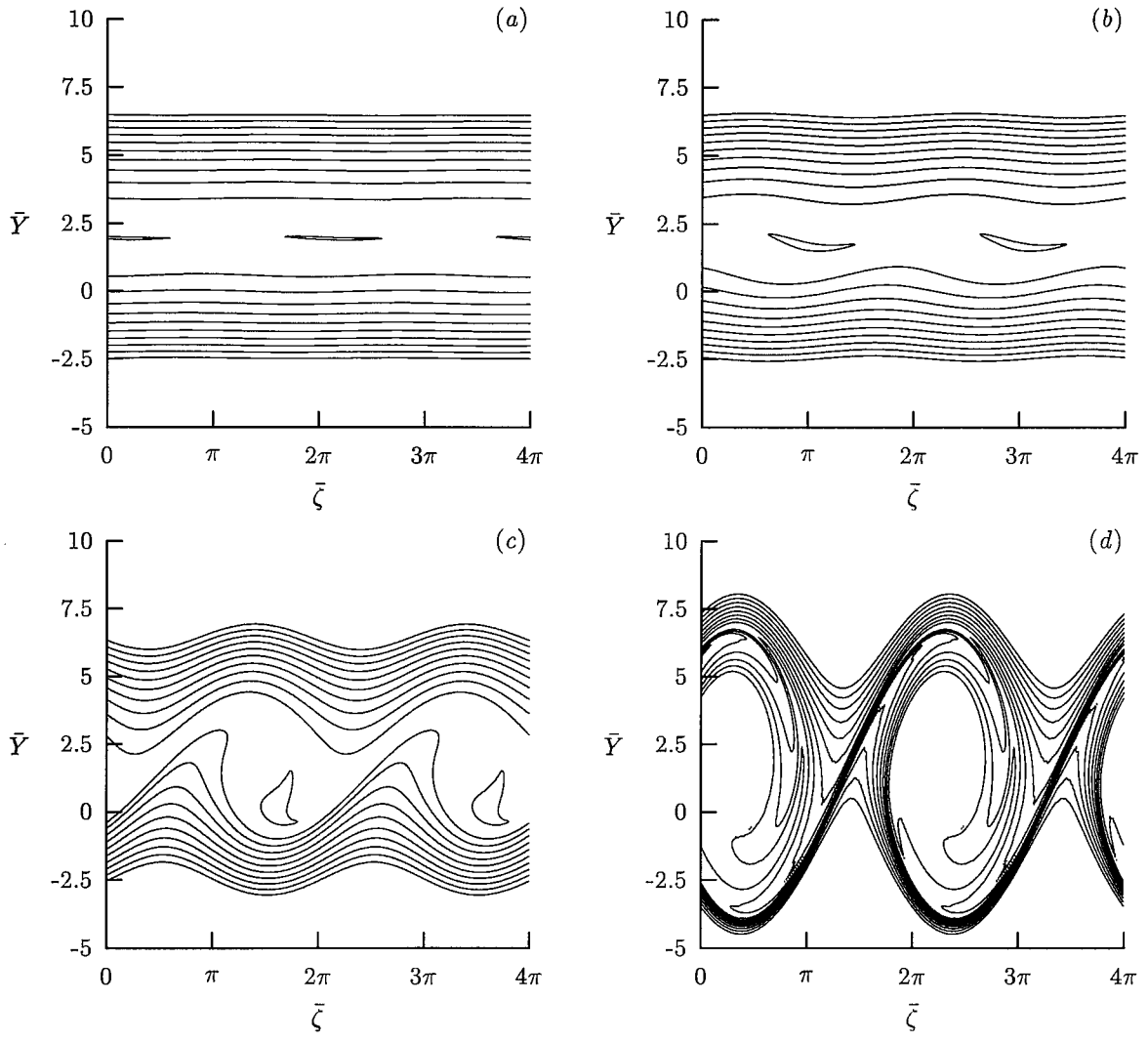


Figure C.6: Vorticity contours in the $(\bar{\zeta}, \bar{Y})$-plane at representative streamwise locations. The parameters are $\bar{U} = 1$, $\beta_T = 1$, $M = 0$ and $\bar{\Lambda} = 0.01$. Contour levels are 0, 2, 4, ..., 18 and 20. (a) $\bar{\mathcal{X}} = -3$; (b) $\bar{\mathcal{X}} = -1$; (c) $\bar{\mathcal{X}} = 1$; (d) $\bar{\mathcal{X}} = 3$. (Contour level 0 is omitted from plot (d).)

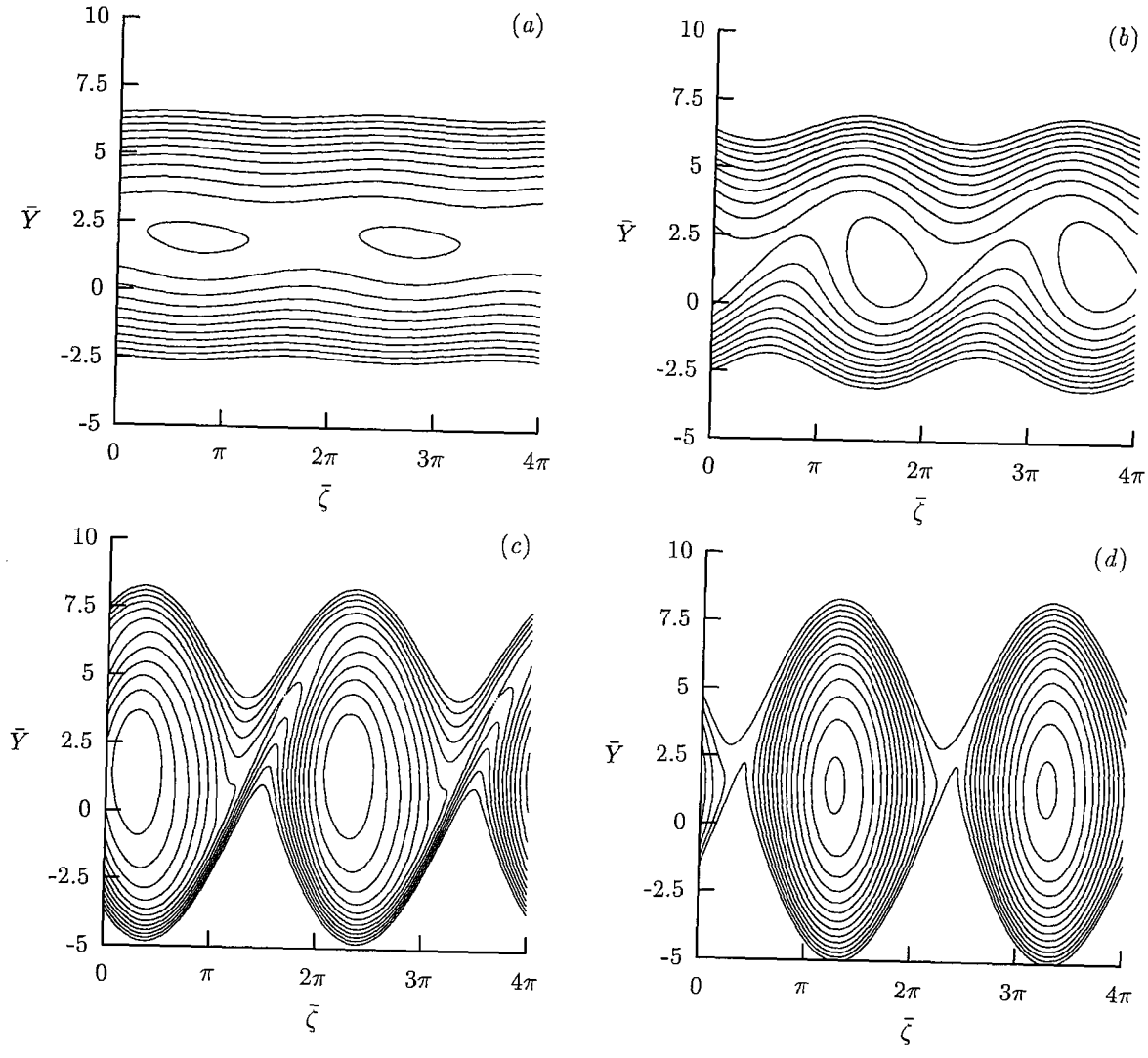


Figure C.7: Vorticity contours in the $(\bar{\zeta}, \bar{Y})$-plane at representative streamwise locations. The parameters are $\bar{U} = 1$, $\beta_T = 1$, $M = 0$ and $\bar{\Lambda} = 1$. Contour levels are 0, 2, 4, ..., 18 and 20. (a) $\bar{\mathcal{X}} = -1$; (b) $\bar{\mathcal{X}} = 1$; (c) $\bar{\mathcal{X}} = 3$; (d) $\bar{\mathcal{X}} = 5$. (Contour level -2 is added to plot (c); contour levels -6, -4 and -2 are added to plot (d).)

with $\bar{U} = (1+\beta_U)/(1-\beta_U)$, i.e. $\bar{U} = f(\beta_U)$ (see appendix B). Note that $\beta_T = 1$ and $M = 0$ imply $T_0 = 1$, and so $\eta = y$.

Since $\beta_T = 1$ and $M = 0$, then $T_c' = 0$ and $T_c'' = 0$, and hence $\bar{T}_m$ is identically zero, so that equation (4.3.30) is the same as their equation (4.2). Further, since $T_c = 1, U_c' = 1, U_c''' = -2$, $\alpha = 1$ and $\mu_c = 1$, the re-scalings (4.3.24)–(4.3.27) agree with their equations (3.9)–(3.15). The re-scaling of κ (see their equation (2.28)) and the factor 1/2 difference between (4.3.16) and their equation (4.1) must be taken into account. Equation (4.3.22) now reads

$$\int_{-\infty}^{\infty} \bar{Q}_1 \mathrm{d}\bar{Y} = -\frac{\mathrm{i}}{2} K_4 \frac{\mathrm{d}\bar{A}}{\mathrm{d}\bar{\mathcal{X}}}. \tag{C2}$$

Since $\tilde{p}_0 = \mathrm{sech} y$ is now the solution of equation (2.4.51), then $K_4 = -2$, and so equation (C2) reproduces their equation (4.3).

The nonlinear numerical method described in chapter 5 was used to solve the resulting simplified nonlinear system. Figures C.3–C.5 show the development of amplitude $\bar{A}$, instantaneous growth rate $\Re\{\bar{A}'/\bar{A}\}$ and wavenumber correction $\Im\{-\bar{A}'/\bar{A}\}$, for $\bar{U} = 1$ and three representative values of the viscous parameter $\bar{\Lambda}$. These results show excellent agreement with their figures $3(a)$, $2(a)$ and $4(a)$. Vorticity contours at selected streamwise locations for the $\bar{U} = 1$, $\bar{\Lambda} = 0.01$ and $\bar{U} = 1$, $\bar{\Lambda} = 1$ cases are displayed in figures C.6–C.7. Again these results are in close resemblance with their figures $5(a)$–$5(d)$ and $6(b)$–$6(e)$.

Acknowledgments

I would like to thank my supervisor, Dr. Xuesong Wu, for his useful advice, perseverance, and thorough understanding of the subject matter.

Financial support from the EPSRC is gratefully acknowledged.

Finally, I would to thank my family and friends for their continued support throughout my postgraduate study.

References

[1] AL-SALMAN, A. 2002 Nonlinear modal interactions in a compressible boundary layer. PhD thesis, University of London.

[2] BALMFORTH, N.J. & MORRISON, P.J. 1999 A necessary and sufficient condition for inviscid shear flow. *Stud. Appl. Math.* **102**, 309–344.

[3] BALSA, T.F. & GOLDSTEIN, M.E. 1990 On the instabilities of supersonic mixing layers: a high-Mach-number asymptotic theory. *J. Fluid Mech.* **216**, 585–611.

[4] BARRE, S., QUINE, C. & DUSSAUGE, J.P. 1994 Compressibility effects on the structure of supersonic mixing layers: experimental results. *J. Fluid Mech.* **259**, 47–78.

[5] BENNEY, D.J. & BERGERON, R.F. 1969 A new class of nonlinear waves in parallel flows. *Stud. Appl. Math.* **48**, 181–204.

[6] BETCHOV, R. & CRIMINALE, W.O. 1967 *Stability of Parallel Flows.* Academic Press, New York.

[7] BLACKABY, N., COWLEY, S.J. & HALL, P. On the instability of hypersonic flow past a wedge. *J. Fluid Mech.* **247**, 369–416.

[8] BLUMEN, W. 1970 Shear layer instability of an inviscid compressible fluid. *J. Fluid Mech.* **40**, 769–781.

[9] BLUMEN, W., DRAZIN, P.G. & BILLINGS, D.F. 1975 Shear layer instability of an inviscid compressible fluid. Part 2. *J. Fluid Mech.* **71**, 305–316.

[10] BOGDANOFF, D.W. 1983 Compressible effects in turbulent shear layers. *AIAA J.* **21**, 926–927.

[11] BROADWELL, J.E. & BREIDENTHAL, R.E. 1982 A simple model of mixing and chemical reaction in a turbulent shear layer. *J. Fluid Mech.* **125**, 397–410.

[12] BROWN, G.L. & ROSHKO, A. 1974 On density effects and large structure in turbulent mixing layers. *J. Fluid Mech.* **64**, 775–816.

[13] CHINZEI, N., MASUYA, G., KOMURO, T., MURAKAMI, A. & KUDO, K. 1986 Spreading of two-stream supersonic mixing layers. *Phys. Fluid* **29**, 1345–1347.

[14] CHURILOV, S.M. & SHUKHMAN, I.G. 1995 Three-dimensional disturbances to a mixing layer in the nonlinear critical-layer regime. *J. Fluid Mech.* **291**, 57–81.

[15] CLEMENS, N.T. & MUNGAL, M.G. 1995 Large-scale structure and entrainment in the supersonic mixing layer. *J. Fluid Mech.* **284**, 171–216.

[16] COWLEY, S.J. & HALL, P. 1990 On the instability of flow past a wedge. *J. Mech. Mech.* **214**, 17–43.

[17] CRAIK, A.D.D. 1985 *Wave Interactions and Fluid Flows.* Cambridge University Press.

[18] CURRAN, E.T., HEISER, W.H. & PRATT, D.T. 1996 Fluid phenomena in scramjet combustion systems. *Ann. Rev. Fluid Mech.* **28**, 323–360.

[19] DAVIS, R.E. 1969 On the high Reynolds number flow over a wavy boundary. *J. Fluid Mech.* **36**, 337–346.

[20] DAY, M.J., MANSOUR, N.N. & REYNOLDS, W.C. 2001 Nonlinear stability and structure of compressible reacting mixing layers. *J. Fluid Mech.* **446**, 375–408.

[21] DORODNITSYN, A.A. 1942 The boundary layer in a compressible gas. *Prikl. Mat. i. Mekh.* **6**, Pt. 6.

[22] DRAZIN, P.G. 2002 *Introduction to Hydrodynamic Stability.* Cambridge University Press.

[23] DRAZIN, P.G. & DAVEY, A. 1977 Shear layer instability of an inviscid compressible fluid. Part 3. *J. Fluid Mech.* **82**, 255–260.

[24] ELLIOTT, G.S., SAMIMY, M. & ARNETTE, S.A. 1995 The characteristics and evolution of large-scale structures in compressible mixing layers. *Phys. Fluids* **7**, 864–876.

[25] FJϕRTOFT, R. 1950 Application of integral theorems in deriving criteria of instability for laminar flows and for the baroclinic circular vortex. *Geofys. Publ., Oslo.* **17**, 1–52.

[26] GOLDSTEIN, M.E. & CHOI, S.W. 1989 Nonlinear evolution of interacting oblique waves on two-dimensional shear layers. *J. Fluid Mech.* **207**, 97–120; and Corrigendum **216**, 659–663.

[27] GOLDSTEIN, M.E. & HULTGREN, L.S. 1988 Nonlinear spatial evolution of an externally excited instability wave in a free shear layer. *J. Fluid Mech.* **197**, 295–330; and Corrigendum **281**, 403–404.

[28] GOLDSTEIN, M.E. & LEE, S.S. 1992 Fully coupled resonant-triad interaction in an adverse-pressure-gradient boundary layer. *J. Fluid Mech.* **245**, 523–551.

[29] GOLDSTEIN, M.E. & LEIB, S.J. 1988 Nonlinear roll-up of externally excited free shear layers. *J. Fluid Mech.* **191**, 481–515.

[30] GOLDSTEIN, M.E. & LEIB, S.J. 1989 Nonlinear evolution of oblique waves on compressible shear layers. *J. Fluid Mech.* **207**, 73–96.

[31] GOLDSTEIN, M.E. & WUNDROW, D.W. 1990 Spatial evolution of nonlinear acoustic mode instabilities on hypersonic boundary layers. *J. Fluid Mech.* **219**, 585–607.

[32] GROSCH, C.E. & JACKSON, T.L. 1991 Inviscid spatial stability of a three-dimensional compressible mixing layer. *J. Fluid Mech.* **231**, 35–50.

[33] GUTMARK, E.J., SCHADOW, K.C. & YU, K.H. 1995 Mixing enhancement in supersonic free shear flows. *Ann. Rev. Fluid Mech.* **27**, 375–417.

[34] HABERMAN, R. 1972 Critical Layers in Parallel Flows. *Stud. Appl. Math.* **51**, 139–161.

[35] HAJJ, M.R., MIKSAD, R.W. & POWERS, E.J. 1992 Subharmonic growth by parametric resonance. *J. Fluid Mech.* **236**, 385–413.

[36] HICKERNELL, F.J. 1984 Time-dependent critical layers in shear flows on the beta-plane. *J. Fluid Mech.* **142**, 431–449.

[37] HICKERNELL, F.J. 1985 An upper bound on the growth rate of a linear instability in a homogeneous shear flow. *Stud. Appl. Math* **72**, 87–93.

[38] HO, C. & HUERRE, P. 1984 Perturbed free shear layers. *Ann. Rev. Fluid Mech.* **16**, 365–422.

[39] HOWARD, L.N. 1961 Note on a paper of John W. Miles. *J. Fluid Mech.* **10**, 509–512.

[40] HOWARTH, L. 1948 Concerning the effect of compressibility on laminar boundary layers and their separation. *Proc. Soc. Lond.* A **194**, 16–42.

[41] HULTGREN, L.S. 1992 Nonlinear spatial equilibration of an externally excited instability wave in a free shear layer. *J. Fluid Mech.* **236**, 635–664.

[42] JACKSON, C.P. 1987 A finite-element study of the onset of vortex shredding in flow past variously shaped bodies. *J. Fluid Mech.* **182**, 23–45.

[43] JACKSON, T.L. & GROSCH, C.E. 1988 Spatial stability of a compressible mixing layer. *NASA CR*-181671.

[44] JACKSON, T.L. & GROSCH, C.E. 1989 Inviscid spatial stability of a compressible mixing layer. *J. Fluid Mech.* **208**, 609–637.

[45] JACKSON, T.L. & GROSCH, C.E. 1990 Absolute/convective instabilities and the convective Mach number in a compressible mixing layer. *Phys. Fluids A* **2**, 949–954.

[46] JACKSON, T.L. & GROSCH, C.E. 1991 Inviscid spatial stability of a compressible mixing layer. Part 3. Effect of thermodynamics. *J. Fluid Mech.* **224**, 159–175.

[47] JAMES, M.L., SMITH, G.M. & WOLFORD, J.C. 1993 *Applied Numerical Methods for Digital Computation: Fourth Edition.* Harper-Collins.

[48] KACHANOV, Y.S. 1994 Physical mechanisms of laminar boundary-layer transition. *Ann. Rev. Fluid Mech.* **26**, 411–482.

[49] KELVIN, W. 1880 On a disturbing infinity in Lord Rayleigh's solution for waves in a plane vortex stratum. *Nature* **23**, 45–46.

[50] LADEINDE, F. & WU, J. 2002 Second order nonlinear spatial stability analysis of compressible mixing layers. *Phys. Fluids* **14** (9), 2968–2986.

[51] LaFARA, R.L. 1973 *Computer Methods for Science and Engineering.* Hayden.

[52] LANDAU, L.D. 1944 On the problem of turbulence. *Dokl. Akad. Nauk SSSR* **44**, 311–314.

[53] LEES, L. & LIN, C.C. 1946 Investigation of the stability of the laminar boundary layer in a compressible fluid. *NACA TN*-1115.

[54] LESSEN, M., FOX, J.A. & ZIEN, H.M. 1965 On the inviscid stability of the laminar mixing of two parallel streams of a compressible fluid. *J. Fluid Mech.* **23**, 355–367.

[55] LESSEN, M., FOX, J.A. & ZIEN, H.M. 1966 Stability of the laminar mixing of two parallel streams with respect to supersonic disturbances. *J. Fluid Mech.* **25**, 737–742.

[56] LEIB, S.J. 1991 Nonlinear evolution of subsonic and supersonic disturbances on a compressible free shear layer. *J. Fluid Mech.* **224**, 551–578.

[57] LEIB, S.J. & LEE, S.S. 1995 Nonlinear evolution of oblique instability waves in a supersonic boundary layer. *J. Fluid Mech.* **282**, 339–371.

[58] LIN, C.C. 1945. On the stability of two-dimensional parallel flows. *Quart. Appl. Math.* **3**, 117–142, 213–234, 277–301 (1946).

[59] LIN, C.C. 1958 On the instability of laminar flow and its transition to turbulence. *IUTAM Symposium on Boundary Layer Research at Freiburg, 1957*, ed. H. Görtler. Springer-Verlag.

[60] LIU, J.T.C. 1989 Coherent structures in transitional and turbulent free shear flows. *Ann. Rev. Fluid Mech.* **21**, 285–315.

[61] LOCK, R.C. 1951 The velocity distribution in the laminar boundary layer between parallel streams. *Quart. J. Mech.* **4**, 42–63.

[62] LU, G. & LELE, S.K. 1993 Inviscid instability of a skewed compressible mixing layer. *J. Fluid Mech.* **249**, 441–463.

[63] MACK, L.M. 1984 Boundary layer linear instability theory. In *Special Course on Stability and Transition of Laminar Flow, AGARD Rep.* R–709, pp. 3–1–3–81.

[64] MACK. L.M. 1987 Review of linear compressible stability theory. In *Stability of Time Dependent and Spatially Varying Flows*, ed. D.L. Dwoyer & M.Y. Hussaini, pp. 164–187. Springer.

[65] MASLOWE, S.A. 1986 Critical layers in shear flows. *Ann. Rev. Fluid Mech.* **18**, 405–432.

[66] MASUTANI, S.M. & BOWMAN, C.T. 1986 The structure of a chemically reacting plane mixing layer. *J. Fluid Mech.* **172**, 93–125.

[67] McMURTRY, P.A., RILEY, J.J. & METCALFE, R.W. 1989 Effects of heat release on the large-scale structure in turbulent mixing layers. *J. Fluid Mech.* **199**, 297–332.

[68] MESSITER, A.F. & DAVIS, D. 1999 A note on nearly two-dimensional weakly nonlinear instability of an incompressible free shear layer. *J. Fluid Mech.* **386**, 373–377.

[69] MIKSAD, R.W. 1973 Experiments on nonlinear interactions in the transition of a free shear layer. *J. Fluid Mech.* **59**, 1–21.

[70] MIKSAD, R.W., JONES, F.L., POWERS, E.J., KIM, Y.C. & KHADRA, L. 1982 Experiments on the role of amplitude and phase modulations during transition to turbulence. *J. Fluid Mech.* **123**, 1–29.

[71] MILLER, M.F., BOWMAN, C.T. & MUNGAL, M.G. 1998 An experimental investigation of the effects of compressibility on a turbulent reacting mixing layer. *J. Fluid Mech.* **356**, 25–64.

[72] MUNGAL, M.G. & DIMOTAKIS, P.E. 1984 Mixing and combustion with low heat release in a turbulent shear layer. *J. Fluid Mech.* **148**, 348–382.

[73] OLSEN, M.G. & DUTTON, J.C. 2003 Planar velocity measurements in a weakly compressible mixing layer. *J. Fluid Mech.* **486**, 51–77.

[74] ORR, W.McF 1907 The stability or instability of the steady motions of a liquid. *Proc. Roy. Irish Acad. A* **27**, 69–138.

[75] OWEN, D.J., SEDDOUGUI, S.O. & OTTO, S.R. 1997 The linear evolution of centrifugal instabilities in curved, compressible mixing layers. *Phys. Fluids* **9**, 2056–2518.

[76] OWEN, D.J., SEDDOUGUI, S.O. & OTTO, S.R. 1998 The nonlinear evolution of centrifugal instabilities in curved, compressible mixing layers. *Phys. Fluids* **10**, 2080–2091.

[77] PAPAGEORGIOU, D.T. 1991 The stability of two-dimensional wakes and shear layers at high Mach numbers. *Phys. Fluids A* **3**, 793–802.

[78] PAPAMOSCHOU, D. & ROSHKO, A. 1988 The compressible turbulent shear layer: an experimental study. *J. Fluid Mech.* **197**, 453–477.

[79] PAVITHRAN, S. & REDEKOPP, L.G. 1989 The absolute-convective transition in subsonic mixing layers. *Phys. Fluids A* **1**, 1736–1739.

[80] RAGAB, S.A. & SHEEN, S. 1992 The nonlinear development of supersonic instability waves in a mixing layer. *Phys. Fluids A* **4**, 553–566.

[81] RAGAB, S.A. & WU, J.L. 1989 Linear instabilities in two-dimensional compressible mixing layers. *Phys. Fluids A* **1**, 957–966.

[82] RAYLEIGH, J.W.S. 1880 On the stability, or instability, of certain fluid motions. *Proc. Lond. Math. Soc.* **11**, 57–70.

[83] REYNOLDS, O. 1883 An experimental investigation of the circumstances which determine whether the motion of water shall be direct or sinuous, and of the law of resistance in parallel channels. *Phil. Trans. Roy. Soc. Lond. A* **174**, 935–982.

[84] ROSSMANN, T., MUNGAL, M.G. & HANSON, R.K. 2002 Evolution and growth of large-scale structures in high compressibility mixing layers. *J. Turbulence.* **3** (9), 1–18.

[85] SANDHAM, N. & REYNOLDS, W.C. 1991 Three-dimensional simulations of a compressible mixing layer. *J. Fluid Mech.* **224**, 133–158.

[86] SATO, H. 1970 An experimental study of nonlinear interaction of velocity fluctuations in the transition region of a two-dimensional wake. *J. Fluid Mech.* **44**, 741–765.

[87] SCHLICHTING, H. 1933 Zur Entstehung der Turbulenz bei der Plattenströmung. *Nachr. Ges. Wiss. Göttingen Math.-phys. Kl.* 1933, 181–208.

[88] SCHLICHTING, H. & GERSTEN, K. 2000 *Boundary-Layer Theory.* Springer-Verlag Berlin Heidelberg.

[89] SCHUBAUER, G.B. & SKRAMSTAD, H. 1947 Laminar boundary-layer oscillations and transition on a flat plate. *J. Nat. Bur. Standards* **38**, 251–292.

[90] SERRIN, J. 1959 On the stability of viscous fluid motions. *Arch. Rat. Mech. Anal.* **3**, 1–13.

[91] SMITH, F.T. 1979 On the Non-Parallel Flow Stability of the Blasius Boundary Layer. *Proc. Roy. Soc. Lond. A* **366**, 91–109.

[92] SMITH, F.T. & BROWN, S.N. 1990 The inviscid instability of a Blasius boundary layer at large values of the Mach number. *J. Fluid Mech.* **219**, 499–518.

[93] SOMMERFELD, A. 1908 Ein Beitrag zur hydodynamische Erklaerung der turbulenten Fluessigkeitsbewegungen. *Proc. 4th Intl Congr. Math.* Rome, vol. III, pp. 116–124.

[94] SQUIRE, H.B. 1933 On the stability of three-dimensional disturbances of viscous flow between parallel walls. *Proc. Roy. Soc. Lond. A* **142**, 621–628.

[95] STEWARTSON, K. 1964 *The Theory of Laminar Boundary Layers in Compressible Fluids.* Oxford Mathematical Monographs. Eds. Temple, G. & James, I. Oxford University Press.

[96] STEWARTSON, K. 1978 The evolution of the critical layer of a Rossby wave. *Geophys. Astrophys. Fluid Dyn.* **9**, 185–200.

[97] STUART, J.T. 1960 On the non-linear mechanics of wave disturbances in stable and unstable parallel flows. Part 1. *J. Fluid Mech.* **9**, 353–370.

[98] SWINNEY, H.L. & GOLLUB, J.P. (Editors) 1981 *Hydrodynamic Instabilities and the Transition to Turbulence.* Topics in Applied Physics (Volume 45). Springer-Verlag.

[99] TAM, C.K.W. & BURTON, D.E. 1984 Sound generated by instability waves of supersonic flows. Part 1. Two-dimensional mixing layers. *J. Fluid Mech.* **138**, 249–271.

[100] TAYLOR, G.I. 1923 Stability of a viscous liquid contained between two rotating cylinders. *Phil. Trans. Roy. Soc. Lond. A* **223**, 289–343.

[101] TOLLMIEN, W. 1929. Über die Entstehung der Turbulenz. *Nachr. Ges. Wiss. Göttingen Math.-phys. Kl.* 1929, 21–44.

[102] URBAN, W.D. & MUNGAL, M.G. 2001 Planar velocity measurements in compressible mixing layers. *J. Fluid Mech.* **431**, 189–222.

[103] VREMAN, A.W., SANDHAM, N. & LUO, K.H. 1996 Compressible mixing layer growth rate and turbulence characteristics. *J. Fluid Mech.* **320**, 235–258.

[104] WARN, T. & WARN, H. 1978 The evolution of a nonlinear critical level. *Stud. Appl. Math.* **59**, 37–71.

[105] WATANABE, S. & MUNGAL, M.G. 2005 Velocity fields in mixing-enhanced compressible shear layers. *J. Fluid Mech.* **522**, 141–177.

[106] WINANT, C.D. & BROWAND, F.K. 1974 Vortex pairing: the mechanism of turbulent mixing-layer growth at moderate Reynolds number. *J. Fluid Mech.* **63**, 237–255.

[107] WU, X. 1993 Nonlinear temporal-spatial modulation of near-planar Rayleigh waves in shear flows: formation of streamwise vortices. *J. Fluid Mech.* **256**, 685–719.

[108] WU, X. 1995 Viscous effects on fully coupled resonant-triad interactions: an analytical approach. *J. Fluid Mech.* **292**, 377–407.

[109] WU, X. 1996 On an active resonant triad of mixed modes in symmetric shear flows: a plane wake as a paradigm. *J. Fluid Mech.* **317**, 337–368.

[110] WU, X. 2005 Mach wave radiation of nonlinearly evolving supersonic instability modes in shear layers. *J. Fluid Mech.* **523**, 121–159.

[111] WU, X., LEE, S.S. & COWLEY, S.J. 1993 On the weakly nonlinear instability of shear flows to pairs of oblique waves: the Stokes layer as a paradigm. *J. Fluid Mech.* **253**, 681–720.

[112] WU, X. & STEWART, P.A. 1996 Interaction of phase-locked modes: a new mechanism for the rapid growth of three-dimensional disturbances. *J. Fluid Mech.* **316**, 335–372.